UNIVERSITY OF SÃO PAULO
SÃO CARLOS SCHOOL OF ENGINEERING
DEPARTMENT OF STRUCTURAL ENGINEERING

ALEX MICAEL DANTAS SOUSA

One-way shear and punching strength of reinforced concrete slabs without transverse reinforcement under concentrated loads

Cisalhamento unidirecional e resistência à punção de lajes de concreto armado sem armadura transversal sob cargas concentradas

SÃO CARLOS - SP
2022

ALEX MICAEL DANTAS SOUSA

One-way shear and punching strength of reinforced concrete slabs without transverse reinforcement under concentrated loads

(Corrected version)
Original version is available at São Carlos School of Engineering

PhD Thesis presented to the Graduate Program in Structural Engineering at the São Carlos School of Engineering, University of São Paulo, Brazil to obtain the degree of Doctor of Science.

Concentration area: Structures

Advisor: Mounir Khalil El Debs

Co-advisor: Eva Olivia Leontien Lantsoght

SÃO CARLOS - SP
2022

Ficha catalográfica elaborada pela Biblioteca Prof. Dr. Sérgio Rodrigues Fontes da EESC/USP com os dados inseridos pelo(a) autor(a).

S725o

Sousa, Alex Micael Dantas de

One-way shear and punching strength of reinforced concrete slabs without transverse reinforcement under concentrated loads / Alex Micael Dantas Sousa; orientador Mounir Khalil El Debs; coorientadora Eva Olivia Leontien Lantsoght. São Carlos, 2022.

Tese (Doutorado) - Programa de Pós-Graduação em Engenharia Civil (Engenharia de Estruturas) e Área de Concentração em Estruturas -- Escola de Engenharia de São Carlos da Universidade de São Paulo, 2022.

1. One-way shear strength. 2. Punching strength. 3. Reinforced concrete slabs without transverse reinforcement. I. Título.

Eduardo Graziosi Silva - CRB - 8/8907

FOLHA DE JULGAMENTO

Candidato: Engenheiro **ALEX MICAEL DANTAS DE SOUSA.**

Título da tese: "Cisalhamento unidirecional e resistência à punção de lajes de concreto armado sem armadura transversal sob cargas concentradas".

Data da defesa: 27/09/2022.

Comissão Julgadora	**Resultado**
Prof. Titular **Mounir Khalil El Debs (Orientador)** (Escola de Engenharia de São Carlos – EESC/USP)	Aprovado
Prof. Titular **Fernando Rebouças Stucchi** (Escola Politécnica/EP-USP)	Aprovado
Prof. Dr. **Daniel de Lima Araújo** (Universidade Federal de Goiás/UFG)	Aprovado
Prof. Dr. **Gustavo Henrique Siqueira** (Universidade Estadual de Campinas/UNICAMP)	Aprovado
Prof. Dr. **Maurício de Pina Ferreira** (Universidade Federal do Pará/UFPA)	Aprovado

Coordenador do Programa de Pós-Graduação em Engenharia Civil (Engenharia de Estruturas):
Prof. Associado **Vladimir Guilherme Haach**

Presidente da Comissão de Pós-Graduação:
Prof. Titular **Murilo Araujo Romero**

ACKNOWLEDGEMENTS

First of all, I would like to thank God for blessing me during all this time. I am sure that all people that arose during this Ph.D. time and that helped me to finish this work were promoted by Him. Since I left home, it has been a long way, and I'm sure he has been by my side until here.

I want to thank professor Mounir El Debs for guiding me since my Master's. It has been a long partnership, and I appreciate all the support and trust placed in my work so far. I also thank you for all the advice, support in the submitted projects, and freedom in constructing my doctorate.

I would like to thank professor Eva Lantsoght for supporting me since the beginning of my Ph.D. I thank you for believing in my potential to develop this work and for all the collaboration on several aspects of this work. It has been a great honor for me to have her collaboration in this PhD.

During this Ph.D., I also had the opportunity and honor to work in collaboration with other professors and researchers, which certainly helped me improve this work. I would like to thank professors Pablo Krahl, Aikaterini Genikomsou, Yuguang Yang and Andri Setiawan for collaborating on some parts of this work. I would also like to thank professor Daniel Araújo, Fernando Stucchi and Vladimir Haach for your encouraging comments and suggestions since my master's degree. And I want to thank professors Maurício Ferreira and Gustavo Siqueira for their valuable remarks on the Ph.D. defense.

This Ph.D. would not be possible without the help of many friends since my master's degree until this defense. I would like to thank to my friends Lucas Antônio, Bernardo Oliveira and Herbert Lopes, with whom I shared a home in São Carlos and many enjoyable moments. I also need to thank many friends that helped me during this time, especially Paula Oliveira, Henrique Barbosa, and Caio Silva, that helped in many aspects of this work since my master's. I would also like to thank my friends Bruno Bianchi, Fernanda Gabriella, José Renan, Filipe Malaquias, Ray Calazans, José Anchieta and Luis Philipe for all the help during the experimental program.

The experimental program from this study was performed in the Structures Laboratory at the São Carlos School of Engineering. I would like to thank all technicians that helped me during this time: Amauri, Mauri, Romeu, Fabiano and Dibo.

Last but not least, I would like to thank my wife Lisiane for all love and support during the time I had to be away. Your love, support and comprehension were always essential during this time. I want to thank here to my family, especially my mom Rejane, and my sisters Amanda and Andresa, for all their support until here.

The following research project would not be possible without the sponsorship from the São Paulo State Foundation for Research (FAPESP), grants #2018/21573-2 and # 2019/20092-3, and their support is greatly appreciated. This study was also financed in part by the Coordenação de Aperfeiçoamento de Pessoal de Nível Superior - Brasil (CAPES) - Finance Code 001.

ABSTRACT

SOUSA, A.M.D. **One-way shear and punching strength of reinforced concrete slabs without transverse reinforcement under concentrated loads.** Thesis (Ph.D), São Carlos School of Engineering, University of São Paulo, 2022.

Most studies that address the shear behavior of reinforced concrete slabs without transverse reinforcement deal with slab strips loaded over the entire width or the punching capacity of flat slabs or slab-column connections. Therefore, these studies focus on slabs subjected to specific shear failure mechanisms. However, in the case of concentrated or partially distributed loads in small areas close to the support of one-way slabs, a frequent situation in bridge deck slabs, both one-way shear and punching shear failure mechanisms can occur. This study developed recommendations to assess the shear and punching shear strength of such slabs using different approaches. In this study, some recommendations were developed that are based on the use of only analytical expressions, others combining analytical expressions with results from linear elastic finite element analyses, others using non-linear finite element analyses, and, finally, using experimental investigations. Since both shear failure mechanisms can be critical for such slabs, the research was addressed in parts. Firstly, the one-way shear behavior of wide beams and slabs loaded over the entire width was addressed. After, different approaches used to define the effective shear width were investigated, combined with code expressions and also mechanical-based models of one-way shear strength. In the next step, the research addressed the combination of analytical expressions with linear elastic finite element analyses to predict the shear and punching shear strength of one-way slabs. In the context of punching, the research addressed the behavior and punching resistance of slabs designed with the rational use of ultra-high-performance fiber-reinforced concrete. Non-linear finite element analyses were also proposed to assess the failure mechanism and ultimate capacity of different kinds of slabs. In the end, an experimental program was performed to investigate the failure mechanism of one-way slabs under concentrated loads after local reinforcement yielding. In summary, this study addresses different approaches to design reinforced concrete slabs under concentrated loads based on a comprehensive review and analyses of different tests from literature and also performed herein. Besides, the experimental program confirmed important aspects of the shear redistribution at failure that resulted in a clear activation of different failure mechanisms.

Key-words: One-way shear strength; shear force; punching capacity; reinforced concrete slabs without transverse reinforcement; concentrated loads.

RESUMO

SOUSA, A.M.D. **Cisalhamento unidirecional e resistência à punção de lajes de concreto armado sem armadura transversal sob cargas concentradas.** Tese (Doutorado), Escola de Engenharia de São Carlos, Universidade de São Paulo, 2022.

A maioria dos estudos que abordam o comportamento ao cisalhamento de lajes de concreto armado sem armadura transversal trata de tiras de laje carregadas em toda a largura ou da capacidade de punção de lajes lisas ou ligações laje-pilar. Portanto, esses estudos focam em lajes submetidas a um mecanismo específico de ruptura por cisalhamento. No entanto, no caso de cargas concentradas ou parcialmente distribuídas em pequenas áreas próximas ao apoio de lajes unidirecionais, uma situação frequente em lajes de tabuleiro, podem ocorrer tanto mecanismos de ruptura por cisalhamento unidirecional quanto por punção. Este estudo desenvolveu recomendações para avaliar a resistência ao cisalhamento ou força cortante e resistência à punção dessas lajes usando diferentes abordagens. Neste estudo, foram desenvolvidas recomendações baseadas apenas em expressões analíticas, outras combinando expressões analíticas com resultados de análises de elementos finitos elásticos lineares, outras usando análises de elementos finitos não lineares e, finalmente, usando investigações experimentais. Uma vez que ambos os mecanismos de ruptura por cisalhamento podem ser críticos para tais lajes, o trabalho foi abordado em partes. Primeiramente, foi abordado o comportamento ao cisalhamento unidirecional de vigas largas e lajes carregadas em toda a largura. Após, diferentes abordagens utilizadas para definir a largura efetiva ou colaborante na resistência à força cortante foram investigadas, combinadas com expressões de diferentes códigos de projeto e também modelos baseados na mecânica da resistência ao cisalhamento unidirecional. Na etapa seguinte, a pesquisa abordou a combinação de expressões analíticas com análises em elementos finitos elástico-lineares para prever a resistência ao cisalhamento e punção dessas lajes. No contexto da punção, a pesquisa abordou o comportamento e a resistência à punção de lajes projetadas com o uso racional de concreto de ultra-alto desempenho reforçado com fibras. Análises não lineares de elementos finitos foram propostas para avaliar o mecanismo de ruptura e a capacidade última de diferentes tipos de lajes. Ao final, foi realizado um programa experimental para investigar o mecanismo de ruptura de lajes unidirecionais sob cargas concentradas após o escoamento local das armaduras. Em resumo, este estudo aborda diferentes metodologias e ferramentas para avaliação de lajes de concreto armado sob cargas concentradas com base em uma ampla revisão da literatura, análise de diferentes ensaios da literatura e também realizados neste estudo. Além disso, o programa experimental confirmou aspectos importantes da redistribuição da força cortante na ruptura que resultaram em uma clara ativação de diferentes mecanismos de resistência.

Palavras-chave: Cisalhamento unidirecional; força cortante; resistência à punção; lajes de concreto armado sem armadura transversal; cargas concentradas.

LIST OF FIGURES

LIST OF TABLES

LIST OF NOTATIONS

α_{cc} factor that accounts for long term effects on the compressive strength and unfavorable effects from the way load is applied

α_s 40, 30 or 20 for interior, edge or corner columns, respectively (α_s = 40 was used)

α_e modular ratio (E_s/E_c) or

α_e fiber engagement parameter according Variable Engagement Model (VEM)

α_f fiber slenderness (l_f/d_f)

β_{rect} ratio of long side to short side of a concentrated load

β, $\beta_{arching}$ reduction factor for the contribution of loads close to the support to the shear force at the support

β_{CC} factor that controls the post-peak branch of the compressive stress-strain model from Carreira and Chu (1985)

β_1 factor relating depth of equivalent rectangular compressive stress block to neutral axis depth

γ_c partial safety factor for concrete

γ_{conc} concrete specific weight (assumed = 24 kN/m³ in this study)

ε_c compressive strain

ε_c^{in} inelastic compressive strain

ε_{c1} compressive strain corresponding to the peak compressive stress

ε_c^{pl} plastic compressive strain

ε_s steel strain

ε_t tensile strain

ε_t^{in} inelastic tensile strain

$\varepsilon_{t,cr}$ tensile strain at peak tensile stress

ε_t^{pl} tensile plastic strain

ε_x the longitudinal strain at mid-depth of the effective shear depth

ε_{ct} strain of concrete by reaching the tensile strength (CWSB)

ε_y flexural reinforcement yield strain

ε_{0c}^{el} elastic compressive strain

ε_{0t}^{el} elastic tensile strain

λ modification factor reflecting the reduced mechanical properties of lightweight concrete in the ACI 318:2019 or shear slenderness

λ_s Size effect modification factor on ACI 318:2019

μ Poisson's coeficiente or viscosity parameter (CDP)

ϕ rebar diameter

ϕ_{eq} equivalent rebar diameter

ζ combined size effect and slenderness factor on *SFSMM* and CCCM

$\mu_{,CSDT}$ friction coefficient for contact area between aggregate particles and matrix, with a proposed value $\mu = 0.4$ according to Walraven (1980)

$\mu_{,Sfsmm}$ dimensionless bending moment $\left(M / \left(f_{ct} \cdot b \cdot d \right)\right)$

ξ dimensionless neutral axis depth

ρ average flexural reinforcement ratio

ρ_l longitudinal reinforcement ratio

ρ_t transverse reinforcement ratio

ρ_s longitudinal reinforcement ratio

$\rho_{\rho,eff}$ reinforcement ratio in the effective area of concrete surrounding the reinforcement

ρ_f fiber volume content

σ normal stress

σ_c compressive stress

σ_{cf0} peak tensile strength of the UHPFRC

σ_{cp} average normal concrete stress over the cross-section, positive in compression (Brazilian code)

σ_{pu} crushing (yielding) strength of matrix, or contact stress at cracked surface

σ_{xm} average normal stress of concrete within the critical width of the shear band (CWSB)

σ_{b0}/σ_{c0} ratio of initial equibiaxial compressive yield stress to initial uniaxial compressive yield stress (CDP)

σ_t tensile stress

σ_{tf} fiber bridging stress

τ shear stress

τ_{ai} shear stress transferred by aggregate interlock

τ_{Rd} design shear capacity of the concrete

τ_{Rc} relative shear capacity, $\tau_{Rc} = V_{Rc} / (bd)$ (CWSB)

τ_c concrete shear capacity

τ_f average fiber-matrix interfacial bond stress

τ_{max} maximum shear stress at the neutral axis (CWSB)

τ_u allowable shear stress in the critical width of the shear band (CWSB)

ψ rotations around the loaded area

ψ_{ij} rotations in each side of the control perimeter

ψ_{CSCT} rotation of slab outside the column region in the CSCT

Δ shear displacement at crack

Δ_{cr} critical shear displacement

Δ_e distance between neutral axis and center of internal lever arm z

Ψ Dilation angle for the concrete damaged plasticity model (CDP)

a distance between the center of support and center of the load

a_v clear shear span: distance between the edge of support and edge of the load

a_t dimensionless coefficients from damage evolution models defined in Alfarah, López-Almansa and Oller (2017)

b width of the structural member

b_c dimensionless coefficients from damage evolution models defined in Birtel and Mark (2006)

b_{eff} effective shear width for one-way shear analyses

$b_{eff,french}$ effective shear width according to the French guidelines(FD P 18-717, 2013)

$b_{eff,prop}$ effective shear width with the proposed approach

b_n the clear width of the structural member

b_{load} size of the concentrated load in the slab width direction

b_{slab} slab width

b_s strip width used to calculate m for punching capacity analyses

b_t dimensionless coefficients from damage evolution models defined in Alfarah, López-Almansa and Oller (2017)

b_0 length of the critical perimeter at a distance $d_{avg}/2$ from the loaded area

$b_{0,red}$ reduced control perimeter

$b_{0,ij}$ side of the control perimeter

$b_{0,x1}$ lengths of segments of control perimeter corresponding to side x1

$b_{0,x2}$ lengths of segments of control perimeter corresponding to side x2

$b_{0,y}$ lengths of segments of control perimeter corresponding to side y1

c_{flex} height of the compression zone

c_{load} size of square plate load

c_{UHPFRC} strip width of the UHPFRC region in the plan

c_1 ; c_2 constants in the tension behavior model from Hordijk (1992)

l_{load}	Size of the concentrated load in the span direction
d_{avg}	average effective depth of reinforcement
d_{ag}	maximum size of the aggregate
d_f	fiber diameter
d_v	average effective depth of reinforcement
d *or* d_l	effective depth toward longitudinal steel
d_t	effective depth toward transverse steel
d_{max}	maximum aggregate size
d_g	maximum aggregate size
d_{g0}	reference aggregate size (= 16 mm)
d_{dg}	parameter that considerers the crack roughness
$d_{b,crit}$	critical width of the shear band (CWSB)
e	flow potential eccentricity (CDP)
f_c	concrete compressive strength
f_c'	average compressive strength of concrete measured on cylinder specimens
f_{ck}	characteristic concrete compressive strength
f_{cm}	mean value of the cylinder concrete compressive
f_{ctm} *or* f_{ct}	mean value of the concrete tensile strength
f_{ctd}	the design value of the concrete tensile strength
$f_{ctk,inf}$	tensile strength of the concrete in the lower quantile
$f_{ct2,f}$	tensile stress in steel fiber-reinforced concrete for w = 3 mm
$f_{c,UHPFRC}$	compressive strength of UHPFRC
$f_{c,NSC}$	compressive strength of NSC
f_{Ftu}	residual tensile strength at an ultimate crack opening w_u

f_y yield strength of reinforcement

f_{yi} steel yielding stress in the evaluated direction

h_{slab} slab thickness

h_{UHPFRC} thickness of the UHPFRC layer

k_b bond factor

k_1 coefficient considering the effects of axial forces on the stress distribution (0.15 in the European code to one-way shear)

k_{EC} factor taking into account the size effect according to NEN -EN 1992-1-1:2005

k_{NBR} factor taking into account the size effect according to ABNT NBR 6118:2014

k_c slope of stress line, k_c = 1.28 according to (KRIPS, 1985)

k_d factor determining the shear capacity in the Swiss Code SIA 262:2013

k_{dg} factor determining the shear capacity in the Swiss Code SIA 262:2013

k_g factor for accounting for the aggregate size d_g in the Swiss code SIA 262:2013

k_v factor accounting for strain effect and member size in the fib Model Code 2010

l_{eq} characteristics length related to the mesh size

l_{load} size of the concentrated load in the span direction

l_{span} span length

l_s length of the sides with one-way shear behavior

l_f fiber length

$l_{cr,m}$ spacing of two neighboring major cracks

m_{Ed} design (factored) moment per unit length in critical section

m_R nominal moment capacity per unit width

m_{Rd} plastic design (factored) moment per unit length in critical section

m_{RR} unitary radial moment

$m_{R,i}$ yielding moment per unit length in the evaluated direction

$m_{R,NSC}$ nominal moment capacity per unit width of a RC strip using only NSC

m_{max} maximum bending moment at the control section for a given applied load

$m_{s,ij}$ averaged acting bending moment at the loading plate edge *ij* within the width b_s

m_{R1} equivalent unitary moment capacity accounting for the distribution of UHPFRC in the slab thickness

m_{R2} equivalent unitary moment capacity accounting for the distribution of UHPFRC in the slab plan

n_e *or* n ratio between elastic modulus of steel and concrete

r_s distance from the column axis to the line of contra-flexure of the bending moments

$r_{s,ij}$ distance between the center of the concentrated load and the point of contraflexure

$s_{cr,CSDT}$ height of fully developed crack

$s_{cr,Sfsmm}$ location of the section where the critical shear crack starts

s_u location of the critical shear section

s_{rm} crack spacing of primary cracks

v shear force per unit length (nominal shear force)

v_{avg} averaged shear force (shear force per unit length)

$v_{c,shear}$ unitary/nominal one-way shear strength

$v_{c,min}$ minimum shear resistance per unit length in (SETIAWAN et al., 2020)

v_c dimensionless contribution to the shear strength of the un-cracked concrete chord (for SFSMM or MASM)

v_{perp} unitary shear force (shear force per unit length)

$v_{perp,max}$ maximum nominal shear force (shear force per unit length)

$v_{R,shear}$ unitary one-way shear resistance

$v_{c,punch}$ unitary/nominal punching strength

$v_{c,punch,eff}$ effective nominal punching strength available in the shear resisting control perimeter

v_{sw} nominal shear stress due to the self-weight and line loads (if available) on the sides considered of the control perimeter.

v_l dimensionless contribution to the shear strength of the longitudinal reinforcement (SFSMM or MASM)

v_s dimensionless contribution to the shear strength of the transverse reinforcement (SFSMM or MASM)

w crack width

w_b crack width at the bottom of the crack

w_c critical crack opening or fracture crack opening in Hordijk (1992)

w_k Crack opening of the primary cracks (CWSB)

w_u ultimate crack opening, assumed equal to $l_f/4$ (MOREILLON, 2013) for UHPFRC-flat slabs according to (MOREILLON, 2013) and $\psi_{CSCT} \cdot d/6$ for NSC-UHPFRC flat slabs

w_1 Crack opening to zero tensile stress of the concrete (CWSB)

x neutral axis depth

x' distance from the peak of the concrete tensile stress to the neutral axis (CWSB)

x'' height of the region with softening of concrete in the tension zone (CWSB)

x_0 distance from the critical shear crack to the support or loaded area CWSB)

x_1 distance from the control section to the support or loaded area (CWSB)

z length of the internal level arm or effective shear depth according to *fib* MC 2010, can be taken as $0.9d$

z_c depth of concrete compression zone

A_x, A_y projected areas of a cracked surface for a unit crack length in two directions

A_s longitudinal reinforcement area

A_{sw} area per unit length of the transverse reinforcement

A_g	gross area of concrete section
A_p	horizontally projected area of the punching shear failure surface
B	slab span length
$C_{Rd,c}$	calibrated semi-empirical coefficient in Eurocode shear strength formula
E_c	modulus of elasticity of concrete
E_s	elastic modulus of steel
F	applied concentrated load
F_{Ed}	design concentrated load
F_f	Fiber factor
$F_{predicted}$	predicted load that causes a one-way shear failure or two-way shear failure
F_{hyp}	arbitrary concentrated load
G_c	modulus of shear deformation for the un-cracked concrete chord
G_c	crushing energy
G_f	concrete fracture energy
$F_{predicted,shear}$	applied concentrated load that causes a one-way shear failure ($V_{predicted}$)
$F_{predicted,punching}$	applied concentrated load that causes a punching failure ($P_{predicted}$)
K_c	ratio of second stress invariants on tensile and compressive meridians (CDP)
K_f	global orientation factor for the Variable Engagement Model
K_{f0}	fiber orientation coefficient according to Model Code 2010
M	sectional moment
M_{cr}	cracking moment
M_{Ed}	design sectional moment
M_{max}	maximum bending moment of the shear span (CWSB)
N_{Ed}	design sectional axial load
P	applied punching load

P_c predicted punching capacity using the ACI 318-19 code expressions

$P_{c,proposed}$ predicted punching capacity using the proposed approach

P_{calc} Predicted punching capacity by an analytical method

P_{exp} experimental punching capacity

P_{flex} concentrated load associated with the slab flexural capacity

$P_{predicted}$ predicted punching capacity

P_{test} measured concentrated load F at failure (regardless of the governing failure mechanism)

P_{EN18} Predicted punching capacity by prEN 1992-1-1:2018

P_{Ed} design concentrated loads

P_{FEM} punching capacity predicted by the FE model or NLFEA

P_{Rd} design punching capacities

$P_{R,shear}$ total shear force resisted by one-way shear mechanisms for punching resistance analyses

$P_{R,punc}$ total shear force resisted by punching shear mechanisms

$P_{R,CSCT}$ punching capacity according with the CSCT

$P_{R,c,CSCT}$ mean value of the concrete contribution to the punching capacity according to CSCT

$P_{R,f,CSCT}$ mean value of the fiber contribution to the punching capacity according to CSCT

P_{Harri} punching capacity predicted by the expressions from Harris (2004)

V sectional shear force for a concentrated load F

V_{ai} shear force transferred by aggregate interlock

V_c shear force transferred in concrete compression zone

$V_{control}$ total shear force going through the evaluated direction along the slab width

V_{calc} Calculated shear force strength

V_d	shear force transferred by dowel action
V_{exp}	Experimental shear force strength from the database tests
$V_{exp,red}$	Experimental shear force reduced by the parameter β
V_f	fiber volume content in percentage
$V_{predicted}$	predicted shear resistance
V_{test}	maximum sectional shear achieved in the tests
V_{AASHTO}	one-way shear capacity calculated according to AASHTO
V_{CEN}	one-way shear capacity calculated according to NEN 1992-1-1:2005
V_{Ed}	design shear force
V_{NB}	shear capacity calculated according to ABNT NBR 6118:2014
V_{EC}	shear capacity calculated according to EN 1992-1-1:2005 (EC)
V_{ACI-14}	shear capacity calculated according to ACI 318-14
V_{ACI-19}	shear capacity calculated according to ACI 318-19
V_{MC}	shear capacity calculated according to Model Code 2010
V_{SIA}	shear capacity calculated according to SIA 262:2013
V_{SFSMM}	shear capacity calculated according to SFSMM
V_{CCCM}	shear capacity calculated according to CCCM
V_{CSDT}	shear capacity calculated according to CSDT
V_{CWSB}	Shear capacity calculated according to CWSB
V_{Fu}	sectional shear force for the maximum applied load F_u (at failure)
V_{Rd}	design shear capacities
$V_{R,CSCT}$	predicted one-way shear resistance with the CSCT expressions
$V_{R,ij}$	punching shear strength corresponding to $b_{0,ij}$
V_{test}	sectional shear force at failure (regardless of the governing failure mechanism)
$V_{predicted}$	predicted sectional shear capacity

$V_{c,proposed}$	predicted sectional shear capacity using the proposed recommendations
AVG	Average value
ACI	American Concrete Institute
COV	coefficient of variation
CDP	Concrete Damaged Plasticity
CSCT	Critical Shear Crack Theory
CSDT	Critical Shear Displacement Theory
CWSB	Critical Width of the Shear Band
CCCM	Compression Chord Capacity Model
SFSMM	Shear Flexure Strength Mechanical Model
MCFT	Modified Compression Field Theory
SMCFT	Simplified Modified Compression Field Theory
MIN	Minimum value
NSC	Normal strength concrete
SS	Experiment carried out close to simple support of the slab
CS	Eperiment carried out close to continuous support of slab
CT	Experiment carried out on cantilever slab
WB	Observed failure mode is wide beam shear failure
P	Observed failure mode is punching failure
WB+P	Observed failure mode combines characteristics of WB and P
UHPFRC	Ultra-high performance fiber-reinforced concrete

SUMMARY

1 INTRODUCTION

In this chapter, the following aspects of the research are described: (i) context, (ii) motivation of the research, (iii) aim of the research and (iv) research strategy and thesis outline.

1.1 Context

The shear and punching capacities can govern the design of reinforced concrete (RC) slabs subject to high concentrated loads or loads partially distributed in small areas. For economic or constructive reasons, design solutions that do not require the use of shear reinforcement are commonly prioritized. An example is the design of bridge deck slabs or foundation structures, in which shear reinforcement can lead to rebar congestion and hamper the reinforcement assembly in the formwork. Unlike other failure mechanisms, such as those associated with flexure, shear and punching failures are brittle and may develop without any signals of risk or warning to the users. For this reason, failures due to shear forces have historically been marked by significant losses of financial and human resources, as in the failure of the La Concorde viaduct (Canada) in 2006 (CALVI; BENTZ; COLLINS, 2018) and in the failure of the American air force hangar in 1955 (YANG, 2014).

A solution widely used to minimize the risk of this failure mechanism is to increase the thicknesses of slabs and beams. However, this solution increases the cost related to the concrete consumption and actions from self-weight on the whole structure. Solutions related to increasing the reinforcement ratios or from the specified concrete strengths are also used. Nevertheless, these solutions also considerably increase the costs of the new structures. In this context, a less-discussed solution is the use of enhanced expressions and approaches to estimate the shear and punching capacity. At this point, for instance, using more accurate expressions to calculate the load-carrying capacity of the members can allow using slabs with lower thickness previously rated as critical in shear by more conservative expressions.

Nowadays, another problem draws attention in assessing older structures, such as bridges-built decades ago, using current design codes. In other words, these structures were frequently designed to serve a less heavy design truck (action side). Besides, these designs used resistance expressions less conservative than the current ones (the predicted nominal shear capacity frequently decreases when using new design expressions calibrated by reliability analyses). Therefore, slabs designed decades ago can be rated as critical in shear using the current design codes of actions and resistance (LANTSOGHT; VAN DER VEEN;

WALRAVEN, 2013; REIßEN, 2016). In these structures, the shear and punching resistances can limit the increase of live loads, for example, or indicate the need for strengthening to fulfill updated codes of practice. (LANTSOGHT et al., 2016). Therefore, for economic and safety reasons, many researchers have been trying to develop enhanced models to estimate slabs' shear and punching capacities, combining satisfactory levels of accuracy, precision and reliability in relation to the real resistance of the elements.

In this context, older structures may also benefit from the compressive strength increase with time due to the delayed hydration of cementum. At this point, the resistance increase after some decades may be significant. In the same way, some structures may also show deficient resistances due to pathological processes. Therefore, in the evaluation of existing structures, it is important to evaluate not only the current design codes and loads but also the real materials' resistance after some decades.

Besides, another aspect shall be pointed with relation to the loads used for the assessment of existing structures. In practice, the service loads from real vehicles are lower than that used in the design (on average). Moreover, the tire area of loading may be significantly greater than that considered in the design truck because of the combination of several wheels to distribute the loading in the heavier axes. Therefore, the evaluation of bridge deck slabs from the design to the service conditions may require the consideration of several aspects. In this study, the scope remained mainly in the evaluation and interpretation of laboratory tests, which represents the first step to improving the understanding of some parts of the real problems, mainly that related to the shear and punching resistance.

One of the types of slabs most frequently rated as critical in shear (despite no signal of distress) are the one-way slabs from solid slab bridges (for instance, Figure 1-1). The main actions on these structures are the concentrated loads from design vehicles (Figure 1-1b). In practice, testing full-scale slab bridges is not frequent for several reasons (economical, technical, etc.). Because of this, this problem is most commonly studied in small-scale experiments, in which the full-design truck can be represented as only one concentrated load over the slab (Figure 1-1c). However, it is also frequently assumed that the concentrated loads from the tests represent only one of the wheel loads from the design truck. In this way, the effect of the superposition of concentrated loads close to the supports is not considered (in practice, the superposition of concentrated loads makes the loading less concentrated in small areas and increases the shear capacity of the slabs for both shear and punching). Therefore, there are two

possible interpretations for such scaling of the tests: (i) one assumes that the concentrated load represents the whole design vehicle and (ii) the other assumes that the concentrated load from the test represents only one of the wheels from the design truck.

Figure 1-1 – Example of one-way slab bridge; b) layout of the design truck according to the Brazilian codes over the slab; c) example of reduced scale tests found in the literature (dimensions in m).

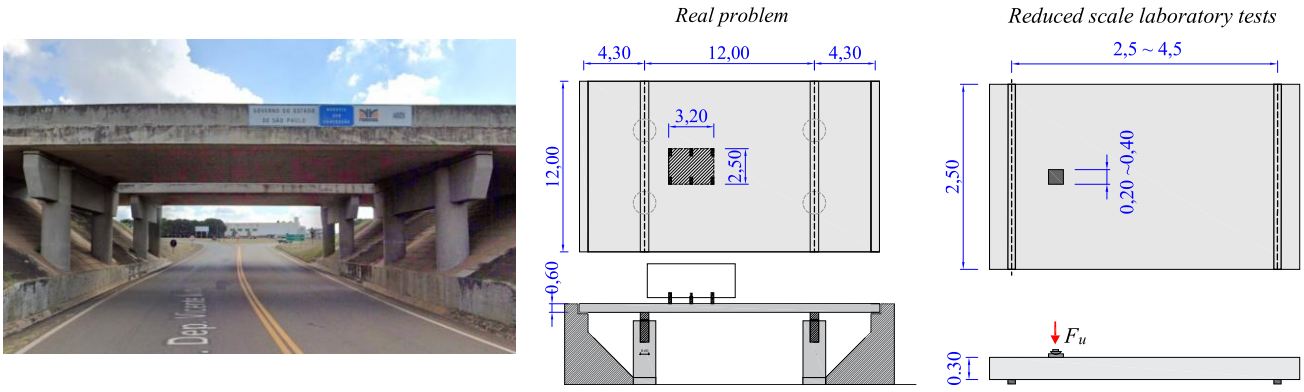

Source: Author.

1.2 Motivation

One-way slabs under concentrated loads develop a flow of forces that, in some aspects, resembles the one-way shear of slabs loaded over the entire width (Figure 1-2a) and also the two-way shear behavior of slab-column connections or flat slabs (Figure 1-2b). For instance, in Figure 1-2c, the flow of forces close to the support tends to be linear, with flow lines almost parallel between each other, reaching the support. Conversely, around the load, the flow lines tend to present a most radial pattern, which is characteristic of punching failures (NATÁRIO; FERNÁNDEZ RUIZ; MUTTONI, 2014). Therefore, both kinds of shear failure mechanisms can be critical for such slabs.

In the literature, the problem of one-way slabs under concentrated loads is frequently evaluated by looking only at the one-way shear failure mechanism (HALVONIK; VIDAKOVIĆ; VIDA, 2020; HENZE; ROMBACH; HARTER, 2020; REIßEN; CLASSEN; HEGGER, 2018). Consequently, the interpretation of test results and proposed recommendations are devised from a narrower perspective. For instance, the proposed models of effective shear width may not work well for the tests failing by punching. In the same way, the existing approaches to evaluate the punching capacity may not work well for one-way slabs that are critical in one-way shear. Since the most critical failure mechanism of a slab may not be easily determined without a test or advanced non-linear finite element models, both one-way

shear and punching shear approaches should provide close predictions of ultimate capacity regardless of whether the most critical failure mechanism is one or other. Therefore, there is a need for more studies addressing both failure mechanisms and including recommendations for both shear and punching capacity predictions.

Figure 1-2 – Sketches of imaginary tests with the expected cracking pattern and shear flow for: a) beams and slabs loaded over the entire width; b) slab-column connections under concentric loads; and c) one-way slabs under concentrated loads close to the line support (the shear flow to the far support was omitted in the sketch for simplicity).

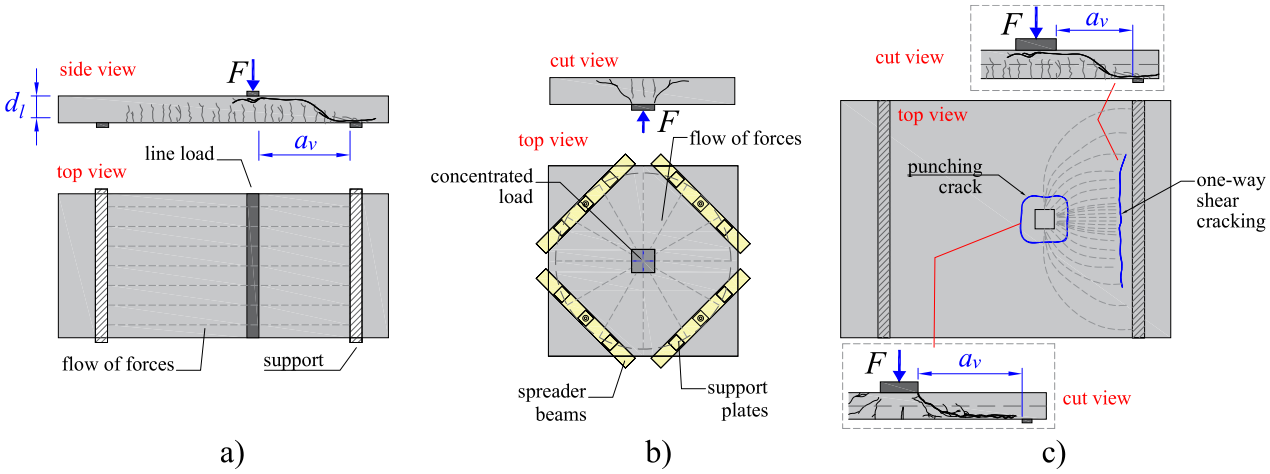

Source: Author.

In the context of existing approaches for predicting the shear and punching capacity of one-way slabs under concentrated loads, some aspects need to be considered. When evaluating the one-way shear capacity of slabs under concentrated loads, it is frequently assumed that only a slab strip, called effective shear width b_{eff} (see example in Figure 1-3a), contributes to the one-way shear capacity V_R (LANTSOGHT; VAN DER VEEN; WALRAVEN, 2013). In general, this approach leads to good levels of accuracy when evaluating one-way slabs under concentrated loads close to the support. Herein, it is assumed that the load is close to the support when the load is placed at distances $a_v < 2d_l \sim 3d_l$, where a_v is the clear distance between the front sides of the load and support, and d_l is the effective depth of the slab towards the longitudinal reinforcement. However, when the loads are placed at higher distances from the support, most approaches to calculating the effective shear width overestimate the length of the contributing width, and the predictions of sectional shear capacity frequently stay on the unsafe side (SOUSA et al., 2021c). In such cases, the punching failure mechanism commonly governs (as it will be shown in the next sections, Figure 4-11). At this point, it would not be critical if the predicted load causing the punching failure is lower than the one predicted to cause a one-way shear failure. Nevertheless, even the predictions of punching capacity can stay on the

unsafe side for slabs with a relation slab width to load size b_{slab}/l_{load} between 3.5 and 10 (depending on the code expressions). In practice, this occurs mainly when the contribution of the sides of the control perimeter that are parallel to the free edges are overestimated and does not consider that an impaired contribution may occur in such regions depending on the ratio between the slab width and the load size (Figure 1-3b). Therefore, enhanced approaches to defining the effective shear width should be devised to avoid unsafe predictions of one-way shear capacity.

Figure 1-3 – a) Example of calculation of the effective shear width for one-way shear capacity analyses; and b) Detail of the regions that may present an impaired contribution or enhanced contribution to the punching capacity.

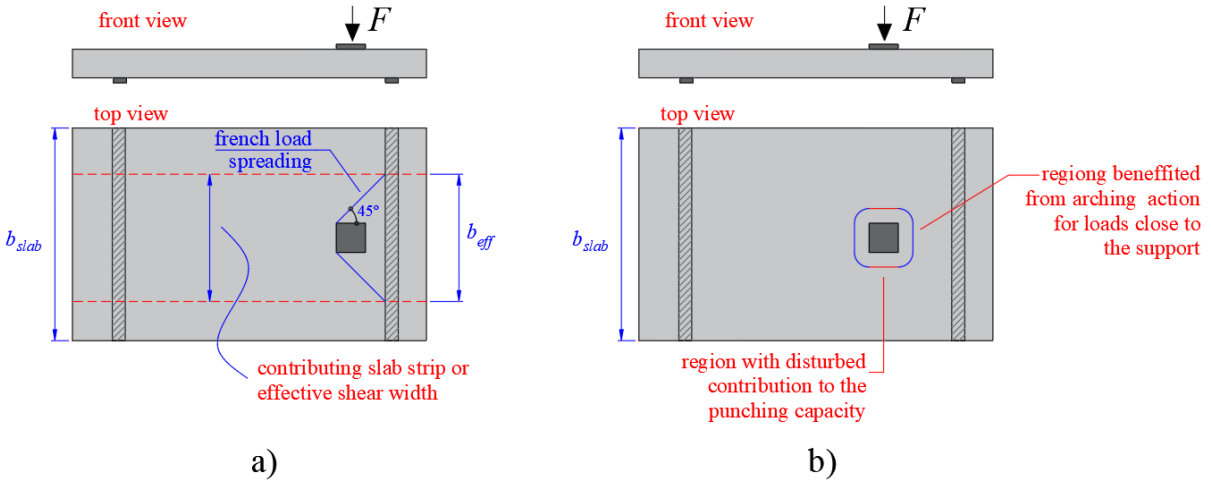

Source: Author.

In the same context, fewer discussions have been given to the predictions of punching capacity for one-way slabs under concentrated loads (NATÁRIO, 2015; VAZ RODRIGUES; FERNÁNDEZ RUIZ; MUTTONI, 2008). In general, for instance, the effect of enhanced load capacity for loads close to the support (a_v <2d_l) is commonly neglected in punching capacity predictions with codes of practice. Consequently, these approaches may lead to overly conservative predictions of punching capacity for loads close to the support. Besides, the predictions of punching capacity for slabs with a reduced slab width may stay on the unsafe side (LANTSOGHT et al., 2015d) by not considering the influence of the free edges disturbing the contribution of some sides of the control perimeter (Figure 1-3b). Therefore, enhanced approaches to predict the punching capacity of one-way slabs under concentrated loads are also necessary.

In the literature, there are many approaches based on different tools to assess the shear and punching capacity of one-way slabs. For instance, someone could make use of only analytical expressions for preliminary evaluations (LANTSOGHT, 2013). In the same way, there are most refined approaches on which analytical expressions can be powered by parameters from simplified finite element models (using shell elements to simulate the slab and assuming a linear elastic behavior to the materials)(NATÁRIO, 2015). Lastly, someone could use an advanced three-dimensional non-linear finite element model to evaluate the failure mechanism of a most complex case (HENZE, 2019; REIßEN, 2016). In practice, each of these approaches will have its advantages and disadvantages. While most publications focused on the use of only analytical expressions, the use of numerical tools (simplified or advanced) stands out as an interesting method to allow a broader insight into the problem. Moreover, approaches based on the use of linear elastic finite element analyses are becoming more spread in design offices and deserve to be better investigated.

Lastly, most publications until now focused on the investigation of slabs with a flexure capacity considerably higher than the shear and punching capacities (in the absence of shear reinforcement). In practice, this allows for reaching the desired shear failure mechanism at laboratory tests and improving the understanding of pure shear and punching failure mechanisms. In practice, however, slabs are frequently designed in such a way that the shear and punching capacities be higher than the flexure capacity to avoid brittle failure mechanisms at failure. Consequently, failures by shear or punching would be achieved only after local reinforcement yielding, for which there are limited tests in the literature. Therefore, tests on which shear and punching failure mechanism develops together with local reinforcement yielding could help to understand if expressions devised to deal with pure shear and punching failures perform well for other circumstances.

1.3 Aim of the research

The research aims to determine/develop enhanced approaches to predict the shear and punching capacity of one-way slabs under concentrated loads using different sets of expressions and tools and considering key parameters in the transition between one-way and two-way shear failures.

This research question is tackled by the following specific aims:

- Review the main characteristics that influence the ultimate loads and the failure mechanism of the tests from the literature, identifying key parameters in the transition from one-way shear to two-way shear failure mechanisms.
- To evaluate different approaches to predict the one-way shear resistance per unit length combined with different approaches of effective shear width, identifying the precision and accuracy of each combination.
- Develop enhanced approaches to predict the effective shear width based on the governing failure mechanism of the tests and tested loads at failure.
- To evaluate different approaches to predict the punching capacity of one-way slabs under concentrated loads using analytical code expressions and mechanical-based models.
- Develop enhanced approaches to predict the shear and punching capacity of one-way slabs combining analytical expressions with outcomes from linear elastic finite element analyses.
- Evaluate experimentally the effect of the clear shear span to effective depth ratio (a_v/d_l) on the ultimate capacity and failure mechanism of reinforced concrete slabs without transversal reinforcement with thicknesses of 150 mm subject to concentrated loads close to the support.
- Developing a non-linear numerical model capable of predicting the governing failure mechanism of one-way slabs under concentrated loads using three-dimensional numerical models, and highlighting possible challenges on this matter.
- Adjust as necessary one-way shear models, punching shear models and effective shear width models based on analytical, numerical and experimental investigations.

1.4 The research question of the thesis

In the end, this thesis intends to answer the following research question: How the predictions of one-way shear capacity and punching capacity for one-way slabs under concentrated loads could be enhanced using different sets of expressions and tools (analytical and numerical)?

In practice, this study intends to present a series of recommendations that can be employed to improve the level of accuracy of the tested-to-predicted resistances ratio of laboratory tests from the literature using different approaches. In this way, an enhanced look can be employed to evaluate existing structures.

1.5 Research strategy and thesis outline

The research methodology proposed comprises a total of 4 approaches: (i) analytical investigations; (ii) investigations with simplified numerical analyses (linear elastic finite element analyses); (iii) investigations with advanced numerical investigations (non-linear finite element analyses); and (iv) experimental investigations. In practice, the study developed in such a way that the level of refinement of the methods increases along the thesis, from fully-analytical based methods to experimentally-based investigations (Figure 1-4).

Figure 1-4 - Overview of chapters.

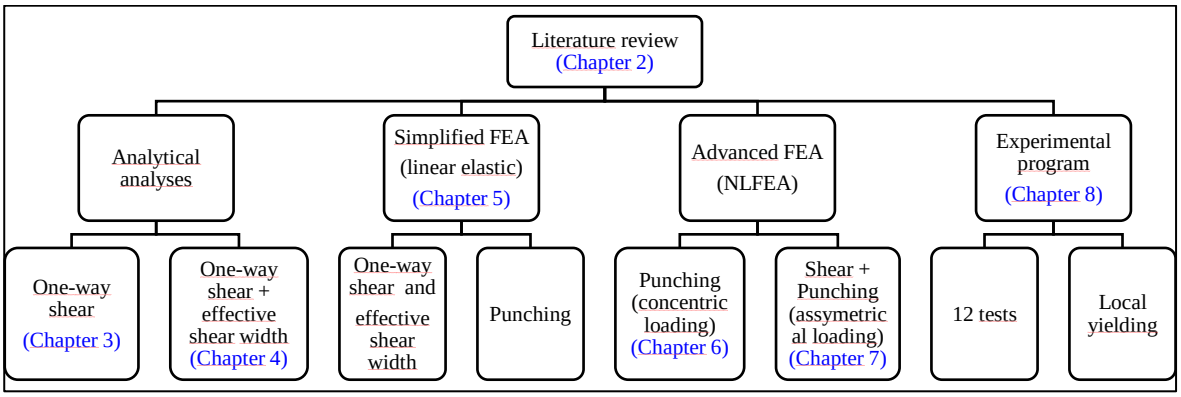

Source: Author.

Since the problem of one-way slabs under concentrated loads comprises an intermediate case between the one-way shear of slabs loaded over the entire width (Figure 1-2a) and the punching shear of slabs under concentric loads (Figure 1-2b), the research was tackled in parts. In practice, this division allowed for developing a solid understanding of different fields before addressing the most complex problem (Figure 1-2c).

Firstly, Chapter 2 shows a literature review on the problem of one-way slabs under concentrated loads. In this chapter, the main shear transfer mechanism and cracking pattern from different experimental programs are reviewed. The distinctions and similarities between one-way shear and two-way shear failure are highlighted. A database of 160 test results from literature is evaluated, highlighting how the tested loads at failure (shear and punching) and the corresponding failure mechanism vary according to parameters such as the shear slenderness (a_v/d_l) and slab width to load size (b_{slab}/l_{load}). The main parameters influencing the transition from one-way shear failures to punching failures and vice versa are discussed.

Nest, Chapter 3 discusses the one-way shear behavior of wide beams and slabs loaded over the entire width in detail (test with predominant one-way shear behavior) (Figure 1-2a). In this chapter, a comprehensive literature review was performed on the behavior of such members according to parameters such as: (i) the structural system or effect of support conditions; (ii)

the degree of rotational restraint at the support and shear slenderness; (iii) the load arrangement (concentrated or distributed in the span direction) and (iv) the shear failure modes in one-way shear. In the same chapter, it is presented an overview of available models or expressions to predict the one-way shear capacity; and a database of wide beams and slabs loaded over the entire width. A parameter analysis was performed to identify the most influencing parameters in the one-way shear capacity of such members and, in the end, a comparative analysis was conducted to evaluate the precision and accuracy of several expressions based on different theories and codes of practice.

Chapter 4 shows in detail the first analytical developments related to the slabs subject to concentrated loads in the span and width directions (Figure 1-2c). In this chapter, the effective shear width expressions are revised and a new one is proposed. The proposed effective shear width expression considers the different failure mechanisms that can take place and enables reaching safe and precise predictions of one-way shear capacity regardless of the governing failure mechanism being shear or punching. Besides, the Critical Shear Displacement Theory (YANG; DEN UIJL; WALRAVEN, 2016) is used as a reference approach to predict the unitary one-way shear capacity of the members. A database of one-way slabs under concentrated loads, including 214 test results, was addressed with the respective classification of the governing failure mechanisms. In the end, the proposed approach to predict the sectional shear capacity is validated against several approaches proposed in the literature.

Chapter 5 describes an enhanced approach to evaluate the shear and punching capacity of one-way slabs under concentrated loads using linear elastic finite element analyses, inspired by the work of Natário (2015). In this approach, outputs from simplified numerical models are used as input in the Critical Shear Crack Theory (CSCT) expressions (MUTTONI, 2008; MUTTONI; FERNANDEZ RUIZ, 2008). In the end, a simplified approach using only analytical expressions and based on the CSCT expressions is proposed and validated against a dataset of one-way slabs. This chapter shows how the predictions can be improved on simplified analytical calculations considering the parameters that influence the transition between one-way shear and two-way shear.

During the development of this research, it was found necessary to improve the understanding related to the punching capacity expressions and to validate the non-linear finite element model proposed to describe the behavior of slabs under concentric punching loads. These developments are related to Chapter 6. In the meantime, the author proposed investigating the behavior and punching capacity of such slabs, including the rational use of

ultra-high-performance fiber-reinforced concrete (UHPFRC). The work was devised using the CSCT expressions and the Concrete Damaged Plasticity model as the constitutive material for the concrete. Despite such kinds of slabs being not one-way, the tools and knowledge of this content improved the understanding of several aspects of the modeling to the problem of pure punching and flexure punching failures.

Chapter 7 describes a non-linear finite element analysis capable of representing both one-way and two-way shear failures of one-way slabs. The Concrete Damaged Plasticity model is used as a material model. Besides that, a parameter study is described to highlight the main influencing parameters on the numerical results. In this context, several aspects of modeling are highlighted to improve future investigations in this field.

Chapter 8 bring contributions to the research based on an experimental program. In this chapter, it was investigated the failure mechanism and ultimate capacity of slabs designed and tested with a close capacity between shear and flexure failure mechanisms. Therefore, this study brings a look at the ultimate capacity of slabs failing by shear after local reinforcement yielding.

Chapter 9 deliver the main conclusions from this thesis based on the literature review, analytical calculations, refined calculations aided by linear elastic finite element analyses, refined calculations based on non-linear finite element analyses, and based on the experimental program.

2 LITERATURE REVIEW

In this chapter, a literature review is presented regarding the problem of one-way slabs under concentrated loads. The main shear-transfer mechanisms and failure mechanisms of such slabs are investigated. The parameters that influence the transition between shear failure mechanisms are also highlighted.

2.1 Initial considerations

One-way slabs under concentrated loads can develop a transitional failure mode between one-way shear, two-way shear, and flexure (LANTSOGHT et al., 2015c). This loading is typical in solid slab bridges (LANTSOGHT; VAN DER VEEN; WALRAVEN, 2013) and garage floors (TENÓRIO et al., 2014) but may also occur in floor slabs with heavily concentrated loads arising from constructive or industrial equipment (BUI et al., 2017b, 2017a). Without shear reinforcement, these slabs may develop a brittle failure mode, which is the most dangerous failure mode for these structures since it provides limited warning signs and does not allow safe user evacuation. Since most design codes do not provide specific recommendations to evaluate the shear and punching capacity of one-way slabs under concentrated loads, research in this field is necessary to guide designers.

Traditionally, most publications deal with the one-way shear capacity of beams or slabs loaded over the entire width (SOUSA; LANTSOGHT; EL DEBS, 2020; REINECK et al., 2013) (Figure 1-2a) or with the punching capacity of the slab-column connections of two-way slabs (Figure 1-2b)(MUTTONI, 2008). However, the shear flow tends to be radial close to the load and linear close to the support (NATÁRIO; FERNÁNDEZ RUIZ; MUTTONI, 2014) when a concentrated load is placed close to line supports (Figure 1-2c - this figure uses the cracking pattern of different test results from Reiβen (2016)). This behavior results in the possibility of varying shear failure mechanisms taking place. Figure 1-2c shows that a simply supported slab may develop a one-way shear failure or wide beam shear failure close to the line support, as well as a punching failure around the concentrated load due to the characteristics of the shear flow in both regions.

Traditional approaches to evaluate the shear capacity in these cases are depicted in Figure 2-1 (LANTSOGHT et al., 2015c, 2015d). Basically, the punching capacity is verified around the concentrated load, assuming a uniform shear force distribution around the critical perimeter (Figure 2-1a). In the critical perimeter with two sides, it is assumed that the shear

stresses develop only in the spanning direction on both sides of the load (Figure 2-1b.1). For eccentric loads over the slab width, the free edges will limit the contribution of the sides of the critical perimeter near the border. Consequently, the decisive critical perimeter is usually one assuming three sides around the load contributing to the punching capacity (Figure 2-1b.2). In the design and assessment of existing structures (REGAN, 1982), as a rule of thumb, the smallest possible critical perimeter is used as it leads to the lowest capacity (LANTSOGHT, 2013).

Figure 2-1 - a) Most traditional critical perimeter definition for punching shear analyses; b) possible critical perimeter for slabs with a small width (b.1) and eccentric load over the slab width (b.2); c) effective shear width b_{eff} defined to assess the one-way shear capacity using the French load spreading (FD P 18-717, 2013).

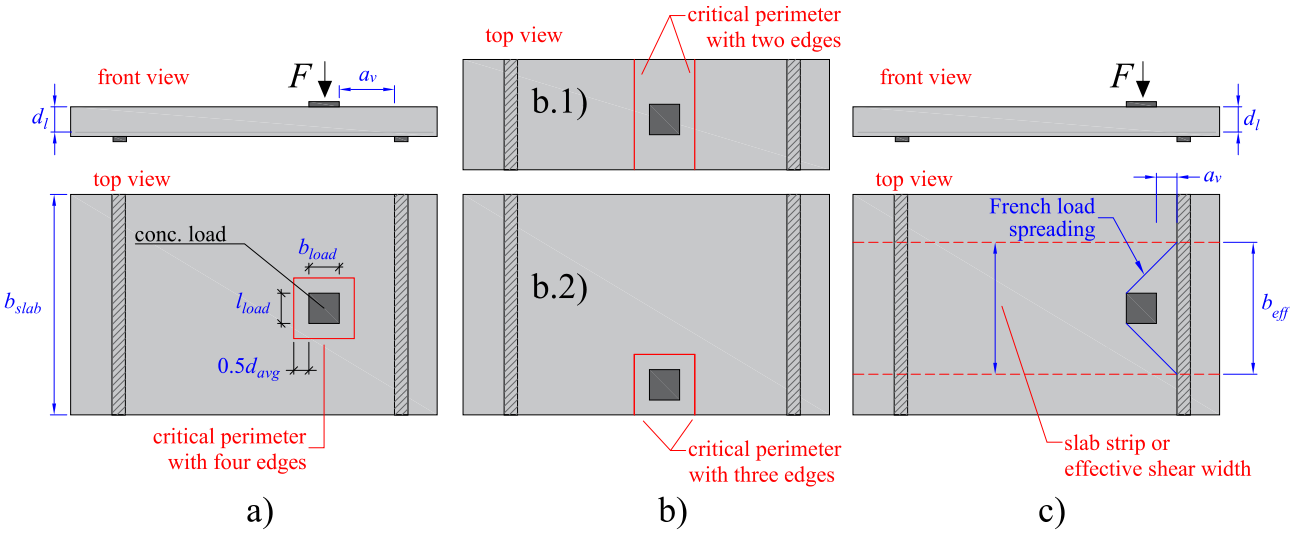

Source: Author.

The one-way shear capacity of slabs is commonly verified by assuming that only a slab strip b_{eff} contributes effectively to the shear capacity (Figure 2-1c) with a uniform shear demand along this length, usually called the effective shear width. The most conventional approach to define the slab strip width contributing to the one-way shear capacity is based on an assumed horizontal load spreading from the far edge of the concentrated load to the support under a 45º angle (BUI et al., 2017a; LANTSOGHT et al., 2015d; LANTSOGHT; VAN DER VEEN; WALRAVEN, 2013), commonly named the French effective shear width(FD P 18-717, 2013), as it originates from France (Figure 2-1c).

Previous studies addressed the accuracy level of analytical shear provisions to predict the shear (LANTSOGHT et al., 2015d; REIßEN; HEGGER, 2015; SOUSA; EL DEBS, 2019) and punching shear capacities (LANTSOGHT et al., 2015d; SOUSA; EL DEBS, 2019) of one-

way slabs under concentrated loads. Lantsoght et al. (2015d), for instance, evaluated 118 one-way slabs and wide beams (after filtering) with the European shear and punching shear code provisions (CEN, 2005). The comparison between experimental and predicted shear capacities showed a large scatter between tests and theoretical predictions with many unsafe predictions. These results mainly occurred because the code expressions and rules of practice were applied without considering that, for example, the punching mechanism could be critical for the tests being evaluated by one-way shear expressions. In the same way, the predictions of punching capacity did not fit well for the tests that failed as wide beams. Therefore, adjustments in the one-way shear and punching shear expressions should be made to account for these cases when using design code expressions devised for members loaded over the entire width or for slabs under concentric loads.

This chapter starts by reviewing the one-way and two-way shear mechanisms involved in the problem of one-way slabs under concentrated loads. Subsequently, the cracking pattern of slabs from different experimental programs is discussed in detail to highlight the most important influencing parameters in the transition from one-way shear failure to two-way shear failures. A database with 160 test results from the literature was organized. Compared to previous works (HALVONIK; VIDAKOVIĆ; VIDA, 2020), different support conditions and failure mechanisms were addressed. In the end, a sensibility analysis with test results was conducted to show how some parameters influence the measured loads at failure and the governing failure mechanism of the tests.

2.2 Background of one-way shear and two-way shear failure mechanisms

There are similarities and distinctions between one-way shear and two-way shear of slabs without stirrups (LANTSOGHT et al., 2015c). The main similarities include the shear transfer mechanisms involved: (i) compression chord capacity (MÖRSCH, 1909), (ii) aggregate interlock (WALRAVEN, 1981), (iii) dowel action (TAYLOR, 1969), (iv) the residual tensile strength of concrete (HORDIJK, 1992), and (v) arching action or strut action (KANI, 1964). According to the Critical Shear Crack Theory (MUTTONI, 2008; MUTTONI; FERNANDEZ RUIZ, 2008), the failure criteria for both one-way shear and two-way shear are governed by strain localization (flexure action), size effect (member thickness), and aggregate interlock effects (MUTTONI; FERNANDEZ RUIZ, 2010a) (roughness of the cracked surface). In the multi-action shear model from Marí et al.(2018), on the other hand, both one-way shear and two-way shear are governed by the compression chord capacity. In addition, these authors

consider that both one-way and two-way shear failures occur when the inclined crack from flexure crosses the compression chord.

The main distinctions between one-way and two-way shear failures relate to the mechanisms that trigger the shear failures and the governing parameters of the crack kinematics: (i) opening and (ii) sliding of the critical shear crack(MUTTONI; FERNANDEZ RUIZ, 2010a). For instance, the opening of the critical shear crack is related to strains at the control section in one-way shear (MUTTONI; FERNANDEZ RUIZ, 2008) and is related to slab rotations for two-way shear (MUTTONI, 2008). Moreover, the relation between the applied load and the opening of the critical shear crack is almost linear for one-way shear but strongly non-linear for two-way shear (MUTTONI; FERNANDEZ RUIZ, 2010a).

Figure 2-2a shows that the distribution of unitary shear forces along the shear span is almost constant for beams and slabs loaded over the entire width (neglecting the influence of the self-weight) (MUTTONI; FERNANDEZ RUIZ, 2010a). However, a different behavior occurs in slabs under concentric loads (Figure 2-2b). Since slabs transfer shear radially, a strong gradient of shear stresses (shear force per unit length, with b_0 being the critical perimeter length around the loaded area) and bending moments takes place around the concentrated loads. Consequently, higher values of shear stresses arise near the concentrated load with significant strain localization in this region, which governs the punching capacity (MUTTONI; FERNANDEZ RUIZ, 2010a) (Figure 2-2b).

Lantsoght et al. (2015c) also point out other differences: (i) for punching, the inclined crack locations always arise immediately adjacent to the concentrated load, while for one-way shear in beams, the inclined crack is free to develop at the weakest section in the shear span a, closer to the support or to the load (CRISWELL; HAWKINS, 1974); (ii) although the inclined cracks may develop at similar shear stresses for beams and slabs, the opening of the critical shear crack for punching occurs only after a marked decrease of the tangential stiffness (HAWKINS; MITCHELL, 1979). Marí et al. (2018) also remarked that, due to the higher confining stresses generated around the column of flat slabs (compression ring), the critical punching crack follows an almost straight path. The inclination of the punching cracks is commonly related to the ratio between the failure load and the slab flexural capacity (MENÉTREY, 2002). Conversely, in one-way shear, the development of two main branches can be observed(YANG; DEN UIJL; WALRAVEN, 2016): an initial flexural crack and an inclined crack crossing the compression chord (Figure 2-2c.1).

Figure 2-2 - Distribution of unitary shear forces and bending moments in the shear span for a) beams and slabs loaded over the entire width; b) slabs under concentric concentrated loads; c.1) beam-shear carrying mechanisms of slender beams; c.2) direct struts and beam-shear carrying mechanisms of slabs under concentric loads.

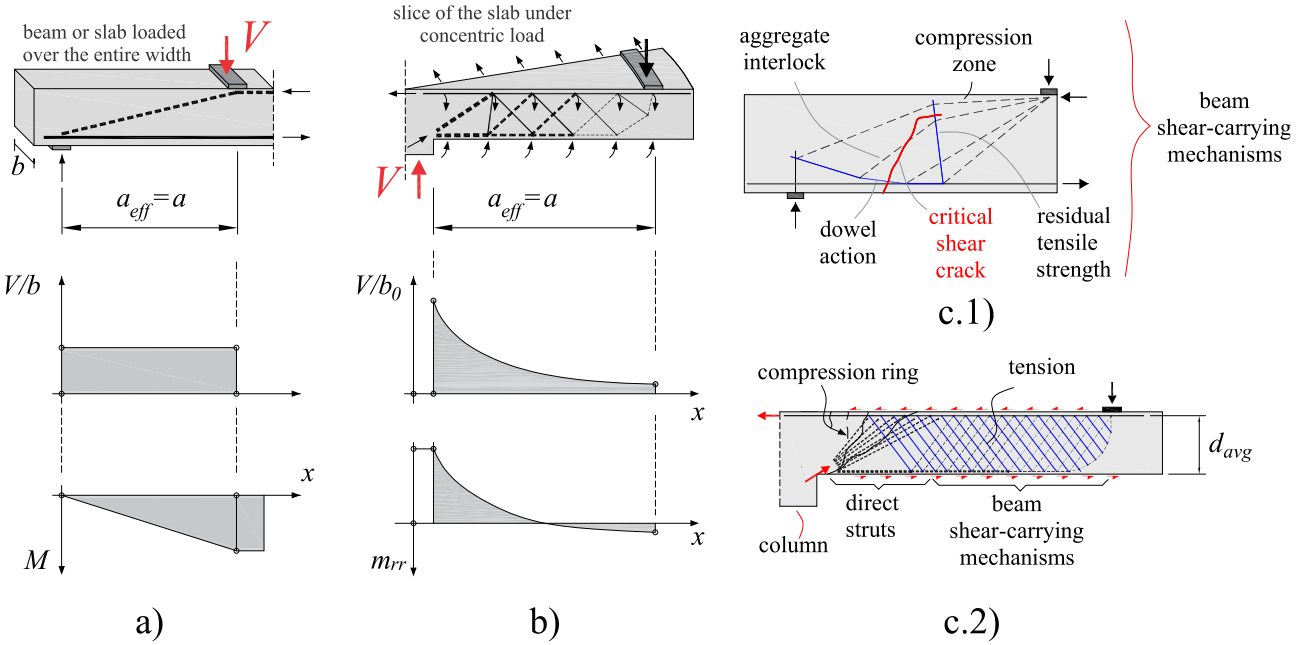

Source: Adapted from Muttoni and Fernandez Ruiz (2010a) and Cavagnis, Fernández Ruiz and Muttoni (2018a).

Another link between one-way shear and punching shear occurs on slab-column connections (MUTTONI; FERNANDEZ RUIZ, 2010a). At large distances from the columns, the shear forces are moderate due to the larger shear transfer surface. Hence, the beam-shear carrying mechanisms from slender beams (shear transfer mechanisms i-iv) may provide the required punching capacity (Figure 2-2c.1). However, close to the concentrated load, the shear forces are carried by a small perimeter, and arching action develops, increasing the unitary shear strength in this region (Figure 2-2c.2). As a result, the unitary shear strength for punching shear (when the critical perimeter is consistently placed closer to the concentrated load) is higher than that for one-way shear (MUTTONI; FERNANDEZ RUIZ, 2010a).

2.2.1 Effect of the slab width to load size ratio b_{slab}/l_{load}

A limited number of studies focus on explaining the transition from one-way to two-way shear failures (DOORGEEST, 2012; LANTSOGHT et al., 2015c), even though some experimental programs reported different shear failure mechanisms in the tests of slabs under asymmetrical concentrated loads (HENZE; ROMBACH; HARTER, 2020; LANTSOGHT; VAN DER VEEN; WALRAVEN, 2013; REIßEN; CLASSEN; HEGGER, 2018).

Reiβen et al. (2018) and Lantsoght et al. (2014) identified experimentally that the one-way shear capacity V_{exp} of slabs under concentrated loads does not increase linearly by increasing the slab width b_{slab} or the ratio b_{slab}/l_{load}, where l_{load} is the width of the loading plate in the transverse direction. Therefore, these results are consistent with the concept of using an effective shear width for wide members under one-way shear (Figure 2-1c). In addition, it was also demonstrated experimentally that the failure load (P_{test}) decreases by decreasing the slab width b_{slab} or the ratio b_{slab}/l_{load} (REIßEN; CLASSEN; HEGGER, 2018). This occurs because slabs with a smaller width develop a more unidirectional shear flow to the support, which decreases the load distribution in the transverse direction. The previous studies (SOUSA et al., 2021a) also showed through linear elastic finite element analyses that as b_{slab} increases, the gradient of bending moments around the concentrated load increases, which favors the occurrence of punching failures over one-way shear failures for wider slabs.

Figure 2-3 - Transition of shear failure mechanisms as a function of a) slab width; b) shear slenderness a_v/d_l for simply supported slabs from Reiβen, Classen and Hegger (2018); c) shear slenderness a_v/d_l for cantilever slabs for the tests from Henze (2019). Note: (WB) = wide beam shear failure; (P) = punching failure. Dimensions in SI units.

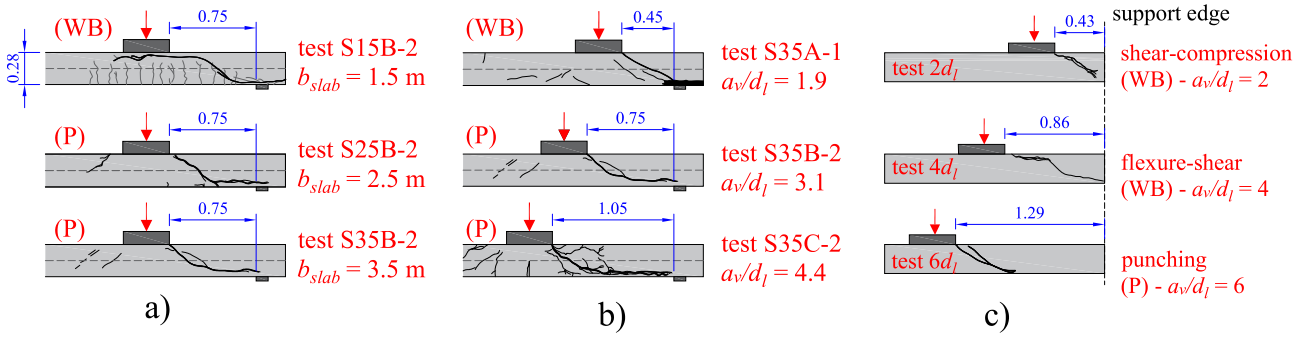

Source: Adapted from Reiβen, Classen and Hegger (2018) and Henze (2019).

Saw cuts of failed specimens can be used to identify the transition of shear failure mechanisms. Figure 2-3a shows the cracking pattern of a set of slabs tested by Reiβen et al. (2018) where the only parameter varied was the slab width (b_{slab}): 1.5 m, 2.5 m, and 3.5 m. The loading arrangement was similar to that shown in Figure 2-1a. The concentrated load was applied on a square area with a size of 0.40 m × 0.40 m with a = 1 m, with a the center-to-center distance between the load and the support. Figure 2-3a shows that the governing shear failure mechanism changed from wide beam shear (WB) to punching shear (P) as b_{slab} increased. Test S15B-2 developed a critical shear crack typical for one-way shear, based on the visible flexure cracks and the horizontal branch of the critical shear crack crossing the compression chord. At the same time, S35B-2 developed a critical shear crack without the horizontal branch at the

compression chord and with the inclined branch of the critical shear crack reaching the edges of the loaded area, as common for punching failures. In S25B-2 and S35B-2, the critical shear crack was more pronounced in the region with the largest shear demand, i.e., in the shear span, and the full punching cone did not develop.

2.2.2 Effect of the shear slenderness a_v/d_l

One of the consequences of using an effective width, as sketched in Figure 2-1c, is that the predicted one-way shear capacity increases with the shear slenderness a_v/d_l (d_l is the effective depth toward longitudinal steel and a_v is the clear shear span: distance between the edge of support and edge of the load). However, some studies (HENZE; ROMBACH; HARTER, 2020; REIßEN; CLASSEN; HEGGER, 2018) showed that increasing a_v/d_l from 1 to 6 in Henze et al. (2020) and from 1.9 to 4.4 in Reiβen et al. (2018), keeping all other parameters constant, the tested one-way shear capacity of the slabs decreased markedly or remained almost the same after a certain value of a_v/d_l. At the same time, Lantsoght et al. (2013) showed that decreasing the ratio a_v/d_l from 1.70 to 0.75 increased the failure loads substantially, even though the calculated effective shear width decreased, which they explained by the formation of a fan of compressive struts between the load and the support. However, the resistance increase due to the arching action was less pronounced in the slab members than in beams (LANTSOGHT; VAN DER VEEN; WALRAVEN, 2013) due to the fan of struts and their resulting load path with varying relations a_v/d_l. Therefore, the increase of arching action was also a function of the slab width(LANTSOGHT et al., 2014).

Figure 2-3b shows the same change in the governing shear failure mechanism as the shear slenderness a_v/d_l increases. Note that S35A (a_v/d_l = 1.9) indicates a shear-compression failure as typical in non-slender beams (inclined critical shear crack between the load and the support without major flexure cracks in the shear span). Figure 2-3c shows the cracking pattern of cantilever slabs with b_{slab} = 4.5 m and cantilever length 1.9 m tested by Henze (2019) as a function of a_v/d_l. Figure 2-3c shows the same transition from one-way to punching shear failures as the shear slenderness a_v/d_l increased for cantilever slabs.

2.2.3 Effect of the transverse reinforcement ratio ρ_t

The reinforcement ratio in the transverse direction of slabs (perpendicular to the shear span) also influences the governing shear failure mechanism of slabs under concentrated loads. Lantsoght, van der Veen and Walraven (2013) observed that higher transversal reinforcement ratios led to a better force distribution in the width direction since the cracking pattern in the

shear span was more similar to that of one-way slabs loaded over the entire width. Instead, slabs with lower transverse reinforcement ratios developed a cracking pattern that was more localized (radial and tangential cracks) around the concentrated load, similar to that of a punching failure (Figure 2-4a). When the transverse and longitudinal reinforcement ratios are different, the unitary shear capacities around the concentrated load are different (SAGASETA et al., 2014; SAGASETA; VOLLUM, 2011). Since the distribution of shear forces around the load is also uneven (NATÁRIO, 2015) and depends on the load position and boundary conditions, failure can be triggered in the region of higher demand or lower resistance.

Figure 2-4 - Effect of the transverse reinforcement ratio ρ_t on the shear/punching capacity and governing failure mechanism for slabs with a) load applied close to simple supports (figures adapted from Lantsoght, van der Veen and Walraven (2013)); b) load applied close to a continuous support and c) load applied on cantilever slabs (figures adapted from Reiβen (2016)).

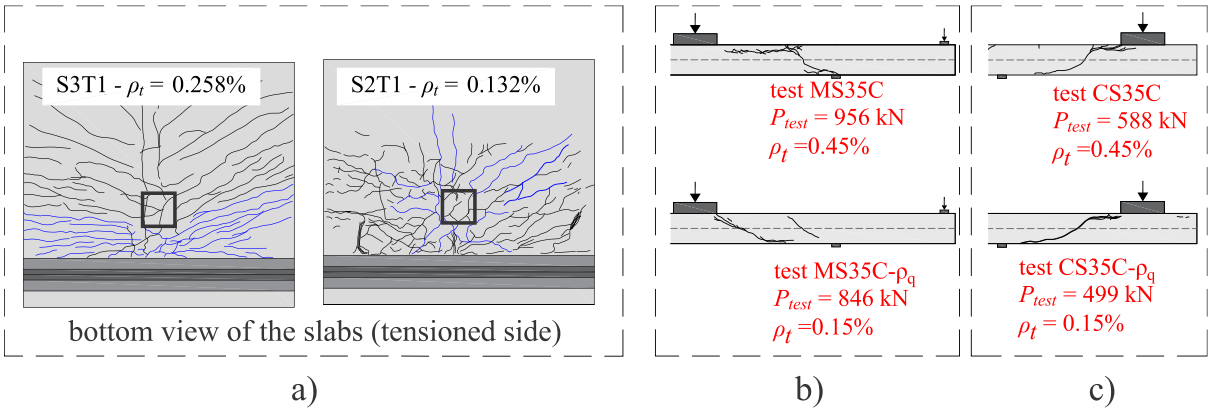

Source: Adapted from Lantsoght, van der Veen and Walraven (2013) and Reiβen (2016).

A similar change in the shear failure mechanism was observed in the continuous slabs tested by Reiβen, Classen and Hegger (2018), where the cracking pattern in cut views of the tests MS35C (ρ_t = 0.45%) and MS35C-ρq (ρ_t =0.15%) indicated that the slab with a lower transverse reinforcement ratio failed in punching shear (Figure 2-4b) while the other one failed by one-way shear. The change in the externally applied load at failure was only 13% between these two tests.

On the other hand, decreasing ρ_t had a more limited effect on the cracking pattern and governing shear failure mechanisms for cantilever slabs. Figure 2-4c shows that decreasing ρ_t from 0.45% to 0.15% for cantilever slabs decreased the failure load (P_{test}) by 18%, and resulted in almost no change in the cracking pattern in the cut views.

2.3 Database

The references gathered in the database and the range/distribution of parameters are presented in Sousa, Lantsoght and El Debs (2022). This study (i) reviews the test results from the literature in a comprehensive way (including failure mechanisms, cracking pattern and ultimate loads); and (ii) presents an enhanced approach to predict the ultimate capacity of slabs under concentrated loads that failed by one-way shear as wide beams (WB), by punching shear (P) and a mixed failure mode between one-way shear and punching shear (WB+P). Only tests with $b_{slab}/d_l > 5$ were considered. The criteria of using only tests with ratio $(b_{slab} - l_{load}) > 4d_{avg}$ was also included as a filter to remove tests with predominant one-way shear behavior. This filter increases the proportion of tests that could present both shear failure modes. In practice, all tests that do not satisfy this criterion failed as wide beams in one-way shear and could introduce a slight bias in the statistical analyses.

In total, Database A includes the results from 160 tests under different support conditions: (i) 77 tests with a load closer to a simple support (SS); (ii) 20 tests with the load closer to a continuous support (CS) and (iii) 46 tests with the load applied on a cantilever slab (CT). Database A is available in the public domain(SOUSA; LANTSOGHT; EL DEBS, 2022) and is based on previous databases of slabs under concentrated loads failing in shear and punching shear (LANTSOGHT et al., 2015d; REIßEN, 2016). This database was used mainly to perform parametric/sensibility analyses of selected parameters in the tested one-way shear loads V_{test} and concentrated loads measured at failure P_{test}. To evaluate the effect of selected parameters, such as the clear shear slenderness a_v/d_l, groups of test results where only a_v/d_l was varied were taken from the Database A(SOUSA; LANTSOGHT; EL DEBS, 2022) to analyze this effect further. In this way, different subsets were organized to evaluate each parameter selected.

- Database A1 brings together test results for which the main parameter varied was the shear slenderness a_v/d_l (75 test results from the following references: Natário (2015), Reiβen (REIßEN, 2016), Rombach and Henze (2017), Lantsoght (2013), Cullington et al. (1996), Ferreira (2006) and Regan (1982).
- Database A2 brings together test results for which the main parameter varied was the slab width to load size ratio b_{slab}/l_{load} (26 tests from the following references: Reiβen (2016), Lantsoght (2013) and Regan and Rezai-Jarobi (1988).

- Database A3 brings together test results for which the main parameter varied was the transverse reinforcement ratio ρ_t (36 tests from the following references: Damasceno (2007), Ferreira (2006), Reiβen (2016) and Lantsoght (2013).

Database B is also a subgroup of Database A but received a different classification since this database was used to evaluate the performance of shear and punching capacity predictions with the ACI code expressions. In Database B, tests that developed flexure-induced punching (F+P) at failure were removed. This database contains 143 test results of one-way slabs under concentrated loads: (i) 40 tests failed by punching (P); (ii) 91 tests failed as wide beams by one-way shear mechanisms (WB) and (iii) 12 tests failed by a mixed-mode between one-way shear and two-way shear (WB+P).

2.4 Parameter analyses on governing shear failure mode

This section evaluates the influence of parameters such as the load position a_v (or shear slenderness a_v/d_l), slab width to load size ratio b_{slab}/l_{load} and transverse reinforcement ratio ρ_t on the sectional shear and concentrated loads applied at failure for one-way slabs under concentrated loads, as well as on the transition between these shear failure modes. For this purpose, different subgroups of Database A were used.

In this study, it is assumed that the full one-way shear capacity may not have been reached in the tests that failed by punching ($V_{test} < V_{exp}$) and, in the same way, the full punching capacity may not have been reached in the tests that failed as wide beams in one-way shear ($P_{test} < P_{exp}$). In other words, V_{exp} should refer only to the one-way shear force measured on the tests that fail in one-way shear, and P_{exp} should refer to the punching capacity of the tests that failed by punching. If the test failed in one-way shear as a wide beam, the concentrated load applied in the test should be interpreted as the reached concentrated load P_{test}, and not as the punching capacity of the test P_{exp}.

Because of this, in the following analyses, the shear (V_{Fu}) and punching capacities (P_{test}) refer respectively to (i) the corresponding sectional shear forces measured at failure due to the concentrated load and (ii) to the maximum concentrated loads measured on the tests. In this text, V_{test} is the total sectional shear measured at failure, including the self-weight influence along the entire slab width:

$$V_{test} = V_{Fu} + v_g \cdot b_{slab} \tag{2.1}$$

With v_g being the shear force per unit length due to the self-weight at the section $a/2$. V_{Fu} is the sectional shear considering only the applied load F_u at failure. As suggested by Reiβen

(2016), this uses V_{Fu} instead of V_{test} to not include the influence of the effective shear width assumed in the calculation of V_{test}.

Some analyses were inspired by the research from Reiβen (2016), who investigated the influence of similar parameters on the one-way shear capacity of slabs under concentrated loads (sectional shear reached in the tests, V_{Fu}). However, to allow a broader insight into different shear failure mechanisms, both sectional shear and concentrated loads applied at failure are addressed in this study. Moreover, the governing failure mechanism is highlighted on all graphs in order to identify the transition between the failure mechanisms according to the parameters investigated. Therefore, these analyses provide a new look at the problem.

The influence of the concrete compressive strength was reduced by normalizing the sectional shear and externally applied load at failure (V_{Fu} and P_{test}) to the square root of the concrete compressive strength $\sqrt{f_c}$, such as recommended in Sousa et al. (2020) and in line with the one-way and two-way shear expressions from ACI 318-19(ACI COMMITTEE 318, 2019) (f_c is the average compressive strength of concrete measured on cylinder specimens). Additionally, the sectional shear and externally applied load at failure (V_{Fu} and P_{test}) were also normalized to the effective depth d_l. Therefore, the ratio $V_{Fu}/d_l \cdot \sqrt{f_c}$ is a measure of the shear capacity on which the effect from the concrete compressive strength and the effective depth was reduced to compare different experimental programs better.

2.4.1 Shear slenderness a_v/d_l

The shear slenderness a_v/d_l is a well-known parameter influencing the shear capacity of beams and wide members loaded over the entire width (SOUSA; LANTSOGHT; EL DEBS, 2020). For ratios $a_v/d_l < 2$, the shear capacity of RC beams without stirrups is enhanced as a result of arching action between the load and the support. Figure 2-5 shows the relation between the normalized shear V_{Fu} and concentrated load at failure P_{test} as a function of a_v/d_l to the Database A1. Lines connect tests in which only the ratio a_v/d_l was varied. The symbols identify the governing failure mechanism based on the cracking pattern and reported information from the original references.

Figure 2-5a shows that both shear (WB) and punching failures (P) were observed for tests with $a_v/d_l < 4.5$ (Figure 2-5a). On the other hand, all tests with $a_v/d_l > 5$ failed by punching (P) or a mixed-mode between shear and punching (P or WB+P). The tests on which a punching failure occurred with $a_v/d_l < 3$ are mainly slabs with thickness $h < 125$ mm. Therefore, the

governing failure mechanism also seems to be influenced by the absolute slab thickness, in addition to the ratio a_v/d_l.

Figure 2-5 - Influence of shear slenderness a_v/d_l on the normalized a) sectional shear and b) failure loads for one-way slabs under concentrated loads using Database A1 with 75 test results. Note: WB = wide beam shear failure (42 results); P = punching shear (22 results); WB+P = mixed mode or not clear which failure mechanism governs (11 results).

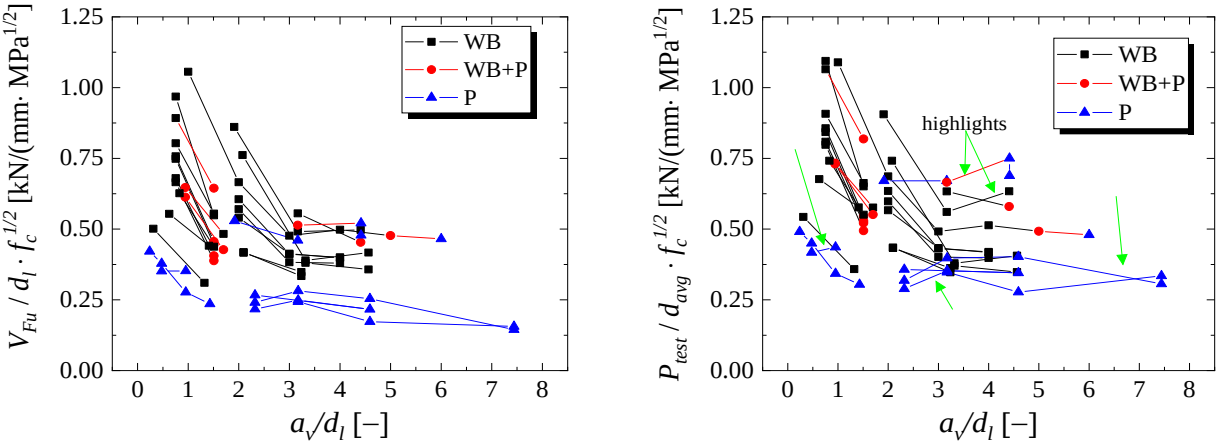

Source: Author.

As already pointed out by Reiβen (2016), an increase in the effective shear width with the shear slenderness cannot be confirmed based on Figure 2-5a. Contrarily, the normalized sectional shear at failure (regardless of governing failure mechanism identified) seems to decrease for most tests as a_v/d_l increases.

In this study, the normalized failure load P_{test} was also evaluated in detail (Figure 2-5b). The highlights in green indicate sets of tests on which an increase of a_v/d_l resulted in an increase of P_{test}. In other words, it was identified that, although the measured sectional shear V_{Fu} decreased for most tests (Figure 2-5a), the failure load P_{test} increased for some tests. Notably, for the cases where the failure load P_{test} increased for an increasing ratio of a_v/d_l, the test with a higher ratio of a_v/d failed in punching (Figure 2-5b - data points in blue). Therefore, tests critical for punching may benefit from the less uneven distribution of shear forces around the load when the shear slenderness increases. Tests critical in one-way shear commonly fail at a lower concentrated load when the shear slenderness increases.

In this study, the increase of the failure loads P_{test} by increasing the ratio a_v/d_l may be better explained by looking at the ratio a/l_{span}. Loads applied at the slab center have an a/l_{span} = 0.5 and no shear stress difference between the front and back faces of the critical perimeter.

Tests with lower a_v/d_l have a $0 < a/l_{span} < 0.5$ and a higher difference between the shear stress at the front and back faces of the critical perimeter, also called non-proportional loading of the punching perimeter. In other words, the tests with higher a_v/d_l and, hence, higher a/l_{span}, benefit from the most balanced shear stress around the critical perimeter. Tests with lower a_v/d_l fail when the most heavily loaded sides of the critical perimeter (between the front and back faces of the load) reach their full capacity. In the tests S35B-2 from Reiβen (2016) (Figure 2-3), for instance, the critical shear crack is visibly more clear at the front face of the load, indicating that failure started at the front face.

2.4.2 Slab width to load size ratio b_{slab}/l_{load}

Figure 2-6 shows how the ratio of b_{slab}/l_{load} influences the sectional shear (Figure 2-6a) and failure load (Figure 2-6b) of one-way slabs under concentrated loads from Database A2. Figure 2-6 shows that the sectional shear at failure increases until a certain threshold when the ratio b_{slab}/l_{load} is increased (by increasing the width of the tested specimen). In the tests from Regan and Rezai-Jorabi (1988) and from Lantsoght (2013), the threshold value occurred when the slabs started to fail by punching instead of one-way shear. In the tests from Reiβen (2016), a change in the rate of increase of sectional shear (change in slope of lines) was observed when the failure mode changed from one-way shear to punching shear or a mixed failure mode.

Figure 2-6 - Influence of the slab width to load size ratio b_{slab}/l_{load} on (a) the sectional shear and (b) the failure load of slabs under concentrated loads from Database A2. Note: WB = wide beam shear failure (20 results); P = punching shear (1 result); WB+P = mixed failure mode (5 results).

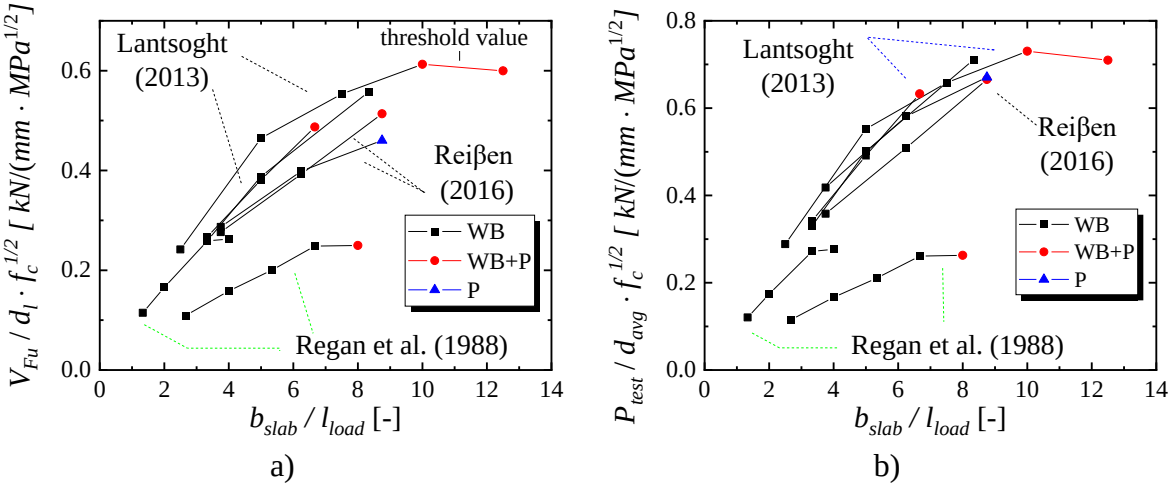

Source: Author.

These findings are in line with Lantsoght et al. (2014) and Reiβen (2016), who observed that by increasing the slab width b_{slab} until a certain value, the shear capacity does not increase anymore, meaning that the effective contributing width to the sectional shear capacity has an

upper limit. It can also be noted that the sectional shear at failure increased almost linearly with b_{slab}/l_{load} for the three experimental programs until a certain point. Notably, the threshold value for the tests from Regan and Rezai-Jarobi (1988) was reached for a smaller value of b_{slab}/l_{load} compared to the tests from Lantsoght (2013) and Reiβen (2016). This occurs because the slabs tested by Regan and Rezai-Jarobi (1988) had a considerably lower thickness than those tested by the other authors (d_l = 83 mm compared to d_l = 265 mm on average). Therefore, it can be concluded that the transition from one-way shear failures to punching failures does not depend exclusively on b_{slab}/l_{load}, but also on the slab thickness. Besides that, based on the test results, it can be stated that punching is the governing failure mechanism for one-way slabs with b_{slab}/l_{load} > 10.

2.4.3 Transverse reinforcement ratio

Figure 2-7 shows the influence of the transverse reinforcement ratio ρ_t on the sectional shear V_{Fu} and failure load P_{test} for Database A3. Figure 2-7 shows that, despite the better distribution in the transverse direction (LANTSOGHT; VAN DER VEEN; WALRAVEN, 2013), the increase in the transverse reinforcement ratio ρ_t did not result in higher sectional shear forces V_{Fu} or failure loads P_{test} for the tests from Lantsoght (2013) (which failed as wide beams).

Figure 2-7 - Influence of the transverse reinforcement ratio on a) the normalized sectional shear and b) failure loads for one-way slabs under concentrated loads from Database A3. Note: WB = wide beam shear failure; P = punching shear; F+P = flexure-induced punching; WB+P = mixed failure mode.

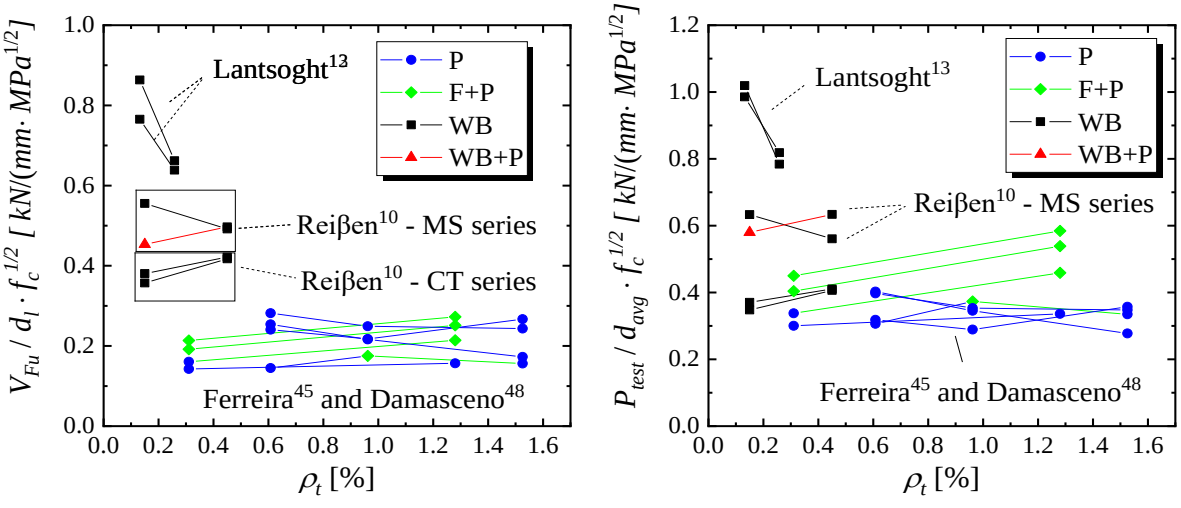

a) b)

Source: Author.

In the tests from Reiβen (2016), no clear relation between the sectional shear V_{Fu} or failure loads P_{test} and ρ_t was identified when the load was applied close to the continuous support (MS-series). In the pair of tests MS35C and MS35C-ρ_q, the normalized sectional shear V_{Fu} increased by increasing ρ_t from 0.15% to 0.45%. In the pair of tests MS35B-ρ_q and MS35-B, conversely, the normalized V_{Fu} decreased slightly by increasing ρ_t. In the cantilever slabs tested by Reiβen (2016) (CT – series), in general, the normalized shear and punching loads at failure increased by increasing ρ_t. However, these increases were less than 20% even though ρ_t increased threefold in the two-test series. Most of these tests developed a cracking pattern based on cut views, with the critical shear crack having two main branches (typical of slender beams (SOUSA; LANTSOGHT; EL DEBS, 2020). Yet, at the same time, the critical shear crack developed closer to the load, as typical of punching failures.

In the one-way slabs from Damasceno (2007), the sectional shear at failure V_{Fu} increased slightly with the increase of ρ_t for most tests. In fact, all these tests failed by punching (P) or flexure-induced punching (F+P). In this experimental campaign, the load was always applied in the slab center and, hence, there was no difference in the shear demand on the front and back faces of the punching perimeter (a/l_{span} = 0.5). Consequently, the shear flow for such slabs favored the expected punching behavior (higher shear and related applied loads by increasing ρ_t due to the higher flexural stiffness (MUTTONI, 2008)). Conversely, the tests from Ferreira (2006), in which the load was applied eccentrically along the span length (varying the ratio a_v/d_l from 2.32 to 7.44 and the ratio a/l_{span} from 0.20 to 0.50), developed a more complex behavior. Some experiments with an increase in ρ_t resulted in an increase in the sectional shear and failure load, while in other experiments, a decrease resulted. These tests failed by punching (P) or flexure-induced punching (F+P). Therefore, no solid conclusion can be drawn about the influence of the transverse reinforcement ratio over the sectional shear capacity when the load is placed asymmetrically in the span direction.

2.5 Discussions from Chapter 2

Many publications related to one-way slabs under concentrated loads focus on the evaluation of only one of the possible shear failure mechanisms: the one-way shear failure as wide beams (HALVONIK; VIDAKOVIĆ; VIDA, 2020; HENZE; ROMBACH; HARTER, 2020; NATÁRIO; FERNÁNDEZ RUIZ; MUTTONI, 2014; REIßEN; CLASSEN; HEGGER, 2018). Despite most of the tests being rated as failing in this way, looking at only one failure mechanism can induce some bias in the interpretations and limit the understanding of the problem. Punching failures are frequently most critical when the shear slenderness $a_v/d_l > 5$

(Figure 2-5a) and the ratio $b_{slab}/l_{load} > 12$ (Figure 2-5b). Therefore, this study tries to provide a comprehensive look at the problem and warning that both one-way shear and punching shear failure mechanisms shall be discussed for such kinds of slabs. At this point, it is not critical to know from which value of a_v/d_l, for instance, which failure mechanism governs, since both failure mechanisms shall be evaluated in design. Nevertheless, it is important that design approaches consider that the governing failure mechanism and ultimate capacity can vary according to these parameters.

The detailed evaluation of the cracking pattern of one-way slabs under concentrated loads allowed us to identify the parameters that influence the transition between one-way shear and two-way shear. These parameters were mainly the shear slenderness a_v/d_l and the slab width to load size ratio b_{slab}/l_{load}. The effective depth (d_l), the load eccentricity a/l_{span}, as well as the transverse reinforcement ratio ρ_t, also lead to changes in the tested loads (V_{test} and P_{test}) and failure mode. However, the results did not follow a homogeneous behavior by varying the last parameter (ρ_t), so further research is necessary. In practice, the parameter a/l_{span} modifies the stress distribution around the control perimeter, which can be understood from the statics of the problem. For punching capacity analyses, the ratio a/l_{span} gives a better insight into the non-proportional stress distribution around the control perimeter. In this study, it is assumed that the uneven shear demand around the control perimeter could induce early failures due to local failure of the most heavily loaded side of the control perimeter, typically between the load and the support. The transverse reinforcement ratio, instead, is more related to the uneven resistance around the critical perimeter but may also influence the load distribution due to the different flexural stiffnesses of the slab in the longitudinal and transverse directions. In summary, the parameters a_v/d_l and b_{slab}/l_{load} seem the most important to be considered in the proposed approaches to calculate the one-way shear resistance and the punching shear resistance.

Previously, other studies demonstrated by testing that, for the case of slabs subjected to concentrated loads, there is a limiting width after which no further increase in maximum load occurs for increasing width (LANTSOGHT, 2013; REGAN; REZAI-JORABI, 1988; REIßEN, 2016). However, the cause for the transition of the failure mode from one-way shear to punching shear was not clear. In this study, it was demonstrated by identifying the failure mechanisms of such slabs that punching failures tend to become more critical by increasing the ratio b_{slab}/l_{load}. As a consequence, an eventual higher one-way shear capacity cannot be achieved if the test fails prematurely by punching. Moreover, it was shown that the ratio b_{slab}/l_{load} for which the punching shear capacity becomes the governing failure mode depends on the slab

thickness. In this way, it is reasonable that most approaches for defining the effective shear width (SOUSA et al., 2021c; FD P 18-717, 2013; FÉDÉRATION INTERNATIONALE DU BÉTON (FIB), 2012) do not predict a higher contributing width by increasing the slab width after a certain value.

Most approaches in the literature predict that the effective shear width increases as the shear slenderness a_v/d_l increases(FD P 18-717, 2013; FÉDÉRATION INTERNATIONALE DU BÉTON (FIB), 2012). If the shear slenderness is not considered in the unitary shear capacity expressions v_c, the one-way shear strength V_c would increase for increasing values of the shear slenderness a_v/d_l. As first demonstrated by Reiβen (2016), this study also found that there is a predominant tendency to decrease the shear capacity V_{Fu} by increasing the shear slenderness (Figure 2-5a). However, if someone consider a decrease in the unitary shear resistance for increasing values of the shear slenderness a_v/d_l (SOUSA; LANTSOGHT; EL DEBS, 2020; MUTTONI; FERNANDEZ RUIZ, 2008), such as performed by Natário, Fernandez Ruiz and Muttoni (2014) using the Critical Shear Crack Theory expressions (MUTTONI; FERNANDEZ RUIZ, 2008), then it can be demonstrated that the effective shear width increases with the shear slenderness until certain limits.

In the literature review, the influence of the transverse reinforcement ratio ρ_t on the governing shear failure mechanism was investigated through the cracking pattern from different experimental programs (LANTSOGHT; VAN DER VEEN; WALRAVEN, 2013; REIßEN; CLASSEN; HEGGER, 2018). However, there are limited tests in the literature that study this effect in detail and conflicting results were found in the review of the sectional shear and failure load (V_{Fu} and P_{test}). For instance, in the evaluation of the sectional shear and failure load of slabs as a function of ρ_t, tests were identified where the increase in transverse reinforcement led to increases in the sectional shear and failure loads for loads far away from the support (DAMASCENO, 2007) ($a_v/d_l > 7$). However, for tests with the load closer to the support, typically with ratios $a_v/d_l <4$, the increase of ρ_t led to a reduction of the sectional shear and failure loads in many tests (Figure 2-7b). Since the increase of ρ_t allows a better distribution of shear forces in the width direction (LANTSOGHT; VAN DER VEEN; WALRAVEN, 2013) and an increase of the punching capacity (MUTTONI, 2008), these reductions of the shear capacity were not expected. Therefore, more experiments on the influence of the transverse reinforcement are necessary.

2.6 Conclusions from Chapter 2

One-way slabs under concentrated loads may fail by one-way shear (as wide beams), punching shear, or a mixed failure mode between them. In the literature, the test results were frequently addressed by evaluating only the one-way shear failure mechanism (HALVONIK; VIDAKOVIĆ; VIDA, 2020; HENZE; ROMBACH; HARTER, 2020; NATÁRIO; FERNÁNDEZ RUIZ; MUTTONI, 2014; REIßEN; CLASSEN; HEGGER, 2018) or the punching shear mechanism(VAZ RODRIGUES; FERNÁNDEZ RUIZ; MUTTONI, 2008). Therefore, the understanding of the problem was commonly discussed using a narrower background. In this study, the main characteristics of the one-way and two-way shear failure mechanisms were reviewed and discussed to allow a broader insight into the mechanics of the problem. From this study, the following conclusions can be drawn:

- Different shear failure mechanisms may occur according to parameters such as the shear slenderness a_v/d_l, slab width to load size ratio b_{slab}/l_{load}, and transverse reinforcement ratio ρ_t. It was identified that the first two are the most important parameters influencing the transition from one-way to two-way shear failure.
- From the literature review and by bringing together test results from several references, it was identified that: (i) both shear and punching failure modes may occur for $a_v/d_l < 4.5$, but punching failures are most frequently the governing failure mechanism for $a_v/d_l > 5$; (ii) the tested shear capacity V_{test} of slabs under concentrated loads usually does not increase by increasing the shear slenderness a_v/d_l; (iii) punching is the governing failure mechanism for one-way slabs with $b_{slab}/l_{load} > 10$.
- The ultimate capacity of one-way slabs under concentrated loads increases only until a certain limit by increasing the ratio b_{slab}/l_{load}. This behavior occurs because there is an upper limit for the effective shear width, as verified by other authors(LANTSOGHT et al., 2014; REIßEN; CLASSEN; HEGGER, 2018), and also because punching failure becomes the governing failure mechanism for slabs after a specific value of b_{slab}/l_{load}.
- While the transverse reinforcement ratio plays a marked influence on the cracking pattern and transverse distribution of shear forces on the slab width, uniform conclusions on the effect of this parameter could not be formulated. Therefore, further experiments are required to study the influence of the transverse reinforcement ratio on the transition between shear and punching failures.

3 ONE-WAY SHEAR STRENGTH OF WIDE REINFORCED CONCRETE MEMBERS WITHOUT STIRRUPS

In this chapter, the focus was on addressing the behavior and ultimate capacity of wide beams and slabs loaded over the entire width before dealing with the problem of one-way slabs under concentrated loads. Therefore, this chapter tries to contribute to a better understanding of one of the shear failure mechanisms that one-way slabs under concentrated loads may develop: shear failure as wide beams. In this chapter, the influence of parameters such as shear slenderness, static system, and slab width-to-effective depth are discussed. In the end, a comparison between tested and predicted resistances according to 10 one-way shear models is presented, including code expressions and also mechanical-based models.

3.1 Introduction of Chapter 3

Reinforced concrete (RC) one-way slabs and wide beams are structural members extensively used in residential buildings, for bridge deck slabs and as transfer elements (CALVI; BENTZ; COLLINS, 2018; LUBELL et al., 2004). Since these members generally do not contain shear reinforcement, the assessment of shear capacity may be critical due to the brittle nature of shear failures. By not taking into account the size effect in thicker members (BAZANT; KIM, 1984) and the reduced aggregate interlock capacity in cracks of high strength concrete (YANG; DEN UIJL; WALRAVEN, 2016), some older design codes could provide higher shear capacities than the real ones in the assessment of existing structures. Besides, the shear reinforcement may be undesirable since it is not cost-effective for large members and can result in reinforcement congestion. Therefore, efforts have been devoted towards the development of reliable and accurate models of shear strength for members without shear reinforcement.

Another matter of concern regarding the shear capacity of RC members is the suitability of current code provisions for assessment of wide members. The current code provisions and main design models for shear (ACI COMMITTEE 318, 2019; CEN, 2005; FÉDÉRATION INTERNATIONALE DU BÉTON (FIB), 2012) have been calibrated by shear tests on narrow beams, with width to effective depth $b/d < 1$. Such beams may not be representative for wide members, whose b/d ratio is higher than 1. A database analysis conducted by Gurutzeaga et al. (2015) revealed the member width b does not appear to influence the shear strength of wide

members significantly. On the other hand, Conforti, Minelli and Plizzari (2017) observed shear strength increases by approximately 25% when the *b/d* ratio increases from 1 to 3.

Such different results have led us to identify the need for a more comprehensive study that includes tests of wide members under different load arrangements and support conditions. Term line loads are used here to describe members loaded at the full width (Figure 3-1a) on the top view (observe the member in Figure 3-1a is subjected to a concentrated load in the span direction that is distributed over the entire width, while in Figure 3-1b, the load is not applied along with the full width). On slabs whose load is concentrated in small areas, e.g. wheel loads on bridge decks, not all of the width of the slab width contributes to the shear strength (LANTSOGHT; VAN DER VEEN; WALRAVEN, 2013). Therefore, an effective width combined with a one-way shear model is used for the calculation of the shear capacity. This study focuses on slabs and wide beams loaded over the full width as the first step for a better understanding of the problem of wide members under shear loads with no influence of an effective width model. Figure 3-1c shows a wide member under line load in the width direction and a uniformly distributed load in the span direction, such as in a cut-in-cover tunnel slab, whose distributed loads can be the main loads (SIGRIST et al., 2013).

Figure 3-1 – Main types of loads on wide members: a) concentrated in the shear span and distributed along the width; b) concentrated in the span and width directions (not included in the scope of this study) and c) distributed load in both span and width direction.

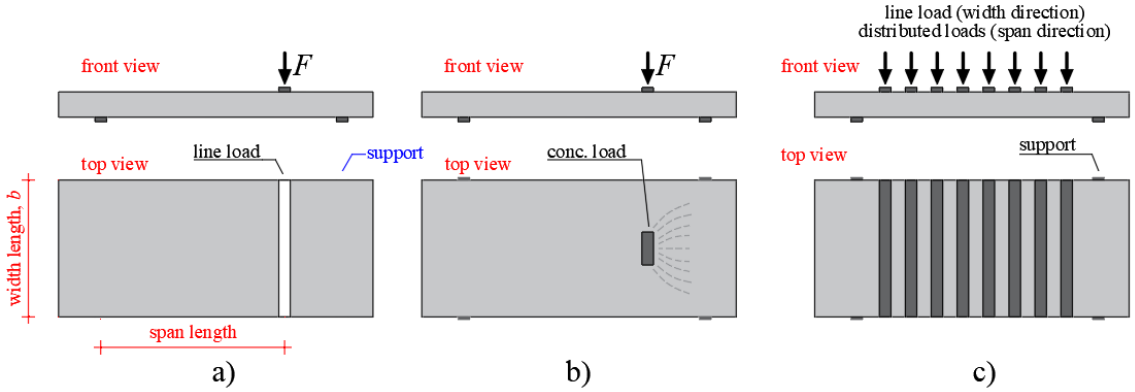

Source: Author.

Apart from geometric differences between narrow beams and wide members (e.g., slabs and wide beams), several design codes (ABNT NBR 6118, 2014; ACI COMMITTEE 318, 2019; CEN, 2005) have established semi-empirical formulas for analyses of shear strength. Although these formulations are useful for hand calculations, most of them show the following limitations: (i) safety is not guaranteed beyond the boundaries of calibration, (ii) very conservative results can be achieved under usual loads (KUCHMA et al., 2019), specifically in

the case of higher axial tensile loads (JØRGENSEN et al., 2013), (iii) aggregate size d_g, which plays a fundamental role in the aggregate interlock is not considered, and (iv) current provisions for the size effect can yield unsafe predictions of shear strength for members of higher effective depths. Several mechanical models have been proposed towards overcoming such limitations. They have taken into account the contributions of one or more shear-carrying mechanisms, i.e. capacity of the uncracked compression zone (REINECK, 1991b; TAYLOR, 1974), aggregate interlock (WALRAVEN, 1981), dowel action (CHANA, 1987) and residual tensile strength of concrete across the crack (GASTEBLED; MAY, 2001; REINECK, 1991a, 1991b). Since Conforti, Minelli and Plizzari (2017) verified the cracking pattern of wide members with $b/d>1$ ratio significantly differs from that of beams with $b/d<1$, some shear-carrying mechanisms are expected to change according to the b/d ratio, which has not been appropriately investigated.

Figure 3-2 - Differences in the cracking pattern of members with different *b/d* ratios identified by Conforti, Minelli and Plizzari (2017).

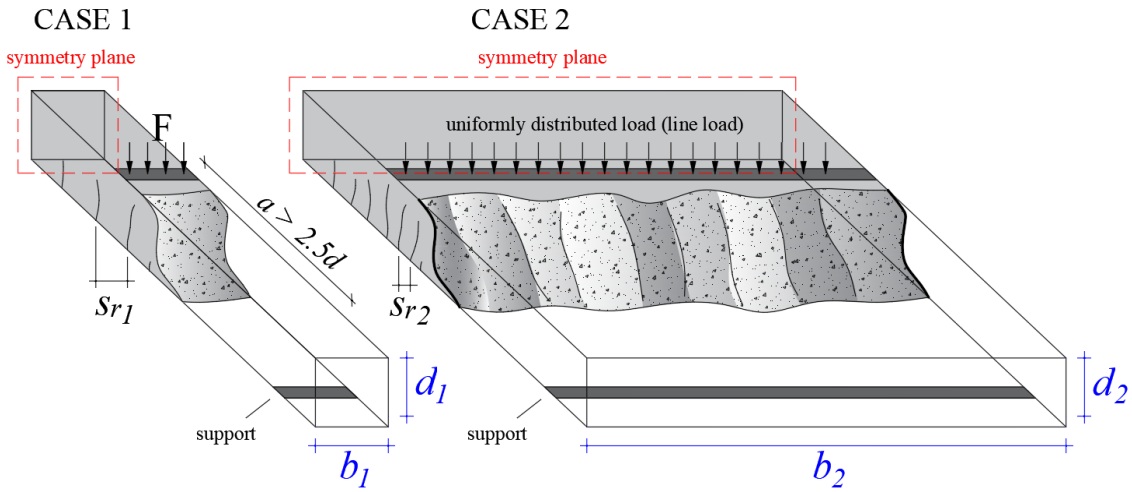

Source: Author.

Figure 3-2 shows some differences in the cracking pattern of members with different *b/d* ratios, identified by Conforti, Minelli and Plizzari (2017). Although the same material and reinforcement layouts are used, the cracking pattern along width direction *b* is more irregular in case 2 for the wider member. It is attributed this behavior to any irregularity in the load application or support condition and more pronounced randomness of cracking formation in the absence of shear reinforcement for large widths. Such an irregularity leads to larger cracked surfaces, which improves the aggregate interlock and can increase the shear capacity (CONFORTI; MINELLI; PLIZZARI, 2017). Another clear distinction is a higher number of flexural cracks develop with minor spacing in members with a higher *b/d* ratio ($S_{r1}>S_{r2}$ in Figure 3-2). Furthermore, flexural cracks that develop in members with higher *b/d* ratios may not

propagate from one face to another due to the more irregular crack profile. Improvements in the aggregate interlock promote higher shear displacements in the critical shear crack accompanied by a larger number of flexural cracks. However, these observations apply for tests under the same load and support conditions.

Most models place the critical section close to the higher moment-to-shear *M/Vd* ratio (FÉDÉRATION INTERNATIONALE DU BÉTON (FIB), 2012; MUTTONI; FERNANDEZ RUIZ, 2008). However, according to other authors (MARÍ et al., 2014, 2015; TUNG; TUE, 2016a, 2016b), the critical section is placed closer to the position where the bending moment reaches the cracking moment. Since these models are based on different failure criteria, a comparison of the accuracy provided by these models could point which one better represents the shear failure. Here, moment-to-shear ratio *M/Vd* or shear slenderness λ represents a normalized parameter of solicitation in the shear span. According to Eq. (3.1), in simply supported members under concentrated loads, the *M/Vd* ratio can be approximated by the shear span to depth ratio *a/d*:

$$\lambda = \frac{M}{V \cdot d} = \frac{V \cdot a}{V \cdot d} = \frac{a}{d} \tag{3.1}$$

In simply supported members under distributed loads, since the shear force in the section of the maximum internal moment is zero, their shear slenderness is defined by the maximum sectional forces in the span, regardless of the sections (ADAM et al., 2019):

$$\lambda = \frac{M}{V \cdot d} = \frac{\left(\frac{q \cdot l}{2} \cdot \frac{l}{2} - q \cdot \frac{l}{2} \cdot \frac{l}{4} \right)}{\frac{q \cdot l}{2} \cdot d} = \frac{\frac{q \cdot l^2}{8}}{\frac{q \cdot l}{2} d} = \frac{l}{4d} = \frac{a_{eq}}{d} \tag{3.2}$$

where a_{eq} can be interpreted as an equivalent shear span defined for simply supported members under uniformly distributed loads.

This study proposes joining the available test results of wide members with shear failures and discussing their behavior under different load arrangements and support conditions/structural systems. In comparison to the databases developed by Gurutzeaga et al. (2015) and Conforti, Minelli and Plizzari (2017), this database includes a more significant number of test results (170) and different structural systems, which were used for the identification of the main parameters that influence the shear strength of wide members. Furthermore, these results were used in an assessment of semi-empirical and mechanical-based

models of shear strength according to (i) the structural system (ii) *b/d* ratio, and (iii) shear slenderness λ. This chapter investigates whether geometric differences, load arrangements and support conditions significantly influence the shear strength of wide members.

3.2 Literature review of Chapter 3

In this section, the following aspects are addressed: (i) structural system or effect of support conditions, (ii) degree of rotational restraint and shear slenderness, (iii) load arrangement, (iv) shear failure modes and (v) overview of available models to predict the one-way shear capacity.

3.2.1 Structural system or effect of support conditions

Recent measurements of the contribution of each shear transfer action to members of different structural systems and load arrangements have shown no unique shear-transfer action governs the shear strength (CAVAGNIS; FERNÁNDEZ RUIZ; MUTTONI, 2015, 2018a). The contribution of different shear transfer mechanisms can vary according to the location, shape, and kinematics of the critical shear crack. Tung and Tue (2016b) observed some members, such as cantilevers under uniformly distributed loads, can be favored regarding shear strength by higher bending moments close to the support. Therefore, questions on a possible influence of the structural system and load arrangement on the main shear-carrying mechanisms may be raised.

Figure 3-3 – a) Arching action produced by a combination of the elbow-shaped strut and direct compression strut in the simply supported beam and b) direct compression strut in a cantilever member.

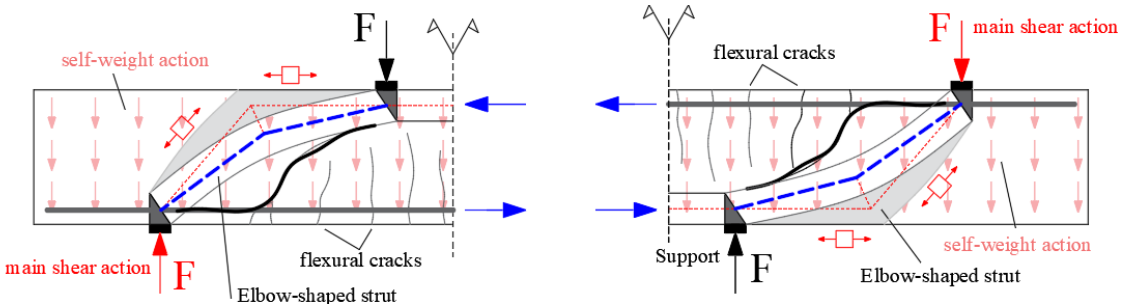

Source: Author.

As highlighted by Muttoni and Fernandez Ruiz (2008), simply supported beams can develop an arching action through a combination of an elbow-shaped strut, enabled by the tensile strength of concrete, and direct compressive struts disturbed or not by flexural cracks. Figure 3-3 shows the only difference between the cantilever and simply supported members failing by shear is the self-weight action in the same direction of the main shear load for

cantilever members and in the opposite direction for simply supported members. Therefore, higher differences in the shear behavior according to the structural system may appear if the self-weight is the main action.

One-way shear models consider the structural system or support conditions indirectly by calculations of internal forces *M* and *V* (*M* is the bending moment and *V* is the shear force. The critical section in models based on the Modified Compression Field Theory (MCFT)(VECCHIO; COLLINS, 1986) and Critical Shear Crack Theory (CSCT)(MUTTONI; FERNANDEZ RUIZ, 2008) is usually close to the section of higher *M/Vd*, where *d* is the effective depth. These models predict the shear strength has an inverse relation with longitudinal concrete strain ε in the critical section, which is directly associated with bending moment *M*. However, according to some experimental results (CALDENTEY et al., 2012; TUNG; TUE, 2016b) the shear strength of members such as cantilever under uniformly distributed loads may benefit from higher bending moment in the section of larger *M/Vd* ratio. Therefore, for such cases, the shear behavior may not be well described without considering the structural system and load arrangement, which can influence the contributions of the main shear-carrying mechanisms.

In models such as MCFT and CSCT, the aggregate interlock is assumed as the main shear transfer action when a critical shear crack arises. However, in cantilever members under distributed loads, the higher bending moment close to the support can improve the compression chord capacity in such a way that the total shear strength can be improved instead of reduced (TUNG; TUE, 2016b).

3.2.2 Degree of rotational restraint and shear slenderness

Previous studies (ISLAM; PAM; KWAN, 1998; REIßEN, 2016; REIßEN; CLASSEN; HEGGER, 2018) investigated the effect of continuous systems by measuring the degree of rotational restraint of slabs on supports, d_r, of continuous members. However, such studies were limited to members subjected to concentrated loads in the span. Parameter d_r can be estimated by Eq. (3) as follows:

$$d_r(\%) = \frac{M_{\text{sup}}}{M_{est}} \cdot 100 \qquad (3.3)$$

where M_{sup} represents the bending moment produced by a cantilever load *f* near the continuous support and M_{est} represents the static moment for a fully clamped support (Figure 3-4). Another way to evaluate the degree of rotation restraint over the internal support in

continuous members is to calculate the ratio a_1/a_2 (distances a_1 and a_2 are illustrated in Figure 3-4a separated by the location of the point of inflection (P.I.)). Such distances can be evaluated from bending moment diagrams, or using the theorem of intersecting lines for single loads (ISLAM; PAM; KWAN, 1998; REIßEN, 2016). The higher a_1/a_2 ratio indicates a higher degree of rotational restraint at on continuous support.

Figure 3-4 –Bending moments in structures with a) fully clamped support and b) partially clamped support.

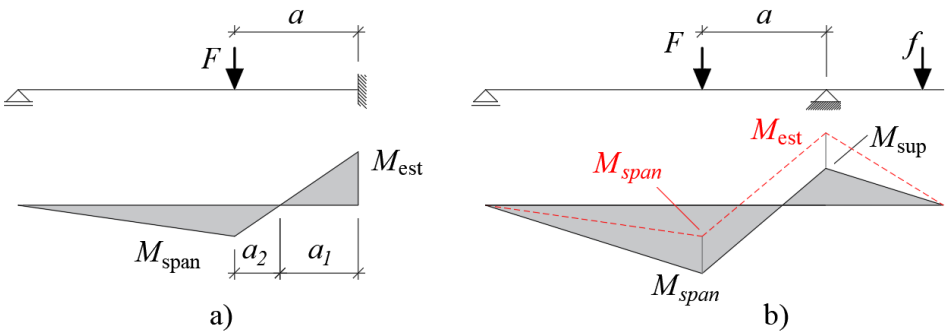

Source: Author.

On the other hand, the shear slenderness is a useful parameter for describing the shear failure modes of members without shear reinforcement, which will be discussed in the next sections. The literature provides the following shear slenderness definitions (λ): (i) *a/d* ratio, which is geometric relations between the shear span and the effective depth of members, mostly used in codes of practice (ABNT NBR 6118, 2014; SIA, 2013); (ii) *M/Vd* ratio, which directly expresses the ratio between the acting internal forces in a section and is equivalent to the *a/d* ratio for simply supported members (ACI COMMITTEE 318, 2014), and (iii) $max(a_1;a_2)/d$ ratio, which accounts for geometric information on the bending moment diagram and covers both simply supported and continuous members (REIβEN, 2016).

Tung and Tue (2016b) observed when $M_{span} > M_{sup}$ in continuous members subjected to uniformly distributed loads (Figure 3-5a), the shear strength is approximately equal to that of simply supported members under uniformly distributed loads (Figure 3-5b). The authors highlighted if $M_{span} < M_{sup}$, the shear strength of continuous beams under distributed loads can be well approximated by the sum of two equivalent cantilevers, i.e., one loaded by the shear force at the point of inflection and another loaded by a distributed load (Figure 3-5c).

Figure 3-5 – a) continuous specimen under distributed load; b) equivalent simply supported member when $M_{sup} < M_{span}$ and c) equivalent problem when $M_{sup} > M_{span}$, based on the CWSB model from Tung and Tue (2016b).

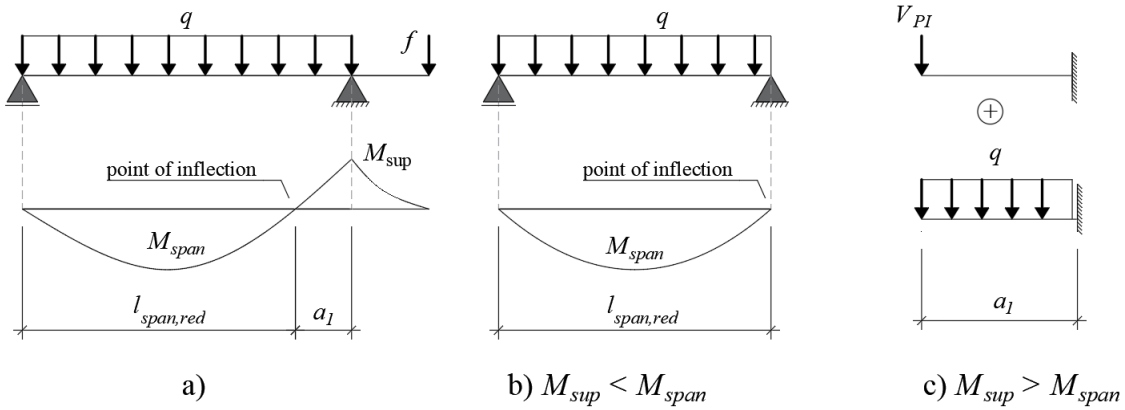

a) b) $M_{sup} < M_{span}$ c) $M_{sup} > M_{span}$

Source: Author.

This study proposes taking into account the observations from Tung and Tue (2016b) for improving the shear slenderness definition of continuous members under distributed loads. It is defined that the ratio $max\{a_1;a_2\}/d$ for such members, when $M_{sup}<M_{span}$, is equal to that of simply supported members under uniformly distributed loads of reduced span length (Figure 3-5b). Table 3-1 shows a summary of calculations for the shear slenderness parameter:

Table 3-1 – Proposed shear slenderness definition according to the static system and internal forces distribution.

Structural system	Load arrangement	Bending moments	Shear slenderness λ
Simply supported	Concentrated load	-	$max\{a_1;a_2\}/d$
	Unif. Distributed load	-	$M_{max}/V_{max}.d = l_{span}/4d$
Cantilever	Concentrated load	-	$max\{a_1;a_2\}/d$
	Unif. Distributed load	-	$max\{a_1;a_2\}/d$
Continuous member	Concentrated load	-	$max\{a_1;a_2\}/d$
	Unif. Distributed load	$M_{sup} < M_{span}$	$l_{span,red}/4d$
	Unif. Distributed load	$M_{sup} > M_{span}$	$max\{a_1;a_2\}/d$

Source: Author.

3.2.3 Load arrangement

Figure 3-6 shows parameters a_1 and a_2 of continuous members under different load arrangements in the shear span, i.e., concentrated loads and uniformly distributed ones. Such definitions were used for the evaluation of tests with different load arrangements through a unique parameter as the $max(a_1;a_2)/d$ ratio.

Figure 3-6 – Geometric parameters of the shear span under a) concentrated loads and b) uniformly distributed loads.

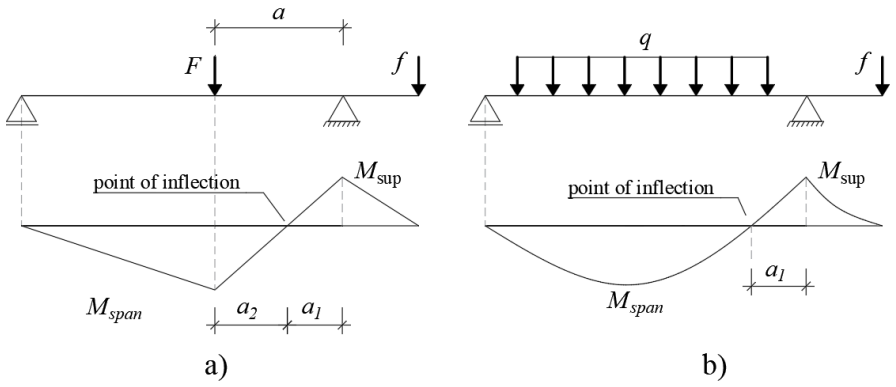

Source: Author.

Figure 3-7 illustrates three cases of load arrangement modifications, in which cantilever members under larger bending moments at the support show higher shear capacities in the span: (i) cantilever span under uniformly distributed loads compared to the same members under concentrated loads (CALDENTEY et al., 2012), (ii) longer cantilever members compared to short ones and (TUNG; TUE, 2016b) (iii) cantilever slabs under concentrated loads, in the span and width directions, combined or not with line loads along the full width (REIßEN; HEGGER, 2013b).

Figure 3-7 – Cases of load arrangement changes that can result in improved shear capacities for cantilever members: (i) under distributed loads instead of concentrated loads; (ii) distributed loads on longer shear spans and (iii) members pre-loaded by line loads.

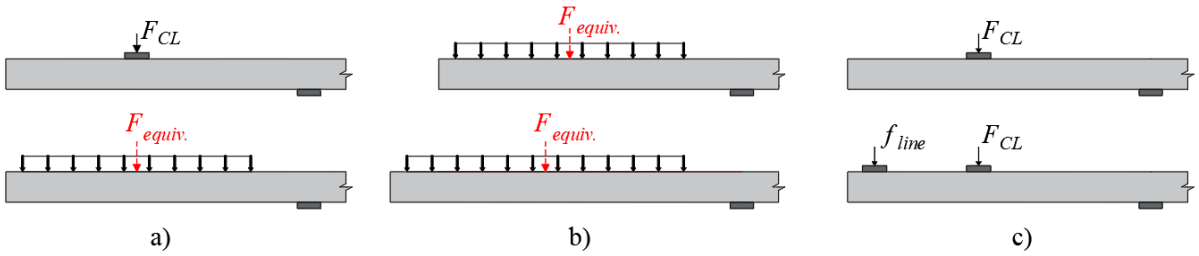

Source: Author.

Caldentey et al. (2012) observed cantilever beams of constant thickness under uniformly distributed loads show a 27% higher capacity than those with concentrated loads in the shear span, which is against some mechanical-based models e.g. *fib* Model Code 2010 and CSCT (MUTTONI; FERNANDEZ RUIZ, 2008). An explanation is a critical shear crack can arise closer to the inner support with reduced shear displacements for some combinations of load arrangement and support conditions. The contribution of the aggregate interlock, i.e., the basis of the above-mentioned models, becomes of minor importance (CAVAGNIS; FERNÁNDEZ

RUIZ; MUTTONI, 2018a). From this study, it can be concluded that the compression chord capacity improvement for cantilever spans under distributed loads can be more pronounced than the negative effect on the aggregate interlock at the critical shear crack.

3.2.4 Shear failure modes

The ratio between the clear shear span-to-effective depth ratio a_v/d and the shear slenderness M/Vd or $max(a_1;a_2)/d$ can be used for distinguishing members subjected to compression-shear failures from those more susceptible to flexural-shear failure (YANG; WALRAVEN; DEN UIJL, 2017). As most models aim to describe second type failures, the accuracy level of models for members subjected to compression-shear failures is unknown. When the critical shear crack arises too close to the support, e.g., when concentrated loads are placed at $a_v < 2.5d$ distances, the aggregate interlock has a minor contribution for the shear strength and the load is carried mainly by direct compression struts, which characterizes the compression-shear failure. For loads far from the support, the critical shear crack can usually arise from flexural shear cracks, and the arching action is composed of a combination of direct compression struts (enabled by the aggregate interlock) and elbow-shaped struts (enabled by the tensile strength of concrete) (MUTTONI; FERNANDEZ RUIZ, 2010a).

The clear shear span-to-effective depth ratio a_v/d has been widely used to reduce design shear force V_{exp} to take into account the beneficial effect from direct compression struts when a concentrated load is placed close to the support by a factor β. Therefore, models that do not considered this shear transfer mechanism tends to be more conservative for reduced values of a_v/d. Such a ratio, from which compressive struts begin to play an important role, depends on the longitudinal reinforcement ratio, the bond between concrete and reinforcement, but usually varies between 2 and 3 (KANI, 1967; MUTTONI; FERNANDEZ RUIZ, 2010a).

3.2.5 Overview of available models

Shear strength models may be divided into semi-empirical, mechanical and purely empirical models (i.e., ANN-based, curve-fitting-based methods and genetic algorithm-based methods (CLADERA; MARÍ, 2004; CLADERA; PÉREZ-ORDÓÑEZ; MARTÍNEZ-ABELLA, 2014). Among codes that still use semi-empirical approaches are ABNT NBR 6118:2014 and NEN-EN 1992-1-1:2005 (CEN, 2005). ACI 318:2019 (ACI COMMITTEE 318, 2019) has incorporated mechanical parameters in comparison to ACI 318:2014 (ACI COMMITTEE 318, 2014), mainly related to the size effect. However, in the present study, both formulations are classified as semi-empirical, since they do not deal directly with the main

shear-carrying mechanisms. Owing to improvements in experimental analyses and a better knowledge of the shear strength problem, mechanical models based on different assumptions about what drives shear failure have been proposed.

fib Model Code 2010 (FÉDÉRATION INTERNATIONALE DU BÉTON (FIB), 2012) has adopted SMCFT (BENTZ; VECCHIO; COLLINS, 2006) as the basis of its formulation and SIA 262:2013 (Swiss Code) (SIA, 2013) has adopted the CSCT model (MUTTONI; FERNANDEZ RUIZ, 2008) with some simplifications (MUTTONI; FERNANDEZ RUIZ, 2008). Such models consider the shear capacity as a function of concrete longitudinal strain ε in a critical section. The MCFT and the CSCT address the shear-transfer mechanisms as a function of a unique parameter and consider both aggregate size and concrete compressive strength play an important role in the roughness of the crack, hence, in the aggregate interlock of members subjected to shear.

Other researchers have developed multi-action models that estimate the shear strength by summing the contribution of the main shear transfer mechanisms (LANTSOGHT et al., 2015c) calculated separately (MARÍ et al., 2015, 2016; YANG; DEN UIJL; WALRAVEN, 2016). According to the Shear-Flexural Strength Mechanical Model (SFSMM) (MARÍ et al., 2015, 2016), after the development of the first branch of the critical shear crack, failure takes place when the stresses at any point of the concrete compression chord reach the assumed biaxial stress failure envelope described by Kupfer and Gerstle (1973). In other words, the authors considered failure takes place when the first branch of the critical crack reaches the neutral axis depth, as proposed by Yu et al. (2015). The Compression Chord Capacity Model (CCCM) (CLADERA et al., 2016) appears as a simplification of the SFSMM to make it easier to use in daily engineering practice. In CCCM, the authors highlighted that for wide members with a low amount of longitudinal reinforcement and without stirrups, such as one-way slabs, the depth in the uncracked compression zone could be reduced as compared to beams. Therefore, the contribution of the residual tensile stresses for such members can be comparable to the compression chord capacity. In these cases, the CCCM incorporated a minimum shear strength parameter that considerer explicitly the residual tensile stress action to avoid very conservative results.

In the Critical Shear Displacement Theory (CSDT) (YANG; DEN UIJL; WALRAVEN, 2016; YANG; WALRAVEN; DEN UIJL, 2017) assumes the critical inclined crack starts from a major flexural crack, which will lead to an overall collapse when the shear displacement Δ of

the crack reaches a critical value and causes a secondary crack (dowel crack) along the reinforcement. According to Yang, Walraven and den Uijl (2017), a dowel crack causes the detachment of the tensile reinforcement from the concrete along with the shear span that significantly reduces the lateral confinement on the crack and the member flexural stiffness. Due to the crack opening in the major crack, an additional vertical shear displacement is required for the recovery of the previous shear stress level in the crack, which feeds the growth of flexural-shear cracks and leads to the brittle collapse of the member.

The Critical Width of a Shear Band model (CWSB) (TUNG; TUE, 2016a, 2016b) focuses on the stress relations just before the critical shear crack formation. According to Tung and Tue (2016a), if the component of normal stress is considered in the tension zone, a shear failure occurs in a shear band when it reaches a critical width value and an inclined crack tends to connect the tips of existing flexural cracks. From this model, the bending moment may have a positive influence on the shear capacity of members such as cantilevers under uniformly distributed loads due to the higher contribution of the compression chord capacity.

Table 3-2, Table 3-3, Table 3-4 and Table 3-5 shows an overview of the aforementioned shear strength models. All symbols used can be found in the list of notations, and a detailed explanation of some parameters can be consulted in the referred papers.

Table 3-2 – Semi-empirical models to calculate the shear strength of members without shear reinforcement.

Code	Expression	
ABNT NBR 6118:2014 (ABNT, 2014)	$V_{Rd1,6118} = \left[\tau_{Rd} k_{NBR} \left(1.2 + 40\rho_1\right) + 0.15\sigma_{cp} \right] b_w d$ with τ_{Rd} and σ_{cp} in [MPa], b_w in [m] and d in [mm]	(3.4)
	$k_{NBR} = \begin{cases} 1 \text{ , if at least } 0.50A_s \text{ does not reach the support} \\ \lvert 1.6 - d \rvert, \text{ with } d \text{ in [m]} \end{cases}$	(3.5)
	$\tau_{Rd} = 0.25 f_{ctd}$	(3.6)
	$f_{ctd} = f_{ctk,\inf} / \gamma_c$	(3.7)
	$f_{ctk,\inf} = 0.7 f_{ctm}$	(3.8)
	$f_{ctm} = \begin{cases} 0.3 f_{ck}^{\ 2/3} \text{ for } f_{ck} \le 50MPa \\ 2.12 \ln\left(1 + 0.11 f_{ck}\right) \text{ for } 50\text{MPa} < f_{ck} \le 90MPa \end{cases}$	(3.9)
	$\sigma_{cp} = N_{Ed} / A_c$	(3.10)
	$\rho_l = A_s / \left(b_w d\right) \le 0.02$	(3.11)

N_{Ed} is the axial force in the evaluated section due to prestressing or other axial action. A_c is the cross-sectional area of concrete; A_s is the cross-sectional area of reinforcement.

In the Brazilian code, the enhanced shear capacity for loads close to the support is considered only for beams. For slabs, no mention of arching action is provided.

NEN 1992-1-1:2005 (CEN, 2005)

$$V_{Rd,c,EC2} = Max\begin{cases}\left[C_{Rd,c}k(100\rho_l f_{ck})^{1/3} + k_1\sigma_{cp}\right]b_w d = V_{Rd,c1} \\ \left(v_{\min} + k_1\sigma_{cp}\right)b_w d = V_{Rd,c2}\end{cases} \quad (3.12)$$

with d in [mm] and f_{ck} in [MPa]

$C_{Rd,c}$ is an empirical factor used for characteristic shear strength calculations and it was derived from comparison with experimental results (REGAN, 1987) and calibrated through reliability analysis on 176 beam tests (KONIG; FISCHER, 1995). In this study, as suggested in the code, $C_{Rd,c}$ = 0.18.

σ_{cp} is the axial stress in the evaluated section due to prestressing or other axial action. k_1 is the factor related to the influence of normal stress in the one-way shear capacity (k_1 = 0.15 is the recommended value in the code).

$$v_{\min} = 0.035k^{3/2} f_{ck}^{1/2} \quad (3.13)$$

$$k = 1 + \sqrt{\frac{200}{d}} \le 2, \quad \text{with } d \text{ in [mm] and } f_{ck} \text{ in [MPa]} \quad (3.14)$$

The NEN 1992-1-1:2005 provides that, for loads applied within a distance $0.5d \le a_v \le 2d$ from the edge of the support (or center of bearing where flexible bearings are used), the contribution of this load (V_{Fu}) to the shear force V_{Ed} may be multiplied by $\beta = a_v/2d$. This reduction may be applied for checking $V_{Rd,c}$ in the Expression (3.12). This is only valid provided that the longitudinal reinforcement is fully anchored at the support. For av < 0.5d the value av = 0,5d should be used. Therefore:

$$\beta = \begin{cases}1, & \text{if } a_v \ge 2d_\ell \\ a_v / 2d_\ell, & \text{if } 0.5d_\ell \le a_v \le 2d_\ell \\ 0.25, & \text{if } a_v \le 0.5d_\ell\end{cases} \quad (3.15)$$

ACI 318:2019 (ACI COMMITTEE 318, 2019)

$$V_{ACI,2019} = \text{Either of} \begin{cases} \left[0.17\lambda\sqrt{f_c} + \frac{N_{Ed}}{6 \cdot A_g}\right] b_w d & \text{(a)} \\ \left[0.66\lambda(\rho)^{1/3}\sqrt{f_c} + \frac{N_{Ed}}{6A_g}\right] b_w d & \text{(b)} \end{cases} \quad \text{if } A_s \geq A_{s,\min}$$

(3.16)

$$V_{ACI,2019} = \left[0.66\lambda_s\lambda(\rho)^{1/3}\sqrt{f_c} + \frac{\sigma_{cp}}{6A_g}\right] b_w d, \quad \text{(c) if } A_s < A_{s,\min}$$

(3.17)

$$\lambda = \begin{cases} 1, \text{ to normalweight aggregate} \\ 0.75, \text{ to lightweight aggregate} \end{cases} \qquad (3.18)$$

$$\lambda_s = \sqrt{\frac{2}{1+0.004d}} \leq 1, \text{ with } d \text{ in [mm] and } f_c \text{ in [MPa]} \qquad (3.19)$$

$$\text{limits}: \begin{cases} \sqrt{f_c} \leq 8.3MPa \\ V_{ACI} \leq 0.42\lambda\sqrt{f_c} b_w d \\ \frac{N_{Ed}}{A_g} \leq 3.45MPa \end{cases} \qquad (3.20)$$

ACI 318:2014 (ACI COMMITTEE 318, 2014)

$$V_{ACI,2014,simplified} = 0.17\sqrt{f_{ck}} b_w d_l \qquad (3.21)$$

$$V_{ACI,2014,\text{detailed}} = \left(0.16\sqrt{f_{ck}} + 17\rho_l \frac{Vd_l}{M}\right) b_w d_l \leq 0.29\sqrt{f_{ck}} b_w d_l$$

(3.22)

with f_{ck} in [MPa], b in [m] and d in [mm]

$$\text{limits}: \begin{cases} \{V_{ACI,2014} \leq 0.29\sqrt{f_{ck}} b_w d \\ \frac{Vd_l}{M} \leq 1 \end{cases} \qquad (3.23)$$

Continuation of Table 3-2

Source: Author.

Table 3-3 – Mechanical models of shear strength – Part I.

Code	Expression
Model Code 2010 (*fib*, 2012)	$V_c = k_v \cdot \sqrt{f_c} \cdot b_w \cdot z,$ with f_c in [MPa] (3.24)
	$k_v = \frac{0,4}{1+1500 \cdot \varepsilon_x} \cdot \frac{1300}{1000 + k_{dg} \cdot z},$ with z in [mm] (3.25)
	$k_{dg} = \frac{32}{16 + d_g} \geq 0.75,$ with d_g in [mm] (3.26)
	$\beta = \begin{cases} 1 & \text{if } a_v \geq 2d_\ell \\ a_v / 2d_\ell & \text{if } d_\ell \leq a_v \leq 2d_\ell \\ 0.5 & \text{if } a_v \leq d_\ell \end{cases}$ (3.27)
	$\varepsilon_x = \frac{1}{2E_s A_s}\left(\frac{M_{Ed}}{z} + V_{Ed} + N_{Ed}\left(\frac{1}{2} \pm \frac{\Delta e}{z}\right)\right)$ (3.28)
SIA 262:2013 (SIA, 2013)	$v_c = k_d \cdot \tau_c \cdot d$ (3.29)
	$\tau_c = 0.3\sqrt{f_c},$ with f_{ck} in [MPa] (3.30)
	$k_d = \frac{1}{1 + \varepsilon_s \cdot d \cdot k_g},$ with d in [mm] (3.31)
	$k_g = \frac{48}{16 + d_g},$ with d_g in [mm] (3.32)
	$\varepsilon_s = \frac{f_y}{E_s}\frac{m_{Ed}}{m_R}$ (elastic domain) or $\varepsilon_s = 1.5\frac{f_y}{E_s}$ (plastic domain) (3.33)
	$m_R = \rho f_y b d^2 \cdot \left(1 - \frac{\rho f_y}{2 f_c}\right)$ (3.34)

Source: Author.

Table 3-4 – Mechanical models of shear strength – Part II.

Model	Expression
SFSMM (MARÍ et al., 2015)	$V_{Sfsmm} = \left(v_c + v_w + v_l + v_s\right) \cdot f_{ct} \cdot b \cdot d$ (3.35)
	$v_c = \frac{V_c}{f_{ct} \cdot b.d} = \zeta \cdot \left(088 \cdot x/d + 0.02\right)\left(0.94 + 0.3\mu\right)$ (3.36)
	$v_w = \frac{V_w}{f_{ct} \cdot b \cdot d} = 167 \cdot \frac{f_{ct}}{E_c} \cdot \left(1 + \frac{2 \cdot E_c \cdot G_f}{f_{ct}^{\ 2} \cdot d}\right)$ (3.37)
	$v_l \simeq 0.23 \frac{\alpha_e \rho}{1-\xi} \simeq 0.25\xi - 0.05$ (3.38)
	$v_s = \frac{0.85 \cdot d \cdot A_{sw} \cdot f_{yw}}{f_{ct} \cdot b \cdot d} = 0.85 \cdot \rho_w \cdot \frac{f_{yw}}{f_{ct}}$ (3.39)
	$\zeta = 1.2 - 0.2a \geq 0.65,$ with a in [m] (3.40)
	$f_{ctm} = \begin{cases} 0.30 \cdot \sqrt[3]{f_{ck}^{\ 2}}, \text{ if } f_{ck} \leq 60MPa \\ 2.12 \cdot \ln\left(1 + \frac{f_{cm}}{10}\right), \text{ if } f_{ck} > 60MPa \end{cases}$ (3.41)
	$E_c = 22 \cdot \left(\frac{f_{cm}}{10}\right)^{0,3}$ (3.42)
	$G_f = 0.028 \cdot f_{cm}^{\ 0.18} \cdot d_g^{\ 0.32}$ (3.43)
	$s_u = s_{cr} + 0,85d$ (3.44)
	$\mu = \frac{M}{f_{ct} \cdot b \cdot d^2},$ for $M = M_{cr} \rightarrow \mu = 0.20$ (3.45)
	$\xi = \frac{x}{d} = \alpha_e \cdot \rho. \left(-1 + \sqrt{1 + \frac{2}{\alpha_e \cdot \rho}}\right)$ (3.46)
	$\alpha_e = E_s / E_c$ (3.47)
CCCM (CLADERA et al., 2016)	$V_{CCCM} = 0.3\zeta \frac{x}{d} f_c^{\ 2/3} bd \geq V_{cu,\min} = 0.25\left(\zeta k_c + \frac{20}{d_0}\right) f_c^{\ 2/3} bd$ (3.48)
	$\zeta = \frac{2}{\sqrt{1 + \frac{d_0}{200}}} \left(\frac{d}{a}\right)^{0.2} \not< 0.45,$ with d_0 in [mm] (3.49)
	$\frac{x_0}{d} = \alpha_e \rho \left(-1 + \sqrt{1 + \frac{2}{\alpha_e \rho}}\right) \simeq 0.75\left(\alpha_e \rho_l\right)^{1/3}$ (3.50)

Source: Author.

Table 3-5 – Mechanical models of shear strength – Part III.

Model	Expression
CSDT (YANG; DEN UIJL; WALRAVEN, 2016)	$V_u = V_c + V_{ai} + V_d$ (3.51)
	$V_c = \frac{2}{3}\frac{z_c}{z}V = \frac{d - s_{cr}}{d + 0.5 s_{cr}}V$ (3.52)
	$V_{ai} = \text{either of} \begin{cases} \sigma_{pu}\int_0^{s_{cr}} b\left(A_x(\Delta, w) - \mu A_y(\Delta, w)\right) ds \\ f_c^{\,0.56} s_{cr} b \frac{0.03}{w_b - 0.01}\left(-978\Delta^2 + 85\Delta - 0.27\right) \\ \int_0^{s_{cr}} \tau_{ai}(\Delta, w) b ds \end{cases}$ (3.53)
	$V_d = 1.64 b_n \phi \sqrt[3]{f_c}$, f_c in [MPa] (3.54)
	$s_{cr} = \left(1 + \rho_l n_e - \sqrt{2\rho_l n_e + (\rho_l n_e)^2}\right) d$ (3.55)
	$\Delta_{cr} = \frac{25d}{30610\phi} + 0.0022 \le 0.025$ mm (3.56)
	$w_b = \frac{M}{z A_s E_s} l_{cr,m}$ (3.57)
CWSB (TUNG; TUE, 2016a)	$V_{CWSB} = \tau_{Rc} \cdot (b_w \cdot d)$ (3.58)
	$\tau_{Rc} = \frac{(2/3)\cdot \tau_{\max} \cdot x + (1/2)\cdot(\tau_{\max} + \tau_u)\cdot x' + \tau_u \cdot (d - x - x')}{d}$ (3.59)
	$\tau_{\max} = \frac{\tau_u}{1 - \left(\frac{x'}{x}\right)^2}$ (3.60)
	$\tau_u = \sqrt{f_{ct} \cdot (f_{ct} - \sigma_{xm})}$ (3.61)
	$\sigma_{xm} = \begin{cases} f_{ct}\left(1 - 0.5 \cdot \frac{d_{b,crit}}{x' + x''}\right), \text{ if } d_{b,crit} < x' + x'' \\ f_{ct}\left(0.5 \cdot \frac{d_{b,crit}}{x' + x''}\right), \text{ if } d_{b,crit} \ge x' + x'' \end{cases}$ (3.62)
	$d_{b,crit}[m] = 0.5 \cdot \frac{(100 \cdot \rho_s)^{0.9}}{f_c}$, f_c in [MPa] (3.63)
	$x = \left[\sqrt{(\rho_s \cdot n)^2 + 2 \cdot \rho_s \cdot n} - \rho_s \cdot n\right] \cdot d$, with $n = E_s / E_c$ (3.64)
	$x' = \frac{\varepsilon_{ct}}{\varepsilon_s} \cdot (d - x)$ (3.65)

$$x'' = \frac{w_1}{w_k} \cdot \left(d - x - x'\right) = \frac{G_f}{f_{ct} \cdot w_k} \cdot \left(d - x - x'\right) \quad (3.66)$$

$$\varepsilon_{ct} = f_{ct} / E_c \quad (3.67)$$

$$\varepsilon_s = \frac{1}{E_s \cdot \rho_s \cdot b_w \cdot d} \cdot \left(\frac{M}{z} + \frac{V}{2}\right) \leq \frac{1}{E_s \cdot \rho_s \cdot b_w \cdot d} \cdot \frac{M_{\max}}{z} \quad (3.68)$$

$$w_k = s_{rm} \cdot \left(\varepsilon_{sm} - \varepsilon_{cm}\right) = s_{rm} \cdot \frac{1}{E_s} \cdot \sigma_s - \left[0.5 \cdot \frac{f_{ct}}{\rho_{\rho,eff}} \cdot \left(1 + n \cdot \rho_{\rho,eff}\right)\right] \quad (3.69)$$

$$w_1 = G_f \,/\, f_{ct} \quad (3.70)$$

$$\rho_{\rho,eff} \approx 4 \cdot \rho_s \quad (3.71)$$

$$s_{rm} = 0.7 \cdot d \quad (3.72)$$

Control section:

$$x_0 = \frac{M_{cr}}{P} + s_{rm} \cdot \left(1.3 - \frac{M_{\max}}{M_y}\right) \leq \frac{M_{cr}}{P} + s_{rm} \quad (3.73)$$

$$x_{control} = x_1 = x_0 + s_{rm} \quad (3.74)$$

With f_c and f_{ct} in [MPa], M, M_{cr} and $M_{\max}$ in [kNm]

Continuation of Table 3-5

Source: Author.

3.3 Database of experiments

This section presents an overview of the databases studied and parameter analyses to highlight the distribution of the tests according to specific parameters.

3.3.1 Overview

The database of wide members under line loads in the member width and under different load arrangements in the span direction contains 170 test results of specimens of *b/d* >1 ratio, which is the criterion for the definition of experiments on wide beams and slabs. The tests were conducted by: Adam, Herbrand and Classen (2018), Adam et al. (2019), Adam, Reiβen and Hegger (2018), Aster and Koch (1974), Bui et al. (2017b), Conforti et al. (2015), Conforti, Minelli and Plizzari (2013, 2017), Furuuchi et al. (1998), Ghannoum (1998), Gurutzeaga et al. (2015), Hegger and McGrath (1980), Jäger (2002), Jäger and Marti (2005), Jäger (2007), Kani et al. (1979), Lantsoght (2013), Leonhardt and Walther (1962), Lubell (2006), Olonisakin and

Alexander (1999), Rajagopalan and Ferguson (1968), Reiβen (2016) and Serna-Ros et al. (2002).

The database is available in the public domain (SOUSA; LANTSOGHT; EL DEBS, 2019). The number of tests available on different support conditions is noteworthy: (i) 61 on continuous members of different degrees of rotational restraint d_r, (ii) 92 on simply-supported specimens and (iii) 17 on cantilever members. Several references have missing information, such as the support overhang (GHANNOUM, 1998; HEGER; MCGRATH, 1980), maximum diameter of the aggregate (LANTSOGHT, 2012; OLONISAKIN; ALEXANDER, 1999; RAJAGOPALAN; FERGUSON, 1968), rebar diameter and rebar spacing (ASTER, H.; KOCH, 1974; HEGER; MCGRATH, 1980; KANI; HUGGINS; WITTKOPP, 1979; LANTSOGHT, 2012; LEONHARDT; WALTHER, 1962; RAJAGOPALAN; FERGUSON, 1968), and size of the loading and support plates (ASTER, H.; KOCH, 1974). For tests supported by rollers, the size of support plates was considered 10 mm (CONFORTI; MINELLI; PLIZZARI, 2017). Whenever possible, information was taken from the original references. In cases whose geometrical information was not provided in the text, measures were estimated from technical drawings and figures when available.

Concerning concrete compressive strength, f_c refers to the average concrete compressive strength measured in cylinders. A 0.85 reduction factor was used for converting the measurements from cubes to cylinders (LANTSOGHT; VAN DER VEEN; WALRAVEN, 2013). The sectional shear strength of all tests was calculated towards the elimination of some inconsistencies related or not to the self-weight consideration based on the applied loads and specimen's geometry. As in many cases, the cracking pattern was not reported and the critical shear crack location was not known in these tests. Therefore, and towards a uniform analysis, the shear capacity at failure was calculated at $a/2$ (with a being the shear span) for members under concentrated loads. For those under distributed loads, the shear force at failure was calculated as the shear force at the inner support.

3.3.2 Parameter ranges in database

Table 3-6 shows the parameters ranges in the database. According to Table 3-6, the limitation of thicknesses tested (<1.01 m) hampers the investigations on the size effect for the collected experiments (ACI COMMITTEE 446, 1991; BAZANT; KIM, 1984; YU et al., 2016). The database includes some experiments with concrete compressive strengths higher than 65 MPa, for which the aggregate interlock may make a minor contribution to the shear strength

due to the smoother crack surfaces (FÉDÉRATION INTERNATIONALE DU BÉTON (FIB), 2012). Regarding parameter a_v/d, as the database includes experiments under concentrated loads with $a_v/d < 2.5$ ratios, the influence of direct shear force transfer by compressive struts on the shear strength could be investigated.

Table 3-6 - Ranges of parameters in database.

Parameter	Min	Max
b (m)	0.21	2.40
h (m)	0.10	1.01
ℓ_{span} (m)	0.60	7.00
b/d [-]	1.00	9.90
ρ_ℓ (%)	0.42	2.75
d_ℓ (m)	0.085	0.916
$Ø_\ell$ (mm)	10	30
s/d [-]	0.11	1.48
f_c (MPa)	13.40	74.62
d_{ag} (mm)	10	30
a/d [-]	1.25	6.07
a_v/d [-]	0.94	5.61
M/Vd [-] or λ [-]	1.25	11.70

Source: Author.

Figure 3-8 shows the frequency distribution of the database parameters. According to Figure 3-8a, most tests were performed in the range of concrete compressive strengths between 25 MPa and 50 MPa. Only four tests were performed with $f_c > 65$ MPa. As it is typical in shear databases, the longitudinal reinforcement ratio is concentrated in ranges larger than 0.75% for the avoidance of flexural failure modes (Figure 3-8b). The small number of tests with effective depths d higher than 600 mm, of major interest for bridge deck slabs, hampers investigations of the size effect on wide members (Figure 3-8c). Figure 3-8d shows approximately half of the tests were performed with loads at a_v/d ratios lower than 3, and therefore are influenced by direct shear loads transfer towards the support through compressive struts. Such members may have failed due to concrete crushing in the compression zone, denoted here as shear compression failure (YANG; WALRAVEN; DEN UIJL, 2017). Since most mechanical models have been formulated for members that show flexural shear failure (a_v/d > 2.5-3), a higher scattering can be expected between experimental and predicted shear capacities. The parameter of rebar spacing-to-effective depth ratio (s/d) in the database shows a concentration of values smaller than 0.8 (Figure 3-8e).

Figure 3-8 - Distribution of parameters in database: (a) concrete compressive strength f_c; (b) reinforcement ratio ρ; (c) effective depth d_l; (d) clear shear span to effective depth ratio a_v/d; e) rebar spacing to effective depth ratio s/d; f) member width to effective depth ratio b/d.

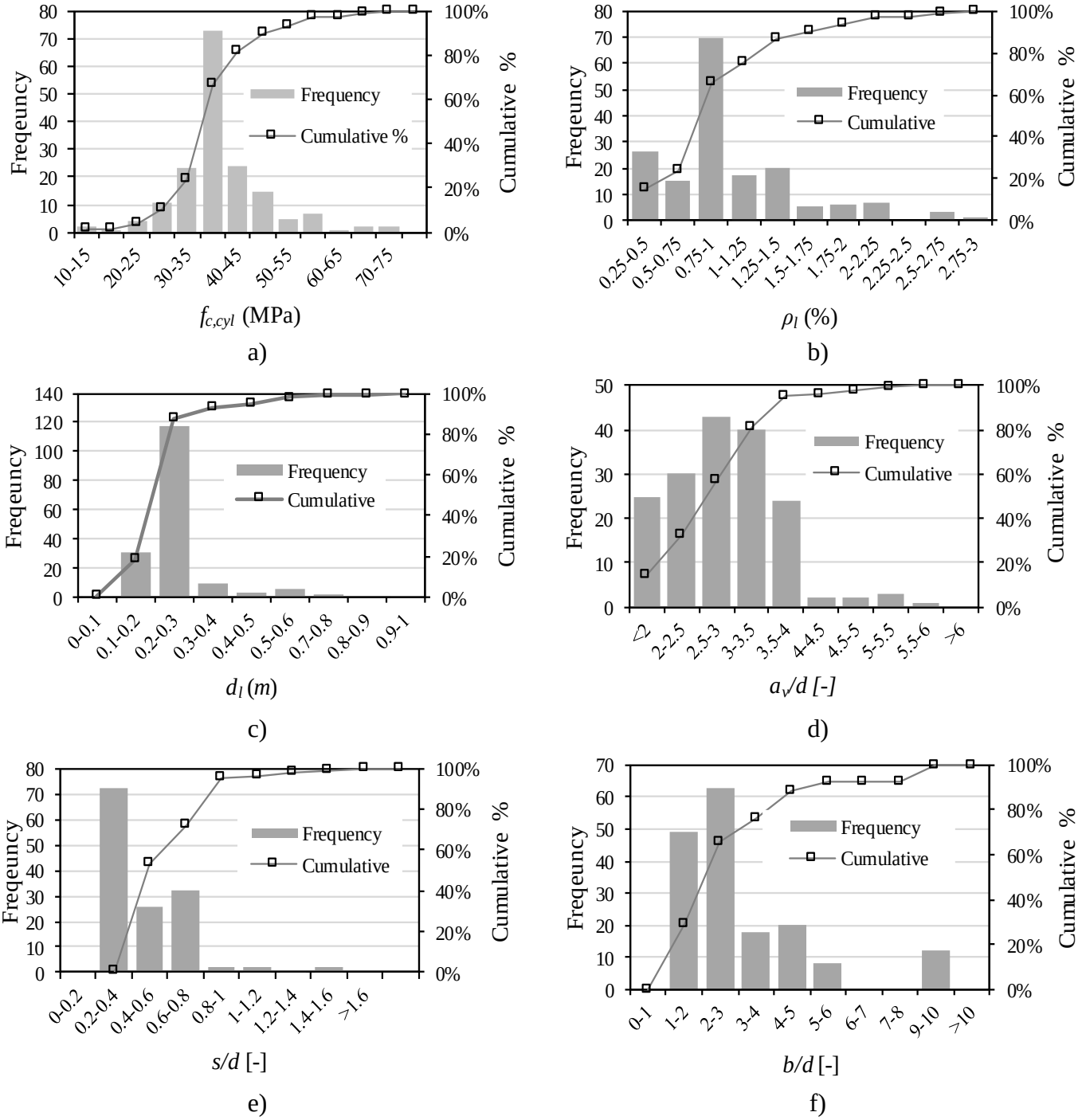

Source: Author.

Figure 3-8f shows a reduced number of members with b/d ratios higher than 5 (< 20%), which can be related to difficulties in performing tests on large members, whose loads required to reach shear failures can be higher than the actuator capacities. According to the available test results, the effect of member width b on the shear behavior will be evaluated mainly in the

range of wide beams, typical of transition members. More test results are required for investigation on the shear behavior of wide members such as one-way slabs. An interesting aspect of this database is the absence of tests under axial loads, for which is supposed the same behavior of beams.

3.4 Results

This section presents the results of the study related to (i) the parameter analyses, (ii) the shear slenderness, and (iii) the comparison between tested and predicted resistances.

3.4.1 Parameter analyses on the shear strength of RC wide members

The tensile strength of concrete plays an important role in the shear behavior of RC members since it controls the crack widths and the ability of transfer shear forces (ASCE–ACI COMMITTEE 445, 1998). However, in design, it is more usual to specify the concrete compressive strength and correlate it with the concrete tensile strength. The Eurocode (CEN, 2005) correlates the tensile strength of concrete with $f_c^{1/3}$, whereas Model Code 2010 (*fib*, 2012) and SIA code (SIA, 2013) adopt relations with $f_c^{1/2}$. In the Brazilian code [36], the concrete tensile strength is estimated by a relation with $f_c^{2/3}$. Toward an evaluation of which of the relations best fits the tensile strength of concrete and a comparison between different groups of tests, the shear capacity V_{exp} was normalized with b and d for finding the shear stress and further normalized with $f_c^{1/3}$ and $f_c^{1/2}$ for determining the normalization for the compressive strength that leads to the most uniform results.

Figure 3-9 - Normalized shear strength by section geometry and: (a) square root of the concrete compressive strength; (b) cube root of the concrete compressive strength.

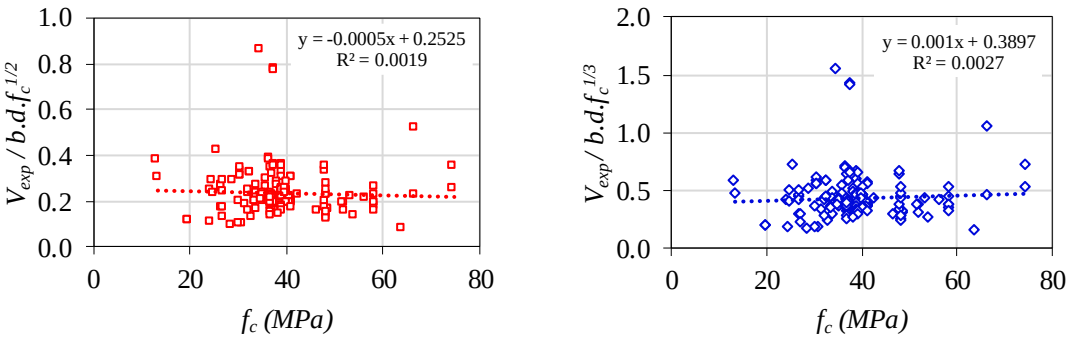

a) b)

Source: Author.

Figure 3-9 shows the shear strength of wide members normalized by the geometry of the section (b and d) and $f_c^{1/2}$ seems the most appropriate, since it provided the smallest inclination of the trendline (Figure 3-9a). Therefore, it is used the normalized shear strength by

$f_c^{1/2}$ in the parameter analysis (Figure 3-10). On the other hand, differences of tendency caused by the use of $f_c^{1/2}$, $f_c^{1/3}$ and $f_c^{2/3}$ can be negligible.

Figure 3-10. Studies on parameters based on normalized shear strength for all entries in the database, influence of (a) longitudinal reinforcement ratio ρ_ℓ; (b) effective depth d; (c) clear shear span to depth ratio a_v/d; (d) shear slenderness M/Vd; (e) flexural rebar spacing to effective depth ratio s/d; f) member width to effective depth ratio b/d.

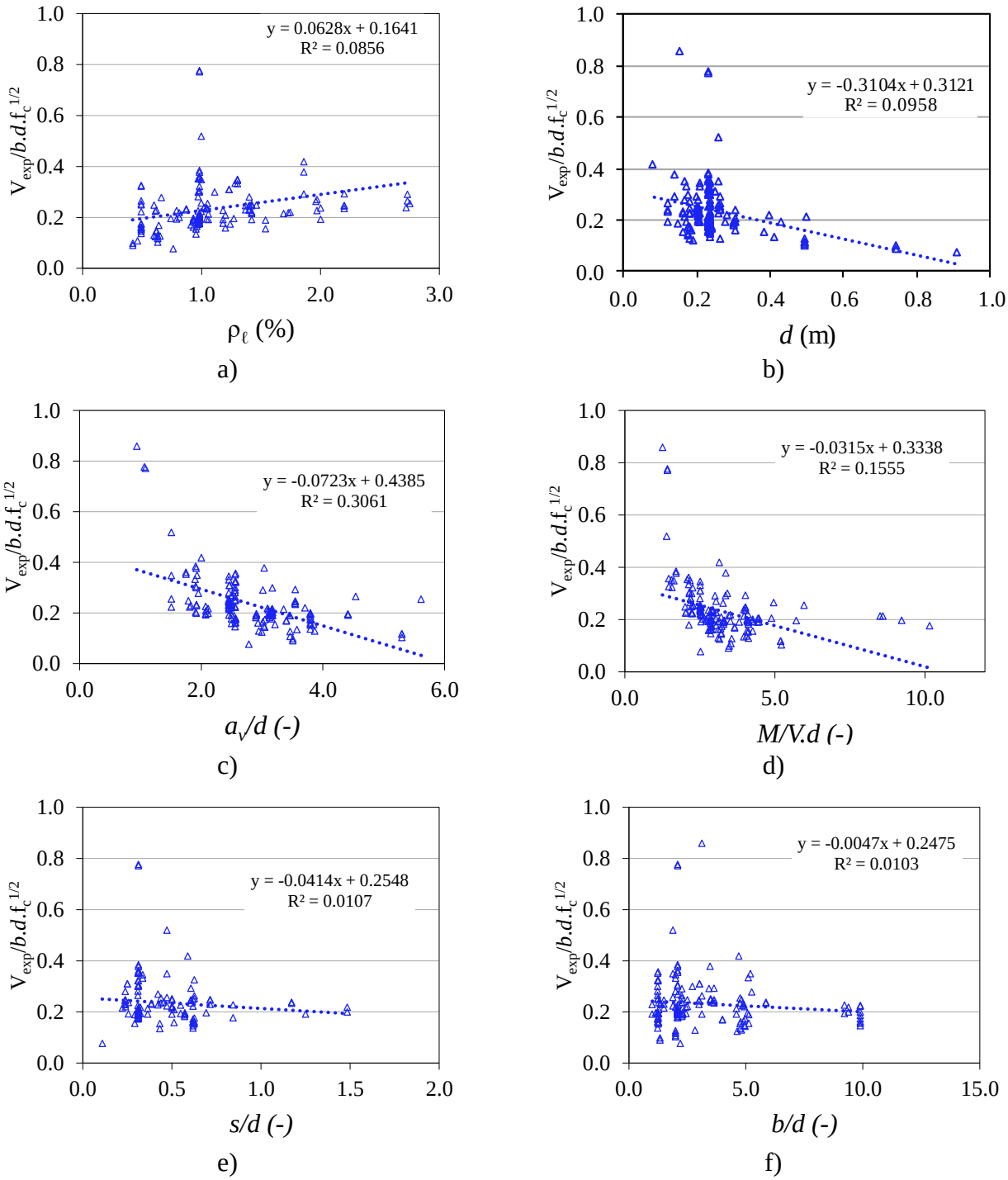

Source: Author.

Table 3-7 - Shear behavior of wide RC members according to the parameters studies showed in Figure 3-10.

Par.	Observation
ρ_ℓ	Some models consider the positive effect of longitudinal reinforcement by controlling the shear crack opening (FÉDÉRATION INTERNATIONALE DU BÉTON (FIB), 2012; FERNÁNDEZ RUIZ et al., 2015; SIA, 2013). On the other hand, others also take into account the higher dowel action due to higher longitudinal reinforcement ratios (YANG; DEN UIJL; WALRAVEN, 2016). Figure 3-10a shows an increase in the shear strength of wide members for higher reinforcement ratios, which confirms the importance of this parameter.
d	Figure 3-10b shows the significant effect of the size effect (BAZANT; KIM, 1984; WALRAVEN; LEHWALTER, 1994), which reduces the normalized shear stress for higher member thickness. However, the small number of members with thicknesses $d > 0.5$ m hamper the development of well-accepted formulations.
a_v/d	Regarding concentrated loads at $a_v/d < 2.5$, the formation of compressive struts helps the shear force transfer directly towards to the support (LANTSOGHT; VAN DER VEEN; WALRAVEN, 2013; VOLLUM; FANG, 2015). Therefore, many design codes enable reductions in the shear design load or increase in the shear capacity (CEN, 2005; FÉDÉRATION INTERNATIONALE DU BÉTON (FIB), 2012). Figure 3-10c shows compressive struts play a key role in increasing the shear strength of wide members for concentrated loads close to the support.
M/Vd	The *M/Vd* ratio can be combined with longitudinal reinforcement ratio ρ_s for accounting the section strains in shear strength analyses (ZSUTTY, 1968); (ACI-ASCE COMMITTEE 326, 1962a, 1962b, 1962c). In models based on MCFT and CSCT, reinforcement strains ε_s are directly considered. Figure 3-10d shows an increase in *M/Vd* reduces the shear strength of wide members. Higher *M/Vd* values result in larger crack openings of the critical shear crack, which reduces the contribution of the aggregate interlock to the shear strength. However, the compression chord can benefit from larger compressive stresses in the uncracked compression zone in cantilever members under distributed loads (TUNG; TUE, 2016b). Therefore, not always will members under larger *M/Vd* ratios show lower shear capacities, as the main shear transfer mechanism may vary according to the structural system and load arrangement.
s/d	The rebar spacing-to-effective depth ratio *s/d* is commonly discussed in design codes with upper limits for guaranteeing the monolithic behavior of RC members. Figure 3-10e shows the limited influence of *s/d* ratio over the shear strength, which is similar to the results of Gurutzeaga et al. (GURUTZEAGA et al., 2015) and Conforti, Minelli and Plizzari (2017). The results indicate in such a range of *s/d* ratios, the behavior of wide members can be governed by a plane stress state, mainly if *s/d* ratio is smaller than 1. Only some tests reported by Gurutzeaga et al. (2015) revealed cracked surfaces with a more irregular profile (undulations along the member width) for members with *s/d* ratio close to 1.5 (I/S/316/t.r and I/S/316/0 tests). Gurutzeaga et al. (2015) attribute possible tridimensional shear carrying mechanisms, formed by inclined struts that extend from the uncracked compression zone to the reinforcement, to higher *s/d* ratios. Such inclined struts result in a three-dimensional state of stress that justifies a more irregular profile of the shear crack along the width direction. Furthermore, due to the larger surface of contact created by the undulations in the shear crack, the aggregate interlock may be improved.
b/d	Models of shear strength used for RC wide members without shear reinforcement are usually based on beam tests. Figure 3-10f shows the *b/d* ratio of the tests in the investigated range presented a lower influence than other parameters, which contradicts some results from Conforti, Minelli and Plizzari (2017). These authors found higher shear capacities for members with a *b/d* ratio between 2 and 3. In tests with $b/d > 2$, Conforti, Minelli and Plizzari (2017) and Adam, Herbrand and Classen (2018) observed the cracked faces can be more irregular, with some undulations and bumps along the member width. Such larger cracked surfaces con offer some benefits in aggregate interlock that explain the higher shear capacities measured by Conforti, Minelli and Plizzari (2017) for simply supported members. On the other hand, when a critical shear crack arises closer to the inner support of continuous members, the aggregate interlock assumes minor importance and no significant improvement in their shear strength is expected.

Source: Author.

Figure 3-10 shows the influence of the parameters evaluated on normalized shear strength. The inclination of the trendlines indicates a higher or lower influence of the parameter evaluated on the normalized shear strength. Table 3-7 shows the main observations displayed in Figure 3-10 regarding the influence of parameters related to material, geometry, reinforcement, and load layout in the shear strength.

3.4.2 Shear slenderness

Some studies have indicated a good correlation between the shear slenderness and the shear strength of beams and wide members subjected to concentrated loads (CL) (ADAM; HERBRAND; CLASSEN, 2018; YANG; WALRAVEN; DEN UIJL, 2017). It is performed an evaluation of the shear slenderness definition, which includes continuous members under uniformly distributed loads (DL). The shear slenderness definition used by Adam et al. (2019), which considers only the location of the point of inflection, was compared with the one shown in Table 3-1, which accounts for moments M_{sup} and M_{span}. The normalized shear strength of the database (170 tests), including more 19 tests almost loaded in the full width from Lantsoght (2013) and Reiβen (2016), was evaluated and only tests with an exclusive variation of the analyzed parameter remained. In the end, 80 test results were considered in the analyses after filtering in Figure 3-11. This dataset includes 32 tests from Lantsoght (2013), 3 tests from Reiβen (2016), 17 tests from Adam, Reiβen and Hegger (2018), 20 tests from Adam, Herbrand and Classen (2018) and 8 tests from Adam et al. (2019).

Figure 3-11a shows that the normalized shear strength follows a tendency by increasing the ratio $max(a_1;a_2)/d$ for wide members under concentrated loads (CL). However, the behavior under uniformly distributed loads (DL) does not show the same clear tendency. In Figure 3-11a, the shear strength of members under DL increases in the initial range of $max(a_1;a_2)/d$, however, it decreases in the last range.

Some of the data points DL were related to continuous members with $M_{sup} < M_{span}$, for which this study proposes calculating the shear slenderness assuming they are simply supported ones of reduced span length (Figure 3-5 and Table 3-1). This study observes a better correlation of the shear strength with $max\{a_1;a_2\}/d$ ratio (Figure 3-11b), and similar behavior in comparison to members under CL. This result agrees with most studies on beams, in which a higher $max\{a_1;a_2\}/d$ leads to wider flexural cracks under the same loads, hence, a lower shear resistance (YANG; WALRAVEN; DEN UIJL, 2017). This relation is more evident and was validated by experimental measurements for structural members and load arrangements whose

aggregate interlock is the main shear-carrying mechanism in the cracked section (CAMPANA et al., 2013).

Figure 3-11 – Relation between experimental shear capacities and different definitions of shear slenderness λ: a) shear slenderness based on the ratio *max{a₁;a₂}/d* regardless of the bending moments M_{sup} and M_{span}; b) definition of *max{a₁;a₂}/d* modified for continuous members under uniformly distributed loads according to M_{sup} and M_{span}. Note: CL = concentrated loads, and DL = distributed loads.

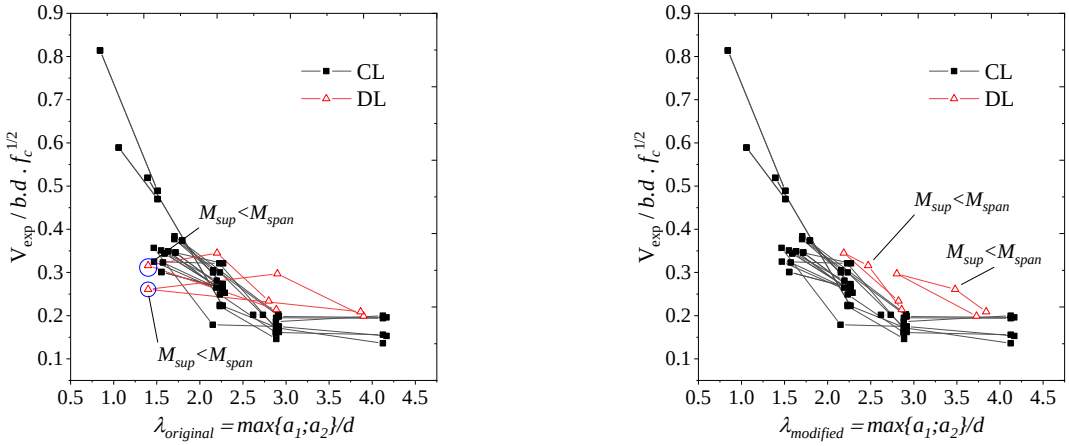

a) b)

Source: Author.

Figure 3-12 – Effect of the degree of rotational restraint d_r on the normalized shear strength of wide members according to the load arrangement. (CL) members subjected to concentrated loads and (DL) members subjected to uniformly distributed loads.

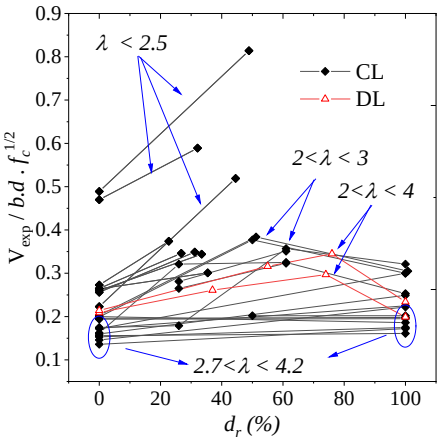

Source: Author.

Another aspect usually neglected in experimental analyses of beams and wide members (GURUTZEAGA et al., 2015; LANTSOGHT et al., 2015c) is the effect of the degree of rotational restraint d_r of continuous members in the internal support. Reiβen (2016) reported

some results limited to members under concentrated loads (CL). Figure 3-12 shows the behavior of continuous members according to the degree of rotational restraint is more heterogeneous in comparison with the shear slenderness (Figure 3-11b). However, this study identified some tendencies in the relation between shear capacity and d_r according to the shear slenderness parameter, shown in Table 3-8. In Figure 3-12, the same dataset of Figure 3-11 was used.

Table 3-8 - Behavior of RC members according to the degree of rotational restraint at the support and the load arrangement: (CL) members subjected to concentrated loads and (DL) members subjected to uniformly distributed loads.

Load arrangement	λ [-]	d_r (%)	Behavior
CL	*<2.5*	0 – 50%	The normalized shear strength of wide members increases between 25% and 69% when d_r increases from 0% (simply-supported members) to almost 50% for tests under concentrated loads (CL), thus indicating greater benefits from direct compressive struts.
DL	*<4*	0 – 75%	In members under distributed loads (DL), the shear capacities increase from 39% to 62% when d_r increases from 0 to 75%. For d_r < 75%, the continuous specimens show higher bending moments in the span ($M_{sup} < M_{span}$) and the critical shear crack develops far from the internal support, thus resulting in better activation of aggregate interlock (CAVAGNIS; FERNÁNDEZ RUIZ; MUTTONI, 2018a) and higher shear capacities. In such cases, the continuous member's behavior is similar to that of simply supported members with a reduced shear span (TUNG; TUE, 2016b).
CL	*2-3*	50 – 100%	An increase in d_r from 50% to 100% reduces approximately 23% of the normalized shear strength of continuous members under concentrated loads (CL). Since at the initial range, an increase in the d_r reduces the shear slenderness up to a limit. Beyond this limit, an increase in d_r increases the shear slenderness. However, the shear strength of fully clamped members (d_r =100%) is, in general, higher than that of simply-supported members (d_r =0), which may indicate benefits in the shear strength provided by different structural systems and load arrangements.
DL	*2-4*	75 – 100%	For members under DL, the shear capacities are reduced by approximately 46% when d_r increases from 75% to 100%, since at d_r closer to 100% the critical shear crack develops closer to the internal support, thus reducing the contribution from the aggregate interlock (CAVAGNIS; FERNÁNDEZ RUIZ; MUTTONI, 2018a). For d_r closer to 100%, the critical shear cracks closer to the internal support limits the formation of direct compressive struts (YANG; WALRAVEN; DEN UIJL, 2017). For such cases, a behavior similar to that of cantilever members loaded at the point of inflection is assumed (TUNG; TUE, 2016b).
CL	*> 2.7*	0-100%	For members under CL and more susceptible to flexural shear failures, λ> 2.7, no significant differences in the shear strength are observed when d_r increases from 0 to 100%, which agrees with the results presented in Figure 3-11 and others studies (REIßEN, 2016).

Source: Author.

3.4.3 Comparison to semi-empirical and mechanical model predictions

The experimental shear strength of 170 tests was compared with the one provided by the following semi-empirical and mechanical models: (i) ABNT NBR 6118:2014 ([36], (ii) NEN 1992-1-1:2005 (CEN, 2005), (iii) ACI 318:2014 (ACI COMMITTEE 318, 2014), (iv) ACI 318:2019 (ACI COMMITTEE 318, 2019), (v) *fib* Model Code 2010 [11], (vi) SIA 262:2013 (SIA, 2013), (vii) Shear Flexural Strength Mechanical Model (SFSSM) (MARÍ et al., 2015), (viii) Compression Chord Capacity Model (CCCM) (CLADERA et al., 2016), (ix) the Critical Shear Displacement Theory CSDT (YANG; DEN UIJL; WALRAVEN, 2016) and (x) Critical Width of the Shear Band Theory (CWSB) (TUNG; TUE, 2016a). The next sections address evaluations of the ratio between experimental and theoretical shear strengths according to the structural system, *b/d* ratio and shear slenderness.

For small values of a_v/d, an arching action leads to larger shear capacities, consequently, models that do not take this aspect into account tend to produce more conservative results for members whose concentrated loads are close to the support. However, in most studies, such conservatism is not quantified for wide RC members. Some mechanical-based models, such as SIA 262 (SIA, 2013) and *fib* Model Code 2010 ((FÉDÉRATION INTERNATIONALE DU BÉTON (FIB), 2012) provide guidance on how to consider the effects of direct compression struts carrying the shear force to the supports. Other models, (e.g., SFSMM (MARÍ et al., 2015), CCCM (CLADERA et al., 2016), CSDT (YANG; DEN UIJL; WALRAVEN, 2016) and CWSB (TUNG; TUE, 2016a), do not include such guidance. In such cases, the factor β_{EC} from NEN 1991-1-1:2005 (CEN, 2005) is considered for reducing V_{exp} for evaluations of the fit of the mechanical models. Items 3.4.5 and 3.4.6, show only the results from mechanical-based models, since they provided better accuracy and precision in the shear strength predictions.

3.4.4 Accuracy according to the structural system

The effect of the structural system on the shear behavior is usually neglected. Towards investigating it, this study compared experimental and predicted shear capacities according to the different structural systems of the tests by different models. Statistical trends can influence the results, since the number of tests in the databases for simply supported specimens (67%) is significantly higher than those for continuous members (23%) and cantilever ones (10%). Therefore, the results of this section should be considered as indicative and more tests are necessary for reliable conclusions.

The ratio between experimental and calculated shear strengths V_{exp}/V_{cal} by semi-empirical models showed a coefficient of variation (COV) higher than 25% for all models

(Table 3-9). The structural system provided the lowest average ratio V_{exp}/V_{cal} for cantilever members (CT) by the semi-empirical approaches. Table 3-9 also shows that semi-empirical approaches sub estimated the shear capacity of the tests between 28% and 102% for continuous members. Physically, most of such results can be explained by the absence of parameters that consider the shear slenderness effect (arching action for small λ), proven by the smallest difference in results between simply supported and continuous members in the detailed model of ACI 318:2014, which considers the ratio M/Vd in the expressions. However, the V_{exp}/V_{cal} ratio is in ACI 318:2014 approximately 25% higher for simply supported members than for cantilever ones.

Table 3-9 - Statistical evaluation of the V_{exp}/V_{cal} ratio with semi-empirical models according to the structural system. AVG = average value; MIN = minimum value; COV = coefficient of variation.

Structural System		Nº		$\frac{V_{\exp,red}}{V_{ABNT}}$	$\frac{V_{\exp,red}}{V_{EC}}$	$\frac{V_{\exp}}{V_{ACI,14,\det}}$	$\frac{V_{\exp}}{V_{ACI,19(C)}}$
CT		17	AVG	0.968	0.970	1.015	1.350
			MIN	0.654	0.828	0.770	1.059
			COV	20.3%	14.0%	14.1%	11.7%
CS		39	AVG	1.289	1.469	1.333	2.024
			MIN	0.887	0.972	0.717	1.262
			COV	25.3%	26.3%	25.0%	30.1%
SS		114	AVG	1.049	1.130	1.253	1.587
			MIN	0.558	0.673	0.464	0.891
			COV	29.6%	22.8%	40.1%	42.6%
All	-	170	AVG	1.096	1.192	1.248	1.664
			MIN	0.558	0.673	0.464	0.891
			COV	29.4%	27.2%	36.1%	39.6%

Source: Author.

Most mechanical models of shear strength consider the structural system indirectly by parameters related to the sectional forces M and V, which are correlated to the shear slenderness. Nevertheless, the V_{exp}/V_{cal} ratio for continuous members was higher than that for simply supported members by all mechanical models (Table 3-10). This difference is limited (10%) with SIA 262 and the CSDT formulations. Table 3-10 shows the V_{exp}/V_{cal} ratio for cantilever members is lower than for simply supported ones by all models, except for CSDT, whose difference can be neglected. Such results suggest if the structural system is considered only by the sectional forces M and V, possible changes in the main shear-carrying mechanisms may be neglected due to alterations in the shear failure mode and cracking pattern according to the moments M_{sup} and M_{span}.

Table 3-10 - Statistical evaluation of the V_{exp}/V_{cal} ratio with mechanical models according to the structural system. AVG = average value; MIN = minimum value; COV = coefficient of variation.

Structural System		N°		$\frac{V_{exp,red}}{V_{MC}}$	$\frac{V_{exp,red}}{V_{SIA}}$	$\frac{V_{exp,red}}{V_{SFSMM}}$	$\frac{V_{exp,red}}{V_{CCCM}}$	$\frac{V_{exp,red}}{V_{CSDT}}$	$\frac{V_{exp,red}}{V_{CWSB}}$
CT		17	AVG	1.169	1.069	0.927	1.142	1.227	1.001
			MIN	0.959	0.821	0.726	0.846	0.894	0.824
			COV	15.0%	13.8%	14.3%	13.6%	13.8%	11.2%
CS		39	AVG	1.404	1.225	1.326	1.455	1.235	1.063
			MIN	0.885	0.876	0.906	1.000	0.884	0.765
			COV	20.3%	17.6%	24.9%	22.1%	18.9%	20.2%
SS	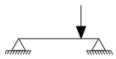	114	AVG	1.213	1.103	1.060	1.202	1.102	1.170
			MIN	0.791	0.737	0.697	0.776	0.827	0.761
			COV	17.5%	18.4%	20.3%	19.5%	13.6%	26.3%
All	-	170	AVG	1.252	1.127	1.108	1.254	1.145	1.129
			MIN	0.791	0.737	0.697	0.776	0.827	0.761
			COV	19.3%	18.4%	24.4%	21.8%	16.0%	24.8%

Source: Author.

In most validations of mechanical-based models with beam tests, a comparison between the proposed models with semi-empirical approaches highlighted better accuracy and precision with mechanical based models (MARÍ et al., 2015; TUNG; TUE, 2016a; YANG; DEN UIJL; WALRAVEN, 2016). In a joint assessment of average value and coefficient of variation of all models, SIA 262:2013 (SIA, 2013) and CSDT models (YANG; DEN UIJL; WALRAVEN, 2016; YANG; WALRAVEN; DEN UIJL, 2017) stand out with the average ratio V_{exp}/V_{calc} ranging between 1.13 and 1.15 and COVs lower than 20%. Equations based on the SFSMM (MARÍ et al., 2015), CCCM (CLADERA et al., 2016) and CWSB (TUNG; TUE, 2016a), provided larger scatter between experimental and predicted capacities (COV > 20%). These results are caused by including members in the database that may have failed by shear compression modes, for which these models were not derived. The same models (CCCM, SFSMM and CWSB) showed an average ratio V_{exp}/V_{cal} between 0.99 and 1.16 with maximum COV of 15.8% for wide RC members that showed flexural shear failure modes, identified as those of $M/Vd > 3$ (76 test results in the databases).

3.4.5 Accuracy according to the *b*/*d* ratio

The experimental shear capacities were compared with predicted ones according to different ranges of *b/d* ratios for investigating whether the available shear models show the same level of accuracy regardless of the ratio *b/d*. According to Table 3-11, the mechanical models show no significant differences in the mean value and COV for V_{exp}/V_{cal} in the different *b/d* ratio ranges. Although the coefficient of variation showed higher values in the range

$1<b/d<2.5$, this result may have been influenced by the higher number of experiments in this range (63% of the tests). Such results agree with the experimental analysis conducted by Adam, Herbrand and Classen (2018), who observed slabs with $b/d > 5$ and beams with $b/d = 1$ exhibited similar shear capacities under identical test conditions. The results are also coherent with the observation that the influence of b/d on the normalized shear strength is limited (Figure 3-10f). On the other hand, they do not validate the observations of Conforti, Minelli and Plizzari (2017), who found higher shear strengths for increasing b/d ratios between 1 and 3. Therefore, the effect of the b/d ratio on the shear strength is still unclear and closely related to the randomness in the cracking pattern of the model, concrete mixture's homogeneity and loading conditions.

Table 3-11 - Statistical evaluation of the V_{exp}/V_{cal} ratio with mechanical models according to the b/d ratio. AVG = average value; MIN = minimum value; COV = coefficient of variation.

b/d	N°		$\frac{V_{\exp,red}}{V_{MC}}$	$\frac{V_{\exp,red}}{V_{SIA}}$	$\frac{V_{\exp,red}}{V_{Sfsmm}}$	$\frac{V_{\exp,red}}{V_{CCCM}}$	$\frac{V_{\exp,red}}{V_{CSDT}}$	$\frac{V_{\exp,red}}{V_{CWSB}}$
$1 \le b/d \le 2.5$	108	AVG	1.259	1.139	1.150	1.295	1.184	1.090
		MIN	0.791	0.794	0.802	0.776	0.827	0.765
		COV	21.2%	18.2%	25.8%	22.3%	15.5%	21.5%
$2.5 \le b/d < 5$	42	AVG	1.239	1.120	1.030	1.178	1.058	1.239
		MIN	0.911	0.737	0.697	0.810	0.835	0.824
		COV	14.9%	20.0%	19.5%	20.6%	15.2%	27.6%
$b/d \ge 5$	20	AVG	1.243	1.079	1.043	1.193	1.116	1.107
		MIN	0.993	0.891	0.760	0.874	0.924	0.761
		COV	16.3%	15.5%	18.2%	16.4%	14.3%	28.7%
All	170	AVG	1.252	1.127	1.108	1.254	1.145	1.129
		MIN	0.791	0.737	0.697	0.776	0.827	0.761
		COV	19.3%	18.4%	24.4%	21.8%	16.0%	24.8%

Source: Author.

3.4.6 Accuracy according to the shear slenderness λ

Most mechanical models have been formulated to deal with flexural shear failures. Table 3-12 shows the similarity among the results provided by mechanical models for tests with flexural shear failure ($\lambda > 3$). The average ratio between experimental and predicted shear capacities ranged from 0.99 to 1.16, whereas the coefficient of variation remained below 20%. For members with possible shear compression failure, the coefficient of variation for $V_{exp,red}/V_{cal}$ ratio is higher than 20% for models based on the CCCM and in the CWSB. However, such models provide more conservative results for most of these tests since the average $V_{exp,red}/V_{cal}$ ratio is higher than 1.24 for them.

Table 3-12 - Statistical evaluation of the V_{exp}/V_{cal} ratio with mechanical models according to the shear slenderness λ. AVG = average value; MIN = minimum value; COV = coefficient of variation.

Range	N°		$\frac{V_{\exp,red}}{V_{MC}}$	$\frac{V_{\exp,red}}{V_{SIA}}$	$\frac{V_{\exp,red}}{V_{Sfsmm}}$	$\frac{V_{\exp,red}}{V_{CCCM}}$	$\frac{V_{\exp,red}}{V_{CSDT}}$	$\frac{V_{\exp,red}}{V_{CWSB}}$
$\lambda < 3$	94	AVG	1.323	1.170	1.205	1.330	1.162	1.201
		MIN	0.791	0.794	0.802	0.776	0.827	0.761
		COV	20.0%	19.2%	25.4%	23.3%	17.5%	27.8%
$\lambda \geq 3$	76	AVG	1.165	1.074	0.988	1.161	1.124	1.039
		MIN	0.882	0.737	0.70	0.810	0.835	0.771
		COV	12.8%	15.0%	14.9%	15.8%	13.8%	15.1%
All	170	AVG	1.252	1.127	1.108	1.254	1.145	1.129
		MIN	0.791	0.737	0.697	0.776	0.827	0.761
		COV	19.3%	18.4%	24.4%	21.8%	16.0%	24.8%

Source: Author.

3.5 Discussions of Chapter 3

Most semi-empirical approaches used in codes of practice do not consider the shear slenderness influence and are calibrated according to simply supported beams tests. Consequently, these formulations could provide very conservative capacities for small shear slenderness and unsafe predictions for higher member thicknesses. This is the case, for instance, of ACI 381-14 code expressions, which were updated in ACI 318-19. In the case of the ABNT NBR 6118:2014, however, the Brazilian guidelines explain that the national code expressions should be used only on members with a thickness lower than 0.6 m. Besides that, the expressions for wide members are also recommended only to members with $b/d \geq 5$ because it is supposed the shear redistribution capacity of wider members is significantly larger than beams. In other words, it is supposed that due to the lower width of beams compared to their depth, the failure can be triggered in localized regions of the beam, while in slabs a shear redistribution could occur and avoid a brittle collapse.

The mechanical models studied, on the other hand, usually assume shear transfer mechanisms are functions of parameters such as (i) tensile strains in the critical section, (ii) shear displacement, and (iii) compression chord capacity. These considerations demonstrate to be valid since the scatter of V_{exp}/V_{pred} for mechanical models is lower than for semi-empirical ones. Such results indicate that the dowel effect does not have a negligible contribution to the shear strength of some members, as observed by Cavagnis, Fernández Ruiz and Muttoni (2018b). Moreover, CSCT and CSDT seem to cover many cases of structural system, load arrangement and shear slenderness at a satisfactory level of accuracy.

A closer look at the database shows most of the tests available were performed on simply supported members of small thicknesses under concentrated loads. The investigation of the size effect, structural system and load arrangement influence on the shear strength require more tests. Due to the size effect, test full-scale wide members is important. Since these members are complex and costly, 3D non-linear numerical simulations can be useful (BELLETTI et al., 2014; GENIKOMSOU; POLAK, 2015). The small number of tests on wide members under distributed loads hampers the drawing of conclusions on the influence of parameters like the degree of rotational restraint. More tests and a combination of experimental results with numerical simulations are required for more comprehensive analyses. A limited number of tests on wide members of concrete compressive strengths higher than 65 MPa is available and the results have significantly varied, which requires more tests. Such tests will enable evaluations of the accuracy and precision levels of formulations that take into account the lower roughness for crack surfaces when the critical shear crack goes through the aggregate particles.

Since the behavior of wide members with $b/d > 1$ is very similar to that of beams, models calibrated for beams can be extrapolated to slabs and wide beams. Regarding possible benefits of the shear strength of wide beams with b/d between 1 and 3, it is conservative for design to neglect this aspect.

In countries such as Brazil, where the construction of residential slabs supported by beams instead of columns is more usual, the thickness of such slabs usually does not exceed 150 mm, and the dowel effect can be influenced by the absence of minimum shear reinforcement and small thicknesses. Therefore, this study recommends testing members with small thicknesses to investigate if models derived from beam tests that account for the dowel action (CSDT) present the same level of accuracy for such wide members.

The shear slenderness based on the $max(a_1;a_2)/d$ ratio shows a clear correlation with the shear strength of wide members under concentrated loads. This study identified a similar correlation for members under uniformly distributed loads by modifying the span length of continuous members according to the relation between the moment over the support (M_{sup}) and the maximum moment in the span (M_{span}).

Aspects such as direct load transfer by compressive struts, improvement in the compression chord by continuity at the supports, and load arrangement effect are usually neglected in design. However, they can be important for the assessment of existing structures,

since they can attribute additional strength to the structure, such a way that repair or replacement of these structures may be avoided.

3.6 Conclusions of Chapter 3

This chapter brings together 170 test results of wide RC members without shear reinforcement and analyzes some of the main semi-empirical and mechanical models available in design codes. It also addresses a discussion on the effect of parameters such as structural system and shear slenderness and a comparison between experimental and predicted shear capacities according to different models. The following conclusions can be drawn:

- An increase in the ratio $max(a_1;a_2)/d$ results in a clear exponential decay of the shear strength to members under concentrated loads (CL) in the shear span. For members under uniformly distributed loads (DL), the shear strength also decreased by considering that continuous members under distributed loads with $M_{sup}<M_{span}$ behave similarly to simply supported ones.
- The shear strength establishes a better correlation with the shear slenderness than with the degree of rotational restraint d_r. While the shear strength mostly reduces with increasing the shear slenderness, the relation between the shear strength and the degree of rotational restraint is more complex.
- Most models provide fewer conservative results for cantilevers members than simple supported ones. Although this result might indicate some influence of the structural system, the database shows a higher number of tests with simply-supported members, which may add some bias to the results. Furthermore, most results are related to members of reduced thickness (<0.5 m), for which the self-weight load is reduced; therefore, differences according to the structural system should be limited.
- Critical Shear Crack Theory and Critical Shear Displacement Theory provide the best predictions of shear strength for wide members under different structural systems, load arrangements and shear slenderness. According the provided analyses, these models show a small COV (<20%) and an average ratio V_{exp}/V_{pred} between 1.13 and 1.15.
- Despite some differences in the cracking pattern between beams and wide members, the same approaches used to assess the shear strength of beams can be extended to wide members in the investigated range of parameters.
- The load arrangement and support conditions play an important role in the shear behavior of wide members since they can change the key parameters of the shear carrying mechanisms: (i) shape, (ii) location and (iii) kinematics of the critical shear crack.

4 EXTENDED CSDT MODEL FOR SHEAR CAPACITY ASSESSMENTS OF BRIDGE DECK SLABS

In this chapter, the study increased the scope of the problem addressed. After a better understanding of the one-way shear behavior of wide members loaded over the entire width, this chapter investigates the problem of one-way slabs under concentrated loads more closely. In this context, this chapter investigates different approaches to define the effective shear width contributing to the sectional shear capacity of the slabs. Despite this chapter focusing on the evaluation of the one-way shear capacity, the different governing failure mechanisms are also discussed for such slabs (shear and punching). In accordance, the proposed effective shear width expressions in this chapter account that the evaluated slabs can be critical in punching instead of one-way shear.

4.1 Introduction of Chapter 4

The shear capacity of bridge deck slabs attracted attention from several researchers and bridge owners in Europe in the last decade since a large number of these structures built between 1960 and 1980 have reached the end of their originally devised service life (HENZE; HARTER; ROMBACH, 2019; LANTSOGHT; VAN DER VEEN; WALRAVEN, 2013; NATÁRIO; FERNÁNDEZ RUIZ; MUTTONI, 2014; REIßEN; CLASSEN; HEGGER, 2018). A number of these bridges do not rate sufficiently for shear according to the currently governing codes, despite no signal of distress. This result indicated that widely accepted semi-empirical approaches of design could be overly conservative. Since conservative predictions of shear strength could indicate the need for replacement or retrofit of these structures, identifying more accurate approaches for predicting the shear capacity of bridge deck slabs involves an economic and environmental issue beyond the user's safety. Apart from that, the design of wide reinforced concrete members prioritizes solutions without shear reinforcement, since installing shear reinforcement is not cost-effective and may result in reinforcement congestion. Therefore, also in design, the use of precise one-way shear models can be essential to ensure adequate safety levels for members without stirrups.

In a previous study on wide beams and one-way slabs loaded over the entire width (SOUSA; LANTSOGHT; EL DEBS, 2020) (Figure 4-1a), it was identified that the Critical Shear Displacement Theory model (CSDT (YANG; DEN UIJL; WALRAVEN, 2016; YANG; WALRAVEN; DEN UIJL, 2017)) showed the best levels of accuracy and precision compared to many semi-empirical and mechanical models of shear strength, with the mean ratio between experimental and predicted shear capacities of 1.15 and COV of 16%. Different from previous publications (CONFORTI; MINELLI; PLIZZARI, 2017; GURUTZEAGA et al., 2015), Sousa, Lantsoght and El Debs (2020) applied the analyses for both slender and non-slender members, in addition to different support and loading

conditions. Therefore, it was decided to further assess the CSDT model for slabs under concentrated loads in non-symmetrical conditions (Figure 4-1b), with emphasis on the one-way shear capacity.

Figure 4-1 - Slabs loaded (a) over the entire width analyses by Sousa, Lantsoght and El Debs (2020) and b) under concentrated loads in non-symmetrical conditions subjected to one-way shear failures.

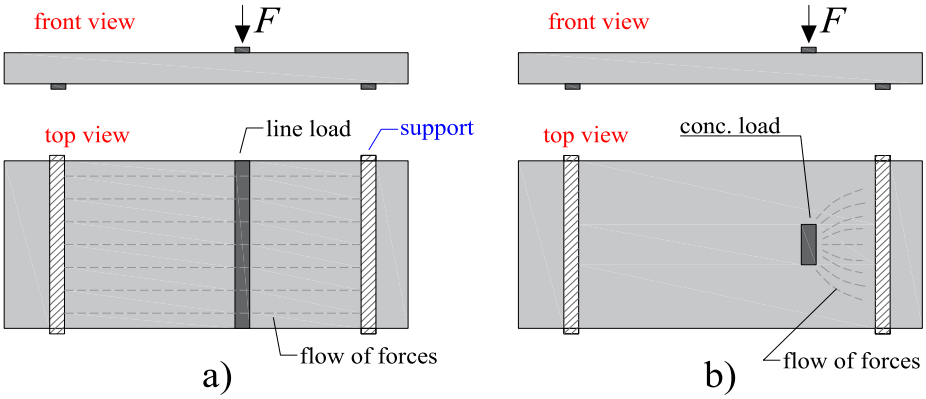

Source: Author.

Although the number of studies on shear in reinforced concrete members increased significantly in the last decade, most of them were focused on the level of precision by semi-empirical code models of shear strength (HENZE; ROMBACH; HARTER, 2020; LANTSOGHT et al., 2015d; REIßEN; HEGGER, 2013a, 2013b). In publications that include mechanical-based models (BUI et al., 2017a; HALVONIK; VIDAKOVIĆ; VIDA, 2020; LANTSOGHT et al., 2015e; NATÁRIO; FERNÁNDEZ RUIZ; MUTTONI, 2014), the analyses focused on one kind of support condition and hence, covered a reduced number of tests. At the same time, only a limited number of studies addressed the fact the slabs under concentrated loads may show a transitional failure mode between one-way and two-way shear (LANTSOGHT et al., 2015c). As a consequence, if the governing failure mode is unknown, the use of a one-way shear model to assess members whose governing failure mode is punching shear may lead to unsafe predictions of shear strength. Therefore, the need for a more comprehensive study was identified, covering slabs under different support conditions, assessed by a mechanical-based model such as the CSDT and accounting for different failure modes that may take place.

In this study, the application of the Critical Shear Displacement Theory Model (CSDT) (YANG; DEN UIJL; WALRAVEN, 2016; YANG; WALRAVEN; DEN UIJL, 2017) is extended to the assessment of the one-way shear capacity of wide reinforced concrete members under concentrated loads in non-symmetrical conditions (Figure 4-1b). Compared to previous studies (HALVONIK; VIDAKOVIĆ; VIDA, 2020; LANTSOGHT; VAN DER VEEN; WALRAVEN, 2013; NATÁRIO; FERNÁNDEZ RUIZ; MUTTONI, 2014; VAZ RODRIGUES; FERNÁNDEZ

RUIZ; MUTTONI, 2008), this chapter covers a wider variety of support conditions (cantilevers, simply supported and continuous members); members under different loading conditions such as single loads and double loads close to the support; and it provides recommendations when the governing failure mode is known or unknown.

The literature is reviewed in order to discuss the influence of the shear slenderness over the governing failure mode of slabs. Furthermore, models for accounting for the slab behavior under concentrated loads (LANTSOGHT et al., 2015c) and approaches for account improved shear capacities for loads close to the support are described and assessed in this chapter. Different databases are used to derive and validate each recommendation proposed. These recommendations differ if the governing failure mechanism of the slabs is known or unknown and, they consider the higher shear strength for slabs under concentrated loads close to the support (LANTSOGHT; VAN DER VEEN; WALRAVEN, 2013; NATÁRIO; FERNÁNDEZ RUIZ; MUTTONI, 2014). The application limits and benefits of each recommendation are highlighted in the chapter, which also compares the results with well-established models from the literature.

4.2 Literature review

This section presents a specific literature review that focuses on the following aspects: (i) shear failure modes of one-way slabs under concentrated loads, (ii) available approaches to calculating the effective shear width, (iii) failure modes and shear transfer mechanisms in one-way shear and (iv) the fundamentals of the critical Shear Displacement Theory Model (CSDT).

4.2.1 Shear failure modes

One-way shear failure and two-way shear failure or punching shear can be critical in bridge deck slabs without shear reinforcement (LANTSOGHT et al., 2015c; NATÁRIO; FERNÁNDEZ RUIZ; MUTTONI, 2014). The critical failure mode can vary according to the gradient of shear forces close to concentrated loads (MUTTONI; FERNANDEZ RUIZ, 2010a). For slabs loaded over the entire width, the shear force per unit length is almost constant over the shear span if the self-weight is neglected. On the other hand, for flat slabs under concentric loads, the gradient of unitary shear forces (shear force per unit length of the critical perimeter) becomes higher near the loaded region, since the perimeter of the shear transfer is reduced (MUTTONI; FERNANDEZ RUIZ, 2010a). Some studies suggest the combination of shear field analyses with one-way and two-way shear models for the determination of the critical failure mode (NATÁRIO; FERNÁNDEZ RUIZ; MUTTONI, 2014; VAZ RODRIGUES; FERNÁNDEZ RUIZ; MUTTONI, 2008), whereas others already highlight that some tests can show the same capacity for one-way and two-way shear (NATÁRIO, 2015). This means that the ratio between the one-way shear effects (V_{exp}) from the acting punching load (P_{exp})

with the calculated one-way shear capacity (V_{calc}) is very similar to the ratio between the acting punching load (P_{exp}) with the calculated punching capacity (P_{calc}). Since the most critical failure mode may change according to the geometry of the load, slab, and support conditions (LANTSOGHT et al., 2015e), the check of both failure modes is essential for the assessment of existing structures, where a precise estimation of the shear capacity is required (NATÁRIO, 2015).

Figure 4-2 shows the complex transition between these two failure modes. For cantilever slabs under concentrated loads, for instance, regions of critical one-way and two-way shear can be better differentiated for large shear spans (Figure 4-2a), whereas for simply supported slabs, such regions intercept each other (Figure 4-2b). Different studies have agreed on the existence of a trend for the punching failure mode to become critical for higher shear slenderness (DOORGEEST, 2012; HENZE, 2019; LANTSOGHT et al., 2015c; NATÁRIO, 2015; REIßEN, 2016).

Attention should be drawn to the fact that both one-way shear expressions and punching shear expressions were derived and calibrated using lab tests designed with idealized boundary conditions. For instance, one-way shear expressions were derived based on simply supported beam tests with point loads (REGAN, 1987); and punching shear expressions were based on punching tests on idealized slab-column connections. One-way slabs typically have boundary conditions and failure modes between the two types of failure modes, therefore, none of these two types of expressions were developed for such structures.

Figure 4-2 - Critical regions of one-way and two-way shear for a) cantilever (adapted from Reiβen (2016)) and b) simply supported members; c) effective width definition for one-way shear analyses (adapted from Reiβen (2016)).

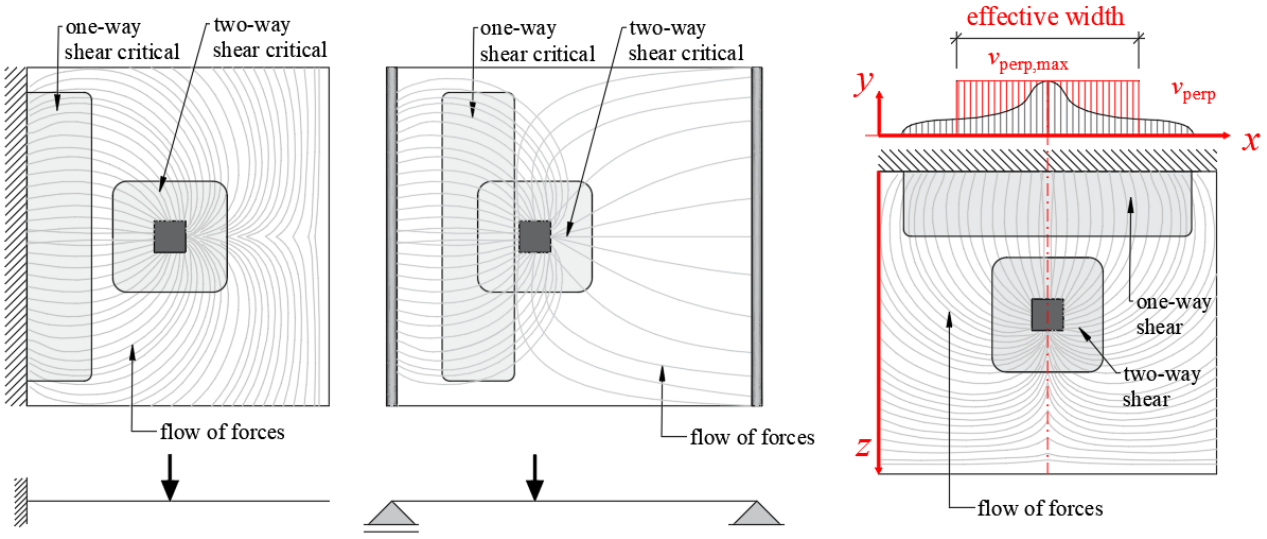

Source: a) adapted from Reiβen (2016), b) Author; c) Adapted from Reiβen (2016).

4.2.2 Effective shear width

When slabs are subjected to concentrated loads, an effective shear width needs to be defined together with a one-way shear model, since not the full slab width carries the same shear stress (LANTSOGHT et al., 2015b; NATÁRIO; FERNÁNDEZ RUIZ; MUTTONI, 2014). Figure 4-2c shows the profile of shear stresses over the support as well as the distribution of shear stresses around the load (HENZE, 2019; LANTSOGHT et al., 2015b; NATÁRIO; FERNÁNDEZ RUIZ; MUTTONI, 2014; REIßEN; CLASSEN; HEGGER, 2018). Integrating the shear stress v_{perp} over the width results in the sectional shear at failure. However, for design, deriving the shear stress distribution over the support is not practical, and therefore a uniform shear stress is commonly considered over a reduced width, which is the effective shear width (Figure 4-2c). The integral of the maximum shear stress $v_{perp,max}$ over the effective width should theoretically approach the integral of the shear stress v_{perp} over the full width. The values of $v_{perp,max}$ can be determined by linear elastic finite element (LEFE) analysis with shell elements adjusting the shear modulus G and the Poisson ratio v to account for cracking and load redistribution (HENZE; ROMBACH; HARTER, 2020; LANTSOGHT; DE BOER; VAN DER VEEN, 2017a; NATÁRIO; FERNÁNDEZ RUIZ; MUTTONI, 2014; SAGASETA et al., 2014; VAZ RODRIGUES; FERNÁNDEZ RUIZ; MUTTONI, 2008). However, the relevant section may vary according to the shear model (between d and $d/2$ away from discontinuities or at the support) and according to the support and loading conditions (NATÁRIO, 2015).

In practice, the effective width is usually defined based on a method of horizontal load spreading from the concentrated load to the support or a section parallel to the support (Figure 4-3). However, some publications already highlighted that the French method (as shown in Figure 4-3) could overestimate the effective width in more than 30% for tests with shear slenderness higher than 5 (REIBEN; HEGGER, 2016). Physically, this horizontal load spreading can be influenced by factors such as the reinforcement ratio in the transverse direction (LANTSOGHT; VAN DER VEEN; WALRAVEN, 2013; REIßEN; CLASSEN; HEGGER, 2018), available member width (LANTSOGHT et al., 2015a; REIßEN; CLASSEN; HEGGER, 2018), and size of the concentrated load (REIßEN, 2016).

Figure 4-3 – Models of effective shear width used in design guides with respective reference lines.

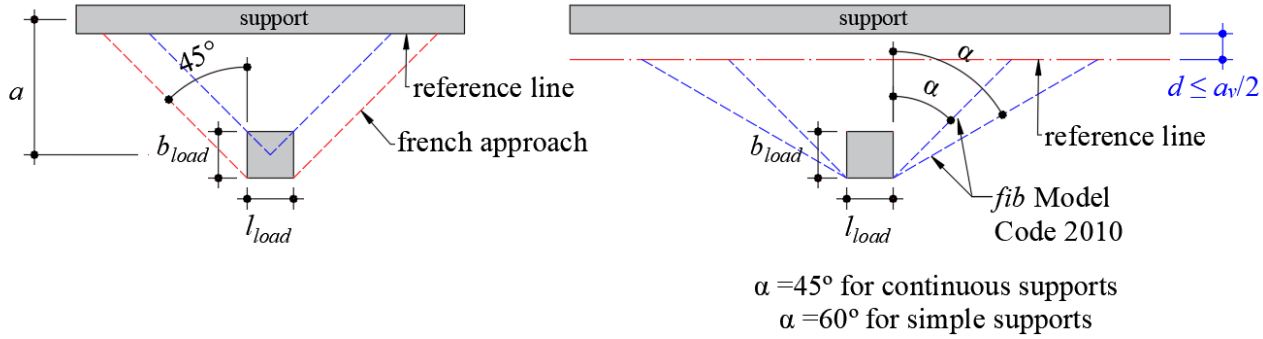

Source: Author.

Table 4-1 shows an overview of expressions for the effective width b_{eff} in the one-way shear strength of reinforced concrete members under concentrated loads at the slab mid-width. However, for loads close to the edge, the effective shear width $b_{eff,edge}$ is equal to $b_r + b_{eff}/2$, where b_r is the distance from the load axis to the free edge of one-way slabs (Figure 4-4).

Figure 4-4 - Sketch of the calculation of the effective shear width for loads close to the free edge (eccentrics in the slab width).

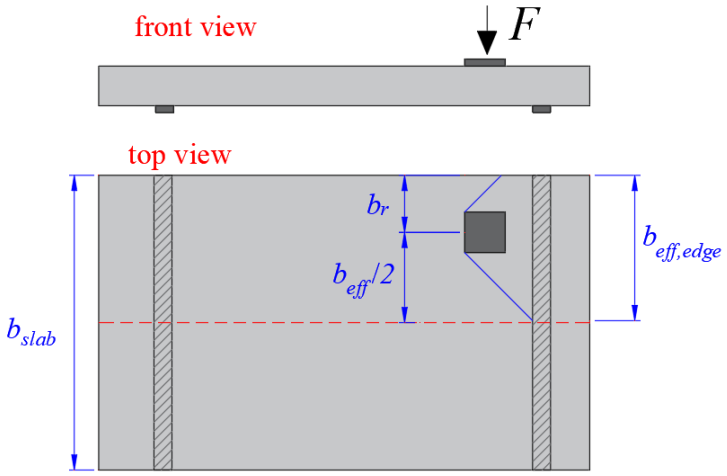

Source: Author.

Table 4-1 displays some replaced design code models, e.g. the Brazilian code from 1980 (ABNT NBR 6118, 1980), since the current codes do not provide recommendations related to the effective shear width. According to the table, most code provisions (ABNT NBR 6118, 1980; FD P 18-717, 2013; FÉDÉRATION INTERNATIONALE DU BÉTON (FIB), 2012; GRASSER; THIELEN, 1991; NORMCOMISSIE 351001, 1995) and some proposed in the literature (BAUER; MÜLLER, 2003; HENZE, 2019; VIDAKOVI; HALVONIK, 2019) assume the effective width increases for larger shear spans. This idea relies on the yield line theory (JOHANSEN, 1972) and experimental investigations (GOLDBECK, 1917), which account for shear forces spreading on

elastic plates under concentrated loads, also confirmed partially by LEFE analyses (NATÁRIO; FERNÁNDEZ RUIZ; MUTTONI, 2014). In summary, most analytical models of effective shear width do not take into account the change in the governing failure mode according to the position of the load (FD P 18-717, 2013; FÉDÉRATION INTERNATIONALE DU BÉTON (FIB), 2012) or were calibrated for specific supporting conditions (HALVONIK; VIDAKOVIĆ; VIDA, 2020). On the other hand, more detailed models of effective shear width that account for the slabs stiffness in both directions and the different support conditions usually require linear (LEFEA) or non-linear finite element analyses (NLFEA) (NATÁRIO; FERNÁNDEZ RUIZ; MUTTONI, 2014; SHU et al., 2019).

Table 4-1 - Overview of analytical models that predict the effective width in analyses of one-way shear strength of wide RC members under concentrated loads close to the support.

Old Dutch approach (NORMCOMISSIE 351001, 1995) (replaced)	$b_{eff\,1} = b_{load} + 2 \cdot a_v$ (4.1)
French (FD P 18-717, 2013)	$b_{eff\,2} = l_{load} + 2 \cdot \left(b_{load} + a_v \right)$ (4.2)
Brazilian code (ABNT NBR 6118, 1980) (replaced)	$b_0 = b_{load} + h$ (4.3) For cantilever members: $b_{NBR} = b_0 + 0.5 \cdot a \cdot \left(1 - \frac{b_0}{\ell} \right) \leq \max\left(b_{slab}; a + 0.5 \cdot b_{NBR} \right)$ (4.4) For other static systems: $b_{NBR} = b_0 + a \cdot \left(1 - \frac{b_0}{l} \right) \leq \max\left(b_{slab}; a + 0.5 \cdot b_{NBR} \right)$ (4.5)
German guideline (DAFSTB, 1991) (replaced)	$t = b_{load} + 2 \cdot h_1 + h$ (4.6) For cantilever members: $b_{H\,240} = \begin{cases} 0.2\ell_k + 0.3a & \text{for: } 0.2\ell_k < a < \ell_k;\ t_y < 0.2\ell_k;\ t_x < 0,2\ell_k \\ t_y + 0.3a & \text{for: } 0.2\ell_k < a < \ell_k;\ 0.2\ell_k < t_y < 0.4\ell_k;\ t_x < 0.2\ell_k \end{cases}$ (4.7) For simply supported members: $b_{H\,240} = t_y + 0.5a$ for: $0 < a < \ell,\ t_y \leq 0.8\ell,\ t_x \leq \ell$ (4.8) For loads close to simple support of continuous members: $b_{H\,240} = t_y + 0.4a$ for: $0.2\ell < a < \ell,\ t_y \leq 0.4 \cdot \ell,\ t_x \leq 0.2\ell$ (4.9) For loads close to continuous supports $b_{H\,240} = t_y + 0.3a$ for: $0.2\ell < a < \ell,\ t_y \leq 0.4\ell,\ t_x \leq 0.2\ell$ (4.10)
Swedish Code (BBK (STATENS	$b_{BBK} = \max \begin{cases} b_{load} + 7 \cdot d_l \\ 0.65 \cdot \left(b_{load} + l_{load} \right) + 10.65 \cdot d_l \end{cases}$ (4.11)

BETONG KOMMITTE), 1979) (replaced)	
fib Model Code 2010 (FIB, 2012)	$b_{effMC} = l_{load} + 2 \cdot \left(b_{load} + a_v - \min\left(d_l ; a_v / 2 \right) \right) \cdot \tan\theta$ (4.12) $\theta = \begin{cases} 45^{\circ}, \text{ cantilever of continuous members} \\ 60^{\circ}, \text{ if load is close to simple support} \end{cases}$
Zheng et al. (2010)	$b_{Zh} = l_{load} + l_{span} \cdot \left(1 - r_{cp} \right) \cdot \tan\Phi$ (4.13) $r_{cp} = \frac{b_{load}}{l_{span}} \leq 0.4$ (4.14) $\Phi\left(^{\circ}\right) = 23.3 \cdot r_{cp} + 35.1$ (4.15)
Bauer and Müller (2003)	$b_{eff,Bauer} = l_{load} + b_{eff\,1}$ (4.16)
Vidaković and Halvonik (2019)	For cantilever members: $b_{eff,VH} = l_{load} + 2 \cdot \left(b_{load} + \min\left(2 \cdot d_l ; a_v \right) \right)$ (4.17)
Reiβen and Hegger (2012, 2013c)	For simply supported members: $b_{eff} = b \cdot \lambda_b \cdot \lambda_{\rho q} \cdot \lambda_l \cdot \lambda_{a/d}$ (4.18) $\lambda_b = 1.2 - 0.12 \cdot b \leq 1, \text{ for } b \leq 5.5\ m$ $\lambda_{\rho q} = 0.74 + 2.2 \cdot \rho_q^{\,0.4}, \text{ for } 0 \leq \rho_q \leq 0.7\%$ $\lambda_l = 0.81 + 0.045 \cdot l \leq 1.04$, for $l \geq 2\ m$ $\lambda_{a/d} = 1.8 - 0.19 \cdot a/d, \text{ for } 2.91 \leq a/d \leq 5.41$ (4.19)
Reiβen (2016)	$b_{\text{Reiβen}} = 7 \cdot d_{l,load} + k_{bf} \cdot l_{load}$ (4.20) With: $d_{l,load} \leq 0.40$ m $k_{bf} = -\frac{5}{8} \cdot \max\left(a_1 ; a_2 \right) / d + \frac{9}{4}, \begin{cases} \leq 1 \\ \geq 0.5 \end{cases}$ (4.21)
Rombach and Velasco (2005)	For LEFE analyses: $b_{RV} = 0.6 + 0.95 \cdot h + 1.15 \cdot a$ (4.22)
Natário et al. (NATÁRIO; FERNÁNDEZ RUIZ; MUTTONI, 2014)	For LEFE analyses on cantilever slabs: $b_{eff} = F_{aplied} / v_{avg,4d}$ (4.23)
Shu et al. (2019)	For NLFE analyses on cantilever slabs: $b_{eff,Shu} = b_w \cdot \beta_{w1} = b_w \cdot \frac{v_{E,avg}}{v_{R,code}}$ (4.24)

Source: Author.

4.2.3 Failure modes and shear transfer mechanisms in one-way shear

Since Kani (1964) and Leonhardt and Walther (1962), it has been known that different shear failure modes can occur as a function of the shear slenderness *M/Vd* and that shear strength increases considerably for short members. Figure 4-5 shows the way the nominal shear strength of wide reinforced concrete members (width-to-effective depth $b/d>1$) increases as the shear slenderness decreases for tests under concentrated loads (CL) (SOUSA; LANTSOGHT; EL DEBS, 2020). The figure also shows how the critical shear crack shape changes according to the shear slenderness (CAVAGNIS; FERNÁNDEZ RUIZ; MUTTONI, 2018a). For concentrated loads close to the support, or shear slenderness $M/Vd < 2.5$, direct load transfer may occur by compressive struts improving the shear capacity. Such members are usually called non-slender members or deep beams for beam-shaped members. The higher concentration of compressive stresses between load and support usually leads to the crushing of concrete at failure (BAIRÁN et al., 2020). This failure mode is called shear-compression failure (YANG; WALRAVEN; DEN UIJL, 2017).

Figure 4-5 - Shear slenderness effect on the one-way shear behavior of wide reinforced concrete members without stirrups.

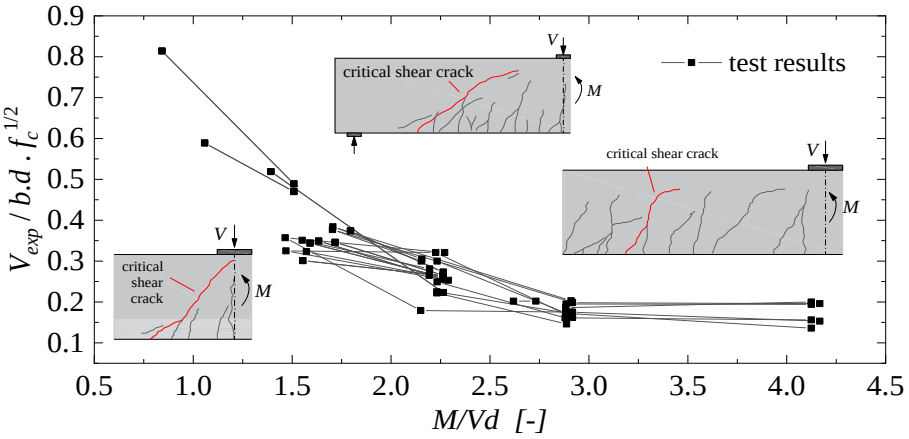

Source: Adapted from Sousa, Lantsoght and El Debs (2020).

Commonly, the same shear strength model derived for flexure-shear failures is used for the design and verification of shear strength of non-slender members through the application of a factor that reduces the acting shear force V_{Ed} or improves the shear capacity V_R in a critical section, as suggested in NEN 1992-1-1:2005 (CEN, 2005) and *fib* Model Code 2010 (FÉDÉRATION INTERNATIONALE DU BÉTON (FIB), 2012). The shear reduction factor β from NEN-EN 1992-1-1:2005 (CEN, 2005) first considered only the bending moment effect on the compression chord or cantilever action (FERNÁNDEZ RUIZ; MUTTONI; SAGASETA, 2015). This means that only the effect of lower crack openings and large compression chord depth were taken into account. In fact, the shear strength enhancement for non-slender members is caused by a combination of the following

mechanisms: (i) higher compression chord capacity (cantilever action (FERNÁNDEZ RUIZ; MUTTONI; SAGASETA, 2015; MUTTONI; FERNANDEZ RUIZ, 2010a)) due to the large compression zone depth (BAIRÁN et al., 2020) and (ii) direct load transfer that occurs by compression arch beyond the inclined cracking load (or strut if it has a straight shape), also named arching action (KIM; KIM; WHITE, 1999; LANTSOGHT et al., 2015c). In the literature, both mechanisms are cited as the source of improved arching action (NATÁRIO; FERNÁNDEZ RUIZ; MUTTONI, 2014).

Table 4-2 - Expressions for reducing the acting shear load V_E for non-slender members according to different references.

Reference	Model
ABNT NBR 6118:2014 (ABNT NBR 6118, 2014) – Brazilian code (expression described for beams) DIN 1045:1988 (DIN 1045, 1988) – German code	$\beta = \frac{a}{2 \cdot d}$ (4.25)
DIN 1045-1:2001 (DIN 1045-1, 2001)– German code	$\beta = \frac{x}{2 \cdot d}$ (4.26) x measured from load axis to support edge
NEN-EN 1992-1-1:2005 (CEN, 2005) – European code	$\beta_{EC} = \frac{a_v}{2 \cdot d} \begin{cases} \leq 1.00 \\ \geq 0.25 \end{cases}$ (4.27)
fib Model Code 2010 (FÉDÉRATION INTERNATIONALE DU BÉTON (FIB), 2012)	$\beta_{MC} = \frac{a_v}{2 \cdot d} \begin{cases} \leq 1.00 \\ \geq 0.50 \end{cases}$ (4.28)
SIA 262:2013 (SIA, 2013) – Swiss code	$\beta_{SIA} = \frac{a_v}{2 \cdot d}$ (4.29)
Reiβen (2016)	$\beta_{\mathrm{R16}} = \frac{\max\{a_1; a_2\}}{2.8 \cdot d} \begin{cases} \leq 1.0 \\ \geq 0.4 \end{cases}$ (4.30)
Natário, Fernández Ruiz and Muttoni (2014)	$\beta_{\mathrm{Nat14}} = \frac{a_v}{2.75 \cdot d} \begin{cases} \leq 1.00 \\ \geq 0.50 \end{cases}$ (4.31)
Yang et al. (2013)	$\beta[M/Vd] = \frac{M}{Vd \cdot 2} \leq 1$ (4.32)

Source: Author.

Table 4-2 shows a summary of the main expressions suggested by different references to account for the increase in shear capacity for loads close to supports – past codes used the shear span to depth ratio *a/d* as the main parameter. The model proposed by Reiβen (2016) was calibrated for the European code shear model and took into account the ratio $max\{a_1;a_2\}/d$ (a_1 and a_2 refer to the

distances from the section of zero bending moment to the support and load axes, respectively) in such a way that it provides precise estimations of strength for both simply supported and continuous members. In this text, the ratio $max\{a_1;a_2\}/d$ has the same meaning as the shear slenderness M/Vd. Since the influence of the shear slenderness is already taken into account in the shear models from *fib* Model Code 2010 and SIA 262:2013 by the calculations of the internal forces, the β factor takes into account the improved arching action only by the clear shear span-to-effective depth ratio a_v/d as a more conservative approach.

4.2.4 Critical Shear Displacement Theory Model

The Critical Shear Displacement Theory (CSDT) (YANG; DEN UIJL; WALRAVEN, 2016; YANG; WALRAVEN; DEN UIJL, 2017) assumes that a critical inclined crack starts from a major flexural crack, which will lead to collapse when the shear displacement Δ of the crack reaches a critical value and causes a secondary crack (dowel crack) along the reinforcement. A dowel crack causes the detachment of the tensile reinforcement from the concrete along the shear span, which significantly reduces the lateral confinement on the crack and the member flexural stiffness (YANG; WALRAVEN; DEN UIJL, 2017). Due to the opening of the main crack, an additional vertical shear displacement is required for the recovery of the previous shear stress level in the crack, which feeds the growth of flexure-shear cracks and leads to a brittle collapse of the member (YANG; WALRAVEN; DEN UIJL, 2017).

Figure 4-6 - Flowchart of the calculations using the CSDT model.

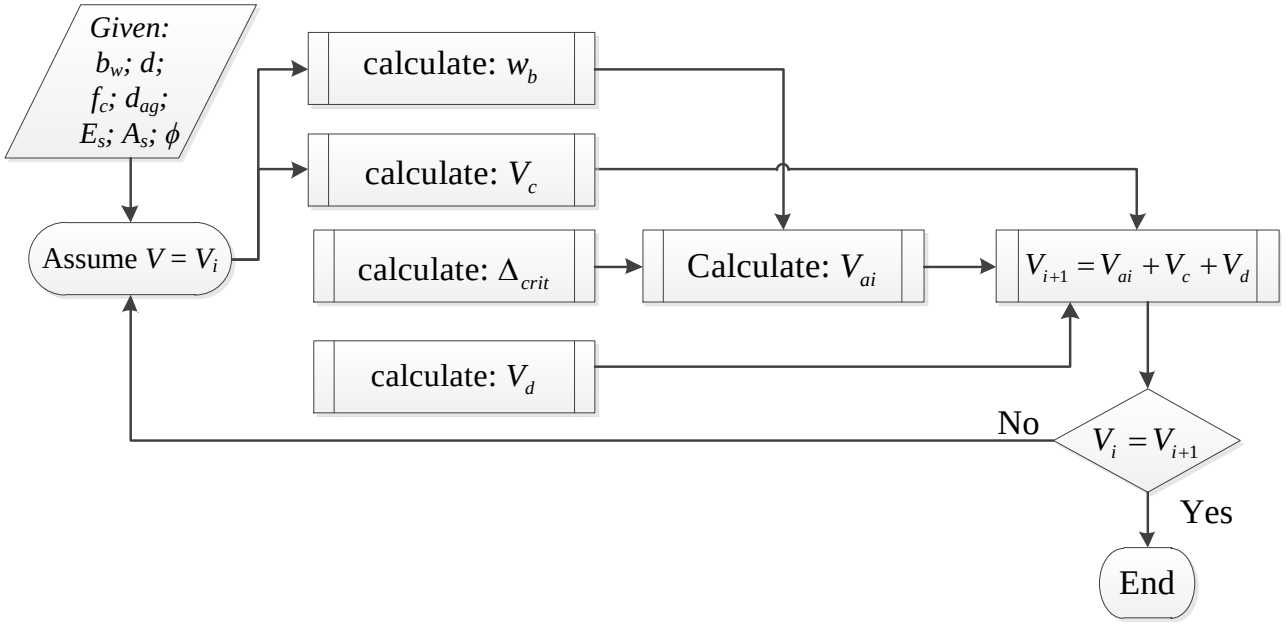

Source: Adapted from Yang; den Uijl and Walraven (2016).

The CSDT assumes that the shear capacity of RC members without stirrups is resisted by (i) compression chord capacity (MÖRSCH, 1909), (ii) dowel action (BAUMANN; RUSCH, 1970), and

(iii) aggregate interlock (WALRAVEN, 1981). The contribution of the residual tensile strength of concrete is neglected at failure (YANG; WALRAVEN; DEN UIJL, 2017), and the aggregate interlock contribution is a function of the crack width w_b at the level of the tensile reinforcement and derived from the shear displacement Δ (CHANA, 1987). Figure 4-6 and Table 4-3 show, respectively, a flowchart of the calculations for the prediction of shear capacity and the base equations used.

Table 4-3 – Expressions used in the CSDT (YANG; DEN UIJL; WALRAVEN, 2016).

Model	Expression
General (YANG; DEN UIJL; WALRAVEN, 2016)	$V_u = V_c + V_{ai} + V_d$ (4.33)
Compression chord (MÖRSCH, 1909)	$V_c = \frac{2}{3}\frac{z_c}{z}V = \frac{d - s_{cr}}{d + 0.5s_{cr}}V$ (4.34)
Aggregate interlock (YANG; DEN UIJL; WALRAVEN, 2016)	$V_{ai} = R_{ai} f_c^{0.56} s_{cr} b \frac{0.03}{w_b - 0.01}\left(-978\Delta^2 + 85\Delta - 0.27\right)$ (4.35)
Dowel action (BAUMANN; RUSCH, 1970)	$V_d = 1.64 b_n \phi \sqrt[3]{f_c}$, f_c in [MPa] (4.36) b_n is the clear width of the structural member; ϕ is the flexural rebar diameter
Factors	**Expression**
Height of fully developed crack	$s_{cr} = \left(1 + \rho_l n_e - \sqrt{2\rho_l n_e + \left(\rho_l n_e\right)^2}\right) d$ (4.37) $n_e = E_s / E_c$ (4.38)
Critical shear displacement	$\Delta_{cr} = \frac{25d}{30610\phi} + 0.0022 \le 0.025$ mm (4.39) ϕ is the flexural rebar diameter
Crack width at the bottom of the crack (w_b)	$w_b = \frac{M}{zA_s E_s} l_{cr,m} \ge 0.04\ mm$ (4.40) $l_{cr,m} = \frac{s_{cr}}{k_c}$, with $k_c = 1.28$ (4.41)
Reduction factor for aggregate interlock for high-strength concrete (YANG; DEN UIJL; WALRAVEN, 2016)	$R_{ai} = 0.85 \cdot \sqrt{\left(\frac{7.2}{f_c - 40} + 1\right)^2} - 1 + 0.34$ (4.42) with f_c in MPa and f_c > 65 MPa

Source: Adapted from Yang; den Uijl and Walraven (2016).

4.3 Databases

This study assumes that checking both shear-critical failure modes, one-way and two-way shear, is essential to identify the governing failure modes of existing bridge deck slabs. Therefore, a careful classification of the failure modes of tests from the literature is of paramount importance to

understand the limits of application of the available one-way and two-way shear models. Moreover, this classification allows a fairer assessment of the precision of one-way and two-way shear models, as well as models of effective shear width for slabs under concentrated loads.

This study will discuss the results of three database subsets which are published in the public domain (SOUSA; LANTSOGHT; EL DEBS, 2020): (i) wide beams and one-way slabs loaded over the entire width failing in one-way shear (Database A); (ii) slabs under a single concentrated load failing in one-way shear, two-way shear or a combination of both (Database B0) and; (iii) slabs subjected to double loads close to the line support (Database C).

4.3.1 Database filtering and organization

The Database B0 includes 214 test results of slabs under single concentrated loads that were classified according to the main failure mode in (i) wide beam shear or one-way shear (WB), (ii) punching shear (P) and (iii) transition mode between wide beam shear and punching shear (WB/P: beam shear cracks at the slab sides combined with punching cracks around the load). More details about the criteria of classification of the governing failure mechanism for the evaluated tests can be consulted in Lantsoght (2013). Since this study focuses on the one-way shear model, tests with signs of punching failure were initially removed from the database B0, which resulted in the database B1 (141 tests). This filtering was based on (i) the cracking pattern of the members, when available in the original references and (ii) the classification reported by other authors (LANTSOGHT, 2013; LANTSOGHT et al., 2015d), which was also based on the cracking pattern and (iii) in the classification of Natário (NATÁRIO, 2015), who combined shear fields from LEFE analyses with one-way shear and punching shear models according to the Critical Shear Crack Theory (CSCT) (NATÁRIO, 2015; NATÁRIO; FERNÁNDEZ RUIZ; MUTTONI, 2014; VAZ RODRIGUES; FERNÁNDEZ RUIZ; MUTTONI, 2008). The main criteria used for the removal of members because of a punching failure in this study were (i) absence of a critical shear crack visible on the edge of the members and (ii) position at which the critical shear crack intercepted the middle depth of the member when the cut view was available. When the internal cracking pattern was not shown in the references, it was considered a punching failure if the cracking pattern was predominantly formed by radial and tangential cracks or if a conical crack could be seen.

The database B1 of slabs under concentrated loads after removing punching tests comprehends 141 test results from the following references: Cullington et al. (1996), Lantsoght (2013), Reiβen (2016), Lubell (2006), Bui et al. (2017b), Regan (1982), Regan and Rezai-Jarobi (1988), Vaz Rodriguez et al. (2006), Rombach and Latte (2008, 2009), Natário et al. 2014, 2015), Rombach and Henze (2017), and Vida et al. (2018). The database entries include the effect of self-

weight on the calculated shear capacities and on the shear slenderness parameters for continuous members.

The database B1, whose organization was inspired by those of Lantsoght et al. (2015d), Reiβen (2016) and Henze et al. (2020), has been published in the public domain (SOUSA; LANTSOGHT; EL DEBS, 2020) and includes 46 tests on cantilever members (CT), 33 tests with concentrated loads close to the internal support of continuous members (CS), and 62 tests with concentrated loads close to the simple supports (SS). It also includes two modes of one-way shear failures, namely shear-compression failures for non-slender members, or shear slenderness M/Vd < 2.5 (55 tests ≡ 39 %), and flexure-shear failures for slender members, or shear slenderness $M/Vd \geq$ 2.5 (86 tests ≡ 61%).

Figure 4-7 displays the main geometrical loading parameters in the database for members with continuity over line supports and subjected to a combination of concentrated loads and line loads. The same definitions have been used for other structural systems.

Figure 4-7 - Geometrical parameters of wide members with continuity over the support.

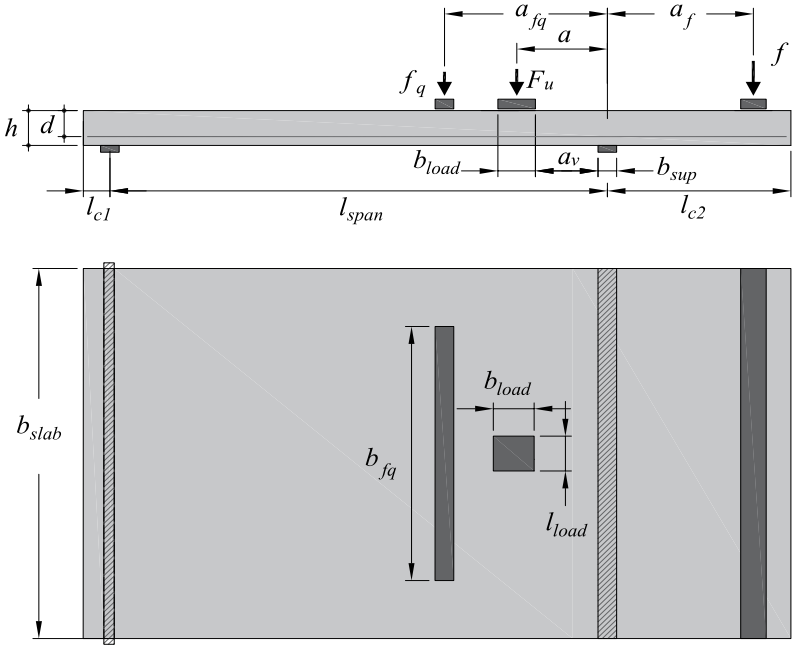

Source: Author.

Figure 4-8 shows the distributions of the parameters related to the tests included in the database B1. Similar to beam-databases (COLLINS; BENTZ; SHERWOOD, 2008; REINECK et al., 2013), most experiments were performed for members of thicknesses less than 600 mm (Figure 4-8a) and on wide members whose ratio between the slab width and load dimensions in the width direction was higher than 5 (Figure 4-8b). The predicted effective shear widths b_{eff} with the french approach

(FD P 18-717, 2013) indicated that the full width of members with $b_{slab}/l_{load} < 5$ was activated in most of these tests, depending on the distance from the load to the support. However, as some models of effective width are overly conservative, some predictions may indicate that the full width was not mobilized. Figure 4-8c shows that the b_{slab}/h aspect ratio (Figure 4-7) was higher than 5 in more than 75% of the tests, and Figure 4-8d highlights the number of tests in the database performed with a shear slenderness M/Vd between 2 and 3. This range indicates that a considerable number of tests were subjected to a transitional failure mode between shear-compression and flexure-shear. Figure 4-8e show that 16 tests from the database have a concrete compressive strength larger than 60 MPa and, hence, the level of accuracy for members with reduced aggregate interlock may be assessed. Figure 4-8f shows that the longitudinal reinforcement ratio ranges between 0.6 and 1.8%, where the larger ratios may not be representative of those used in bridge deck slabs.

Figure 4-8 – Distribution of parameters in the database B1 for the following parameters: a) thickness of the slab at the support edge, b) ratio of slab width-to-load dimension in the width direction, c) ratio of slab width-to-effective depth, d) shear slenderness; e) concrete compressive strength and f) longitudinal reinforcement ratio.

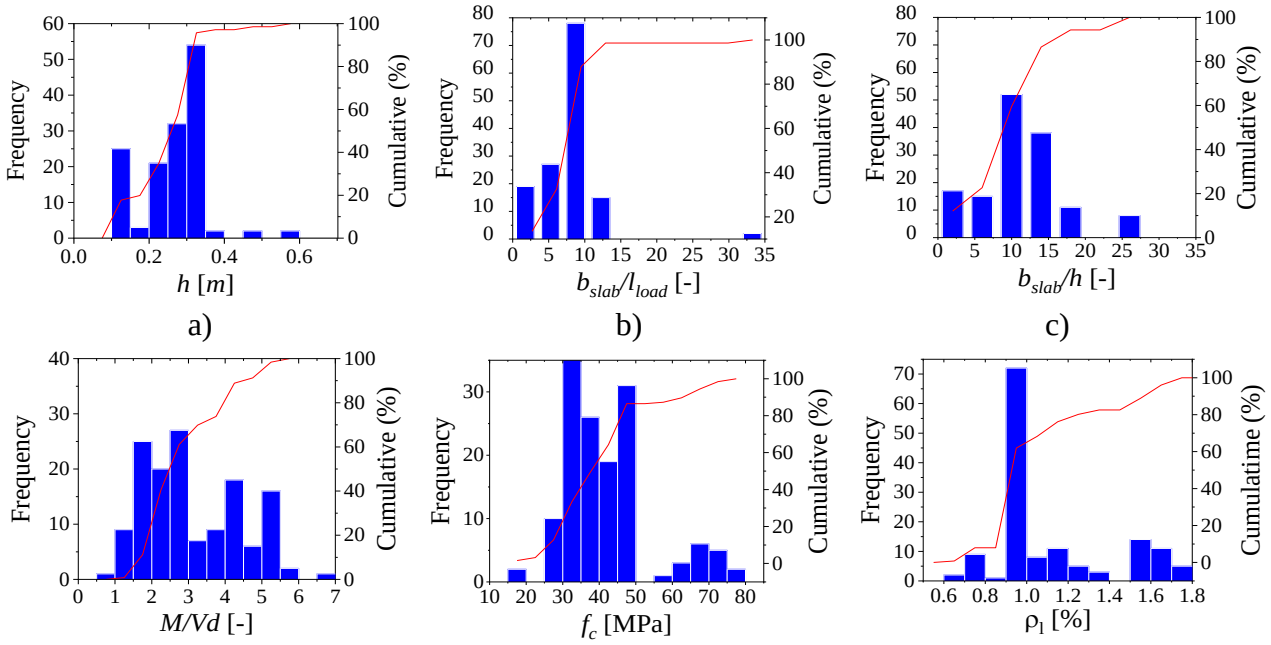

Source: Author.

4.4 Proposed recommendations

This section details the proposed recommendations related to (i) the control section to be evaluated, (ii) how to consider the arching action for loads close to the support and (iii) how to calculate the effective shear width.

4.4.1 Section for internal forces calculations

Since most mechanical based models of shear strength were derived for shear slenderness *M/Vd* higher than 2.5, the assumption of the section far from *d* or *d/2* from the highest bending moment axes (MUTTONI; FERNANDEZ RUIZ, 2008; YANG; DEN UIJL; WALRAVEN, 2016) or from geometrical discontinuity (FÉDÉRATION INTERNATIONALE DU BÉTON (FIB), 2012) does not play an important influence. However, when using these models for lower slenderness (*M/Vd* < 2.5), the location of this section assumes a major influence. Because of this, a previous investigation was made in order to identify the section that could balance precision and safety for the ratio V_{exp}/V_{cal} in both ranges of shear slenderness and for different support conditions (Figure 4-9b,c,d). Assuming that the shear capacity is reduced due to an increase in the opening of the critical shear crack (BENTZ; VECCHIO; COLLINS, 2006; MUTTONI; FERNANDEZ RUIZ, 2008; YANG; DEN UIJL; WALRAVEN, 2016), the control section for the calculations of the internal forces M_{Ed} and V_{Ed} remain at sections close to the higher bending moment for all models. The control section for cantilever members was assumed at the support edges instead of at distances of *d* or *d/2* from the support edge in order to reach better predictions for these support conditions (SOUSA; LANTSOGHT; EL DEBS, 2020). Since the critical shear crack develops from the major flexural crack, which occurs at the position of higher bending moment (YANG; DEN UIJL; WALRAVEN, 2016), the assumption adopted for cantilever slabs is still valid.

Figure 4-9 – a) reference lines to calculate the effective shear width in French model (FD P 18-717, 2013) and proposed approach (note that in the proposed approach the equivalent spreading angle is not fixed and varies as a function of the load position – explanation in section 4.4.3); critical sections used for b) cantilever members, c) simply supported members, and d) continuous members.

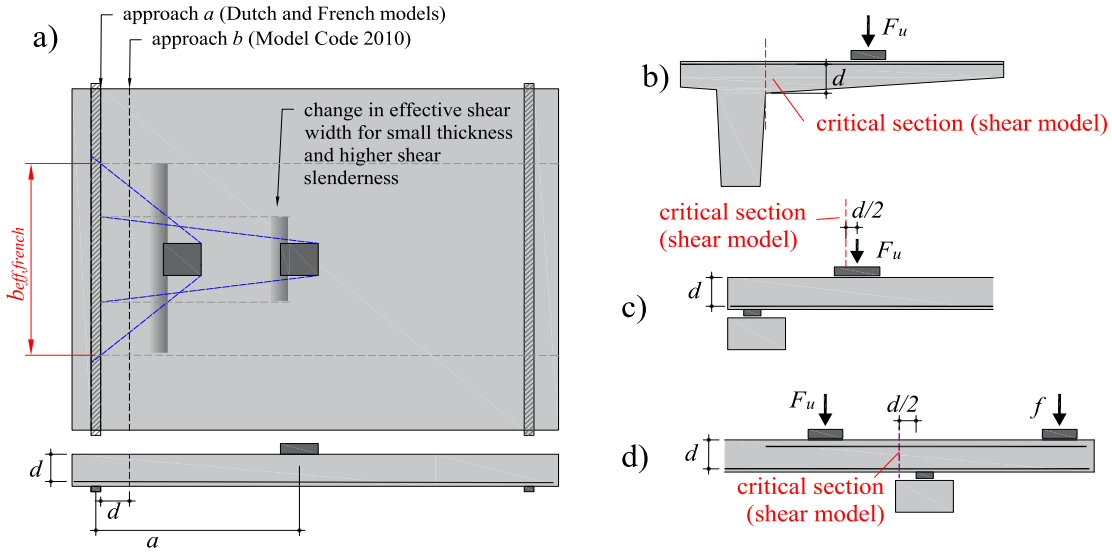

Source: Author.

4.4.2 Arching action

This study proposes to combine the CSDT result with a semi-empirical coefficient β based on the ratio a_v/d (Equation (4.43)) to extend the CSDT model to predict the shear capacity of non-slender members without additional iterative calculations:

$$\beta_{\text{Prop}} = \frac{a_v}{2.5 \cdot d} \begin{cases} \leq 1.00 \\ \geq 0.40 \end{cases} \tag{4.43}$$

The combination of the CSDT with reduction factor β for non-slender members should be understood as an engineering approach comparable to empirical simplifications used by most design codes (CEN, 2005; FÉDÉRATION INTERNATIONALE DU BÉTON (FIB), 2012) and strain-based models (NATÁRIO; FERNÁNDEZ RUIZ; MUTTONI, 2014). Theoretically, this approach is not exact because the shear failure mechanism for non-slender members is different from that for slender ones: the shape and relative contribution of the main shear-transfer mechanisms vary significantly when the shear slenderness decreases since the vertical branch of the assumed crack profile of the critical shear crack becomes not representative anymore (Figure 4-10).

Figure 4-10 - a) and b) Crack profile simplification for specimens with *M/Vd* > 3, c) main parameters of CSDT, and d) crack profile for non-slender members (*M/Vd* < 2).

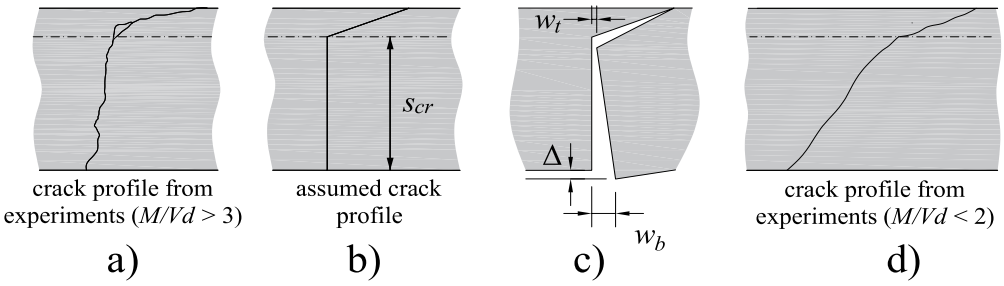

Source: Author.

For lower shear slenderness, the inclination of the major flexural crack increases in such a way that the contribution of the aggregate interlock decreases significantly, while the contribution of the compression chord V_c increases according to internal equilibrium (CAVAGNIS; FERNÁNDEZ RUIZ; MUTTONI, 2015). The use of strut-and-tie models for continuous members with maximum shear slenderness $M/Vd < 2$ may better represent the problem (YANG, 2014): plane sections do not remain plane, and shear strains become dominant for those members (MIHAYLOV; BENTZ; COLLINS, 2013). However, this approach may not be practical for the slabs studied since the problem is strongly three-dimensional. As such, for practical purposes, this study considers the choice of including β as adequate.

4.4.3 Effective shear width

In design and assessment of existing structures, two kinds of analyses may occur (i) the governing failure mode is unknown, and a conservative prediction of the shear capacity may be adequate for preliminary design, and (ii) a more precise estimation of the shear capacity is required, usually in the assessment of existing structures preliminarily rated as critical in shear (LANTSOGHT; DE BOER; VAN DER VEEN, 2017b). In the latter case, a detailed analysis of the governing failure mode would be essential to determine the shear capacity, which requires LEFE analyses combined with a mechanical-based model, such as conducted by Natário (2015) or using one-way and two-way shear models adjusted to slabs under concentrated loads in non-symmetrical conditions.

Since the governing failure mode of the tests in the database B1 is known, this study proposed two kinds of analyses. The first group of analyses investigates the accuracy of different effective shear width models combined with the CSDT model using a database with the governing failure mode known (one-way shear – Database B1). From these analyses, recommendations were derived for the assessment of existing structures when the governing failure mode is known (one-way shear), and precise estimation of the shear capacity is the main purpose.

The second group of analyses aims to assess the shear capacity of slabs when the governing failure mode is unknown (Database B0). This means that one-way or two-way shear failures were included in the analyses. In order to provide consistent predictions of shear capacity regardless of the critical failure mode and covering different support conditions, the General Effective Shear width model (GESW) was developed. This model proposes that, if the punching capacity is the governing failure criteria of the slab, the predicted one-way shear capacity should be decreased by predicting a smaller effective shear width.

The idea of the GESW model is to provide a simple alternative to assess the shear capacity of slabs using only a one-way shear model combined with an effective shear width. The proposed model is based on the French effective shear width model (FD P 18-717, 2013) adjusted by a correction factor α. This factor considers that increasing the shear slenderness ($\lambda=M/Vd$) or decreasing the effective depth of the reinforcement, the punching shear failure becomes governing. Therefore, a reduced effective shear width should be predicted for slabs on which punching shear may be critical. The values of α were derived based on regression analyses to improve the average and coefficient of variation of the ratio V_{exp}/V_{calc} with the CSDT model combined with the French model of effective shear width. These regression analyses were organized according to the support conditions of the tests (Figure 4-11). The shear slenderness M/Vd was chosen as the main parameter in the GESW model

for all support conditions for two reasons: (i) based on the literature review discussed in Section 2 and (ii) based on the behavior of V_{exp}/V_{cal} according to shear slenderness M/Vd (Figure 4-11).

Figure 4-11 - Ratio of V_{exp} / V_{cal} of the CSDT combined with the original French effective shear width model and $\beta_{proposed}$ for account improved arching action for loads close to the support.

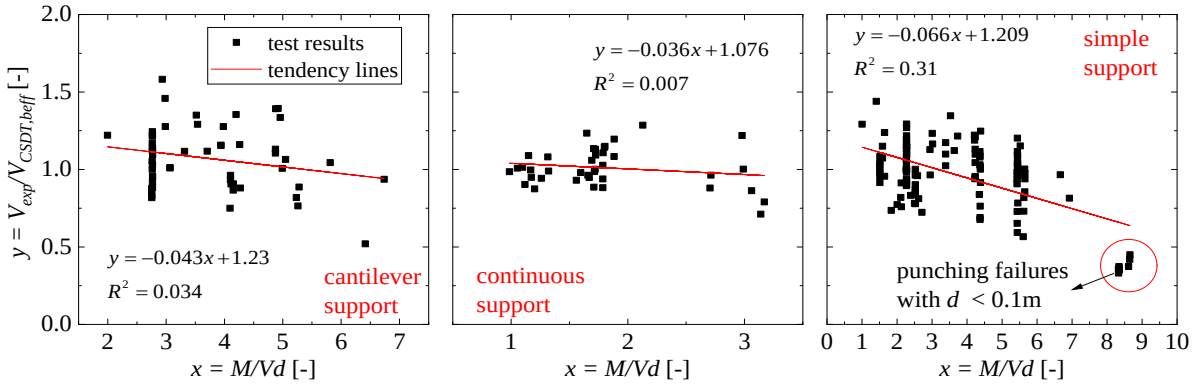

Source: Author.

Table 4-4 shows the equations for the proposed model of effective shear width. The parameter α was determined based on the statistical regression analyses observing the relationship between the predictions $V_{exp}/V_{CSDT,beff}$ with the parameter $x = M/Vd$. In Table 4-4, this study considered the effective depth d only for simply supported members by two reasons: (i) the thickness variation is small in the database for other support conditions and (ii) to improve the predictions of tests with punching failure and effective depth lower than 0.1 m (Figure 4-11). At this point, this study highlighted that this approach seeks to provide a model for the design or preliminary assessment of existing structures. When higher levels of approximation are required, the use of one-way and two-way shear models is essential to determine the governing failure mode, as this study will discuss in the next sections. Figure 4-9a illustrates physically how the predicted effective shear width decreases by increasing the shear slenderness M/Vd with the GESW model, while Figure 4-12 shows the calculated factors alfa according with the shear slenderness for simply supported slabs of small thickness.

Table 4-4 - General effective shear width model proposed (GESW) according to the support conditions, shear slenderness $\lambda=M/Vd$, and effective depth d of the longitudinal reinforcement.

General model	$b_{GESWM} = b_{eff,French} \cdot \alpha$	(4.44)
Cantilever slabs	$b_{GESWM} = b_{eff,French} \cdot (-0.05 \cdot \lambda + 1.05)$	(4.45)
Simple support	$b_{GESWM} = b_{eff,French} \cdot [(0.31 \cdot d - 0.103) \cdot \lambda + 1.08]$	(4.46)
Continuous support	$b_{GESWM} = b_{eff,French} \cdot (-0.072 \cdot \lambda + 1.08)$	(4.47)

Source: Author.

Figure 4-12 – Variation of the factor α according to the shear slenderness and effective depth of reinforcement for the simply supported slabs.

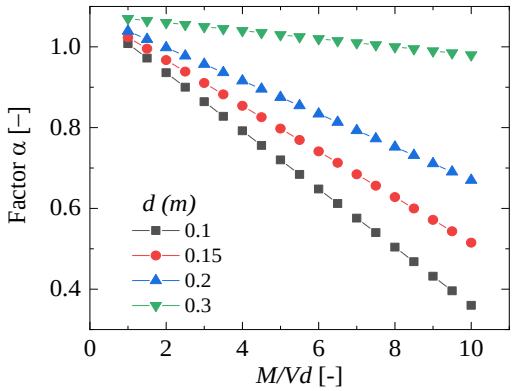

Source: Author.

4.5 Results of Chapter 4

This section addresses a comparison between the experimental shear strengths from the databases A, B0, B1 and C (SOUSA; LANTSOGHT; EL DEBS, 2020), and those predicted by the CSDT model. Firstly, the level of accuracy (average value - AVG) and precision (coefficient of variation - COV) of the V_{exp}/V_{cal} ratio for a database of wide members loaded over the entire width was assessed according to the shear slenderness, with no influence of the effective shear width model (Database A - Section 4.5.1). In a second step, the analyses involved the database of slabs under single concentrated loads failing in one-way shear (Database B1 - Sections 4.5.2, 4.5.3 and 4.5.4). Then this study compared the predicted one-way shear capacities with the experimental ones for 8 tests of slabs subjected to double concentrated loads parallel to the support (Database C - Section 4.5.5). Finally, this study discusses the results of analyses conducted for the overall database of slabs under single loads (Database B0- Sections 4.5.6) using one-way and two-way shear models.

4.5.1 Members loaded over the full width – Proposal for $\beta_{arching}$

This analysis aims to assess only the proposed factor regarding the improved arching action for non-slender members, without the influence of the effective shear width models. For this study, a database of wide beams and one-way slabs loaded over the entire width was used (Database A). This database is published in the public domain (SOUSA; LANTSOGHT; EL DEBS, 2020) and covers different support conditions and a comprehensive range of shear slendernesses. The database includes 36 tests with $M/Vd \leq 2.5$ and 146 tests with $M/Vd > 2.5$.

Figure 4-13 shows a β factor derived based on a regression analysis with exponential adjustment according to the shear slenderness $\lambda=M/Vd$. This graph highlighted that the scatter between predicted and calculated shear strengths in the range of shear slenderness lower than 3 is

considerably higher compared to the other range. This occurs because the arching action is highly influenced by the cracking pattern, which shows a higher variability for short slenderness (YANG; DEN UIJL; WALRAVEN, 2013). Since the CSDT model already takes into account the shear slenderness by the calculations of M and V in the estimation of crack width at the bottom of the crack w_b, the β factor based on the ratio M/Vd could lead to overly optimistic predictions of resistance, mainly when arching action does not play an influence as a result of the occurring cracking pattern (see test without arching action in Figure 4-13). Because of this, some authors proposed to adopt the inclined cracking load instead of the ultimate shear load as the failure criterion since this parameter shows a considerably lower scatter (YANG; DEN UIJL; WALRAVEN, 2013). However, as most references do not report the inclined cracking load for slab tests as this cracking is harder to observe in slabs under concentrated loads than in beam members, the ultimate shear load was considered in the regression analyses.

Figure 4-13 – Alternative β factor derived based on exponential fitting between experimental and predicted shear strengths. Note: $\lambda = M/Vd$.

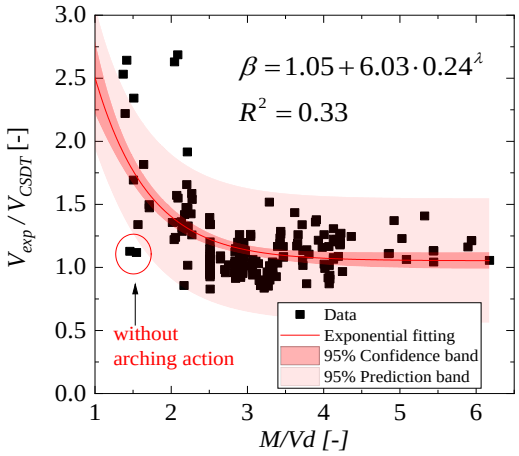

Source: Author.

Figure 4-14 shows the V_{exp}/V_{calc} ratio according to the shear slenderness M/Vd with and without taking into account improved arching action for non-slender members by a β factor. The gray ranges represent ±1 standard deviation from the mean value.

Figure 4-14 - Effect of factor β on the statistics of V_{exp}/V_{cal} for tests loaded over the entire width (line loads). (CS = continuous support; CT = cantilever support and SS = simple support).

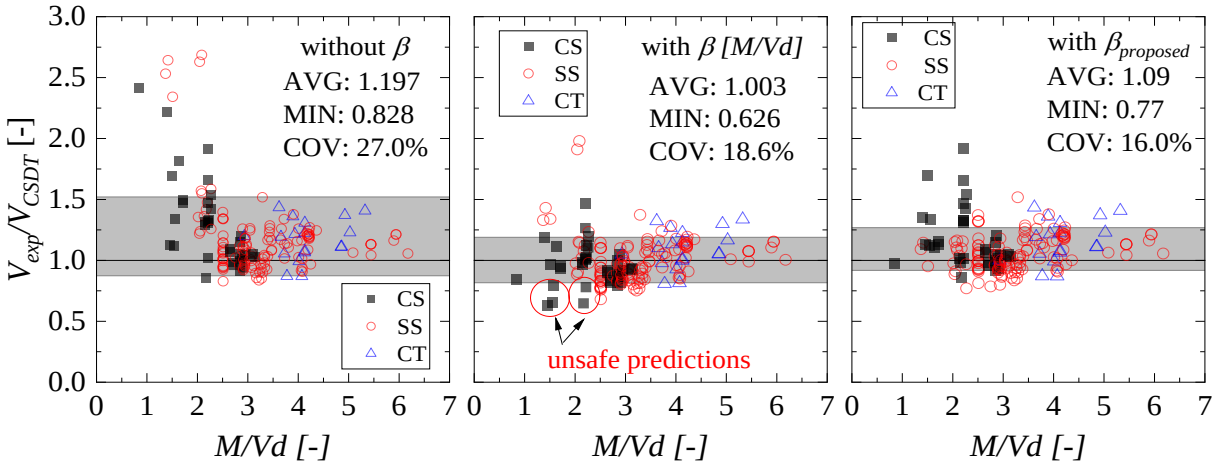

Source: Author.

According to Figure 4-14, applying an improved arching action factor with the CSDT reduces the coefficient of variation from 24.7% to 18.6% when using $\beta[M/Vd]$ (Figure 4-13), and to 16.0% when using $\beta_{proposed}$ (Equation (4.43)). Any approach shows a wider scatter between experimental and predicted shear capacities for continuous members (CS), due to the higher variability in the position of the critical shear crack. Although the theoretical critical section was at *d/2* from the position with the maximum bending moment, this procedure is still conservative for most tests. Table 4-5 shows that the average (AVG) V_{exp}/V_{cal} ratio ranged from 1.197 to 1.093 with the proposed factor β_{prop}. In Table 4-5, $V_{exp,red}$ refers to the experimental shear capacity reduced by the different parameters β (note that in this analysis, the members are loaded over the entire width and hence, the effective shear width does not play influence). The lower scatter between experimental and predicted shear capacities occurred with the $\beta_{proposed}$ and β_{EC}.

Table 4-5 - Statistical results of the predicted to calculated shear strengths according to different approaches to account the arching action for non-slender members.

	$\frac{V_{exp}}{V_{CSDT}}$	$\frac{V_{exp,red}}{V_{CSDT}}$	$\frac{V_{exp,red}}{V_{CSDT}}$	$\frac{V_{exp,red}}{V_{CSDT}}$
Approach	*Without* β	*With* β_{EC}	*With* $\beta_{Figure\ 4\text{-}13}$	With $\beta_{proposed}$
AVG	1.197	1.134	1.003	1.093
MIN	0.828	0.828	0.626	0.770
COV	0.270	0.172	0.186	0.160

Source: Author.

Considering only the tests with $M/Vd < 2$ from Table 4-5, the ratio $V_{exp,red}/V_{CSDT}$ with $\beta_{proposed}$ presented an average value equal to 1.18 with a coefficient of variation equal to 16.8%. Using β_{EC},

the ratio $V_{exp,red}/V_{CSDT}$ presented an average value equal to 1.35 with a with a coefficient of variation equal to 14.8%.

4.5.2 Effective shear width models

The database B1 gathered according to the descriptions in Section 3 (SOUSA; LANTSOGHT; EL DEBS, 2020) was used in the next analyses of the level of accuracy of the CSDT combined with different approaches for the effective shear width. Table 4-6 and Table 4-7 show statistical results from the V_{exp}/V_{calc} ratio for different ranges of shear slenderness $\lambda=M/Vd$. The results are shown as a function of the ratio M/Vd instead of the ratio a_v/d since the former is a more useful parameter to distinguish members subjected to shear-compression failure from those subjected to flexure-shear failures, mainly for continuous slabs. $\beta_{proposed,}$ which accounts for improved arching action for non-slender members, was adopted in most analyses. Since some tests did not fulfill conditions related to loading conditions for using the effective width model from the German guidelines (DAFSTB, 1991), Equations (4.6) to (4.10) in Table 4-1, this model was not evaluated. In the same way, the model provided by Halvonik et al. (2020) was not evaluated since this was purposed only for cantilever specimens.

Table 4-6 - Statistics of V_{exp}/V_{calc} according to the range of shear slenderness $\lambda = M/Vd$ and effective width model provided in design codes.

			$\frac{V_{\exp,red}}{V_{CSDT}}$	$\frac{V_{\exp,red}}{V_{CSDT}}$	$\frac{V_{\exp,red}}{V_{CSDT}}$	$\frac{V_{\exp,red}}{V_{CSDT}}$
		b_{eff}	ABNT	Swedish	French	*fib*
λ	Nº of tests	$\beta_{arching}$	Prop	Prop	Prop	Prop
<2.5	55	AVG	1.401	0.706	1.044	1.092
		MIN	0.869	0.481	0.773	0.758
		COV	21.9%	23.5%	11.4%	20.8%
≥2.5	86	AVG	2.009	0.981	1.070	1.192
		MIN	0.818	0.438	0.723	0.513
		COV	40.8%	18.7%	15.8%	23.7%
All	141	AVG	1.772	0.873	1.060	1.153
		MIN	0.818	0.438	0.723	0.513
		COV	41.2%	25.4%	14.3%	23.0%

Source: Author.

According to Table 4-6, older design code models of effective shear width, such as the Brazilian model (ABNT NBR 6118, 1980), lead to overly conservative predictions in most cases (mean $V_{exp,red}/V_{CSDT}$ = 1.772). The Swedish provisions (BBK (STATENS BETONG KOMMITTE), 1979), on the other hand, lead to unsafe predictions, with average ratios of V_{exp}/V_{cal} of 0.706 and 0.981 in the different ranges of shear slenderness evaluated. The *fib* model of effective shear width leads to average values of V_{exp}/V_{cal} of 1.092 and 1.192 for non-slender and slender members, respectively. The

best accuracy and precision over the different slenderness ranges assessed were achieved by the French model of effective shear width (FD P 18-717, 2013), thus indicating, on average, that the French approach provides reasonable predictions of effective shear width for slabs failing in one-way shear.

Table 4-7 shows that the average value of V_{exp}/V_{cal} ranged from 1.089 to 1.772 with the approaches studied for the definition of an effective shear width. The effective width from Zheng et al. (ZHENG et al., 2010) provided a wider scatter between experimental and predicted shear capacities (COV > 30% on average) and a V_{exp}/V_{cal} mean value much lower than 1 for non-slender members. Since the approach of Reiβen (2016) includes the effect of the improved arching action on non-slender members in the effective width model by using the factor k_{bf} (Equation (4.21) in Table 4-1), the experimental shear capacities were not reduced for these calculations. The model provided conservative predictions of shear strength for all tests assessed and a 25.7% coefficient of variation. Bauer and Muller's approach (BAUER; MÜLLER; BLASE, 2005) resulted in the most conservative predictions for slender members (V_{exp}/V_{cal} = 2.009), but with a wider scatter (COV = 40.8%). The proposed GESW model provided good AVG (1.197) and COV (20.3%) values compared to the other models. Comparing Table 4-6 and Table 4-7, both GESW model and French model provide an accurate estimation of the test results. However, the GESW turns out to be slightly more conservative for Database B1 as it was derived to assess slabs under both failure modes (one-way shear and two-way shear).

Table 4-7 - Statistics of V_{exp}/V_{calc} according to the range of shear slenderness $\lambda = M/Vd$ and effective width models suggested in the literature.

			$\frac{V_{\exp,red}}{V_{CSDT}}$	$\frac{V_{\exp}}{V_{CSDT}}$	$\frac{V_{\exp,red}}{V_{CSDT}}$	$\frac{V_{\exp,red}}{V_{CSDT}}$
		b_{eff}	Zheng	Reißen	Bauer	Prop (GESW)
λ	Nº of tests	$\beta_{arching}$	Prop	-	Prop	Prop
< 2.5	55	AVG	0.755	1.601	1.401	1.043
		MIN	0.512	1.113	0.869	0.748
		COV	22.7%	17.7%	21.9%	12.2%
≥ 2.5	86	AVG	1.302	1.638	2.009	1.295
		MIN	0.459	0.983	0.818	0.830
		COV	34.0%	29.6%	40.8%	19.2%
All	141	AVG	1.089	1.624	1.772	1.197
		MIN	0.459	0.983	0.818	0.748
		COV	41.3%	25.7%	41.2%	20.3%

Source: Author.

4.5.3 Sensitivity of parameters

Since the first purpose is to derive recommendations for precise predictions of shear strength when the one-way shear failure mode is governing (Database B1), the CSDT combined with the French effective shear width model and β_{prop} was further assessed with parameter studies (Figure 4-15).

Figure 4-15 - V_{exp}/V_{cal} ratio as a function of: a) aggregate size d_g, b) longitudinal reinforcement ratio ρ_l, c) concrete compressive strength f_c, d) effective depth d, e) width-to-effective depth ratio b/d, and (e) shear slenderness M/Vd. (CS = continuous support; CT = cantilever support and SS = simple support).

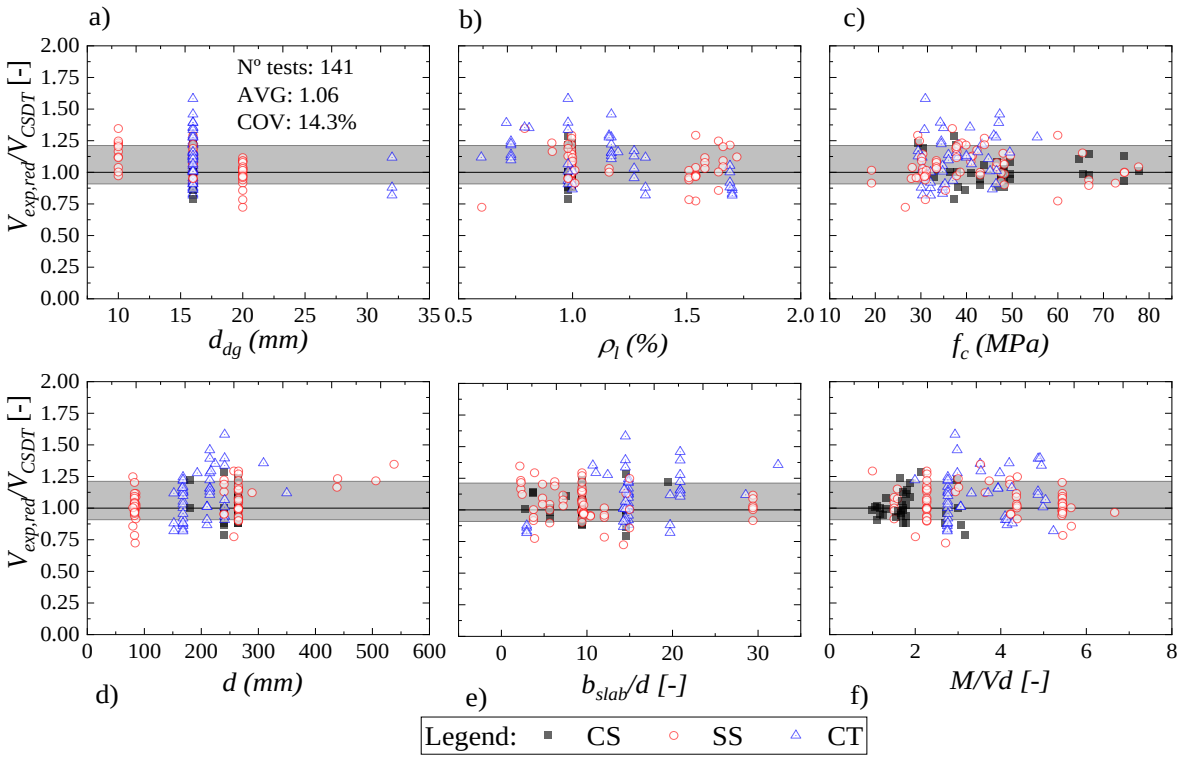

Source: Author.

Figure 4-15 shows the ratio of $V_{exp,red}/V_{cal}$ as a function of different parameters. The results indicate no significant influence of the aggregate size (Figure 4-15a) and reinforcement ratio (Figure 4-15b) on the predictions of shear strength with the studied approach. Wider scatter in some regions (see Figure 4-15a) for 16 mm aggregate size can be assigned to a higher number of tests. Figure 4-15c shows that the CSDT provides accurate and precise predictions of shear strength for members of high strength concrete (f_c > 65 MPa), for which a lower contribution of the aggregate interlock is accounted for by the parameter R_{ai} from the CSDT (however, it shall be mentioned that the number of tests in this range is significantly lower than for f_c < 60 MPa). This approach also handled well the range of thicknesses studied (Figure

4-15d) and is did not shows be influenced by the slab width-to-effective depth ratio b_{slab}/d (Figure 4-15e). Although the range of thickness studied is not representative of solid slab bridges (LANTSOGHT et al., 2015d), the available results are of interest for slab-between-girders bridges. Moreover, the studied approach enabled accurate predictions, regardless of the shear slenderness parameter *M/Vd* (Figure 4-15f).

4.5.4 Comparison with design code provisions

Table 4-8 shows a comparison of different code-based approaches for the one-way shear capacity of the experiments gathered in database B1 described in Section 3. The French model is used for determining the effective width in combination with code provisions from Europe (CEN, 2005; SIA, 2013) and North America (AASHTO, 2017). The *fib* Model Code 2010 (FÉDÉRATION INTERNATIONALE DU BÉTON (FIB), 2012) is the only code which includes guidance for improved arching action and effective width for concentrated loads close to the support. The same factor β_{prop} for use with the CSDT was adopted in combination with the Swiss code SIA 262:2013 model (SIA, 2013) and with the AASHTO code provisions for bridges (AASHTO, 2017).

Table 4-8 - Statistics of V_{exp}/V_{calc} according to the range of shear slenderness $\lambda = M/Vd$ for different design code approaches.

			$\frac{V_{\exp,red}}{V_{CSDT}}$	$\frac{V_{\exp,red}}{V_{CSDT}}$	$\frac{V_{\exp,red}}{V_{AASHTO}}$	$\frac{V_{\exp,red}}{V_{CEN\,04}}$	$\frac{V_{\exp,red}}{V_{MC}}$	$\frac{V_{\exp,red}}{V_{SIA262}}$
		b_{eff}	French	GESW	French	French	*fib* MC	French
λ	Nº of tests	$\beta_{arching}$	Prop	Prop	Prop	CEN (2005)	*fib* MC	Prop
<2.5	55	AVG	1.044	1.043	1.421	1.704	1.762	1.096
		MIN	0.773	0.748	0.986	1.095	1.176	0.819
		COV	11.4%	12.2%	16.5%	18.0%	22.6%	14.8%
>2.5	86	AVG	1.070	1.295	1.476	1.122	1.479	1.037
		MIN	0.723	0.830	0.918	0.606	0.749	0.733
		COV	15.8%	19.2%	33.3%	24.0%	29.0%	16.4%
All	141	AVG	1.060	1.197	1.454	1.349	1.589	1.060
		MIN	0.723	0.748	0.918	0.606	0.749	0.733
		COV	14.3%	20.3%	28.2%	29.8%	27.6%	15.9%

Source: Author.

Table 4-8 shows that the code provisions studied provided a mean ratio of V_{exp}/V_{cal} between 1.043 and 1.704 for $\lambda < 2.5$. The most precise results were achieved by the French effective shear width model combined with the one-way shear model based on the CSDT, as proposed in this study when the governing failure mode is known and is one-way shear. The predictions with the AASHTO code provisions were more conservative, with a mean ratio

between experimental and calculated shear strengths higher than 1.4 on both ranges of shear slenderness studied.

Table 4-8 also shows that the average ratio of V_{exp}/V_{cal} ranged from 1.060 to 1.589 for a shear slenderness higher than 2.5. Remarkably, the Swiss code provisions reached the same level of accuracy and precision of CSDT when combined with the French model of effective shear width and use of β_{prop}. Although these models (CSDT and SIA 262:2013) were derived in different ways, this result occurs because both models rely on some similar ideas, such as the higher influence of aggregate interlock in the shear strength and the decrease of the shear strength for increasing shear slenderness. Since both AASHTO models and *fib* Model Code Models were derived based on the Simplified Modified Compression Field Theory (SMCFT (BENTZ; VECCHIO; COLLINS, 2006)), the statistical differences can be attributed to the models to account for improved arching action and the effective shear width used.

4.5.5 Test with double loads

The number of tests with double loads parallel to line supports is very limited. There are only 8 tests in the literature conducted by Rombach and Henze (2017), Vaz Rodrigues et al. (2008) and Reiβen et al. (2018). Most of these tests were conducted on cantilever slabs (7/8). The test with 4 loads close to the line support conducted by Vaz Rodrigues et al. (2008) showed a punching failure and was not analyzed in this study because it showed a transitional failure between the one-way and two-way shear. Table 4-9 shows the statics of the ratio between experimental and predicted one-way shear resistances for these tests. In summary, the level of accuracy of the CSDT model combined with the French effective shear width was close to that of slabs subjected to a single load. However, additional tests are needed to confirm these findings. The most unsafe prediction in Table 4-9 (V_{exp}/V_{pred} = 0.89) occurred for the only test with a ratio $a_v/d < 2.5$. Therefore, the proposed factor to consider arching action (β_{prop}) may have been too optimistic for this type of loading.

Table 4-9 - Statistical of the experimental to calculated shear strengths for tests with double loads close to a line support.

Authors	Test	$\frac{V_{\exp,red}}{V_{CSDT,beff\ \text{French}}}$
Vaz Rodrigues, Fernández Ruiz and Muttoni (2008)	DR1b	1.26
	DR2a	1.03
	DR2b	1.07
Rombach & Henze (2017)	2d x 2	0.89
	3d x 2	0.99
	4d x 2	1.06
	5d x 2	1.01
Reißen, Classen and Hegger (2018)	MS35BB-22	1.04
AVG		1.04
COV (%)		9.78

Source: Author.

4.5.6 General approach for one-way and two-way shear

An alternative approach to assessing the one-way shear models applicable to members with possible punching failure is to decrease the effective shear width accordingly with the shear slenderness, as discussed in the proposed GESW model (Section 4). In this study, it is assumed that the French effective shear width should be multiplied by the parameter α (Equation (4.44)).

Table 4-10 shows the statistics of the ratio between experimental and predicted shear capacities with one-way and two-way shear models according to the failure mode for the database with 214 test results of slabs under single concentrated loads (Database B0). For the punching shear provisions, the proposed model from prEN 1992-1-1:2018 (MUTTONI et al., 2018) was used (based on the CSCT), while for the one-way shear models it is combined the CSDT models with the French and GESW models. Table 4-10 shows that the level of precision reached with the CSDT combined with the GESW model is very similar for both failure modes, while the other approaches provide precise estimations only for their respective failure modes.

Table 4-10 - Comparison of predictions with the CSDT and the punching shear provisions from prEN 1992-1-1:2018 (MUTTONI et al., 2018) according to the failure mode.

Failure mode	Nº of tests		$\frac{P_{exp}}{P_{EN18}}$	$\frac{V_{exp,red}}{V_{CSDT}}$	$\frac{V_{exp,red}}{V_{CSDT}}$
		b_{eff}	-	French	GESW
P	51	AVG	1.092	0.808	1.044
		MIN	0.724	0.331	0.712
		COV	20.0%	31.6%	21.2%
WB	141	AVG	1.219	1.060	1.197
		MIN	0.466	0.723	0.748
		COV	31.9%	14.3%	20.3%
WB/P	22	AVG	1.220	1.007	1.121
		MIN	0.942	0.712	0.833
		COV	21.5%	13.4%	15.6%
All	214	AVG	1.189	0.994	1.153
		MIN	0.466	0.331	0.712
		COV	29.2%	21.0%	20.8%

Source: Author.

4.6 Discussions of Chapter 4

Previous publications on the field of one-way slabs under concentrated loads usually concentrate on the accuracy of semi-empirical models applied to reduced databases (HENZE; ROMBACH; HARTER, 2020; LANTSOGHT et al., 2015d). When mechanical-based models are investigated, usually the analyses concentrate on one kind of support condition (HALVONIK; VIDAKOVIĆ; VIDA, 2020). Most of them neglect the governing failure mode of the tests (HENZE; ROMBACH; HARTER, 2020; REIßEN; HEGGER, 2015). Therefore, a gap of more comprehensive studies is realized related to the shear capacity of slabs under concentrated loads failing in different modes.

Tests with a presumed punching failure were initially removed from the database B1. Only members with predominant one-way shear failure were used in the first statistical analyses. Therefore, part of the higher level of accuracy in Section 5.2 with the French effective shear width can be attributed to the improved database selection. However, it was highlighted that the classification of the failure modes for some members may not be an easy task. For such cases, the experiments must be classified as governed by a mixed failure between one-way shear and two-way shear, as made in previous publications (LANTSOGHT et al., 2015d). In these tests, both conical cracks at the top/bottom face and flexure-shear cracks at the edges of the slab arise at failure. Some studies have claimed that one-way and two-way shear capacities can be very similar is terms of strength ratio (V_{exp}/V_{calc} similar to P_{exp}/P_{calc}) (NATÁRIO, 2015),

which was also verified in this study for some tests during the classification of the failure modes. Particularly, this is also in line with the ACI 318-19 punching provisions (ACI COMMITTEE 318, 2019), where the punching capacity is assumed to be governed by one-way shear when the load becomes very rectangular.

Since most mechanical models, such as the CSDT (YANG; DEN UIJL; WALRAVEN, 2016), CSCT (MUTTONI; FERNANDEZ RUIZ, 2008), and SMCFT (BENTZ; VECCHIO; COLLINS, 2006) were derived from flexure-shear failures, one could question their possible extension to non-slender members, whose predominant failure mode is a shear-compression failure. In fact, some studies, as well as the current ACI 318-19 (ACI COMMITTEE 318, 2019), have highlighted those members should be assessed by strut-and-tie models, instead of sectional strain-based models (SAGASETA; VOLLUM, 2010; VOLLUM; FANG, 2015). However, most engineers have raised the possibility of covering a more extensive range of cases with the same model. In particular, for the shear assessment of existing RC slab bridges, there is a need for uniform approaches that allow checking all cross-sections and load positions in a preprogrammed way. Such an approach requires the checking of models for non-slender members in an approach similar to the one suggested in design guides, e.g., NEN 1992-1-1:2005 (CEN, 2005) and *fib* Model Code 2010 (FÉDÉRATION INTERNATIONALE DU BÉTON (FIB), 2012), i.e. based on the reduction of the acting shear load close to the support. It has been highlighted that such analyses should be used only as a first assessment of structures without stirrups. As such, they are in line with the need for a preprogrammed method for the assessment of a large number of existing RC slab bridges.

The level of accuracy reached by the CSDT with the presented method for arching action and the French model of effective width is similar to that obtained by the CSCT (NATÁRIO; FERNÁNDEZ RUIZ; MUTTONI, 2014), but removes the need for finite element calculations. The proposed CSDT extension excels due to its easy application. The overall V_{exp}/V_{cal} average ratio with the CSDT is 1.06, with a 14.3% coefficient of variation for a set with 141 test results. Comparatively, Natário (2015) achieved a 1.12 V_{exp}/V_{calc} average ratio with 11% COV for simply supported members (62 tests) and 1.07 AVG and 16% COV for cantilever members (27 tests). However, Natário's study did not include continuous members or members with combinations of loads (concentrated loads combined with line loads). The database B0 has 33 tests with loads close to continuous supports. The mean ratio between experimental and predicted shear capacities by the CSDT model with the French effective shear width and β_{prop} is 1.01 with a COV of 11.3%. Therefore, this study comprehends a larger variety of support and

loading conditions. The narrow scatter between experimental and predicted shear capacities with the CSDT demonstrates its accuracy and precision in assessing the one-way shear capacity of wide RC members under concentrated loads, such as slab bridges.

Different from other studies (HALVONIK; VIDAKOVIĆ; VIDA, 2020; REIBEN; HEGGER, 2016), it has been identified that the use of the French approach for determining the effective shear width provides reasonable levels of accuracy combined with the one-way shear strength model based on the CSDT. Regarding studies on simply supported members in which the French model leads to unsafe predictions of the shear strength (HALVONIK; VIDAKOVIĆ; VIDA, 2020; REIBEN; HEGGER, 2016), the presented analysis indicates that these experiments presented signals of punching failures and, therefore, should also be evaluated by two-way shear strength models to reach more precise predictions.

Notably, the CSDT combined with the GESW model provides homogeneous levels of precision in predicting the shear capacity for specimens with one-way and two-way shear failures in the database B0, capturing well the complex transition between these two failure modes. The reason for this observation is that the precision and accuracy of the predictions with the GESW model were similar between different failure modes, shear slenderness, and support conditions. In addition, the level of precision was considerably better than that obtained with current semi-empirical code models (LANTSOGHT et al., 2015d; REIßEN; HEGGER, 2015), for which COVs are usually larger than 35%. Therefore, in a programmed approach of assessment, the CSDT combined with the GESW model may be used as the only model to check shear failures when the governing failure mode is unknown.

4.7 Conclusions of Chapter 4

This study presents an extension of the Critical Shear Displacement Theory model for wide members under concentrated loads. Different databases were used to assess (i) the proposed arching action factor, (ii) the accuracy and precision of the CSDT combined with different models of effective shear width for slabs under single concentrated loads; (iii) the accuracy of the CSDT model to assess members with double concentrated loads parallel to the support and (iv) to assess slabs that showed different failures modes in shear. The following can be concluded:

- The model for improved arching action for non-slender members can be combined with the CSDT as a first step for the determination of their shear strength. This approach was

validated against databases of wide members loaded over the entire width, as well as for slabs under concentrated loads failing in one-way shear.

- The CSDT, combined with the effective width model from the French design guides (FD P 18-717, 2013), provides accurate shear strength results for wide members with predominant one-way shear failure, regardless of the shear slenderness and support conditions. The same level of precision was reached for slabs under double concentrated loads parallel to the support.
- The level of accuracy of the proposed approach based on the CSDT combined with the French effective shear width was higher than that of most design code models, regardless of the parameters analyzed. Since the proposed approach requires only analytical calculations (without finite element analysis), it can easily be implemented in the daily engineering practice for first levels of approximation.
- Despite the simplicity of the French effective width model, it seems to represent well most one-way slabs under concentrated loads that failed in one-way shear (Database B1). However, for members with punching failure, the approach may lead to unsafe predictions of shear strength, as verified in this study. Since the governing failure mode may not be known in preliminary analyses, both failure modes must be checked in the daily engineering practice for higher levels of approximation.
- The most general effective shear width model (GESW) leads to good levels of accuracy for slabs under concentrated loads (Database B0) since it deals with both one-way and two-way shear failures. Moreover, the proposed approach addresses in a novel manner the transition between one-way shear and two-way shear failures of slabs under concentrated loads. However, it should be highlighted that this approach should be used only for preliminary designs and global assessment of a large number of assets, since it does not determine the governing failure mode physically. Apart from that, further studies are required in order to include the effects of other parameters, such as the slab width b in the transition between one-way and two-way shear failures.
- This study shows that traditional models of effective shear width and punching shear do not provide precise predictions of shear strength when the critical failure mode is other than that assumed by the model (Section 5.6). Because of this, adjustments are required on each model to extend the applications of them for both failure modes. In this study, different approaches are shown to assess the shear capacity when the governing failure mode is known or unknown. The proposed approaches apply to wide beams and slabs

under different support conditions (simple, continuous, and cantilever support), different loading conditions (loaded over the entire width or concentrated on the width direction).

5 SHEAR AND PUNCHING CAPACITY PREDICTIONS FOR SLABS UNDER CONCENTRATED LOADS AIDED AND NOT AIDED BY LEFEA

In this chapter, the one-way shear capacity and punching capacity of one-way slabs under concentrated loads are addressed with the same importance. In this context, two approaches are investigated herein to describe the ultimate capacity of such slabs: (i) one based on the combination of analytical expressions with the results from linear elastic finite element analyses, and (ii) one based only on the use of analytical expressions.

5.1 Introduction of Chapter 5

One-way slabs under large concentrated loads are commonly found in practice in bridge deck slabs but may also occur during the building or use of residential and industrial floor slabs. Typically, the one-way shear capacity for such members is checked by assuming that only a slab strip of a width called the effective shear width, contributes to the sectional shear capacity (LANTSOGHT; VAN DER VEEN; WALRAVEN, 2013) (Figure 5-1a). In this approach, the shear forces are assumed as uniformly distributed on the effective shear width. Conversely, the punching capacity predictions are usually performed with the same expressions derived from slab-to-column connections under concentric loads and assuming a uniform distribution of punching shear stresses around the shear-resisting control perimeter (LANTSOGHT et al., 2015d) (Figure 5-1b). In reality, the shear forces are not evenly distributed on the critical sections for one-way shear and punching shear and depend on parameters such as the load position (NATÁRIO; FERNÁNDEZ RUIZ; MUTTONI, 2014) and slab width (SOUSA et al., 2021a). Consequently, if the assumed distribution of shear stresses on the critical sections for shear and punching deviates a lot from the assumed ones in the analytical expressions, inconsistent shear and punching capacity predictions may be found.

Figure 5-1 - General approaches to evaluate the a) one-way shear and b) punching capacity of one-way slabs under concentrated loads.

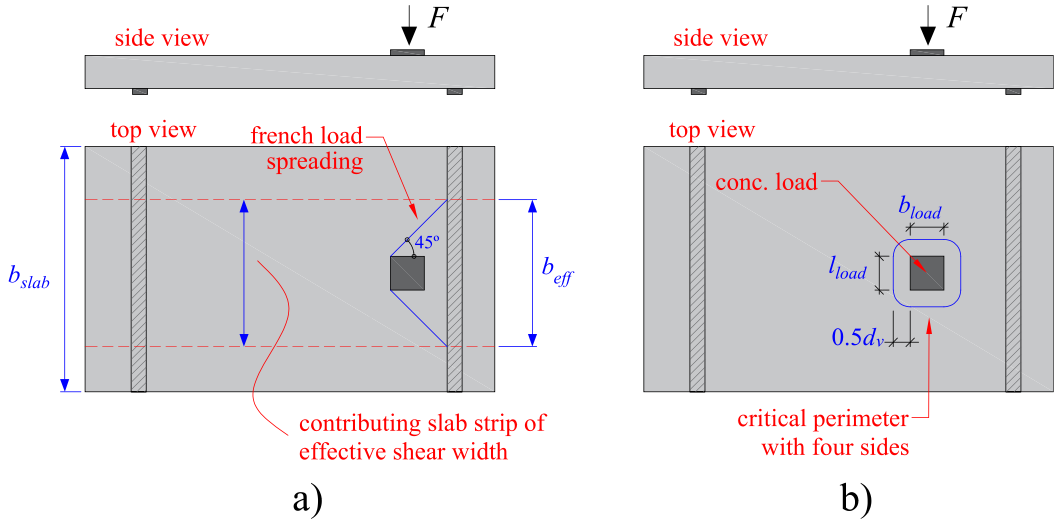

Source: Author.

When evaluating the one-way shear capacity of slabs under concentrated loads, the effective shear width used has a marked influence on the predictions (HALVONIK; VIDAKOVIĆ; VIDA, 2020; LANTSOGHT et al., 2015d). A common approach to predict the effective shear width at failure is based on a horizontal spreading of the load under a 45º angle from the back sides of the load, also called the French effective shear width as it is used in the French guidelines (BUI et al., 2017a; FD P 18-717, 2013) (Figure 5-1a). However, a number of studies have already pointed out some shortcomings related to this approach, which should be considered in the assessment of existing structures (HALVONIK; VIDAKOVIĆ; VIDA, 2020; REIßEN, 2016). While this approach provides good accuracy to predict the sectional shear capacity of slabs under concentrated loads close to the support ($a_v < 2d_l$) (SOUSA et al., 2021c; LANTSOGHT et al., 2015d; LANTSOGHT; VAN DER VEEN; WALRAVEN, 2013), unconservative results may be found for loads further away from the support (HALVONIK; VIDAKOVIĆ; VIDA, 2020; REIßEN, 2016). For instance, the predicted sectional shear capacity may overestimate the sectional shear significantly at failure (HALVONIK; VIDAKOVIĆ; VIDA, 2020; LANTSOGHT et al., 2015d), mainly when the tests fail by punching instead of one-way shear. As a consequence, changes are required in the predicted effective shear width to assure conservative predictions of sectional shear capacity for tests that may be at the transition point to punching shear failure modes, a topic which is seldomly discussed in the literature.

In turn, the punching capacity of one-way slabs under concentrated loads is considerably less discussed than the one-way shear capacity. Until now, most evaluations of the punching

capacity of one-way slabs were performed using only semi-empirical code expressions (LANTSOGHT et al., 2015d; SOUSA; EL DEBS, 2019). These investigations found a large scatter between theoretical and tested resistances, mainly when the tests fail by one-way shear or a transitional shear failure mode instead of punching (LANTSOGHT et al., 2015d).

Natário (2015) presented an interesting approach to assess the shear and punching capacity of one-way slabs under concentrated load. This approach was based on using the Critical Shear Crack Theory (CSCT) expressions for shear and punching and estimating parameters such as the shear force and bending moment distribution based on Linear Elastic Finite Element Analysis (LEFEA). Figure 5-2 shows the results of predictions by Natário (2015) for 48 simply supported slabs using the proposed approach for one-way shear (Figure 5-2a) and for two-way shear (Figure 5-2b) as a function of the clear shear span to effective depth ratio (a_v/d_l). a_v is the clear shear span: distance between edge of support and edge of load. In Figure 5-2, all result values were taken directly from the tables of Natário's dissertation (2015) and presented herein in figure format. V_{test} and $V_{predicted}$ are the maximum sectional shear achieved in the tests and the predicted shear resistance by Natário (2015), respectively; P_{test} and $P_{predicted}$ are the maximum applied concentrated load at failure and the punching capacity predicted by Natário (2015), respectively. In the proposed approach by Natário (2015), the effective shear width b_{eff} for one-way shear and the control perimeter for two-way shear calculations account for the uneven distribution of shear forces in the evaluated sections and regions. The effective shear width, for instance, was calculated by the relation between the total shear force $V_{control}$ (force unit) and an averaged shear force v_{avg} (unit of force per unit length) determined on a specific control section of the slab. Consequently, this approach allows considering the spatial load transfer towards the support and distribution of inner forces in the slab in a more realistic way. These parameters were calculated aided by LEFEA, such as will be described in more detail in the next sections. Figure 5-2a shows that the predictions of one-way shear capacity with the presented approach were precise and conservative (on average) regardless of the failure mode of the tests being wide beam shear (WB), punching (P) or a mixed-mode between wide beam shear and punching shear (WB+P). However, the presented approach presented a small shortcoming in the punching predictions (Figure 5-2b). Figure 5-2b shows that the predictions of punching capacity for the tests that failed as wide beams in shear (WB) are on the unsafe side. At this point, this does not represent a serious problem since, in practice, the one-way shear predictions are governing (more conservative) in the calculations. In other words, the proposed approach by Natário (2015) captures that the concentrated load to

cause a wide beam shear failure is lower than that to cause a punching failure since $V_{test}/V_{predicted}$ is higher than $P_{test}/P_{predicted}$ for such tests. Figure 5-2c shows, for instance, that combining the predictions of one-way shear and punching to identify the most critical strength ratio (SR = max{$V_{test}/V_{predicted}$; $P_{test}/P_{predicted}$}), the proposed approach by Natário (2015) provides safe and precise predictions of the shear capacity. However, it is clear that improvements may be included in the proposed approach for punching calculations to reach a similar performance as for the one-way shear predictions.

Figure 5-2 - Relation between tested and predicted resistances for a) one-way shear; b) punching shear and c) considering the most critical relation (conservative prediction) between the one-way shear and punching shear predictions reported by Natário (2015).

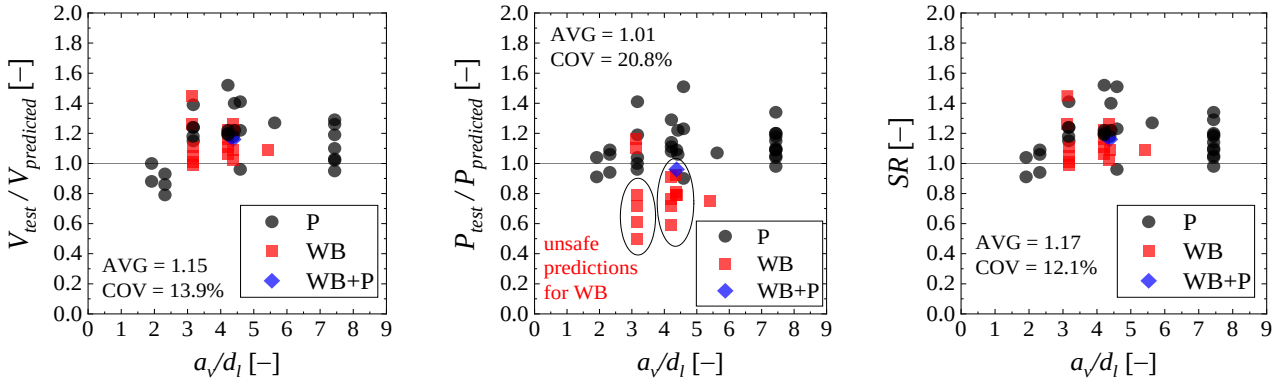

Source: Author.

For a preliminary assessment of slabs, the use of LEFEA is frequently not common. In practice, simplified and conservative calculation models are applied in preliminary evaluations, and LEFEA is used when more precise estimations are required. According to the design philosophy included in the current *fib* Model Code 2010 (FÉDÉRATION INTERNATIONALE DU BÉTON (FIB), 2012), detailed methods could be simplified in a conservative way to allow reaching quick and conservative predictions of resistance. This approach of using simplified and detailed expressions keeping the same theoretical background is also called the "Levels of Approximations Approach," and it was implemented in the shear and punching expressions of the *fib* Model Code 2010 (FÉDÉRATION INTERNATIONALE DU BÉTON (FIB), 2012). In this way, someone could question how to perform simplified estimations of shear and punching capacity for the tests evaluated by Natário (2015) with the CSCT expressions without the use of numerical models, which was not addressed by Natário (2015). In the literature, it was identified that simplified approaches to evaluate the shear capacity of one-way slabs under concentrated loads without accounting for both possible shear failure modes might lead to

unsafe predictions of resistance (HALVONIK; VIDAKOVIĆ; VIDA, 2020; LANTSOGHT et al., 2015d; SOUSA; EL DEBS, 2019). Moreover, most studies focus on evaluating cantilever slabs (HALVONIK; VIDAKOVIĆ; VIDA, 2020; NATÁRIO; FERNÁNDEZ RUIZ; MUTTONI, 2014; ROMBACH; HENZE, 2017; VIDA; HALVONIK, 2018). Therefore, further investigations are required to provide guidelines to assess both shear and punching capacities of simply supported slabs under concentrated loads using only analytical expressions.

In this study, a fully analytical approach is proposed to evaluate the shear and punching capacity of one-way slabs under concentrated loads based on the CSCT expressions. Parameters such as the load position, slab width and load size were considered in the proposed approach. Herein, one of the main novelties in this study compared to other publications is that the relation between the slab width and the load size (b_{slab}/l_{load}) was considered to determine the effective contribution of some sides of the control perimeter to the punching capacity. First, an approach of a higher Level of Approximation (LoA) to predict the shear and punching capacities of such slabs inspired by the work of Natário (2015) is described using LEFEA. This approach uses LEFEA to estimate parameters of the CSCT expressions, such as the bending moment and unitary shear force on the critical sections. In this study, the punching capacity approach of Natário (2015) was enhanced by including parameters related to the slab width and load size. In a next step, it is described how parameters and expressions from the refined approach using LEFEA can be estimated or considered in a simplified approach to predict the shear and punching capacity of the slabs also using the CSCT expressions. In the end, both approaches are compared.

5.2 Research significance of Chapter 5

Nowadays, the use of Linear Elastic Finite Element Analyses (LEFEA) in the design of new structures and assessment of existing structures has become common practice. However, a limited number of studies provide detailed guidelines on how to use this tool together with one-way shear and punching shear expressions. Therefore, this chapter provides detailed guidance on how to use LEFEA to predict the shear and punching capacity of one-way slabs under concentrated loads. In addition, a simplified approach using only analytical expressions is proposed for the preliminary design or assessment of existing structures. Both approaches are based on the Critical Shear Crack Theory expressions, which is based on the mechanics of the shear problem.

5.3 Background

In this section, the following aspects are addressed: (i) the shear flow in one-way slabs under concentrated loads, (ii) the analytical approaches to evaluate the shear and punching capacity and (iii) the calculations related to effective shear width and reduced control perimeter based on LEFEA.

5.3.1 Shear flow

The shear flow of one-way slabs under concentrated loads combines characteristics from the one-way shear in beams and the two-way shear around slab-to-column connections (LANTSOGHT et al., 2015c; NATÁRIO; FERNÁNDEZ RUIZ; MUTTONI, 2014). Beams and slabs loaded over the entire width develop a shear flow predominantly unidirectional, with the flow lines parallel to each other along the slab width. Flat slabs under concentric loads create a shear flow with lines radially distributed around the load. In Figure 5-3a, for the case of one-way slabs under concentrated loads, the shear flow lines are almost parallel in the vicinity of the support, such as for beam shear, while its distributions assume a radial pattern around the load typical from punching (NATÁRIO; FERNÁNDEZ RUIZ; MUTTONI, 2014). Considering the shear flow characteristics, both shear failure modes may take place for such slabs.

5.3.2 Analytical approaches to evaluate the shear and punching capacity

Current approaches to predict the one-way shear capacity of slabs subjected to large concentrated loads are based on the assumption of a horizontal load spreading with a 45º angle to the support for defining the contributing width, commonly called the effective shear width (see Figure 5-3b). Over this length, the unitary shear stresses are assumed as constant. This approach is well spread in the literature since it provided fair approximations of the maximum bending moments at the support of cantilever slabs (FERNÁNDEZ RUIZ; VAZ RODRIGUES; MUTTONI, 2009). However, several works demonstrated that the maximum unitary shear forces at the support could be underestimated with these approaches (FERNÁNDEZ RUIZ; VAZ RODRIGUES; MUTTONI, 2009; HENZE; ROMBACH; HARTER, 2020; NATÁRIO, 2015). Because of this, LEFEA became an interesting tool to estimate a more realistic distribution of shear stresses and bending moments on slabs. The punching capacity calculations using analytical methods are also based on the assumption of even distribution of shear stresses on the control perimeter for punching regardless of the load position in the span (Figure 5-3c.1), where statics lead to nonproportional shear loading on the front and back faces of the loading plate unless the load is placed at midspan. The use of LEFEA allows considering the uneven distribution of shear stresses around the control perimeter (Figure 5-3c.2) and, in

this way, determining a reduced (effective) control perimeter accounting for the load layout and boundary conditions (VAZ RODRIGUES; FERNÁNDEZ RUIZ; MUTTONI, 2008).

Figure 5-3 - Shear flow in a.1) cantilever slabs and a.2) simply supported slabs under symmetrical concentrated loads (adapted from Natário et al. (2014)); b) assumed distribution of shear stresses at the support by analytical models of effective shear width (b.1) and captured by LEFEA (b.2), and c) distribution of shear stresses on the control perimeter for punching assumed in simplified calculations (c.1) and captured by LEFEA (c.2).

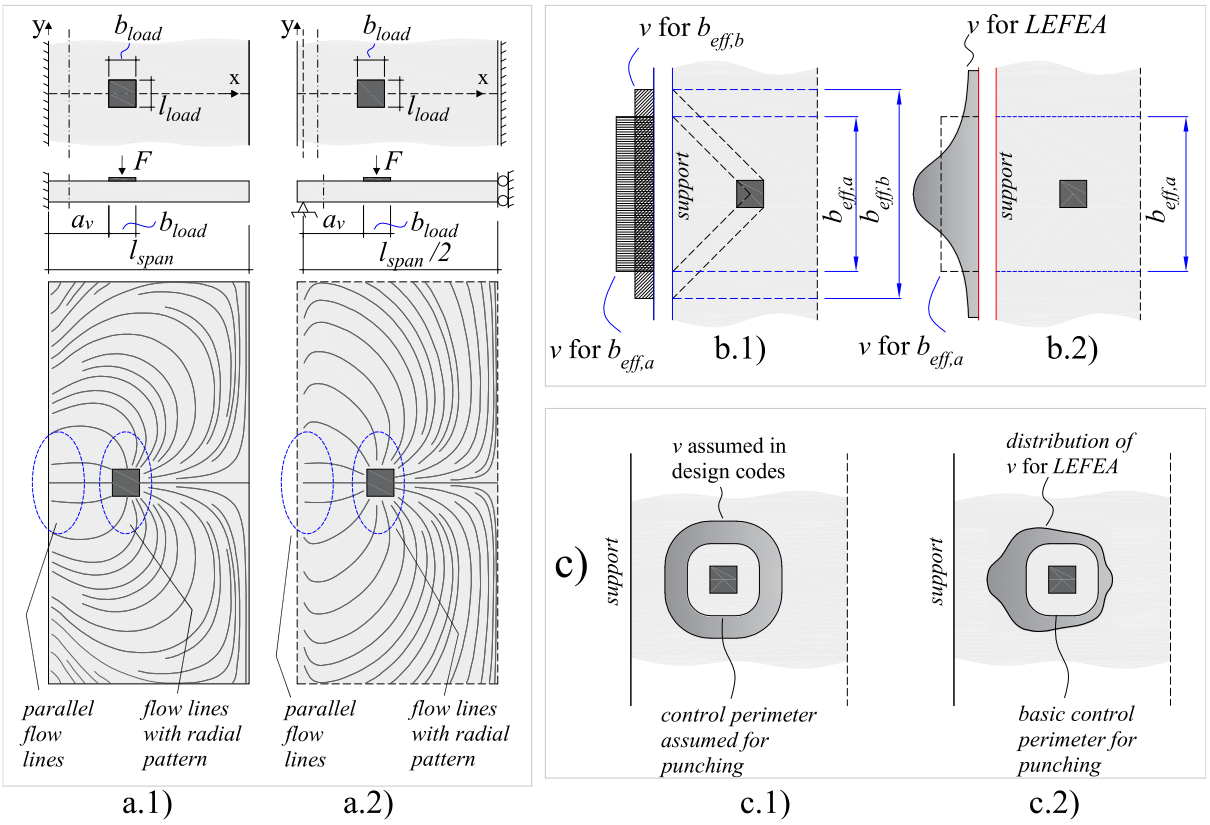

Source: a) adapted from Natário et al. (2014); b) and c) Author.

5.3.3 Effective shear width and reduced control perimeter based on LEFEA

Two groups of approaches can be distinguished when using the LEFEA to evaluate the one-way shear capacity of slabs under concentrated loads: (i) one is based on the definition of an effective shear width as proposed by Goldbeck (1917) to be multiplied by the unitary shear strength; the comparison between load effects and sectional resistances is made in terms of force (NATÁRIO; FERNÁNDEZ RUIZ; MUTTONI, 2014); (ii) others are based on the definition of a distribution width on which the peak shear stress from LEFEA are averaged (rounded/distributed) to be compared to the code-based unitary shear strength (LANTSOGHT; DE BOER; VAN DER VEEN, 2017a); the comparison between load effect and resistances is made in terms of unitary forces or shear stresses.

The effective width is determined based on the stress or force distribution over the member's width v_{perp} (GOLDBECK, 1917; GOLDBECK; SMITH, 1916). The classical definition is that the shear force V due to the maximum shear force $v_{perp,max}$ distributed over the effective width b_{eff} equals the shear force due to the variable stresses v_{perp} over the entire width b_{slab} (LANTSOGHT et al., 2014) (see Figure 5-4a). In other words: $v_{perp,\max} \cdot b_{eff} = \int_0^{b_{slab}} v_{perp} \cdot ds$.

Here, $v_{perp,max}$ is the maximum value of the unitary or nominal shear force (i.e., shear force per unit length along the control section). Some studies proposed distributing the peak shear force over a certain length (calculating v_{avg}) and calculating the effective shear width based on the averaged shear force v_{avg} instead of peak values $v_{perp,max}$. This approach aims to consider possible redistribution of shear force due to concrete cracking (NATÁRIO; FERNÁNDEZ RUIZ; MUTTONI, 2014; REIßEN; CLASSEN; HEGGER, 2018). As b_{eff} increases by decreasing v, the predicted effective shear widths increase with these modified approaches.

Figure 5-4 – a) Definition of the effective shear width based on Goldbeck's studies (GOLDBECK, 1917); b) definition of an effective (reduced) control perimeter based on the uneven distribution of shear stresses around the load (adapted from Fernandez Ruiz, Vaz Rodrigues and Muttoni (2009)).

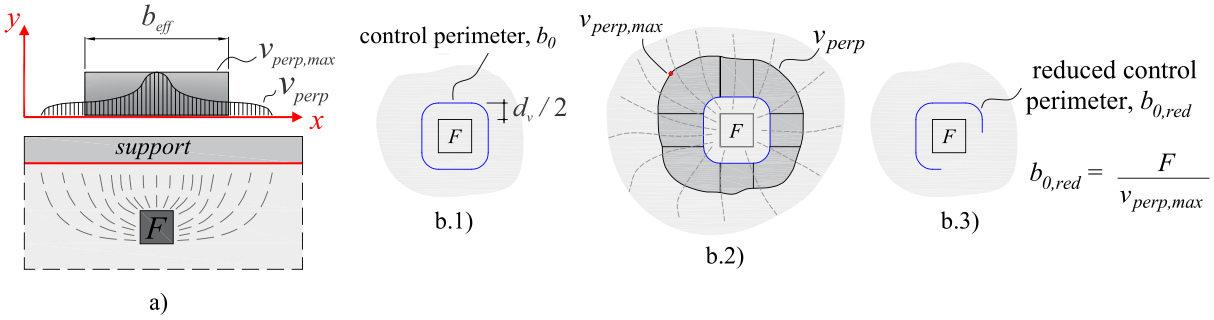

Source: a) Author; b) adapted from Fernandez Ruiz, Vaz Rodrigues and Muttoni (2009).

Lantsoght et al. (2013; 2017b) investigated over which distribution width (slab strip) the peak shear stress from LEFEA should be averaged to represent the test results. In other words, it was investigated over which length the peak shear stress should be averaged to provide the shear stress that could be compared to the code-based shear capacity (LANTSOGHT; DE BOER; VAN DER VEEN, 2017a). In their analyses, the loads corresponding to a certain degree of that reached in the tests (40% and 90%) were applied in the numerical models, and the shear stress distribution was evaluated at the supports. Tests instrumented with load cells at the support were used to assess the distribution of experimental reaction forces. The reaction forces

were converted into shear stresses assuming that the reaction force was uniformly distributed over the influence length of each bearing point. It was concluded that the peak shear stress from LEFEA could be distributed over a length of $4d_l$ to provide precise and still safe predictions of shear capacity for the test results. Posteriorly, Natário (2015) suggested using $4d_l$ as the distribution length to calculate the effective shear width for cantilever slabs and $4d_l + l_{load}$ for simply supported slabs.

For punching, Vaz Rodrigues, Fernandez Ruiz and Muttoni (2008) suggested using a similar approach, based on the effective shear width; to define an effective control perimeter, commonly named reduced control perimeter $b_{0,red}$ (see Figure 5-4b) rounded corners were assumed as suggested by Muttoni (2008) in the CSCT expressions. In practice, using the reduced control perimeter based only on the peak shear demand does not allow considering shear redistribution at failure. This limitation is contoured by evaluating each portion of the control perimeter separately and considering the unequal distribution of shear resistance around the load (SAGASETA et al., 2011). This method is referred to as CSCT ($\psi_x - \psi_y$) (SAGASETA et al., 2011).

While the LEFEA allows a better insight into the distribution of internal forces on the slab (action side), the shear and punching resistances can be predicted based on the CSCT expressions. The CSCT for beam shear and punching shear have some similarities (MUTTONI; FERNANDEZ RUIZ, 2010a). For shear and punching mechanisms, it is assumed that that the unitary shear strength of members without transverse reinforcement is related to the width w and roughness of the critical shear crack, which develops through the inclined compression strut carrying shear (MUTTONI, 2008; MUTTONI; FERNANDEZ RUIZ, 2008). For one-way shear, the opening of the critical shear crack is related to the strains at the control section ε and, hence, of the sectional bending moments m (MUTTONI; FERNANDEZ RUIZ, 2008). For punching, the opening of the critical shear crack w is related to the slab rotation ψ around the load, which is also dependent on the internal moments m around the load (MUTTONI, 2008). In the following sections, more details are given regarding the calculations using the CSCT expressions for shear and punching.

5.4 Proposed refined approach: coupling LEFEA and CSCT expressions

In this section, the calculations of the refined approach are detailed for (i) one-way shear capacity predictions and (ii) punching shear capacity predictions.

5.4.1 Refined approach for one-way shear analyses

The one-way shear capacity of the slabs was calculated according to the Critical Shear Crack Theory developed by Muttoni and Schwartz (1991) and modified by Muttoni and Fernandez Ruiz (2008). The principle of this theory is that the flexural shear strength is governed by a flexural crack which develops diagonally (the critical shear crack) and disturbs the shear transfer actions. The main shear transfer mechanisms of slender beams according to the CSCT are (MUTTONI; FERNANDEZ RUIZ, 2008): (i) compression chord capacity or cantilever action (KANI, 1964), (ii) aggregate interlock (WALRAVEN, 1981) and (iii) dowel action (DULACSKA, 1972; TAYLOR, 1969). According to this model, the one-way shear capacity $V_{R,CSCT}$ depends on the sectional geometry, the concrete compressive strength, the critical shear crack width w_{cr} and the crack's roughness. The roughness is assumed as related to the aggregate size d_g (VECCHIO; COLLINS, 1986), while the crack width w_{cr} is supposed to be proportional to the reference longitudinal strain ε times the effective depth of the member d_l. The reference longitudinal strain ε is evaluated in the control section at a depth of $0.6d_l$ from the compression face, assuming that plane sections remain plane and neglecting the tensile strength of the concrete (which is assumed to behave linear elastically in compression). The depth of $0.6d_l$ is defined as the position on which the width of the critical shear crack is adequately represented. In the absence of external normal forces, the reference strain ε at the control depth and height of the compression zone c_{flex} are given by (MUTTONI; FERNANDEZ RUIZ, 2008) (SI units; d_l in m; m_{max} in kN/m):

$$c_{flex} = d_l \cdot \rho_l \cdot \frac{E_s}{E_c} \cdot \left(\sqrt{1 + \frac{2 \cdot E_c}{\rho_l \cdot E_s}} - 1 \right) \tag{5.1}$$

$$\varepsilon = \frac{m_{max}}{b_w \cdot d_l \cdot \rho_l \cdot E_s \cdot \left(d_l - c_{flex} / 3 \right)} \cdot \frac{0.6 \cdot d_l - c_{flex}}{d_l - c_{flex}} \tag{5.2}$$

where m_{max} is the maximum bending moment at the control section for a given applied load, ρ_l is the flexural reinforcement ratio, E_c is the elastic modulus of concrete, E_s is the elastic modulus of steel and c_{flex} is the height of the compression zone in the cross-section. In this way, the unitary shear capacity $v_{R,shear}$ or failure criterion is calculated as (SI units: f_c in MPa; d_g in mm):

$$v_{R,shear} = \frac{d_l \cdot \sqrt{f_c}}{3} \cdot \frac{1}{1+120 \cdot \frac{\varepsilon \cdot d_l}{16+d_g}} \quad (5.3)$$

where d_g is the measured maximum aggregate size if f_c < 60 MPa and 0 if higher. The one-way shear capacity is calculated by combining the predicted unitary shear strength $v_{R,shear}$ with an effective shear width b_{eff} (derived from LEFEA with shell elements) and accounting for some influence of arching action in the one-way shear resistance for concentrated loads close to the support by β_{shear}:

$$V_{R,CSCT} = \frac{v_{R,shear} \cdot b_{eff}}{\beta_{shear}} \quad (5.4)$$

In this approach, the parameters that need to be evaluated in the numerical models are the distribution of unitary shear forces v (to calculate v_{avg} and b_{eff}), unitary bending moments m (to calculate m_{max}) and the total shear force going through the control section $V_{control}$ (Figure 5-5 – to calculate b_{eff}) for a given applied load. Alternatively, $V_{control}$ can be directly determined from beam statics. Further details on the numerical models will be given in the next sections.

The effective shear width b_{eff} is calculated by dividing the total shear force going through the evaluated direction along the slab width ($V_{control}$) by an averaged unitary shear force over the control sections v_{avg} (BELLETTI et al., 2015; NATÁRIO; FERNÁNDEZ RUIZ; MUTTONI, 2014) determined with the finite element model (Eq. (5.5)). To be consistent with the CSCT principles, the control section to calculate the averaged unitary shear forces and the maximum bending moments is placed at $0.5d_l$ from the edge of the support on cantilever slabs and at $0.5d_l$ from the face of the load for simply supported slabs (Figure 5-5a). The length of the control section (distribution width) over which v is averaged to calculate v_{avg} is assumed $4d_l$ for cantilever slabs and $4d_l + l_{load}$ for simply supported slabs (Figure 5-5). In other words, it is used a distribution width to calculate an averaged shear force v_{avg} and the effective shear width b_{eff} is calculated based on v_{avg}:

$$b_{eff} = \frac{V_{control}}{v_{avg}} \quad (5.5)$$

The arching action that takes place for loads close to the support, which increases the one-way shear resistance for such conditions, is accounted for by β_{shear} (NATÁRIO, 2015) (Equation (6)). At this point, however, it shall be remembered that the CSCT was derived

assuming flexural-shear failures and that the β_{shear} is only a simplification to allow estimating the enhanced resistance in the case of possible shear-compression failures.

$$\beta_{shear} = \frac{a_v}{2.75 \cdot d_l}, \text{ with } d_l \le a_v \le 2.75 d_l \tag{5.6}$$

The shear and moment-related redistribution due to cracking is accounted for in the numerical models by assuming a Poisson ratio μ = 0 and a reduced shear modulus (G_c = E_c/16)(NATÁRIO; FERNÁNDEZ RUIZ; MUTTONI, 2014; SAGASETA et al., 2014). For slabs influenced by arching action (loads close to the support), using b_{eff} allows to include the effect of the arching action in the load portion from F that is transferred directly to the support. Conversely, for slabs subjected to a load further away from the support, the use of b_{eff} could be suppressed. For such cases, someone could simply compare the design load F_{Ed} with the calculated load that causes a one-way shear failure $F_{predicted}$.

Figure 5-5 - Control section location and averaged shear force v_{avg} definition for a) simply supported slabs and b) cantilever slabs. Adapted from Natário (2015).

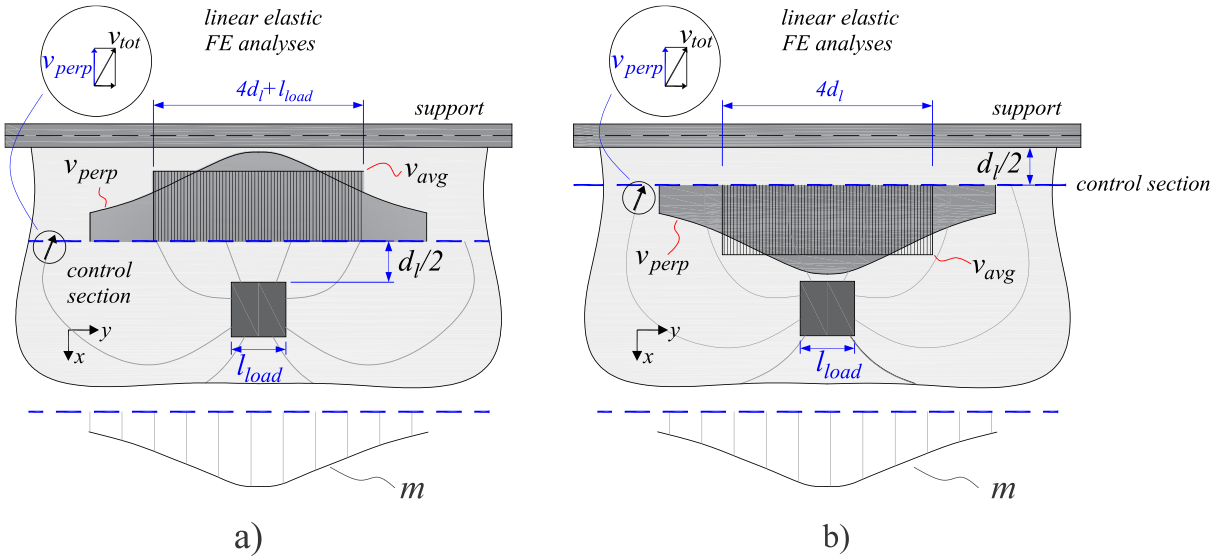

Source: Adapted from Natário (2015).

Figure 5-6a shows the flowchart of calculations performed combining LEFEA outputs with the CSCT shear expressions. Firstly, a unitary force F_{hyp} = 1 kN is applied to the numerical model to compute the averaged shear force $v_{avg,1kN}$ and the maximum bending moments $m_{max,1kN}$ over the control section. Then, the effective shear width b_{eff} is calculated according to Eq. (5.5) and Figure 5-5. In the end, a subroutine is used to find the applied concentrated load $F_{hyp,i}$ iteratively that equals the unitary shear resistance $v_{R,i}$ with the average shear demand $v_{avg,i}$ over the control section (see Figure 5-6b). When the iterative process ends, the one-way shear

capacity (in force units) V_R is calculated, accounting for the effective shear width b_{eff} and the arching action for loads close to the support (a_v < 2.75 d_l). With this procedure, the externally applied load ($F_{predicted}$) that causes the sectional shear failure and one-way shear resistance ($V_{R,CSCT}$) are predicted. $F_{predicted}$ is the last value of $F_{hyp,i}$ in the iterative process that makes $v_{R,i}$ is equal to $v_{avg,i}$. At this point, it shall be noted that the value of b_{eff} is calculated only once with the numerical model and that the unitary shear resistance can be calculated iteratively by any other software.

Figure 5-6 – a) Flowchart of the main steps for evaluating the one-way shear resistance following CSCT; b) Sketch of the iterative process combining the shear demand v_{avg} and shear resistance v_R.

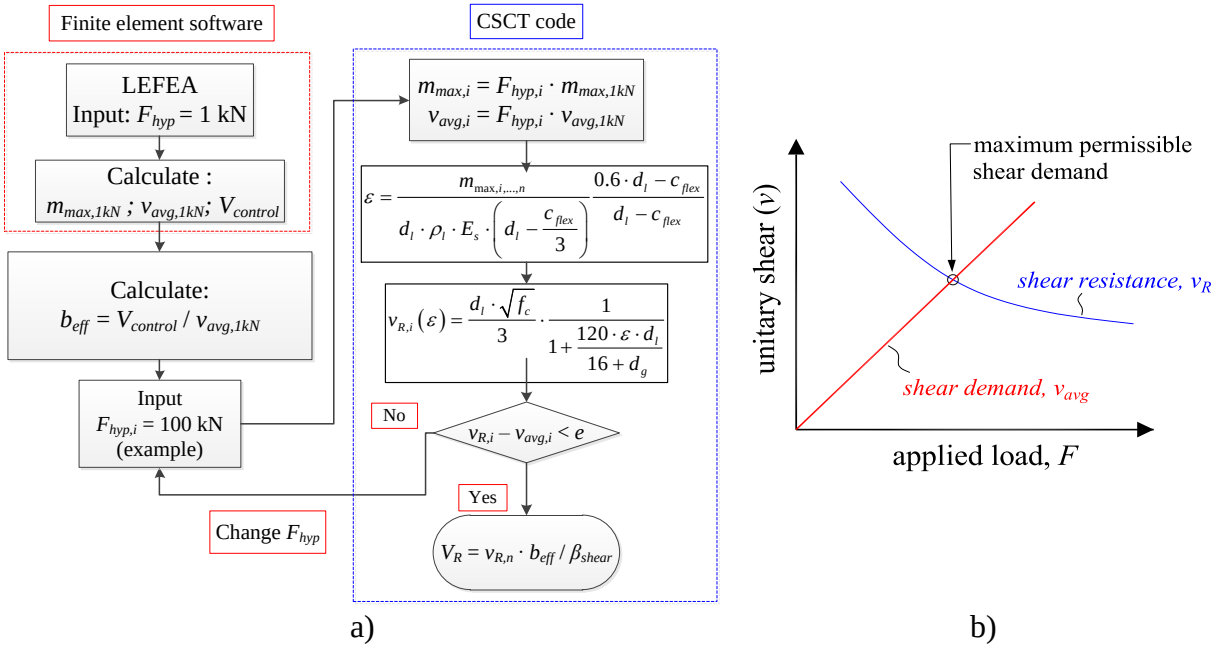

Source: a) Adapted from Belletti et al. (2015); b) Author.

Since the relation between the applied load and the sectional shear force depends only on the load position and support layout, the comparison between tested and predicted resistances could be performed directly in terms of the applied concentrated loads in the tests F_{test} and the predicted value $F_{predicted}$. In other words, for loads that are not influenced by arching action, the comparison between the tested and predicted failure loads ($F_{test}/F_{predicted}$) equals the ratio between tested and predicted shear resistances ($V_{test}/V_{predicted}$). Therefore, for such cases, the calculation of the effective shear width would not be necessary. In this study, however, the effective shear width was calculated for all tests as a way to include the influence of arching action when applicable, as recommended by Natário (2015).

5.4.2 Refined approach for two-way shear analyses

The punching shear capacity is assessed by the CSCT ($\psi_x - \psi_y$) method (SAGASETA et al., 2011, 2014) inspired by the work of Natário (2015) with some small changes. In this method, the control perimeter is placed at $d_v/2$ from the load edges, where d_v is the mean depth of the flexural reinforcement in both directions. The CSCT expressions for punching shear assume that increasing the width of the critical shear crack w_{cr} reduces the strength of the compression strut carrying shear around the loaded area (MUTTONI; SCHWARTZ, 1991). The width of the critical shear crack w_{cr} is assumed proportional to the product between the slab rotation ψ and the effective depth of the reinforcement d_v (MUTTONI, 2008; MUTTONI; SCHWARTZ, 1991).

The CSCT considers the shear redistribution around the loaded area in a simplified way. In this method, the slab rotations depend on the considered direction and are uneven along the control perimeter, meaning that some parts of the slab reach their ultimate strength while others still have a potential strength capacity (NATÁRIO, 2015; SAGASETA et al., 2011, 2014). The control perimeter is usually divided into four segments assuming constant rotations ψ_x-ψ_y and unitary strengths $v_{R,x}$-$v_{R,y}$ for each segment. The control perimeter without round corners was adopted in the refined approach to simplify the post-processing of the numerical results. The punching shear strength is given by:

$$V_R = v_{R,x1} \cdot b_{0,x1} + v_{R,x2} \cdot b_{0,x2} + v_{R,y1} \cdot b_{0,y1} + v_{R,y2} \cdot b_{0,y2} \tag{5.7}$$

where $b_{0,ij}$ are defined in Figure 5-7 (i refer to the directions evaluated, direction x or y, and j refer to the side of the control perimeter in the evaluated direction, sides 1 or 2); the unitary/nominal shear strength in each segment $v_{R,ij}$ is calculated as (FÉDÉRATION INTERNATIONALE DU BÉTON (FIB), 2012) (SI units: f_c in MPa; d_g in mm):

$$v_{R,ij} = \frac{(3/4) \cdot d_v \cdot \sqrt{f_c}}{1 + 15 \cdot \left[\psi_{ij} \cdot d_v / \left(d_g + d_{g0} \right) \right]} \tag{5.8}$$

$$d_{g0} = \begin{cases} 16, \text{ if } f_c < 70MPa \\ 0, \text{ if } f_c \geq 70MPa \end{cases} \tag{5.9}$$

The rotations ψ_{ij} in each side of the control perimeter were calculated according to Level of Approximation III from the *fib* Model Code provisions (FÉDÉRATION

INTERNATIONALE DU BÉTON (FIB), 2012), which are based on the CSCT (MUTTONI, 2008). In each segment of the control perimeter, the rotation was calculated as:

$$\psi_{ij} = 1.2 \cdot \frac{r_{s,ij}}{d_i} \cdot \frac{f_{yi}}{E_s} \cdot \left(\frac{m_{s,ij}}{m_{R,i}} \right)^{3/2} \tag{5.10}$$

$$m_{s,ij} = \frac{1}{b_s} \cdot \int_{-b_s/2}^{+b_s/2} \left| m_{ij} \right| \cdot di \quad i \perp j$$

$$m_{s,x1} = \frac{1}{b_s} \cdot \int_{-b_s/2}^{+b_s/2} m_{x1} \cdot dy \; ; \; m_{s,x2} = \frac{1}{b_s} \cdot \int_{-b_s/2}^{+b_s/2} m_{x2} \cdot dy \; ; \; m_{s,y1} = \frac{1}{b_s} \cdot \int_{-b_s/2}^{+b_s/2} m_{y1} \cdot dx \; ; \; m_{s,y2} = \frac{1}{b_s} \cdot \int_{-b_s/2}^{+b_s/2} m_{y,2} \cdot dx \tag{5.11}$$

Natário (2015) explains that $r_{s,ij}$ is the distance between the center of the concentrated load and the point where the acting unitary bending moment in the direction of the relevant reinforcement is zero (Figure 5-7a), d_i is the effective flexural depth in the appropriate direction, f_{yi} is the steel yielding stress, E_s is Young's modulus of steel, $m_{s,ij}$ is the averaged acting bending moment at the loading plate edge ij within the width b_s (Figure 5-7c) and $m_{R,i}$ is the yielding moment per unit length in the evaluated direction. The support strip width b_s is calculated as:

$$b_s = \min \left\{ 1.5 \cdot \sqrt{r_{s,ij} \cdot r_{s,ji}} \right\} \quad i \perp j \tag{5.12}$$

Figure 5-7 - Definition of (a) rsi distances; b) reduced control perimeters for square loads; and c) averaged acting bending moments at the edges of the concentrated load and support strip widths. Adapted from Natário (2015).

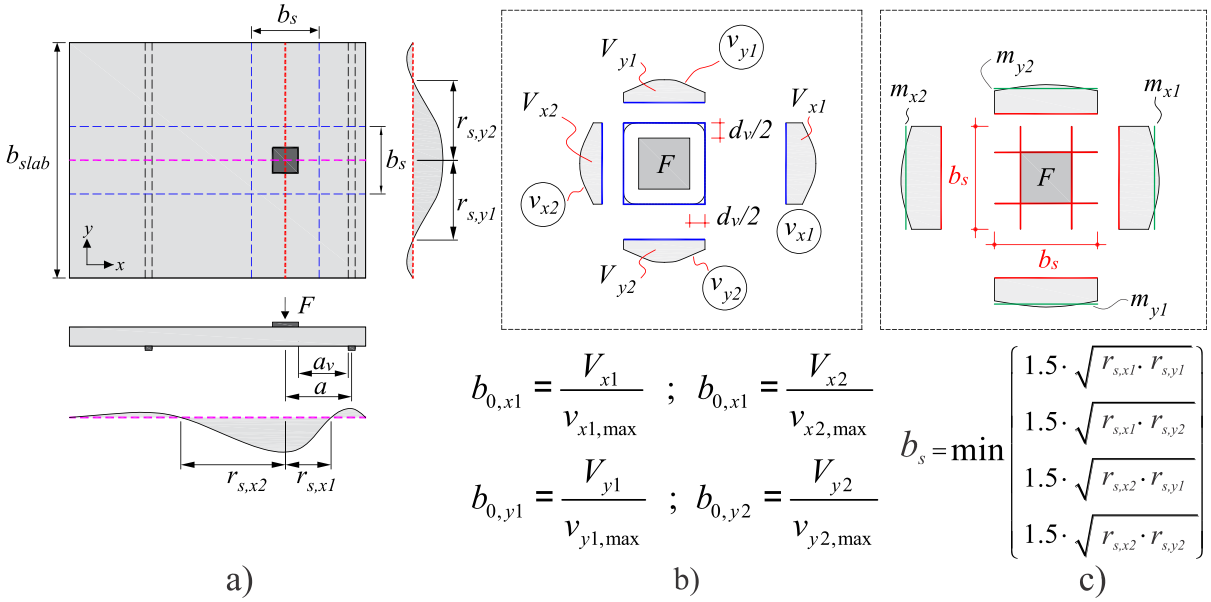

Source: Adapted from Natário (2015).

The length of each segment of the control perimeter ($b_{0,x1}$, $b_{0,x2}$, $b_{0,y1}$ and $b_{0,y2}$), calculated without rounded corners as in Natário (2015), was given by the ratio between the maximum applied unitary shear force perpendicular to the control perimeter ($v_{x1,max}$, $v_{x2,max}$, $v_{y1,max}$ and $v_{y2,max}$,) and the total shear force going through that perimeter (V_{x1},V_{x2},V_{y1},V_{y2}) (Figure 5-7b).

Figure 5-8 – a) Flowchart of the main steps for the evaluation of the punching capacity with the CSCT ($\psi_x - \psi_y$) method; b) Sketch of how the punching capacity is determined in the iterative process.

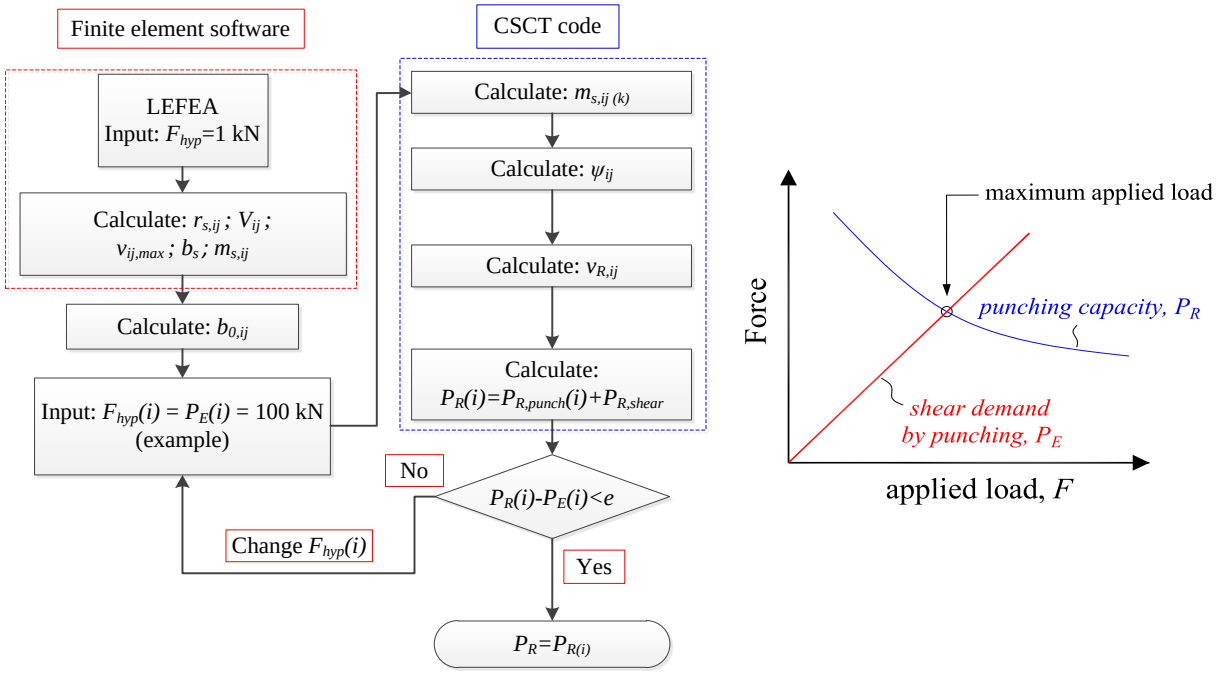

Source: Author.

Figure 5-8 shows the main steps to predict the punching shear capacity of slabs coupling LEFEA with the CSCT model for non-axis-symmetrical punching (SAGASETA et al., 2014). First, a LEFEA is carried out to compute the distribution of shear forces ($v_{ij,max}$ = $v_{x1,max}$, $v_{x2,max}$, $v_{y1,max}$, $v_{y2,max}$) and averaged bending moments ($m_{s,ij}$ = m_{x1}, m_{x2}, m_{y1}, m_{y2}) over the control sections for an applied load equals 1 kN. At this step, the total shear force on each portion of the control perimeter (V_{x1} , V_{x2} , V_{y1} and V_{y2}) and the slab strip width b_s shall also be calculated. Afterwards, the reduced control perimeter segments $b_{0,ij}$ are calculated for each side of the control perimeter. These values are entered as input in a subroutine that calculates iteratively the punching load $P_E(i)$ that is equal to the punching resistance $P_R(i)$. Notably, the number of outputs of the LEFEA is higher than that required for one-way shear since control perimeter segments are applied.

A factor was derived by linear regression analyses to avoid overly unsafe predictions of punching capacity for the tests that failed as wide beams in shear (WB) highlighted in Figure 5-2b. Due to the shear flow characteristics of one-way slabs, a smaller portion of the load is transferred by the lateral sides of the control perimeter when the slab width is small (see Figure 5-9). As a consequence, these sides of the control perimeter may have a small contribution to the punching capacity for small values of b_{slab}/l_{load}. The influence of the ratio slab width-to-load size into the effective contribution of the sides of the control perimeter to the punching capacity (see Figure 5-9) was not considered by Natário (2015) and is considered herein by multiplying the punching resistance $V_{R,y1}$ and $V_{R,y2}$ by a factor CF_{width}. This factor was derived assuming that the factor should vary between 0 and 1 and that the contribution of the lateral sides of the control perimeter increase by a square polynomial function. The constants of the polynomial function were adjusted to improve the predictions of punching capacity for a larger dataset of one-way slabs under concentrated loads presented by Sousa et al. (2021c).

$$CF_{width} = \begin{cases} 1, \text{ if } b_{slab}/l_{load} > 12.5 \\ 0.0016 \cdot \left(b_{slab}/l_{load}\right)^2 + 0.065 \cdot \left(b_{slab}/l_{load}\right) - 0.0666, \text{if } 1 \le b_{slab}/l_{load} \le 12.5 \end{cases} \quad (5.13)$$

Figure 5-9 - Influence of the ratio b_{slab}/l_{load} on the shear flow crossing the sides of the control perimeter parallel to the free edges.

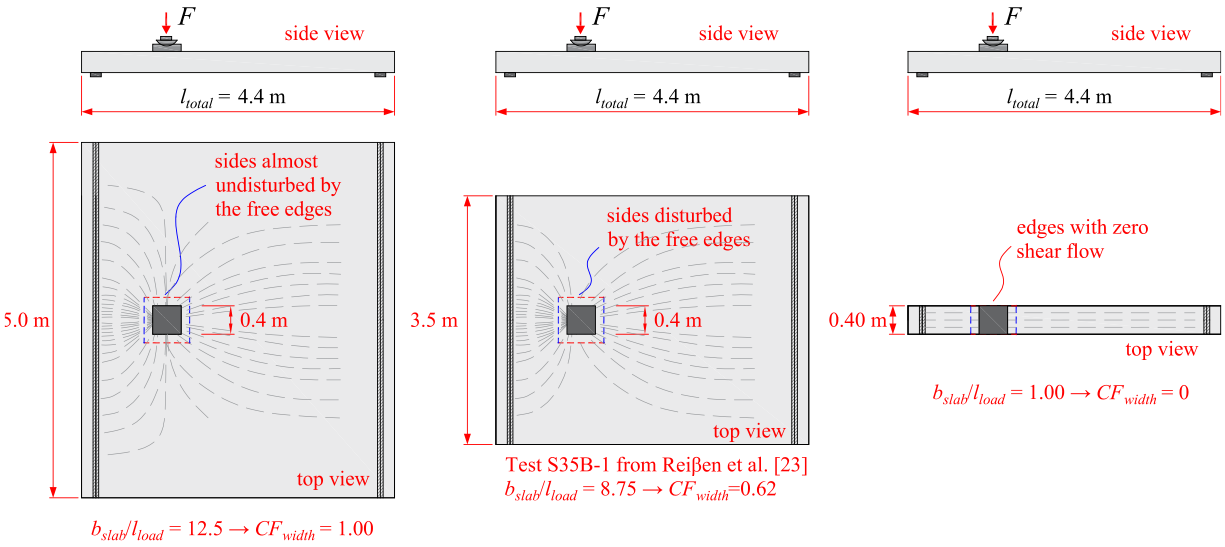

Source: Author.

Therefore, the following calculations are used to compute the contribution of each side of the control perimeter into the punching capacity (SI units: f_c in MPa; d_g in mm):

$$V_{R,x1} = \frac{(3/4)\cdot d_v \cdot \sqrt{f_c}}{1+15\cdot\left[\psi_{x1}\cdot d_v/\left(d_g+d_{g0}\right)\right]}\cdot b_{0,x1} \quad (5.14)$$

$$V_{R,x2} = \frac{(3/4)\cdot d_v \cdot \sqrt{f_c}}{1+15\cdot\left[\psi_{x2}\cdot d_v/\left(d_g+d_{g0}\right)\right]}\cdot b_{0,x2} \quad (5.15)$$

$$V_{R,y1} = \frac{(3/4)\cdot d_v \cdot \sqrt{f_c}}{1+15\cdot\left[\psi_{y1}\cdot d_v/\left(d_g+d_{g0}\right)\right]}\cdot b_{0,y1}\cdot CF_{width} \quad (5.16)$$

$$V_{R,y2} = \frac{(3/4)\cdot d_v \cdot \sqrt{f_c}}{1+15\cdot\left[\psi_{y2}\cdot d_v/\left(d_g+d_{g0}\right)\right]}\cdot b_{0,y2}\cdot CF_{width} \quad (5.17)$$

The punching capacity for square loads or not elongated (rectangular) loads ($l_{load} < 3d_v$ and $b_{load} < 3d_v$) is then given by the sum of the capacities of the perimeter segments:

$$P_{R,punch} = V_{R,x1} + V_{R,x2} + V_{R,y1} + V_{R,y2} \quad (5.18)$$

Slabs subjected to elongated loads develop some particular characteristics that need to be considered. The shear flow assumes a radial pattern in the corners, with a high concentration of shear flow in these regions. Conversely, the shear flow in the elongated sides has lines almost parallel to each other with lower demand in this region (Figure 5-10a). Following the approach proposed by Natário (2015) and inspired by the works from Sagaseta et al. (2014), the contribution of the control perimeter in the corners is calculated by the two-way shear expressions ($P_{R,puch}$). In Natário's approach, the same expressions to calculate the one-way shear capacity of such slabs were used in the region with one-way shear behavior, which increased the post-processing effort of the numerical models. In this study, a simplification was performed on this part of the calculations based on the work from Setiawan et al. (2020).

When the loaded area is elongated on one of the sides ($l_{load} > 3d_v$ or $b_{load} > 3d_v$), the contribution of the elongated sides not included in the computation of $b_{0,x1}$, $b_{0,x2}$, $b_{0,y1}$ and $b_{0,y2}$ shall be considered assuming a one-way shear behavior for such lengths (blue lines in Figure 5-10b). These limits to define the regions considered with two-way shear behavior or one-way shear behavior are based on the current *fib* Model Code 2010 (FÉDÉRATION INTERNATIONALE DU BÉTON (FIB), 2012). However, the control perimeter herein was defined without rounded corners to simplify the post-processing of the numerical models. In practice, four sides of the load can be higher than $3d_v$ and the shape of the load be square, but the idea remains similar to that applied for elongated loads.

Figure 5-10 – a) Sketch of distribution of nominal shear forces along the control perimeter of elongated loads (assuming only two sides > 3d_v) with the concentration of shear forces at the corners; b) lengths of the sides of the control perimeter with two-way shear and one-way shear (control perimeter without rounded corners used in the calculations); c) sketch of the areas that shall be integrated to determine the shear force distribution around the control perimeter.

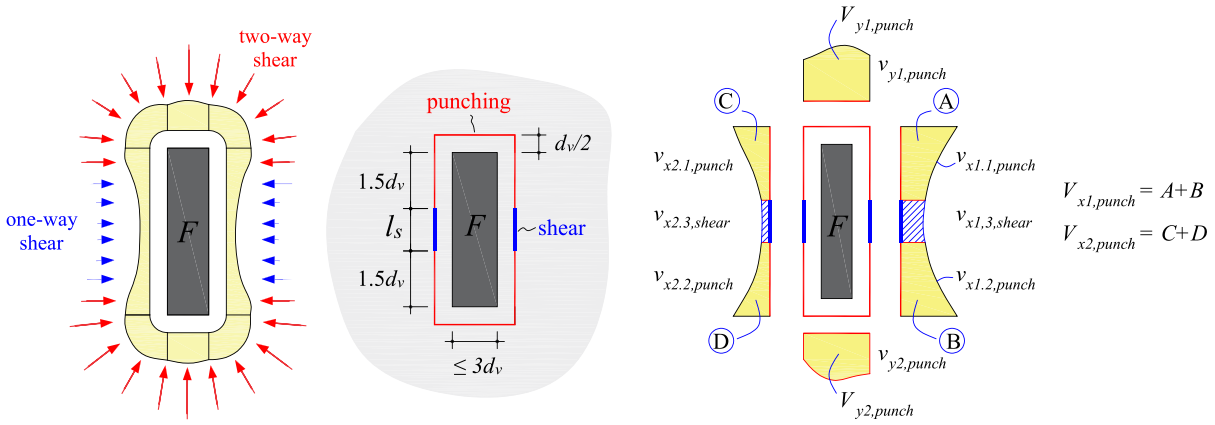

Source: Author.

In this study, the contribution of the sides l_s (Figure 5-10b) is computed according to Setiawan et al. (SETIAWAN et al., 2020) and Cavagnis, Fernández Ruiz and Muttoni (2018a) (assuming only two sides of the load larger than 3d_v):

$$P_{R,shear} = v_{c,\min} \cdot (2 \cdot l_s) = \frac{k \cdot d_v \cdot \sqrt{f_c}}{\sqrt{\varepsilon_y \cdot \frac{d_v}{d_{dg}}}} \cdot (2 \cdot l_s) \qquad (5.19)$$

Herein, $v_{c,min}$ is the minimum shear resistance per unit length (assuming reinforcement yielding), k = 0.019, ε_y = is the flexural reinforcement yield strain (= 0.0025), l_s is the length of the sides assumed with one-way shear behavior (Figure 5-10), and d_{dg} is the parameter that considerers the crack roughness, which is calculated as follows (SI units: f_c in MPa; d_g in mm):

$$\begin{aligned} d_{dg} &= \min(40\text{ mm}, 16 + d_g) \text{ for } f_c \le 60 MPa \\ d_{dg} &= \min\left(40\text{ mm}, 16 + d_g \cdot \left(\frac{60}{f_c}\right)^2\right) \text{ for } f_c > 60 MPa \end{aligned} \qquad (5.20)$$

The total punching capacity for elongated loads is given by:

$$P_{predicted} = P_{R,\,punching} + P_{R,shear} \tag{5.21}$$

5.5 Proposed approach for simplified calculations

In this section, the calculations of the simplified approach are detailed for (i) one-way shear capacity predictions and (ii) punching shear capacity predictions.

5.5.1 Proposed analytical approach for one-way shear predictions

The one-way shear resistance v_R was calculated with the same expressions described previously in the refined approach, assuming a beam behavior to determine the relation between F_{hyp}, m_i and v_i. In practice, this means using a static system of a beam with a unitary width to compute the unitary bending moments and shear forces assumed constant along this length. After defining the unitary shear resistance in the iterative process (Figure 5-6), the predicted sectional shear resistance is found multiplying the calculated unitary resistance by the predicted effective shear width.

As identified in previous studies (SOUSA et al., 2021c; LANTSOGHT; VAN DER VEEN; WALRAVEN, 2013), the French effective shear width ($b_{eff,french}$) works reasonably well when the governing failure mechanism is one-way shear. This occurs mainly when the load is placed at positions with a_v/d_l lower lower than 2.75 (the region that may benefit from arching action). Herein, a_v/d_l is the clear shear span to effective depth ratios. However, for thin slabs and slabs under a concentrated load far away from the support (a_v/d_l > 2.75), the predicted effective shear width with this approach may overestimate the one-way shear capacity (SOUSA et al., 2021c; HALVONIK; VIDAKOVIĆ; VIDA, 2020). This commonly occurs when the governing shear failure mode is punching instead of one-way shear. To solve this issue, this study proposes to use a modified effective shear width according to the clear shear span to depth ratio (a_v/d_l):

$$\begin{aligned} b_{eff\,,\,french} &= l_{load} + 2\cdot\left(b_{load} + a_v\right) \le b_{slab} \\ CF_{shear} &= 0.1143\cdot a_v / d_l + 1.3143 \le 1 \\ b_{eff\,,\,proposed} &= b_{eff\,,\,french}\cdot CF_{shear} \begin{cases} \le b_{slab} \\ \ge l_{load} + d_l \end{cases} \end{aligned} \tag{5.22}$$

In this approach, the predicted effective shear width $b_{eff,proposed}$ decreases for large distances of the load to the support. Herein, it is assumed that when the shear transfer is not benefited from arching action (a_v/d_l > 2.75), the predicted effective shear width should be adjusted.

Figure 5-11a shows a sketch of the practical effect of CF_{shear} according to the load position. Moreover, Figure 5-11b shows the cracking pattern of tests performed by Reiβen (2016), which clearly indicates a change of governing failure mechanism by varying the load position and, hence, the clear shear span to effective depth ratio a_v/d_l.

Figure 5-11 - Modified effective shear width according to the ratio a_v/d_l and b) cracking pattern of tests from Reißen, Classen and Hegger (2018) varying the load position and that developed different failure shear mechanisms.

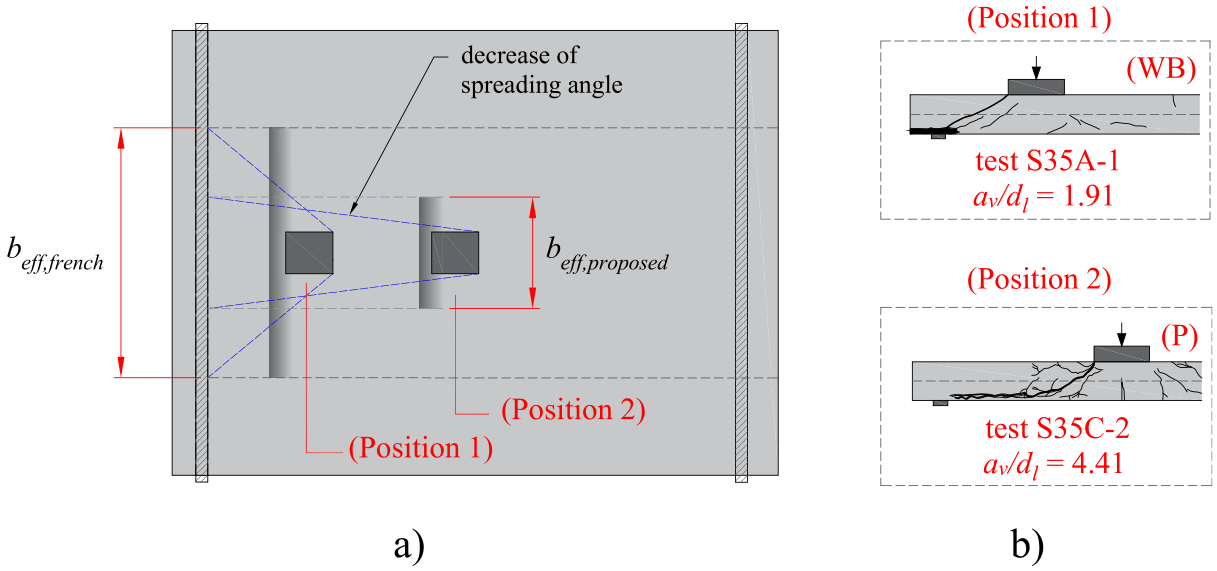

Source: Author.

5.5.2 Proposed analytical approach for two-way shear predictions

To allow a simplified estimation of the rotations without the use of LEFEA, it is proposed in this study to use expressions based on the ratio between the applied concentrated load P and the flexural resistance P_{flex} estimated by yield line analyses. The expressions used to compute the rotations around the loaded area of simply supported slabs are:

$$\psi_{x1} = 1.2 \cdot \frac{a}{d_l} \cdot \frac{f_{yl}}{E_s} \cdot \left(\frac{P}{P_{flex}} \right)^{3/2}$$

$$\psi_{x2} = 1.2 \cdot \frac{\left(l_{span} - a \right)}{d_l} \cdot \frac{f_{yl}}{E_s} \cdot \left(\frac{P}{P_{flex}} \right)^{3/2} \qquad (5.23)$$

$$\psi_{y1} = \psi_{y2} = 1.2 \cdot \frac{\left(b_{slab} / 2 \right)}{d_t} \cdot \frac{f_{yt}}{E_s} \cdot \left(\frac{P}{P_{flex}} \right)^{3/2}$$

For a conservative prediction, the maximum rotation computed shall be used (ψ_{max}). In the proposed approach, the punching-resisting control perimeter is calculated without rounded corners (to allow a fair comparison with the approach based on LEFEA) and without any

reduction due to the distribution of shear stresses on the perimeter (Figure 5-7b). Therefore, the sides of the control perimeter are calculated as:

$$b_{0,x1} = b_{0,x2} = \min\{l_{load}; 3 \cdot d_v\} + 1 \cdot d_v$$
$$b_{0,y1} = b_{0,y2} = \min\{b_{load}; 3 \cdot d_v\} + 1 \cdot d_v \quad (5.24)$$

Three yield line mechanisms, suggested by Belletti et al. (2014), were evaluated to predict the flexural capacity of slabs under concentrated loads P_{flex} (Figure 5-12). A comparison between tested and predicted flexural capacities of slabs under concentrated loads using these yield lines was performed previously. Mechanism 1 (with the yield line extending across the whole slab width) provided the best fit with the experimental results. Therefore, the flexural capacity of the slabs was predicted by the following expression:

Figure 5-12 - Yield line mechanisms for simply supported slabs under CL based on Belletti et al. (2014).

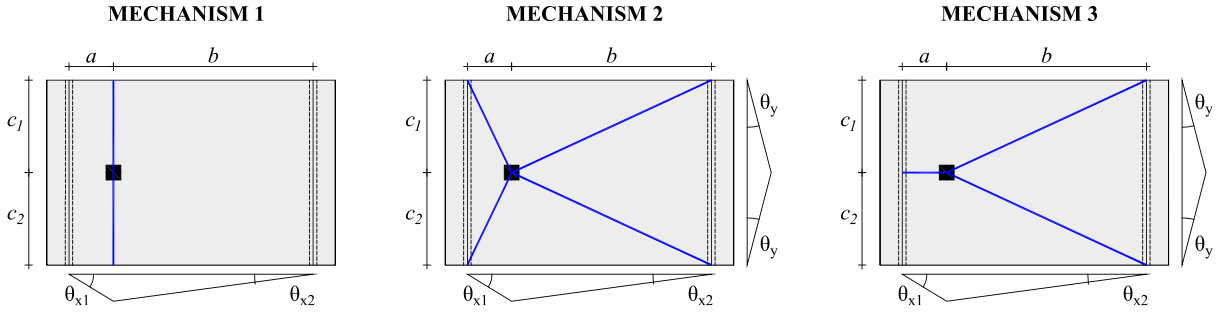

Source: Adapted from Belletti et al. (2014).

$$P_{flex} = \begin{cases} \dfrac{m_{R,x} \cdot b_{slab}}{a} + \dfrac{m_{R,x} \cdot b_{slab}}{(l_{span} - a)} - \left(l_{span} \cdot b_{slab} \cdot \gamma_{conc} \cdot h_{slab} \cdot 0.5\right), & \text{for 1 load in the span} \\ \dfrac{m_{R,x} \cdot b_{slab}}{a} - \left(l_{span} \cdot b_{slab} \cdot \gamma_{conc} \cdot h_{slab} \cdot 0.5\right), & \text{for 2 symmetrical loads in the span} \end{cases}$$

(5.25)

The same factors and approaches used to compute the effect of the free edges on the contribution of the lateral sides of the control perimeter are applied in this simplified approach. The same calculations were also performed to compute the contribution of the elongated sides with predominant one-way shear when applicable.

5.6 Predicting the governing shear failure mode

In a design or assessment task, the most critical failure mechanism would be defined by the lower ratio between the design loads and load effects (V_{Rd}/V_{Ed} and P_{Rd}/P_{Ed}). Here, V_{Rd} and V_{Ed} are the design shear capacities and design shear actions, respectively. P_{Ed} and P_{Rd} are the

respective design concentrated loads and design punching capacities. Knowing the tested concentrated loads and shear forces at failure (P_{test} and V_{test}) from the laboratory tests, Natário (2015) suggests that the governing failure mode would be related to the maximum ratio between $P_{test}/P_{predicted}$ and $V_{test}/V_{predicted}$, where P_{test} and $P_{predicted}$ are the tested and predicted punching capacities, respectively; V_{test} and $V_{predicted}$ are tested and predicted one-way shear capacities. Since using the term one-way shear capacity for tests that failed by punching or punching capacity for the tests that failed by shear could be inconsistent, a different definition was used along with this study. The tested one-way shear capacity means the maximum sectional one-way shear occuring in the test. In the same way, the tested punching capacity means the externally applied load at failure. V_{test} and P_{test} include the influence of the self-weight. The tested one-way shear capacity considers the control section for computing the self-weight influence halfway between the load and the support.

Therefore, if the ratio $V_{test}/V_{predicted}$ is larger than $P_{test}/P_{predicted}$, one-way shear is theoretically more critical than punching shear, and the predicted governing failure mode is one-way shear. Another way to see how this makes sense is to look for the lower predicted resistance compared to the tested load (for shear and punching predictions), which also gives the larger ratio between tested and predicted resistances. In this study, the strength ratio SR = max $\{V_{test}/V_{predicted}; P_{test}/P_{predicted}\}$ is defined to predict the most critical failure mechanism without knowing the observed failure mode on the tests. Besides, this parameter is also used to investigate the level of conservatism of the investigated approaches combining the shear and punching predictions.

5.7 Finite element models for the refined approach

In this study, the finite element software ABAQUS (version 6.14) (DASSAULT SYSTEMS SIMULIA CORP., 2014) is used to evaluate the distribution of bending moments and shear forces at the control sections for one-way and two-way shear analyses (Figure 5-13). A 4-node shell element with reduced integration (S4R), hourglass control and finite membrane strains is used to simulate the slab. An 8-node linear brick element with reduced integration and hourglass control is used to simulate the plate supports (C3D8R). Interface properties of (i) hard contact (free to uplift) and (ii) frictionless are assumed at the contact between the plate supports and the slab surface. Alternatively, compression-only supports could be used along the support axis from the slab instead of including solid elements with interaction properties between the shell and solid elements, such as made by Natário (2015). The reinforcement was not modeled

in the finite element models since its influence on the results was accounted for in the analytical shear and punching shear expressions.

Figure 5-13 - Overview of the numerical models developed highlighting the evaluated regions for one-way shear and punching shear analyses.

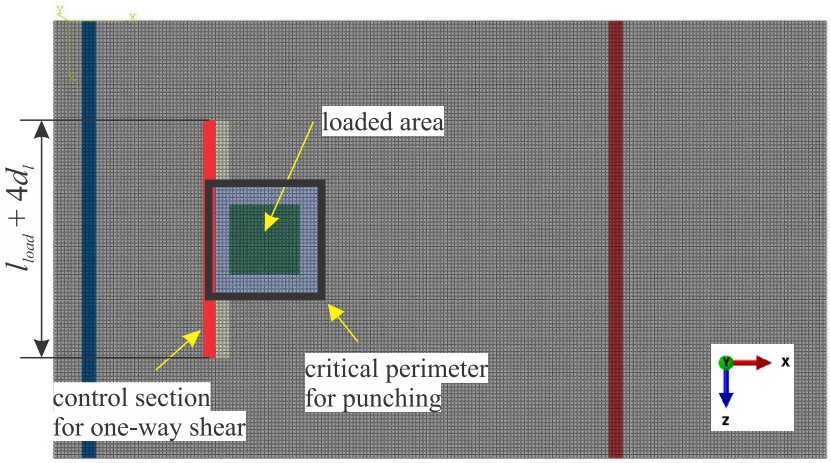

Source: Author.

The mesh size chosen varied according to the numerical models between 10 mm and 20 mm. In practice, the mesh size was chosen to assure a minimum amount of 8 elements distributed along the load edges. Based on mesh studies, the results seem to be mesh independent when at least 8 finite elements are distributed along the load edges. The vertical displacements are constrained at the support axis on the bottom face of the solid elements, simulating simple supports. The load is simulated by applying a uniform pressure with a resulting load equal to 1 kN on the loading plate. Further details about the control sections and calculations of internal forces can be consulted elsewhere (SOUSA et al., 2021a; NATÁRIO, 2015). The concrete shear modulus used $G_{c,used}$ is taken as 1/8 of G_c based on Natário (2015) (this value was calibrated based on comparisons between the test results and calculated ones and represents the cracked concrete at failure), with G_c calculated as:

$$G_c = \frac{E_c}{2 \cdot (1 + \mu)} \tag{5.26}$$

The Poisson's coefficient μ is assumed as equal zero to account for the concrete cracking (NATÁRIO, 2015; NATÁRIO; FERNÁNDEZ RUIZ; MUTTONI, 2014; SAGASETA et al., 2014; VAZ RODRIGUES; FERNÁNDEZ RUIZ; MUTTONI, 2008). For simply supported slabs, a line of vertical displacement was constrained at the middle width of the support plates with free rotation (example in Figure 5-14).

Figure 5-14 - Example of boundary conditions applied in the numerical models.

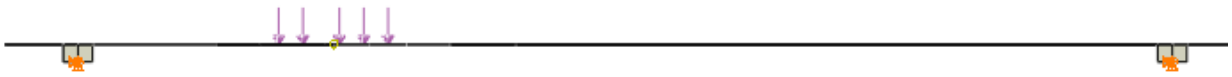

Source: Author.

5.8 Dataset from literature

In this study, the same dataset used by Natário (2015) (here named Dataset A) was investigated in order to allow a fair comparison between results. This dataset includes 48 tests from the following references: Damasceno (2007), Ferreira (2006), Regan and Rezai-Jarobi (1988), and Reiβen et al. (2018). Only simply supported slabs were evaluated.

In this dataset, 30 tests were classified as failing by a clear punching (P, with none or some reinforcement yielding at failure). Two tests were classified as failing by a mixed-mode between one-way shear and two-way shear (WB+P) and 16 tests were classified as failing by one-way shear as wide beams (WB).

The majority of the tests were designed to achieve shear or punching failure modes. As a consequence, more than 95% of the tests have reinforcement ratios larger than 0.98%. All tests have a shear span to effective depth ratio a/d higher than 3. However, five tests were identified with ratio $a_v/d_l < 3$ and, hence, may have been influenced by the formation of direct compressive struts between the load and the support, such as identified in Figure 5-11b by the cracking pattern. The thickness of the tests varied between 100 mm and 280 mm. Due to the limited thickness in the tests with 100 mm [3.93 in] of thickness, some of these developed a punching failure with reinforcement yielding.

5.9 Results of Chapter 5

Predicting the most critical failure mode is one of the main tasks in the assessment of existing structures but is seldomly treated in the literature. Figure 5-15 compares the tested and predicted resistances for dataset A in terms of shear and punching capacities. The maximum strength ratio SR was calculated as the maximum of $V_{test}/V_{predicted}$ and $P_{test}/P_{predicted}$, and used to identify the most critical failure mechanism (theoretically). The most critical failure mechanism is the one providing the higher values between $V_{test}/V_{predicted}$ and $P_{test}/P_{predicted}$. Figure 5-15a,b,c uses only analytical expressions to define the effective shear width (one-way shear) and the

punching capacity (using the ratio P/P_{flex} in calculating the slab rotations ψ). Figure 5-15d,e,f combines the outputs from LEFEA with the expressions based on the CSCT for shear and punching, such as proposed by Natário (2015). In this way, the benefits of using LEFEA can be investigated.

In Figure 5-15a, the average (AVG) ratio $V_{test}/V_{predicted}$ was 1.06, with a coefficient of variation (COV) equal to 15.4%. Using the punching expressions, the average ratio between tested and predicted resistances $P_{test}/P_{predicted}$ was 1.14 with a 13.1% of COV (Figure 5-15b). The lower scatter observed for the punching expressions is reasonable since most of the tests in the dataset developed a punching failure mode. In practice, the most unsafe predictions of one-way shear capacity occurred for the tests that failed by punching, and the most unsafe predictions of punching occurred for the tests that failed as wide beams in shear. In general, however, both approaches provided a good precision if considering the complexity of the problem.

Compared to the approach presented by Natário (2015) (Figure 5-1), the results of the proposed analytical approach were slightly more accurate, which is expected since this study calibrated the correction factors for shear and punching predictions to achieve a better performance of the proposed approach. Besides, the predictions of the punching capacity using the proposed analytical recommendations were more precise and conservative because the influence of the slab width and load size was considered by CF_{width} (see Figure 5-2b). The ratio SR achieved an AVG equal to 1.18 with a COV equal to 12.6% (Figure 5-15c), which is a level of accuracy and precision comparable to the models of one-way shear or two-way shear expressions used to evaluate datasets of beams (MUTTONI; FERNANDEZ RUIZ, 2008) and flat slabs (MUTTONI, 2008). The correct failure mechanism was determined in 69% of the tests, which is also interesting since only analytical expressions were used.

Similar results were observed combining the outputs from LEFEA into the CSCT expressions (Figure 5-15d,e,f). First, the one-way shear expressions provided an AVG ratio equal to 1.16 with a COV equal to 13.3% (Figure 5-15d). Therefore, the level of precision of the one-way shear expressions was excellent, even though most tests in Dataset A failed by punching. This occurs because the most critical section for one-way shear and punching are close to the load edge and, when the one-way shear resistance at the face of the load is achieved, the punching capacity of the slab will also be critical in this region. Proof of this explanation is that an asymmetrical punching cone, with the critical shear crack visible at only the face of the

load, was identified in the tests of Reiβen et al. (2018) that failed by punching (Figure 5-11b). Herein, it should be noted that the factor CF_{shear} was not applied in the approach including LEFEA for one-way shear predictions.

Figure 5-15 - Comparison between tested and predicted resistances for shear and punching and statistics of tested to predicted values. Notes: P = punching; WB = wide beam shear failure (one-way shear); WB+P = mixed failure mode or not clear between WB and P.

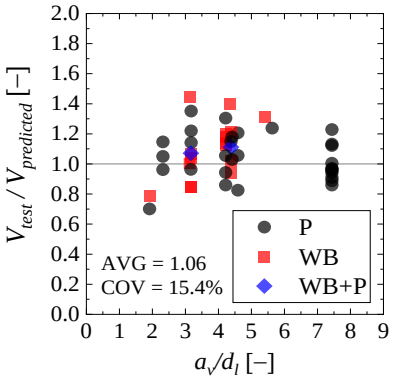

a) V_{test}/V_{pred} **using only analytical expressions ($b_{eff,proposed}$ as suggested in equation (23)) – proposed approach**

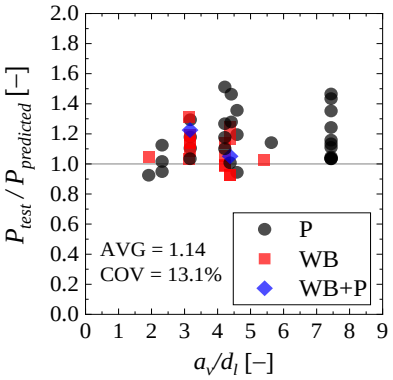

b) P_{test}/P_{pred} **using only analytical expressions (YLM for ψ) - proposed approach**

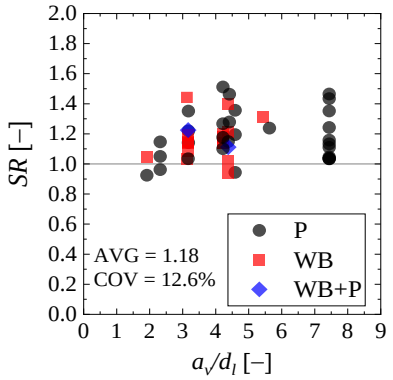

c) **SR based on a) and b) results - proposed approach**

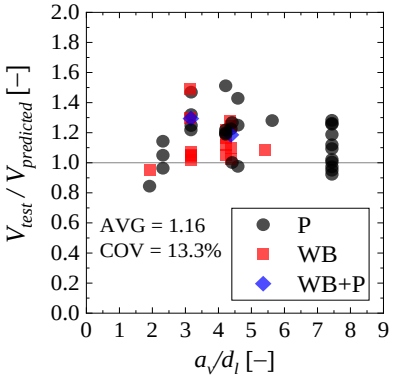

d) V_{test}/V_{pred} **combining LEFEA with the CSCT expressions for shear** (MUTTONI; FERNANDEZ RUIZ, 2008)

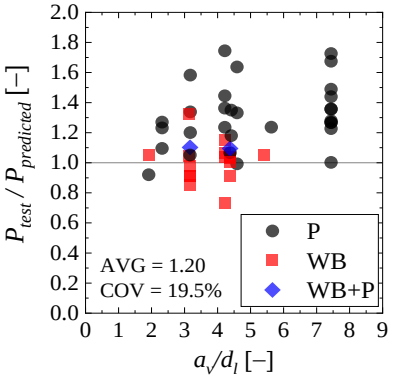

e) P_{test}/P_{pred} **combining LEFEA with the CSCT expressions for punching** (MUTTONI, 2008)

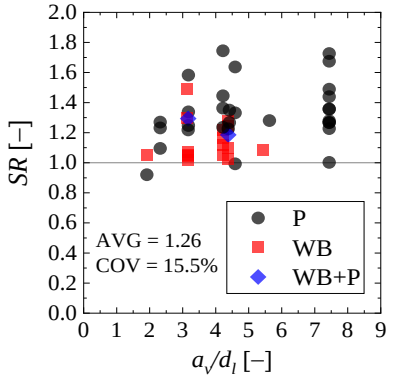

f) **SR calculated based on the results of d) and e)**

Source: Author.

The punching expression combined with LEFEA reached an average ratio equal to 1.20 with a coefficient of variation of 19.5% (Figure 5-15e). Therefore, the predictions in the proposed approach using LEFEA were slightly better than those presented by Natário (2015) (see Figure 5-2b). In practice, the predictions of punching capacity improved for the tests that failed as wide beams in shear using LEFEA and including the semi-empirical factor CF_{width}

related to the ratio b_{slab}/l_{load}. The average strength ratio SR was 1.26 with COV equal to 15.5% (Figure 5-15e). The correct failure mechanism was predicted in 88% of the cases. Therefore, using LEFEA allowed improving the predictions of the governing failure mechanism and decreasing the conservatism of the predictions slightly. Comparatively, Natário (2015) correctly predicted the governing failure mechanism in 69% of the cases (Figure 5-2) using a similar approach and including LEFEA.

5.10 Discussions of Chapter 5

Most studies related to one-way slabs under concentrated loads close to the support focused on the assessment by the combination of one-way shear models with an effective shear width (HALVONIK; VIDAKOVIĆ; VIDA, 2020; HENZE; ROMBACH; HARTER, 2020; NATÁRIO; FERNÁNDEZ RUIZ; MUTTONI, 2014; REIßEN; CLASSEN; HEGGER, 2018). Besides, most models of effective shear width (SOUSA et al., 2021c; LANTSOGHT et al., 2015a) based on the horizontal spreading of the load to the support predict an increasing effective shear width by increasing the clear shear span a_v or the ratio a_v/d_l. Based on this, a larger shear capacity $V_{predicted}$ could be expected for slabs under loads at large distances from the support if the shear slenderness effect is not accounted for in the one-way shear resistance expressions, such as and ACI 318-19 (ACI COMMITTEE 318, 2019), for instance. If the shear slenderness is accounted for, as for the CSCT expressions (MUTTONI, 2008; MUTTONI; FERNANDEZ RUIZ, 2008) which include the influence of the bending moment, an increase of the effective shear width could be counterbalanced by the decrease of the unitary shear resistance by increasing a_v/d_l. Consequently, the sectional shear at failure V_{test} would not be as much influenced by a_v/d_l.

For larger ratios a_v/d_l (for instance, > 4), slabs commonly fail by punching or in a transitional failure mode between one-way shear and two-way shear (SOUSA et al., 2021a; LANTSOGHT et al., 2015c) or in flexure. Because of this, the available one-way shear capacity may eventually not be reached. In this case, the predictions of one-way shear capacity using only analytical expressions may become unsafe, such as observed in other publications (HALVONIK; VIDAKOVIĆ; VIDA, 2020; LANTSOGHT et al., 2015d) when using the French effective shear width. In this study, this problem was countered in the fully analytical approach by including a semi-empirical factor to decrease the effective shear width predicted with the French approach when the shear slenderness increases. In the approach using LEFEA, the predicted effective shear width (Figure 5-6) provides a conservative measurement even for the tests that failed by punching (Figure 5-15a). When evaluating the punching capacity of one-

way slabs, conversely, the effect of the slab width and load size play a marked influence on the predictions. Lantsoght et al. (2015d) and Natário (2015) found unsafe predictions of punching capacity for many tests that failed as wide beams using different approaches (fully analytical or combined with LEFEA). Until now, no specific publication addressed this problem, which was simplistically accounted for in this study by a semi-empirical factor CF_{width} that considers a lower contribution for some edges of the control perimeter depending on the relation between the slab width and the load size in the width direction.

In this study, it was used a comparison between the ratios $V_{test}/V_{predicted}$ and $P_{test}/P_{predicted}$ to determine the most critical failure mechanism. In practice, one could also perform a comparison between the predicted load F that causes a one-way shear failure and F that causes a punching failure to determine the most critical value of the concentrated load. However, in this study, this approach was not used because it would require further adjustments on how to include the effect of arching action on the predicted failure load F.

One of the main ideas of using Levels of Approximations is that improved predictions of shear and punching capacity could be achieved by devoting more time and computational effort to estimating parameters required in the expressions (FÉDÉRATION INTERNATIONALE DU BÉTON (FIB), 2012). In this study, the statistical properties of the analytical approach were slightly more accurate than the refined one due to the way in which the correction factors were derived in the fully analytical approach. The predictions using the simpler approach (only analytical expressions) can become more conservative, as would be expected in a Level of Approximation I, by multiplying the factors CF_{width} and CF_{shear} by reduction factors not included herein. It draws attention that both simplified and refined approaches led to a small coefficient of variation in the predictions (COV < 20%). In addition to allowing a broad insight into the distribution of shear and internal moments of the slabs, the data from LEFEA allowed improving predicting the governing failure mechanism, which increased from 69% at LoA I to 88% at LoA II. In practice, it can be stated that the refined approach is a more powerful tool since it may be extended directly to most complex cases not covered in laboratory tests.

5.11 Conclusions of Chapter 5

In this study, the one-way and two-way shear expressions based on the CSCT were investigated from different viewpoints: (i) how accurate these expressions can be to predict the most critical shear failure mode of slabs that failed in different modes using only analytical

expressions or combined to LEFEA and (ii) how the predictions are improved using LEFEA to predict the correct failure mechanism. From this study, the following conclusions can be drawn:

- The proposed approach using only analytical expressions combined with the CSCT allows predicting precisely the shear and punching capacity of simply supported slabs in a conservative way, regardless of the governing failure mechanism of the tests. The predictions of the shear and punching capacity were improved by including two semi-empirical factors (CF_{width} and CF_{shear}) related to the transition from one-way shear to punching failures according to parameters such as the ratio a_v/d_l or b_{slab}/l_{load} (expression 5.13 for punching shear and expressions 5.22 for one-way shear).
- The coupling of the CSCT expressions with LEFEA allows improving the predictions of the governing failure mechanism. In practice, this approach is more suitable for the assessment of existing structures when higher levels of approximation are required.
- The transition of the governing failure mechanisms according to parameters such as the shear slenderness and the slab width to load size can be reasonably captured with the proposed semi-empirical factors. In this study, CF_{shear} was applied in the simplified approach and CF_{width} was applied in the simplified and refined approaches.
- One of the main advantages of using LEFEA to assess the shear and punching capacity of slabs under concentrated loads is that a more precise prediction of the governing failure mechanism is achieved. Besides that, the distribution of shear forces and moments around the interest according to the boundary conditions are captured more realistically.

In summary, LEFEA is an interesting tool for assessing existing structures or reaching a more rational design of new structures since it allows to predict more accurately the governing failure mechanism of slabs. At the same time, the proposed analytical expressions have been shown to lead to good results for the shear and punching capacity in the absence of finite element software.

6 BEHAVIOR AND PUNCHING CAPACITY OF FLAT SLABS WITH THE RATIONAL USE OF UHPFRC: NLFEA AND ANALYTICAL PREDICTIONS

One-way slabs under concentrated loads may fail either by one-way shear as wide beams or by two-way shear (punching). Because of this, it would be important to develop studies that address one-way shear and two-way shear in depth before exploring the problem of one-way slabs under concentrated loads. As we also developed a specific study emphasizing the one-way shear behavior of wide members (Chapter 3), we also tried to develop a specific study focused on the two-way shear behavior of slabs under concentrated loads. In this way, a solid understanding of both one-way shear and punching shear failures could be supported.

In this chapter, the focus was addressing the punching capacity of slab-column connections designed with the rational use of ultra-high-performance fiber-reinforced concrete. In practice, this chapter allowed addressing one of the possible failure mechanisms of one-way slabs under concentrated loads more closely: punching. In this context, the punching capacity of flat slabs with different reinforcement ratios was investigated. Herein, the predictions of punching capacity were developed in the framework of the Critical Shear Crack Theory expressions after several non-linear finite element analyses (NLFEA). Therefore, this chapter has also introduced another tool that can be used to assess reinforced concrete slabs under concentrated loads: the NLFEA. At this point, it's important to note that this chapter allowed calibration and validate the proposed modeling approach to deal first with the concentric punching failures before applying the same approach to one-way slabs under concentrated loads in asymmetrical positions.

Besides, the use of UHPFRC in line with this study in another context. Sometimes, slabs preliminary rated as critical in shear or punching need to be strengthened. Nowadays, one of the alternatives is to add a thin layer of UHPFRC over the existing slab after adequate surface preparation. In practice, this thin layer is most frequently added on the tensiled side of the slabs. However, some studies indicated that adding this layer on the compressed side would be more efficient. Therefore, some aspects of the strengthening and design of slabs with the rational use of UHPFRC need further investigation.

6.1 Introduction of Chapter 6

Ultra-high-performance fiber-reinforced concrete (UHPFRC) is a cementitious material produced with Portland cement, pozzolans, small-size aggregates, inert fillers, superplasticizers, and surface-treated steel fibers (FEHLING et al., 2014; KRAHL; CARRAZEDO; EL DEBS, 2018). The outstanding properties of (i) high compressive strength (GRAYBEAL, 2007; KRAHL; GIDRÃO; CARRAZEDO, 2018; KRAHL; GIDRÃO; CARRAZEDO, 2019), (ii) low permeability of the hardened composite, and (iii) high residual tensile strength compared to normal strength concrete (NSC) and steel fiber-reinforced concrete (SFRC) (GRAYBEAL et al., 2020) make this material a promising solution to improve the punching capacity, durability, and deformation capacity of reinforced concrete (RC) flat slabs, and in particular slab-column connections (AL-QURAISHI, 2014; HARRIS, 2004; JOH; HWANG; KIM, 2008; MOREILLON, 2013; NAAMAN; LIKHITRUANGSILP; PARRA-MONTESINOS, 2007; NGUYEN; NGUYEN; PANSUK, 2017; SHOUKRY; TARABIA; YASSIN, 2020; SPASOJEVIC; REDAELLI; MUTTONI, 2009; ZOHREVAND et al., 2014). For instance, in the case of RC beams failing in shear, experimental studies already showed that a total replacement of NSC by UHPFRC allowed increasing the normalized shear capacity by more than 70% and improved the deformation capacity at failure (POURBABA; JOGHATAIE; MIRMIRAN, 2018).

Although UHPFRC is more costly than NSC, its improved structural properties usually decrease the material consumption, reinforcement ratios, maintenance costs and increase the service life (AZMEE; SHAFIQ, 2018; ZHU et al., 2018), which balance the overall cost of using UHPFRC for structural applications (GRAYBEAL et al., 2020). Traditionally, the main hurdle for spreading the use of UHPFRC as a building material for structural elements has been the lack of structural design guidance for this class of material (GRAYBEAL et al., 2020). Since the number of tests on slab-column connections built with UHPFRC is limited (MOREILLON, 2013; NGUYEN; NGUYEN; PANSUK, 2017; SUTER; MOREILLON, 2010; ZOHREVAND et al., 2014), the use of non-linear finite element analyses (NLFEA) could be a valuable tool to extend the knowledge about the behavior of such connections.

Several studies investigated numerical modeling approaches to predict the punching shear behavior of slab-column connections made entirely with NSC (NSC flat slabs) with and without shear reinforcement (BALOMENOS; GENIKOMSOU; POLAK, 2018; GENIKOMSOU; POLAK, 2015, 2016, 2017a, 2017b; MILLIGAN; POLAK; ZURELL, 2020, 2021; NAVARRO; IVORRA; VARONA, 2018, 2020). In these, the NLFEA aided

understanding and evaluating the effect of parameters such as openings close to the column on the structural response of flat slabs (GENIKOMSOU; POLAK, 2017a; MARQUES et al., 2020) and the compressive membrane action effect (GENIKOMSOU; POLAK, 2017b). On the other hand, only a few studies described modeling approaches for using UHPFRC in slab-column connections (MENNA; GENIKOMSOU, 2021; WU et al., 2019). In these studies (MENNA; GENIKOMSOU, 2021; WU et al., 2019), the UHPFRC was used only as an extra layer at the slab tensile side (strengthening material). The main acting forces were tangential stresses at the interface between the NSC and the UHPFRC and tensile forces induced by flexure at the UHPFRC layer. Therefore, these applications do not take advantage of the higher compressive strength of the UHPFRC compared to NSC. Moreover, there is a low number of numerical studies on using UHPFRC as the main material in the shear-critical regions (KADHIM et al., 2021; KADHIM; JAWDHARI; PEIRIS, 2021).

At the same time, a reasonable amount of experimental studies investigated the punching capacity of slab-column connections designed with the rational use of advanced composites on the slab-column connection, such as SFRC (CHENG; PARRA-MONTESINOS, 2010; GOUVEIA; FARIA; RAMOS, 2019a, 2019b; THEODORAKOPOULOS; SWAMY, 1993) and ultra-high-performance concrete (UHPC – without fibers) (INÁCIO et al., 2020; INÁCIO; LAPI; PINHO RAMOS, 2020). Although UHPFRC combines the higher compressive strength of the UHPC and the higher residual tensile strength compared to the SFRC, only a few studies investigated the performance of slab-column connections with the rational use of UHPFRC at the shear-critical regions (QI et al., 2021; ZOHREVAND et al., 2014).

Therefore, the present study examines the behavior of flat slabs designed with the rational use of UHPFRC in shear-critical regions (Figure 6-1) aided by three-dimensional NLFEA. Moreover, parametric analyses investigate the influence of the (i) reinforcement ratio and (ii) geometry of the UHPFRC layer on the punching capacity of NSC-UHPFRC flat slabs. Since analytical methods are preferable in daily engineering for preliminary designs, this chapter also proposes an analytical approach based on the critical shear crack theory (CSCT) (MUTTONI, 2008) to assess the punching capacity of flat slabs designed with the rational use of UHPFRC.

Figure 6-1 – Detail of the slab-column connection with the rational use of UHPFRC.

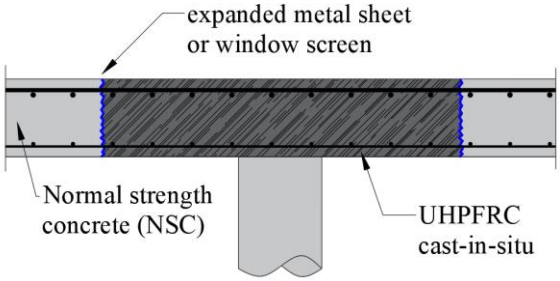

Source: Adapted from Moreillon (2013).

Firstly, control slabs were used to validate the non-linear finite element models (FEM) developed. After that, a parametric study was conducted to investigate the influence of (i) the reinforcement ratio and (ii) different configurations of the UHPFRC layer on the punching capacity of NSC-UHPFRC flat slabs. In the end, the experimental control results, as well as the numerical results from the parametric analyses, were evaluated by the proposed analytical approach.

6.2 Control specimens from literature

In this section, the following aspects are addressed: (i) the choice of the control tests from the literature, (ii) the geometry and (iii) the material properties of the control tests.

6.2.1 Choice of control specimens

All ten slab-column connections used in this study as control experiments were tested by Zohrevand et al. (2014). These specimens were chosen because they include three groups of specimens: (i) NSC flat slabs, (ii) UHPFRC flat slabs and (iii) flat slabs combining NSC and UHPFRC, with the last rationally used at the slab-column connection (NSC-UHPFRC flat slabs). Therefore, these tests allow validating separately the material models used to simulate the NSC and the UHPFRC. Moreover, the experimental program from Zohrevand et al. (2014) also stood out by including specimens with high and lower reinforcement ratios (1.8% and 0.6%, respectively). Since flat slabs under punching loads may show different failure modes according to the reinforcement ratio, such as brittle punching failure or flexure-induced punching with reinforcement yielding (GUANDALINI; BURDET; MUTTONI, 2009), the selected control specimens allowed to validate the NLFEA under different failure mechanisms.

6.2.2 Geometry of control experiments

Figure 6-2 shows the geometry of the control experiments tested by Zohrevand et al. (2014). The experimental program considered three groups of slabs: (i) fully made with NSC (C1.8 and C0.6, where 1.8 and 0.6 refer to the reinforcement ratio of the slab); (ii) fully made with UHPFRC (U1.8 and U0.6) and (iii) hybrid slabs with the rational use of UHPFRC, which

means that UHPFRC was used only on the slab-column connection area, while NSC was used for the remaining slab (Figure 6-2). Table 6-1 describes the geometry of the strengthened area with UHPFRC and the reinforcement ratio for the ten tests investigated in this study. Note that the specimens CU-A-F and CU-C-F used the UHPFRC layer over the entire thickness, while the specimens CU-B-H used UHPFRC only for half of the thickness.

All slabs were square with 1219 mm × 1219 mm in plan and with 114 mm of thickness. These slabs were loaded at the center on an area of 76 mm × 76 mm. Each specimen was supported on rigid frames over a length of 152.5 mm on all four sides free to lift. At the interface between the slabs and the rigid frame, the authors (ZOHREVAND et al., 2014) described using a gypsum cement layer to level the slabs over the support. Moreover, some figures also indicated the use of a thin, flexible plastic sheet between the slabs and the supports. No information was reported about the stiffness and thickness of these materials and where they were applied, which required additional attention in this numerical study.

Figure 6-2 – a) Geometry of the slabs tested by Zohrevand et al. (2014): a) specimens fully made of NSC or UHPFRC; b) specimens with the rational use of UHPFRC over the full depth of the slabs and c) specimens with UHPFRC limited to only half of the slab thickness. (All dimensions are in mm).

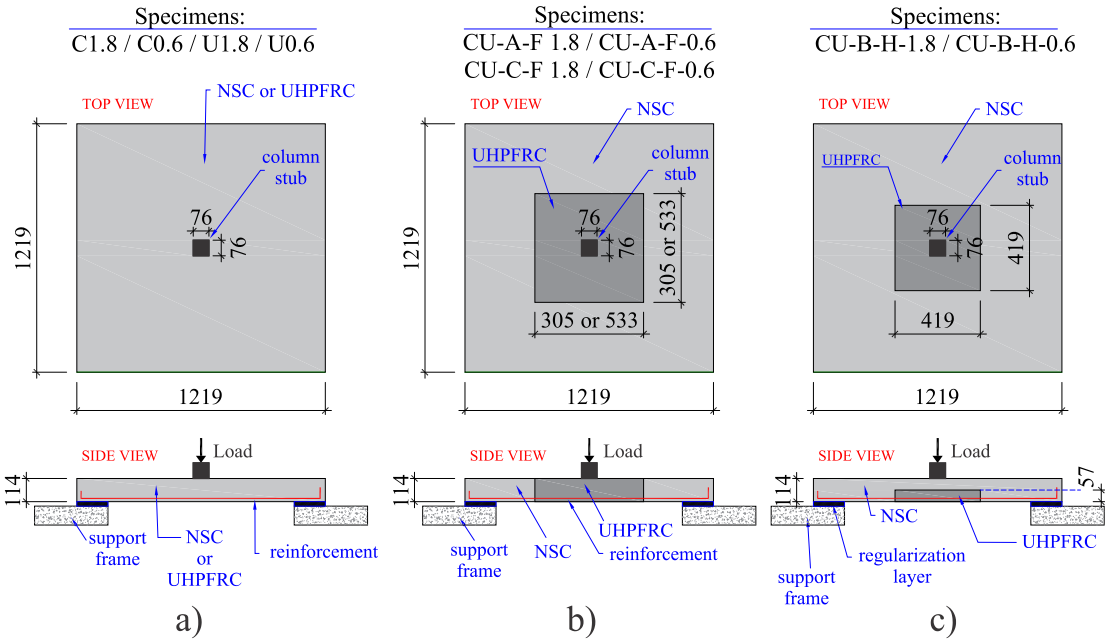

Source: Adapted from Zohrevand et al. (2014).

Table 6-1 - Geometry of the control slabs.

Model Identification	Geometry of the UHPFRC layer (mm)	ρ_l (%)	ρ_t (%)	ρ (%)
C1.8	-	1.70	1.97	1.8
C0.6	-	0.56	0.65	0.6
U1.8	-	1.70	1.97	1.8
U0.6	-	0.56	0.65	0.6
CU-A-F-1.8	533 × 533 × 114	1.70	1.97	1.8
CU-A-F-0.6	533 × 533 × 114	0.56	0.65	0.6
CU-C-F-1.8	305 × 305 × 114	1.70	1.97	1.8
CU-C-F-0.6	305 × 305 × 114	0.56	0.65	0.6
CU-B-H-1.8	419 × 419 × 57	1.70	1.97	1.8
CU-B-H-0.6	419 × 419 × 57	0.56	0.65	0.6

Note: ρ_l and ρ_t denote the reinforcement ratios of the slabs in the longitudinal and transversal directions. The longitudinal reinforcement is associated with the higher effective depth. ρ is the mean reinforcement ratio calculated as $\rho = (\rho_l . \rho_t)^{1/2}$. Source: Zohrevand et al. (2014).

6.2.3 Material properties of control slabs

Table 6-2 describes the material properties of the concretes used in the tests. The main properties of the UHPFRC reported are the measured tensile and compressive strengths on cylindrical specimens (102 mm × 203 mm) with traditional compressive and splitting tensile tests, respectively. Therefore, no information is available about the hardening and softening behavior of UHPFRC under tension and compression. Several batches were used to cast the UHPFRC-slabs and hybrid slabs, with their 28-day compressive strength ranging from 129 MPa to 151 MPa. The tensile strength of the UHPFRC varied between 6 MPa and 10 MPa for the different batches, with an average value of 8 MPa (ZOHREVAND et al., 2014). A single batch of NSC was used for the control slabs, with an average compressive strength of 45 MPa and coarse aggregate with a maximum size of 9.5 mm. The tensile strength of the NSC-batch was not reported.

Straight steel fibers were used in the UHPFRC mix. These copper-coated micro steel fibers were 13-mm long with a diameter of 0.2 mm and tensile strength of 2800 MPa. The reinforcement of the slabs consisted of Nº 13M steel bars spaced at 76 mm (ρ = 1.8%) and 229 mm (ρ = 0.6%) on center. The reinforcement was placed in two orthogonal directions on the tension side of the slab, with a clear cover of 13 mm. The yield strength of the reinforcement was 414 MPa (ZOHREVAND et al., 2014).

Table 6-2 – Material properties described in Zohrevand et al. (2014).

Concrete	NSC		UHPFRC					
Model Identification	f_{cm} (MPa)	d_{ag} (mm)	f_{cm} (MPa)	f_{ct} (MPa)	ρ_f (%)	l_f	$f_{y,fiber}$ (MPa)	d_f (mm)
C1.8	45	9.5	-	-	-	-	-	-
C0.6								
U1.8	-	-	128.6	AVG = 8 MAX = 10 MIN = 6	2	13	2800	0.2
U0.6			136.8					
CU-A-F-1.8	45	9.5	150.3					
CU-A-F-0.6			151.4					
CU-C-F-1.8			147.4					
CU-C-F-0.6			139.7					
CU-B-H-1.8			139.7					
CU-B-H-0.6			139.7					

Source: Zohrevand et al. (2014).

6.3 Finite element simulations

This section describes the details of the modeling in relation to (i) boundary conditions, (ii) interfaces (iii) mesh discretization and finite element type, and (iv) material models.

6.3.1 Overview

The finite element software ABAQUS/CAE (DASSAULT SYSTEMS SIMULIA CORP., 2014) was used to model the control slabs. By considering specimens' symmetry, a quarter of the slabs was modeled to reduce the computational effort (Figure 6-3a).

In all analyses, the load was applied in displacement-controlled conditions in order to evaluate the governing punching failure mode. To make a fair comparison between experimental and numerical results in terms of force-displacement graphs, due to the uncertainties in slab-support interactions and loading protocol, a spring was coupled to the loading plate of the numerical models (Figure 6-3b) and its stiffness was calibrated to reproduce the initial stiffness of the experimental results. In this study, it is assumed that the graphs reported in reference (ZOHREVAND et al., 2014) were influenced by the calibration of the actuator and by soft materials between the frame support and the slab surface based on the test pictures (ZOHREVAND et al., 2014).

Figure 6-3 – Details of the boundary conditions used: a) overview of the model and b) detail of the displacement-controlled loading.

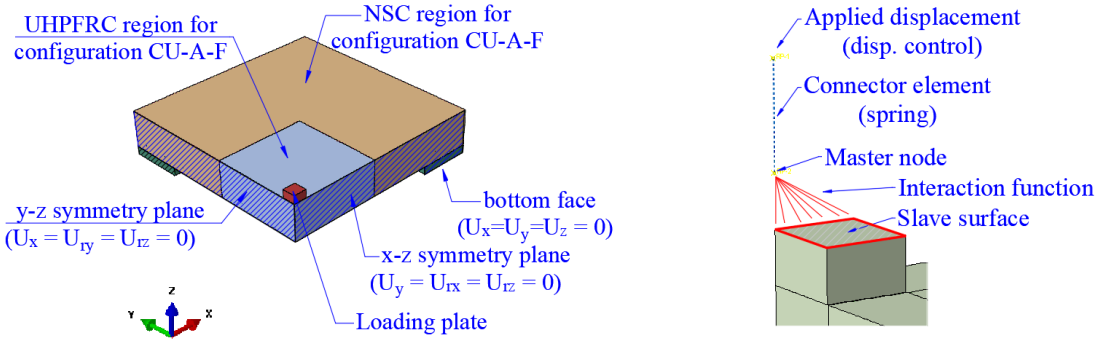

a) b)

Source: Author.

6.3.2 Boundary Conditions

Zohrevand et al. (2014) described that the specimens were leveled between the bottom slab surface and the rigid support frame using gypsum cement layers. The same material was also used between the loading plate and the slab surface to ensure a vertical concentric load. However, pictures of the specimens also show a thin, flexible plastic sheet between the slab and the rigid support frame. Based on this information, a soft material layer between the slabs and the rigid frame was assumed. In this study, instead of modeling the full support frame, only a support layer of 25 mm in thickness was modeled, and a small value of Young's modulus (4 MPa) was assigned to this material to simulate the soft material between the slab and the support in the tests.

6.3.3 Interfaces

Since the NSC and UHPFRC interface did not show any signal of damage or crack opening in the tests, a rigid interaction (perfect bond) between NSC and UHPFRC (no sliding) was assumed. Other experimental studies also support the outstanding bonding properties between UHPFRC and NSC (MOMAYEZ et al., 2005; SAHMARAN et al., 2014; WEI et al., 2020; ZHU; LEUNG; CAO, 2011). The interface between the support frame and loading block surface with the slab was modeled assuming (i) hard contact (allowing separation of the surfaces) and (ii) frictionless. As no anchorage failure was reported in the experiments and the main aim of the numerical model was to predict the punching capacity, bond-slip was not considered in the simulations and a perfect bond between reinforcement and concrete was assumed.

6.3.4 Mesh and Procedure of solution

Concrete, supporting pad and loading plates were simulated with 8-node hexahedral solid elements with reduced integration (C3D8R). Reduced integration was used to avoid the shear locking of the brick elements based on the Reissner-Mindlin theory (DASSAULT SYSTEMS SIMULIA CORP., 2014; NANA et al., 2017). For solid elements, hourglass control has also been activated to avoid distortion associated with mesh discretization and linear approximation for the element displacement field. The reinforcement was modeled with 2-node truss elements (T3D2).

Figure 6-4 – Behavior in terms of the applied load versus mid-span displacement according to the finite element size for: a) slab C1.8, and b) slab U1.8; comparison of the cracking patterns predicted by the FEM (herein evaluated through the qualitative distribution of the maximum principal plastic strains) according to the finite element size: c) slab C1.8 and d) slab U1.8.

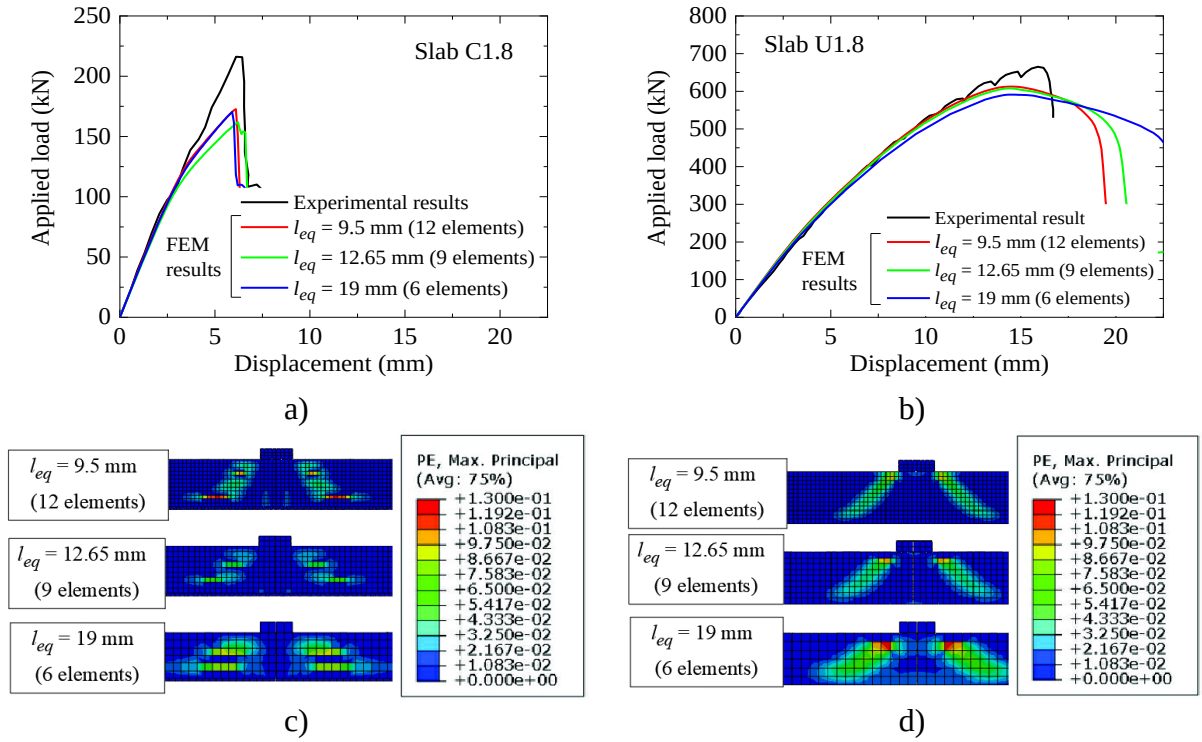

Source: Author.

Figure 6-4 shows the summary of the mesh sensibility study performed, which comprehended the slabs C1.8, C0.6, U1.8 and U0.6. Here, only the results from the slabs C1.8 and U1.8 are described as the findings from C0.6 and U0.6 are similar. Figure 6-4 shows that the governing failure mode and global response of the FEM did not change significantly with the mesh discretization due to the consistency of the material models adopted (Section 3.5). The finite element size was chosen as 9.5 mm, which allows having 12 elements over the thickness of the slab model. Despite requiring a higher time to perform the numerical analyses,

the finer mesh discretization allowed tracking the cracking pattern evolution from the FEM and better represented the post-peak behavior from the load versus mid-span displacement graphs (Figure 6-4b).

Figure 6-5a shows the mesh discretization of two models, highlighting the areas of UHPFRC and NSC in different colors. A more refined mesh discretization was required to allow varying the thickness of the UHPFRC layer in the parametric study (Section 7), assuring at least three elements over the UHPFRC layer thickness (Figure 6-5b).

Figure 6-5 – Mesh discretization of a) slab CU-A-F-18 and b) example of a slab with a small thickness of the UHPFRC layer on the compression side used in the parametric study (Section 6.7). Note: Only a quarter was modeled.

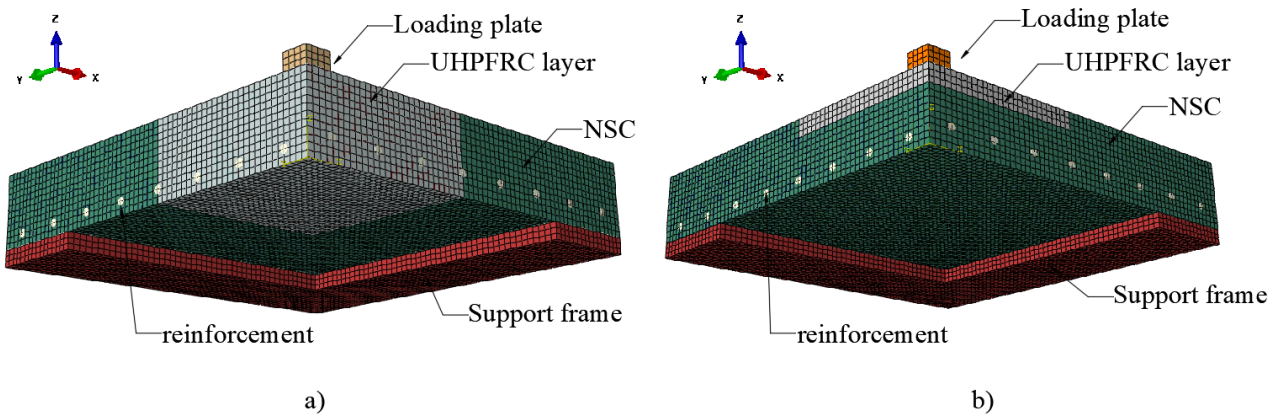

Source: Author.

6.3.5 Material modeling

Table 6-3 shows the material models used for describing the stress-strain behavior of NSC under compression (CARREIRA; CHU, 1985) and tension (HORDIJK, 1992). The model of Hordijk (1992) considers the crack bandwidth length l_{eq} to reduce the mesh sensitivity through the same approach described by Genikomsou and Polak (2015). In this study, l_{eq} was assumed equal to the finite element size (9.5 mm).

Table 6-3 – Stress-strain behavior models for NSC.

Tension behavior – Hordijk (1992)	$\frac{\sigma_t(w)}{f_{ct}} = \left[1+\left(c_1 \cdot \frac{w}{w_c}\right)^3\right] \cdot e^{-c_2 \cdot \frac{w}{w_c}} - \frac{w}{w_c} \cdot \left(1+c^3\right) \cdot e^{-c_2}$ (6.1) With: c_1 = 3; c_2 = 6.93; w_c is the critical crack opening or fracture crack opening: $w_c = 5.14 \cdot \frac{G_f}{f_{ct}}$ (6.2) The tensile strain after cracking can be described in terms of the crack opening from the following kinematic relation: $\varepsilon_t = \frac{f_{ct}}{E_c} + \frac{w}{l_{eq}} = \varepsilon_{t,cr} + \frac{w}{l_{eq}}$ (6.3)
Compression behavior – Carreira and Chu (1985)	$\frac{\sigma_c(\varepsilon)}{f_{cm}} = \frac{\beta_{CC} \cdot (\varepsilon / \varepsilon_{c1})}{\beta_{CC} - 1 + (\varepsilon / \varepsilon_{c1})^{\beta}}$ (6.4) $\beta_{CC} = \frac{1}{1 - \frac{f_{cm}}{\varepsilon_{c1} \cdot E_c}}$ (6.5)

Source: Hordijk (1992) and Carreira and and Chu (1985).

The fracture energy G_f and concrete tensile strength f_{ct} were calculated according with *fib* Model Code 2010:

$$G_f = 0.073 \cdot f_{cm}^{0.18} \quad (6.6)$$

$$f_{ct} = 0.3 \cdot \sqrt[3]{f_{cm}^{\,2}}, \text{ for } f_{cm} < 50MPa \quad (6.7)$$

$$\varepsilon_{c1} = 0.7 \cdot \frac{f_{cm}^{0.31}}{1000} \quad (6.8)$$

Table 6-4 shows the damage evolution models used for the NSC. The model of Alfarah, López-Almansa and Oller (2017) was chosen since it accounts for the bandwidth length l_{eq} in tension (l_{eq} = 9.5 mm). Therefore, this model can reduce mesh sensitivities due to tension cracking.

Table 6-4 – Damage evolution laws used for NSC.

Reference	Tension damage
Alfarah, López-Almansa and Oller (2017)	$d_t = 1 - \frac{1}{2+a_t}\left[2\left(1+a_t\right)\exp\left(-b_t\varepsilon_t^{in}\right) - a_t\exp\left(-2b_t\varepsilon_t^{in}\right)\right]$ (6.9) $a_t = 1;\ b_t = \frac{f_{ct}\cdot l_{eq}}{G_f}\cdot\left(1+\frac{a_t}{2}\right)$
	Compression damage
Birtel and Mark (2006)	$d_c = 1 - \frac{\sigma_c\cdot E_c^{-1}}{\varepsilon_c^{pl}\cdot\left(1/b_c - 1\right) + \sigma_c\cdot E_c^{-1}}$ (6.10) $b_c = 0.9;\ \varepsilon_c^{pl} = \varepsilon_c^{in}\cdot b_c$

Source: Alfarah, López-Almansa and Oller (2017) and Birtel and Mark (2006).

Table 6-5 - Stress-strain behavior models used for UHPFRC.

Reference	Tension behavior
Fehling et al. (2014).	$\sigma_t\left(w\right) = \sigma_{cf\,0}\cdot\left(1 - 2\cdot\frac{w}{l_f}\right)^2$ (6.11) $\sigma_{cfo} = f_{ct}$ of the UHPFRC: $\sigma_{cf\,0} = 0.3\cdot\sqrt[3]{f_{cm}^{\ 2}}$; l_f = 13 mm in this study.
	Compression behavior
Carreira and Chu (1985) modified by Mansur et al. (1999)	$\frac{\sigma_c\left(\varepsilon\right)}{f_{cm}} = \frac{k_1\cdot\beta_{CC}\cdot\left(\varepsilon/\varepsilon_{c1}\right)}{k_1\cdot\beta_{CC} - 1 + \left(\varepsilon/\varepsilon_{c1}\right)^{k_2\cdot\beta_{CC}}}$ (6.12) $\beta_{CC} = \frac{1}{1 - \frac{f_{cm}}{\varepsilon_{c1}\cdot E_c}}$ (6.13) $k_1 = \left(\frac{50}{f_{cm}}\right)^3\cdot\left[1 + 2.5\cdot\left(\frac{\rho_f\cdot l_f}{d_f}\right)^{2.5}\right]$ (6.14) $k_2 = \left(\frac{50}{f_{cm}}\right)^{1.3}\cdot\left[1 - 0.11\cdot\left(\frac{\rho_f\cdot l_f}{d_f}\right)^{-1.1}\right]$ **(6.15)** $\varepsilon_{c1} = \left(0.0005 + 0.00000072\cdot\left(\frac{\rho_f\cdot l_f}{d_f}\right)\right)\cdot f_{cm}^{\ 0.35}$ **(6.16)**

Source: Fehling et al. (2014), Carreira and Chu (1985) modified by Mansur et al. (1999).

Table 6-5 shows the proposed stress-strain models used to describe the behavior of UHPFRC under tension and compression. The only available information about the UHPFRC, despite the volume fraction and material properties of the fibers, are the average tensile strength and the compressive strength for each batch. In the absence of detailed information about the strain-hardening behavior, UHPFRC was assumed as a strain-softening material in tension

using the stress-crack opening relationship described by Fehling et al. (FEHLING et al., 2014). The parameter σ_{cf0} was assumed equal the peak tensile strength of the UHPFRC. In compression, the model of Carreira and Chu (CARREIRA; CHU, 1985) modified by Mansur et al. (MANSUR; CHIN; WEE, 1999) was considered, as used in Krahl, Carrazedo and El Debs (2018).

The models from Krahl, Gidrão and Carrazedo (2019) and Alfarah, López-Almansa and Oller (2017) were used to describe the damage evolution laws under compression and tension for the UHPFRC, respectively (Table 6-6).

Table 6-6 – Damage evolution laws used for UHPFRC.

Reference	Tension damage
Alfarah, López-Almansa and Oller (2017)	$d_t = 1 - \frac{1}{2+a_t}\begin{bmatrix} 2(1+a_t)\exp\left(-b_t\varepsilon_t^{ck}\right) \\ -a_t\exp\left(-2b_t\varepsilon_c^{ck}\right) \end{bmatrix}$ (6.17) $a_t = 1;\ b_t = \frac{f_{ct}\cdot l_{eq}}{G_f}\cdot\left(1+\frac{a_t}{2}\right);\ l_{eq} = 9.5$ mm
	Compression damage
Krahl, Gidrão and Carrazedo (2019)	$d_c = \left(\tanh\left(m\cdot\varepsilon_c\right)\right)\cdot\left(r\cdot\exp\left(-n\cdot\varepsilon_c\right)^k\right)$ (6.18) For ρ_f = 2%: m = 106.2; n = 188.5; k = 3.05; r = 0.93

Source: Alfarah, López-Almansa and Oller (2017) and Krahl, Gidrão and Carrazedo (2019).

6.3.6 Plasticity parameters

The parameters used for NSC were chosen based on the literature review (GENIKOMSOU; POLAK, 2015, 2016, 2017a; MILLIGAN; POLAK; ZURELL, 2020, 2021; NANA et al., 2017). The dilation angle adopted for NSC was 30º. Notably, this value is close to that expected by Poliotti and Bairan (2019) for the maximum dilation angle of NSC (Ψ = 32º) based on inverse analyses of experimental investigations. The fracture energy adopted for NSC was calculated according to the *fib* Model Code 2010 (FÉDÉRATION INTERNATIONALE DU BÉTON (FIB), 2012) since the values with the Model Code 1990 (COMITÉ EURO-INTERNATIONAL DU BÉTON, 1993) underestimated the punching capacity of the numerical models. The default value of the ratio σ_{b0}/σ_{c0} in ABAQUS is 1.16 for NSC. This value is based on the experimental tests of Kupfer et al. (1973; 1969). However, it should be highlighted that this value was found for NSC with a concrete compressive strength lower than 60 MPa.

The parameters used for the UHPFRC were mainly based on inverse analyses of experimental results proposed by Krahl, Carrazedo and El Debs (2018). The higher dilation angle used for UHPFRC was based on reverse analysis of triaxial tests (SPECK, 2008;

ZOHREVAND; MIRMIRAN, 2011). However, other experimental investigations with triaxial tests also support that higher dilation angles for UHPFRC than for NSC are suitable since the addition of fibers and the better matrix packing allows increasing the toughness of the concrete (BABANAJAD; FARNAM; SHEKARCHI, 2012; ÖZTEKIN; PUL; HÜSEM, 2016). For UHPFRC specimens, where the fibers induce more toughness in compression, Krahl, Carrazedo and El Debs 2018) found a value of σ_{b0}/σ_{c0} = 1.07 based on the tests of Speck (SPECK, 2008) (compression-compression tests) and Lee et al. (2017) (tension-compression tests).

6.3.7 Summary of the material parameters of the reference FEM

In order to ease the identification of the material parameters used in the reference finite element models, Table 6-7 summarized the main information of the materials models used for the stress-strain behavior and damage evolution of NSC and UHPFRC.

Table 6-7 – Concrete damaged plasticity (CDP) model parameters used for the reference numerical analyses.

Parameter	**NSC**	**UHPFRC**
Yield criterion		
Compressive behavior (σ_c x ε_c)	Carreira and Chu (1985)	Mansur et al. (1999)
Tensile behavior (σ_t x ε_t)	Hordijk (1992)	Fehling et al. (2014).
Damage evolution		
Compression damage (d_c x ε_c^{in})	Birtel and Mark (2006)	Krahl, Gidrão and Carrazedo (2019)
Tensile damage (d_t x ε_t^{ck})	Alfarah, López-Almansa and Oller (2017)	Alfarah, López-Almansa and Oller (2017)
Plasticity parameters		
Dilation angle, Ψ *(º)*	30	54 (KRAHL; CARRAZEDO; EL DEBS, 2018)
σ_{b0}/σ_{c0}	1.16 (KUPFER; GERSTLE, 1973; KUPFER; HILSDORF; RUSCH, 1969)	1.07 (KRAHL; CARRAZEDO; EL DEBS, 2018)
Parameter K_c	0.66 (DASSAULT SYSTEMS SIMULIA CORP., 2014)	0.66 (KRAHL; CARRAZEDO; EL DEBS, 2018)
Eccentricity, e	0.1	0.1
Viscosity parameter, μ	0.00001	0.00001
Fracture energy, G_f	*fib* Model Code 2010	-
f_{ct}	*fib* Model Code 2010	Hoang and Fehling (2017): $f_{ct} = 0.3 \cdot \sqrt[3]{f_{cm}^{\ 2}}$

Source: Author.

The stress-inelastic strain values used for NSC (slab C1.8) and UHPFRC (slab U1.8) are listed in Table 6-8, as provided in other numerical studies (MARTÍN-SANZ et al., 2020; ZHU et al., 2020). In order to avoid numerical convergence problems, the maximum value for the damage parameters was assumed as 0.9, which is also consistent with experimental measurements from this variable for both materials (FELIPE et al., 2019; KRAHL; GIDRÃO; CARRAZEDO, 2019).

Table 6-8 – Information used to define the stress-strain behavior of NSC and UHPFRC under compression and tension in the CDP (values used for slabs C1.8 and U1.8).

Compression behavior of NSC			Tension behavior of NSC		
Compressive stress (MPa)	Inelastic strain (-)	Damage parameter (-)	Tensile stress (MPa)	Inelastic strain (-)	Damage parameter (-)
18.00	0.00000	0.000	3.80	0.00000	0.0000
30.17	0.00009	0.029	2.69	0.00106	0.2545
38.99	0.00027	0.067	1.94	0.00212	0.4640
43.69	0.00057	0.120	1.27	0.00369	0.6846
45.00	0.00098	0.183	0.85	0.00576	0.8495
44.00	0.00146	0.256	0.65	0.00783	0.9000
35.82	0.00306	0.470	0.50	0.00990	0.9000
29.02	0.00440	0.611	0.37	0.01197	0.9000
18.41	0.00744	0.807	0.26	0.01404	0.9000
8.84	0.01410	0.900	0.16	0.01611	0.9000
2.70	0.03523	0.900	0.08	0.01817	0.9000
Compression behavior of UHPFRC			Tension behavior of UHPFRC		
Compressive stress (MPa)	Inelastic strain (-)	Damage parameter (-)	Tensile stress (MPa)	Inelastic strain (-)	Damage parameter (-)
99.43	0.000000	0.0000	7.64	0.00000	0.00000
112.73	0.000023	0.0000	7.04	0.02737	0.23729
123.69	0.000086	0.0056	6.47	0.05474	0.43850
128.60	0.000266	0.0154	5.92	0.08211	0.59539
107.13	0.002873	0.2312	4.89	0.13684	0.79736
57.96	0.007109	0.6373	3.53	0.21895	0.90000
34.21	0.010857	0.7805	2.40	0.30105	0.90000
22.45	0.014373	0.8523	1.48	0.38316	0.90000
14.36	0.018915	0.8985	0.60	0.49263	0.90000
10.90	0.022272	0.9000	0.20	0.57474	0.90000
8.58	0.025607	0.9000	0.01	0.65684	0.90000

Source: Author.

6.4 Analytical predictions with mechanical-based models

This section reviews the proposed approach by Maya et al. (2012) to calculate the punching capacity of SFRC slabs. After that, the proposed approach to calculate the punching capacity of reinforced concrete slabs designed with the rational use of UHPFRC is presented.

6.4.1 CSCT-based model for SFRC

The punching shear capacities of the control slabs (ZOHREVAND et al., 2014), as well as those predicted by the FEM developed in the parametric study (Section 7), were compared to those provided by the CSCT developed by Muttoni (2008) and modified by Maya et al. (2012) to cover SFRC flat slabs. In this model, the punching capacity is calculated by:

$$P_{R,CSCT} = P_{R,c,CSCT} + P_{R,f,CSCT} \tag{6.19}$$

where, $P_{R,c,CSCT}$ and $P_{R,f,CSCT}$ are the contribution of the concrete and the fibers to the punching capacity, respectively (MAYA et al., 2012). The contribution of concrete, which represents the failure criterion of NSC flat slabs without transverse reinforcement, can be calculated as (MAYA et al., 2012):

$$P_{R,c,CSCT} = \frac{3/4 \cdot \sqrt{f_{cm}}}{1+15 \cdot \frac{\psi_{CSCT} \cdot d}{d_{g0} + d_{ag}}} \cdot (b_0 \cdot d) \tag{6.20}$$

where, ψ_{CSCT} is the slab rotation at failure; d is the effective depth of the slab; b_0 is the control perimeter at a distance of $d/2$ from the face of the column; f_{cm} is the average compressive strength of the concrete; d_{ag} is the maximum aggregate size of the concrete, and d_{g0} is a reference aggregate size set to 16 mm (MAYA et al., 2012). For symmetrical slab-column connections, the rotation ψ_{CSCT} at failure can be estimated according to the provisions of *fib* Model Code 2010 at the Level of Approximation III (FÉDÉRATION INTERNATIONALE DU BÉTON (FIB), 2012; MUTTONI et al., 2013; MUTTONI; FERNÁNDEZ RUIZ, 2012):

$$\psi_{CSCT} = 1.2 \cdot \frac{r_s}{d} \cdot \frac{f_y}{E_s} \cdot \left(\frac{P}{P_{flex}} \right)^{3/2} \tag{6.21}$$

with r_s equal to the distance from the column axis to the line of contra-flexure of the bending moments, f_y the average yield strength of the flexural reinforcement, and E_s the modulus of elasticity of the longitudinal reinforcement (MUTTONI, 2008). The flexural capacity P_{flex} for the square slabs tested by Zohrevand et al. (2014) as well the slabs in the parametric analysis, was calculated as suggested by Zohrevand et al. (2014):

$$P_{flex} = 8 \cdot m_R \cdot \left(\frac{1}{1 - \frac{c_{load}}{B}} - 3 + 2\sqrt{2} \right) \tag{6.22}$$

where B and c_{load} are the dimensions of the slab and plate load, respectively (both in mm); m_R is the average flexural strength per unit width in the support strip. The yield flexural

strength per unit width m_R for SFRC, which includes the contribution of the fibers, is calculated as Maya et al. (2012):

$$m_R = \rho \cdot d^2 \cdot f_y \cdot \left[1 - \frac{\beta_1 \cdot \left(\rho \cdot f_y + f_{ct2,f} \cdot h/d\right)}{2 \cdot \left(\alpha_{cc} \cdot f_{cm} + f_{ct2,f}\right)}\right] + h^2 \cdot \frac{f_{ct2,f}}{2} \cdot \left[1 - \frac{\rho \cdot f_y \cdot d/h + f_{ct2,f}}{\left(\alpha_{cc} \cdot f_{cm} + f_{ct2,f}\right)}\right] \cdot \left[1 + \frac{\rho \cdot f_y \cdot d/h + f_{ct2,f}}{\alpha_{cc} \cdot f_{cm} + f_{ct2,f}} \cdot \left(1 - \beta_1\right)\right] \quad (6.23)$$

β_1 is the factor that is the parameter that defines the depth of the equivalent rectangular stress block, calculated as $\beta_1 = 0.80 - (f_{cm}\text{-}50)/400$; $f_{ct2,f}$ is the residual tensile strength or tensile stress in fiber-reinforced concrete for a crack opening w = 3 mm. In this study, $f_{ct2,f}$ was calculated as:

$$f_{ct2,f} = \begin{cases} f_{Ftu} = f_{R1}/3, \text{with} \quad f_{R1} = 7.5 \cdot \left(\dfrac{\rho_f \cdot l_f}{d_f}\right)^{0.8}, \text{for SFRC} \\ 0.3 \cdot \sqrt[3]{f_{cm}^{\ 2}}, \text{for UHPFRC (proposed in this study)} \end{cases} \quad (6.24)$$

α_{cc} is factor that accounts for long-term effects on the compressive strength and unfavorable effects from the way load is applied (GOUVEIA et al., 2019a).

In the simplified form Maya et al. (2012), the contribution of the fibers $P_{R,f,CSCT}$ to the punching capacity can be calculated as:

$$P_{R,f,CSCT} = A_p \cdot \sigma_{tf} \quad (6.25)$$

In Eq. (6.25), A_p is the horizontally projected area of the punching failure surface and σ_{tf} is the fiber bridging stress, which can be calculated according to the Variable Engagement Model (VOO; FOSTER, 2003):

$$\sigma_{tf} = K_f \cdot \alpha_f \cdot \rho_f \cdot \tau_b \quad (6.26)$$

where K_f is the global orientation factor; ρ_f is the fiber volume content; τ_b is the bond stress between the fibers and the concrete matrix, and α_f is the aspect ratio of the fibers, defined as the ratio between the length (l_f) and diameter (d_f) ($\alpha_f = l_f/d_f$) (MAYA et al., 2012). According to Voo and Foster (2004, 2003), K_f can be estimated by:

$$K_f = \frac{1}{\pi} \arctan\left(\alpha_e \cdot \frac{w}{d_f}\right) \cdot \left(1 - \frac{2}{l_f}\right)^2 \quad (6.27)$$

where α_e is defined as an engagement parameter that can be taken as α_e = 3.5. According to Maya et al. (2012), the interfacial bond strength between the matrix and the fiber τ_b is given by:

$$\tau_b = k_b \cdot \sqrt{f_{cm}} \quad (6.28)$$

6.4.2 Proposed approaches for UHPFRC and NSC-UHPFRC flat slabs

The equations developed to calculate the unitary flexural capacity of SFRC flat slabs could underestimate the flexural capacity of UHPFRC slabs due to the lower residual tensile strength from the SFRC compared to the UHPFRC. In this way, a set of equations, based on the work from Fehling et al. (2014), was devised for estimating the unitary moment capacity m_{R1} of slab cross-sections with UHPFRC distributed over (i) the full depth, (ii) at the tension side and (iii) at the compression side of the slabs (Table 6-9).

Table 6-9 - Equations for estimating the compression zone depth (x) and unitary moment capacity (m_{R1}) for sections with different distributions of UHPFRC over the thickness.

Full depth
$x = A_s \cdot f_y + 0.81 \cdot h_{slab} \cdot b_w \cdot f_{Ftu} / \left(0.5 \cdot b_w \cdot f_{c,UHPFRC} + 0.81 \cdot b_w \cdot f_{Ftu}\right)$ $m_{R1} = 0.5 \cdot x \cdot b_w \cdot f_{c,UHPFRC} \cdot \left(d - \frac{x}{3}\right) - 0.81 \cdot (h - x) \cdot b_w \cdot f_{Ftu} \cdot (d - 0.45 \cdot x - 0.55 \cdot h)$ (6.29)
Tension side
$x = A_s \cdot f_y + 0.81 \cdot h_{slab} \cdot b_w \cdot f_{Ftu} / \left(0.5 \cdot b_w \cdot f_{c,NSC}\right)$ $m_{R1} = 0.5 \cdot x \cdot b_w \cdot f_{c,NC} \cdot \left(d - \frac{x}{3}\right) - 0.81 \cdot h_{UHPFRC} \cdot b_w \cdot f_{Ftu} \cdot \left(\frac{h_{UHPFRC}}{2} - (h_{slab} - d)\right)$ (6.30)
Compression side
$x = \left(A_s \cdot f_y + 0.81 \cdot h_{UHPFRC} \cdot b_w \cdot f_{Ftu}\right) / \left(0.5 \cdot b_w \cdot f_{c,UHPFRC} + 0.81 \cdot b_w \cdot f_{Ftu}\right)$ $m_{R1} = 0.5 \cdot x \cdot b_w \cdot f_{c,UHPFRC} \cdot \left(d - \frac{x}{3}\right) - 0.81 \cdot (h_{UHPFRC} - x) \cdot b_w \cdot f_{Ftu} \cdot (d - 0.55 \cdot h_{UHPFRC} - 0.45 \cdot x)$ (6.31)

Source: Author.

Figure 6-6a shows the assumed stress distribution and internal forces on the cross-sections with UHPFRC distributed over the entire thickness. Figure 6-6b shows the locations from the resulting tensile force carried by the fibers upon reaching the ultimate limit state (F_{fd}) assuming a more realistic stress distribution on the cross-section (FEHLING et al., 2014). Figure 6-6c shows the equivalent stress blocks for Figure 6-6b that make the calculations more straightforward and provide similar flexural capacity results (FEHLING et al., 2014). Similar assumptions described in Figure 6-9 were considered in evaluating the flexural capacity for cross-sections NSC-UHPFRC accounting for the thickness of the UHPFRC layer.

The equations shown in Table 6-9 were used to predict the equivalent bending moment due to the different materials used over the slab thickness (m_{R1}) in the region around the concentrated load (see Figure 6-6d). The unitary bending moment over the remaining region that contains only NSC ($m_{R,NSC}$) was calculated according to Muttoni (2008):

$$m_{R,NSC} = \rho \cdot d^2 \cdot f_y \cdot \left(1 - \frac{\rho \cdot f_y}{2 \cdot f_{c,NSC}}\right) \tag{6.32}$$

Figure 6-6 - a) Stress distribution and resultant internal forces for the cracked cross-section; b) realistic stress distribution and resultant tensile force carried by the fibers upon reaching the ultimate limit state; c) stress blocks equivalent to b) (adapted from Fehling et al. (2014)); and d) outlined regions with different flexural capacities and equivalent flexural capacities.

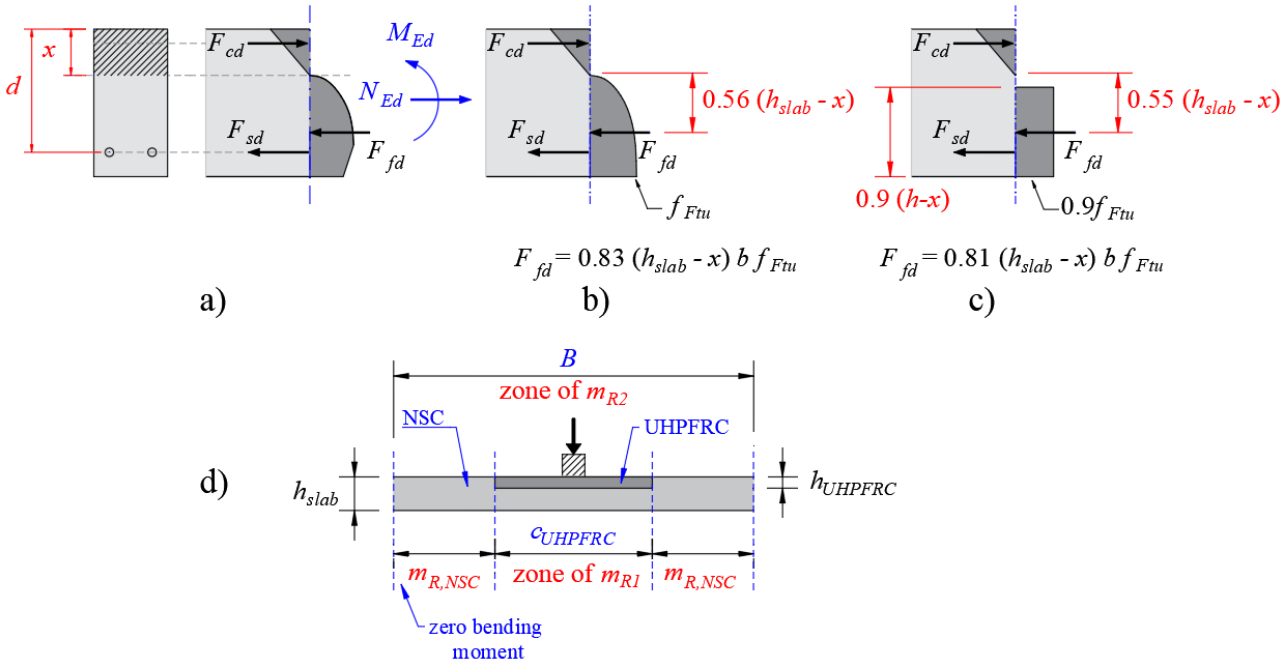

Source: Author.

For slabs with the rational use of UHPFRC, the different distributions of UHPFRC over the slab plan were also accounted for (Figure 6-6d). The equivalent moment capacity per unit width m_{R2} at the support strip was calculated based on Gouveia et al. (2019a) by the following expression:

$$m_{R2} = \frac{m_{R1} \cdot c_{UHPFRC} + m_{R,NSC} \cdot \left(B - c_{UHPFRC}\right)}{B} \tag{6.33}$$

where c_{UHPFRC} is the strip width of the UHPFRC region in the plan and B is the slab span length. In Table 6-9, f_{Ftu}, was calculated according to Hoang and Fehling (2017):

$$f_{Ftu} = 0.3 \cdot f_{c,UHPFRC}^{\ 2/3} \tag{6.34}$$

The first investigated approach to predict the punching capacity of UHPFRC flat slabs, as well as NSC-UHPFRC flat slabs, was based on trying to adjust the failure criterion derived for SFRC from Maya et al. (2012) using characteristics from the UHPFRC. The higher packing of UHPFRC compared to SFRC allows reaching enhanced bond factors k_b for straight steel fibers, such as used in the experiments by Zohrevand (2014). Supported by the experimental results from (LANWER et al., 2019) and (DENARIÉ; HABEL; BRÜHWILER, 2003) with similar micro-coated steel fibers, the bond factor k_b was assumed equal to 1 in the calculations with the CSCT derived for SFRC (MAYA et al., 2012). In order to consider the thickness of the UHPFRC layer into the computed contribution from the fibers, the following expression was used:

$$P_{R,f,CSCT} = A_p \cdot \sigma_{tf} \cdot \left(\frac{h_{UHPFRC}}{h_{slab}} \right) \tag{6.35}$$

The term h_{UHPFRC}/h_{slab} was added to Eq. (6.35) to deal with the rational use of the UHPFRC over the slab thickness. h_{UHPFRC} and h_{slab} are the thickness of the UHPFRC layer and the slab thickness, respectively.

The second approach investigated was based on the modified failure criterion proposed by Moreillon (2013), which suggests the following simplified failure criterion for UHPFRC flat slabs, also based on the CSCT:

$$P_{R,f,CSCT} = \frac{1}{K_{fo}} \cdot \frac{f_{Ftu} / \gamma_f}{1 + \frac{\psi_{CSCT} \cdot d}{w_u}} \cdot b_0 \cdot d \cdot \left(\frac{h_{UHPFRC}}{h_{slab}} \right) \tag{6.36}$$

where K_{f0} is the fiber orientation coefficient for general effects (taken equal to 1 for most applications (MOREILLON, 2013)), and f_{Ftu} is the residual tensile strength at an ultimate crack opening w_u. In this study, f_{Ftu} for the UHPFRC was assumed as the peak tensile strength (expression (6.34)).

For slabs that use only UHPFRC (for instance, U1.8 and U0.6), w_u assumed a value equals $l_f/4$, as suggested by Moreillon (2013). On the other hand, for specimens with the rational use of UHPFRC, the value of $w_u = \psi_{CSCT} \cdot d/6$ suggested by Maya et al. (2012) fitted better the experimental (ZOHREVAND et al., 2014) and numerical results (Section 7). The different values of w_u were justified here because the deformation capacity of NSC-UHPFRC flat slabs can be limited by the punching capacity from the outer region without UHPFRC, such as identified by Zohrevand et al. (2014).

In order to account for the different contributions of the concrete ($P_{R,c,CSCT}$) between the NSC and the UHPFRC, this parameter was weighted according to the thickness of the enhanced material in the slabs with the rational use of the UHPFRC:

$$P_{R,c,CSCT} = \frac{3/4 \cdot \sqrt{f_{c,UHPFRC}}}{1+15 \cdot \frac{\psi_{CSCT} \cdot d}{d_{g0}+d_{ag}}} \cdot (b_0 \cdot d) \cdot \left(\frac{h_{UHPFRC}}{h_{slab}} \right) + \frac{3/4 \cdot \sqrt{f_{c,NSC}}}{1+15 \cdot \frac{\psi_{CSCT} \cdot d}{d_{g0}+d_{ag}}} \cdot (b_0 \cdot d) \cdot \left(1 - \frac{h_{UHPFRC}}{h_{slab}} \right) \quad (6.37)$$

where $f_{c,UHPFRC}$ and $f_{c,NSC}$ are the compressive strengths of the UHPFRC and NSC, respectively.

6.5 Validation of the fem and modeling choices study

This section presents the validation of the FEM proposed to simulate the behavior and punching capacity of reinforced concrete slabs fully made with NSC or fully made with the UHPFRC.

6.5.1 Validation of the proposed FEM for NSC flat slabs

Figure 6-7 compares the FEM results with the experiments using NSC in terms of the punching capacity and failure mode. The proposed FEM reproduced reasonably well not only the punching capacity (Figure 6-7) but also the governing failure mode of the control slabs according to the cracking pattern (Figure 6-8). As described in reference (ZOHREVAND et al., 2014), the slab C0.6 developed reinforcement yielding at failure (characteristic of flexure-induced punching) and C1.8 showed a brittle punching failure without yielding of the reinforcement at failure. Figure 6-8 confirms that the numerical models accurately predicted the cracking pattern and failure mechanisms of the specimens.

Figure 6-7 - Comparison between load-displacement of experiment and NLFEA for a) C1.8 and b) C0.6.

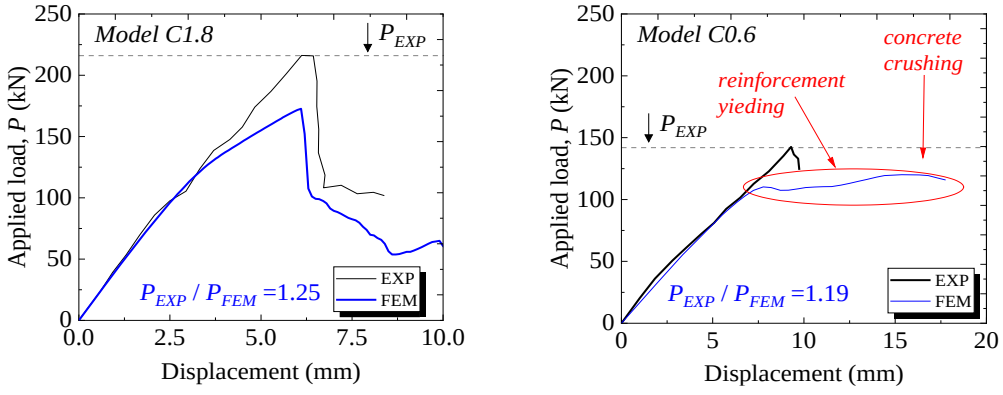

Source: Author.

Figure 6-8 - Comparison between crack patterns after the failure of experimental tests and NLFEA for a) C1.8 and b) C0.6. Note: PE is the tension plastic strain.

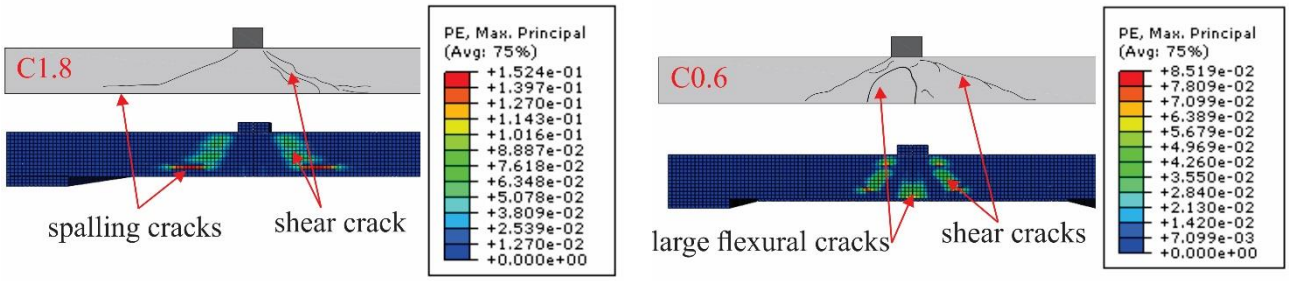

a) b)

Source: Author.

Figure 6-7b shows that at failure, the FEM of the test C0.6 showed a slight drop in the measured punching force followed by an increase in capacity until a higher peak load. This behavior indicates that the FEM allowed load redistribution with the reinforcement yielding until reaching concrete crushing at the compression side of the slab. This behavior was not identified in the test because the test was potentially stopped when the first significant drop in the measured load occurred and major cracks had formed. Another explanation is that the tests may have been conducted by force control instead of displacement control. Therefore, some differences between the experimental and numerical graphs are reasonable for the post-peak load branch.

6.5.2 Validation of the proposed FEM for UHPFRC flat slabs

Figure 6-9 and Figure 6-10 compare test and numerical results in terms of crack pattern and predicted punching shear capacity for the flat slabs built with UHPFRC and different reinforcement ratios. The proposed NLFEA accurately predicted the crack pattern of U0.6 and U1.8 at the bottom side and in the cut views (Figure 6-9a and Figure 6-10a). The punching capacity predictions with the NLFEA differed from the experimental ones by less than 20%. The load-displacement graphs from the numerical models reproduced well the main characteristics observed at the tests: (i) punching capacity and (ii) yielding of the reinforcement prior to failure, (iii) the shape of the load-displacement graph in the non-linear branch for U0.6 (Figure 6-9b) and (iv) sharp decrease of the punching load after a certain degree of reinforcement yielding for U1.8 (Figure 6-10b). Since the cracking pattern based on the tensile damage (DAMAGET) of concrete for U0.6 and U1.8 was diffuse due to the higher post-peak tensile strength from the UHPFRC, the cracking pattern was evaluated at these FE models by the compressive damage (DAMAGEC) in Figure 6-9a and Figure 6-10a. The results confirm

that the failure mode of U1.8 was governed by reaching the full capacity of the compressive struts close to the loaded area.

Figure 6-9 - Cracking pattern of slab U0.6 a) experimental test and numerical model; b) prediction of the punching capacity. Note: DAMAGEC is the damage variable in compression.

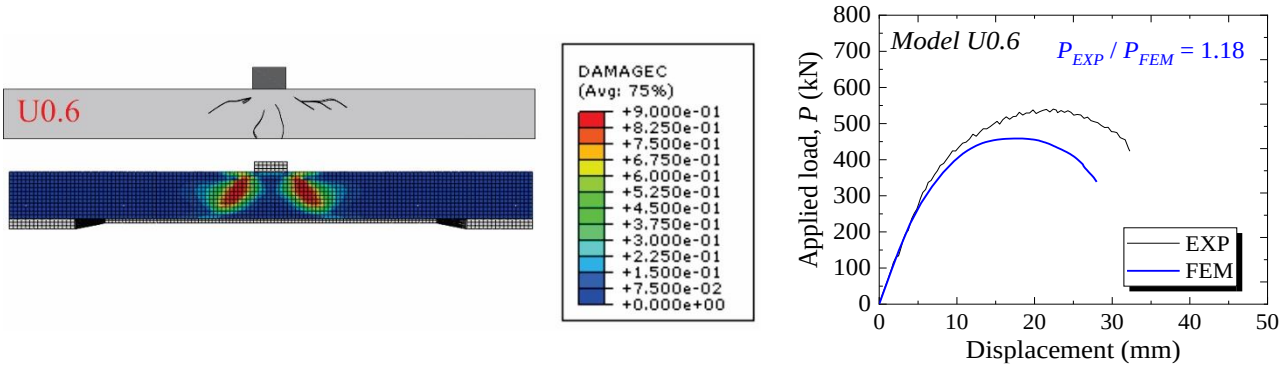

a) b)

Source: Author.

The main differences between the experimental and numerical curves relate to the vertical displacements at failure. While the numerical model reached the maximum capacity at a displacement lower than the control experiment for U0.6 (Figure 6-9b), the numerical model of U1.8 failed at a higher vertical displacement than the experimental model (Figure 6-10c). Since the punching capacity and cracking pattern were well-represented by the numerical models, these differences in capturing the deflections at failure were considered acceptable. In this study, these differences can be related to the different stiffness of the support conditions used in the tests.

Figure 6-10 – Cracking pattern and load-displacement graph of slab U1.8 a) experimental test and numerical model; b) prediction of the punching capacity. Note: DAMAGEC is the damage variable in compression.

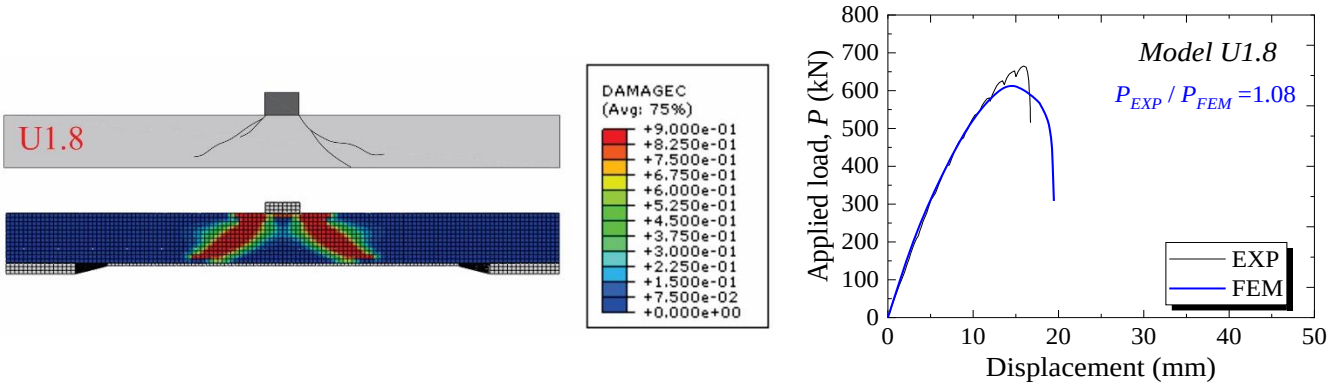

a) b)

Source: Author.

Figure 6-10 shows that the specimens with a higher amount of reinforcement (U1.8) failed at the struts that carry shear close to the loaded area, while the specimen with a lower reinforcement ratio (U0.6) failed by a combination of reinforcement yielding (softer decrease of the measured load) with the concrete crushing close to the loaded area. Proof that the UHPFRC material model was adequately represented in the FEM was that the governing failure mode of the tests was well-predicted despite the significant difference in the reinforcement ratios between slabs U1.8 and U0.6 and a relatively small difference in the punching capacities of these tests (22%).

6.6 Predicting the punching capacity of NSC-UHPFRC flat slabs

This section presents the validation of the FEM to simulate the behavior and punching capacity of slabs that combined the use of NSC and UHPFRC. Besides, this section also presents the comparison between tested and predicted resistances using the analytical and numerical approaches.

6.6.1 NLFEA results for NSC-UHPFRC-flat slabs

This section investigates the level of accuracy of the FEM proposed to describe the behavior of slabs with the rational use of UHPFRC at shear-critical regions (NSC-UHPFRC flat slabs). In this section, the material parameters described in Table 6-7 were used to model the non-linear behavior of NSC and UHPFRC, respectively.

Figure 6-11 shows that the proposed material models for NSC and UHPFRC allowed predicting the punching capacity and the behavior of the hybrid flat slabs accurately. Since the tests from Zohrevand et al. (2014) may have been unloaded after reaching the maximum punching capacity, all reported force-displacement curves at failure could be misinterpreted as a brittle failure mode due to the sharp decrease of load at failure. Because of this, Figure 6-11 reports if reinforcement yielding was measured in the tests. Notably, when a brittle failure mode was observed in the control slabs, a sharp decrease of the load was also observed in the NLFE models at failure. Moreover, the finite element models captured reinforcement yielding of all control slabs that showed flexure-induced punching. The maximum error in the predicted punching capacities was 21%, which is within the mean error of material parameters such as the concrete tensile strength. Therefore, the level of accuracy reached was considered satisfactory.

Figure 6-11 – Punching capacity predictions with the NLFEA for the members with the rational use of UHPFRC (NSC-UHPFRC flat slabs) tested by Zohrevand et al. (2014).

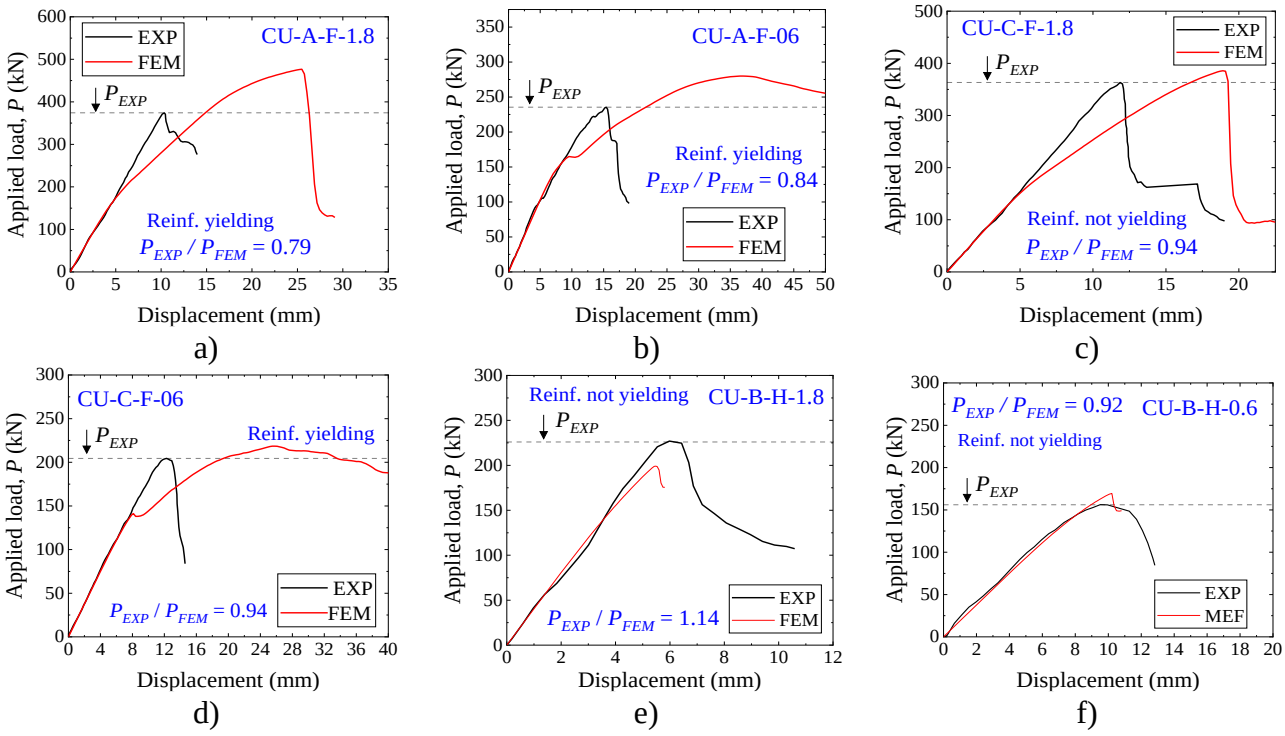

Source: Author.

Figure 6-12 shows that the FE models reproduced the cracking pattern in the control slabs at failure well. Minor differences were related to the development of the flexural crack at the interface between NSC and UHPFRC in some numerical models (Figure 6-12a), which were not identified for the control slabs.

Figure 6-12 - Comparison between crack patterns observed in the tests and in NLFEA for CU-A-F-1.8 and CU-B-H-1.8. Note: DAMAGET is the damage variable in tension.

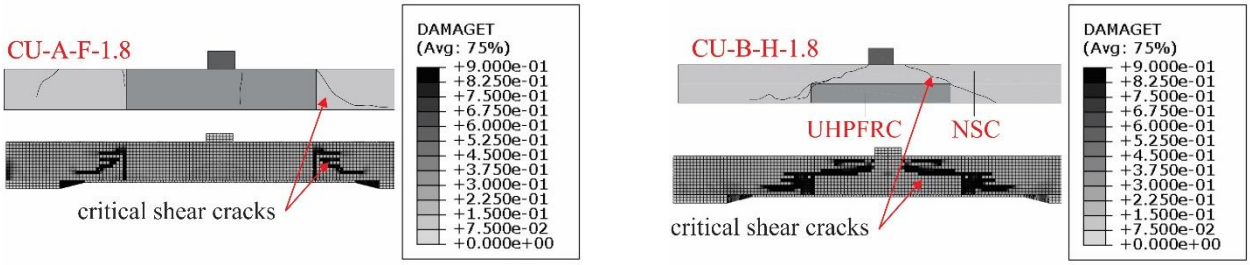

Source: Author.

The higher tensile damage at the shear crack in NSC indicates that the crack opening at the shear crack was higher than in the UHPFRC, despite the higher flexural action and shear concentration in the column vicinity. Consistently, no visible cracks were identified in the

UHPFRC at failure (ZOHREVAND et al., 2014). This behavior may be related not only to the higher tensile and compressive strength of the UHPFRC compared to NSC but also to its capacity to redistribute inner forces due to its higher residual tensile strength after cracking.

6.6.2 Analytical results and comparison with NLFEA

Table 6-10 shows that the punching capacities predicted for NSC flat slabs (C1.8 and C0.6) with the CSCT (MUTTONI, 2008) are similar to those predicted with NLFEA, such as shown by Millingan et al. (2021) in similar analyses. However, limited information is available about the level of accuracy of the CSCT and NLFEA to predict the punching capacity of UHPFRC flat slabs (MOREILLON, 2013). Table 6-10 shows that the proposed NLFE models predicted well the punching capacity of the UHPFRC flat slabs. The values reached with the CSCT were more conservative using the failure criteria derived for SFRC (MAYA et al., 2012), despite using some adjustments to account for the improved performance from the UHPFRC (Section 4.2) (P_{exp}/P_{calc} equal to 1.51 and 1.36, respectively for U1.8 and U0.6, see Table 6-10). However, improved predictions of the punching capacity were found using the simplified failure criteria proposed by Moreillon (2013) (P_{exp}/P_{calc} equal to 1.25 and 1.26, respectively). Comparatively, the predictions with the semi-empirical model from Harris (HARRIS, 2004), whose results were reported in Zohrevand et al. (2014) underestimated the punching capacities significantly for all tests. The model proposed by Harris (2004) is inspired by ACI 318-11 (ACI COMMITTEE 318, 2011) and was calibrated for experiments with unreinforced UHPFRC flat slabs. In this model, a shear cone starting from the column face and propagating at a 34° angle was assumed.

Table 6-11 then shows a similar comparison for the control slabs with the rational use of UHPFRC in the region close to the loaded area. The contribution of $P_{R,f,CSCT}$ was neglected for tests CU-B-H-1.8 and CU-B-H-0.6 since these did not develop a critical shear crack crossing the fibrous material (ZOHREVAND et al., 2014). This comparison shows that the proposed FE models accurately predicted the punching capacity. The mean ratio between experimental and predicted punching capacities was equal to 0.93 with a coefficient of variation (COV) of 13%, which is a reasonable value given the complexity of the problem and several parameters involved.

Table 6-10 – Comparison between experimental and predicted punching capacities (P_{exp}/P_{calc}) according to NLFEA, Harris (2004), the CSCT models for SFRC (MAYA et al., 2012; MUTTONI, 2008), and modified for UHPFRC (MOREILLON, 2013).

Model	Grade	P_{exp} / V_{FEM}	P_{exp} / V_{Harris}[a]	P_{exp} / P_{CSCT}[b]	P_{exp} / P_{CSCT}[c]
		NLFEA	Harris (2004)	$P_{R,f,CSCT}$ by Maya et al. (2012)	$P_{R,f,CSCT}$ by Moreillon (2013)
C1.8	Full depth	1.25	4.15	1.10	1.10
C0.6	Full depth	1.19	2.68	1.05	1.05
U1.8	Full depth	1.08	3.72	1.51	1.25
U0.6	Full depth	1.18	3.04	1.36	1.26
	AVG	1.17	3.40	1.25	1.16
	COV	6.1%	19.5%	17.1%	8.84%

[a] P_{Harris} values reported by Zohrevand et al. (2014). [b] $P_{R,c,CSCT}$ given by eq. (6.20) and $P_{R,f,CSCT}$ by eq. (6.25); [c] $P_{R,c,CSCT}$ given by eq. (6.20) and $P_{R,f,CSCT}$ calculated by eq. (6.36); Source: Author.

Table 6-11 – Comparison between experimental and predicted punching capacities with the investigated approaches.

Model	Grade	P_{exp} / P_{FEM}	P_{exp} / P_{Harris} [a]	P_{exp} / V_{CSCT} [b]	P_{exp} / V_{CSCT} [c]
		NLFEA	Harris (HARRIS, 2004)	$P_{R,f,CSCT}$ by Maya (MAYA et al., 2012)	$P_{R,f,CSCT}$ by Moreillon (MOREILLON, 2013)
CU-A-F-1.8	Full depth	0.78	2.10	0.92	1.09
CU-A-F-0.6	Full depth	0.84	1.31	0.85	0.86
CU-C-F-1.8	Full depth	0.94	2.32	0.92	1.11
CU-C-F-0.6	Full depth	0.94	1.31	0.97	0.97
CU-B-H-1.8	Half depth	1.14	2.27	0.95	0.95
CU-B-H-0.6	Half depth	0.92	1.56	0.94	0.94
	AVG	0.93	1.81	0.93	0.99
	COV	13.0%	26.1%	4.44%	9.72%

[a] P_{Harris} reported by Zohrevand et al. (2014); [b] $P_{R,f,CSCT}$ calculated by eq. (6.35); [c] $P_{R,f,CSCT}$ calculated by eq. (6.36); Source: Author.

Comparatively, this level of accuracy from the FEM was similar to that reported by Wu et al. (2019) for a numerical study using the UHPFRC as an extra strengthening layer. Moreover, the predicted punching capacities with FEM were more accurate than semi-empirical approaches such as those proposed by Harris (2004). The predictions of the CSCT using the models from Maya (2012) and Moreillon (2013), adjusted for slabs with the rational use of UHPFRC, reached similar levels of accuracy to those provided by the NLFEA.

6.7 Parametric analyses

This section presents the parametric study results with three focuses: (i) investigate the influence of the position of the UHPFRC layer; (ii) investigate the influence of the thickness and size of the UHPFRC layer on the compressed side of the slab, (iii) investigate the accuracy

of the proposed approach to predict the punching capacity of slabs built in the parametric analyses.

6.7.1 Position of the UHPFRC on the slab depth

While some authors investigated the performance of hybrid slabs with the improved material at the tension side of the slab (ZOHREVAND et al., 2014), others used it at the compression side (INÁCIO; LAPI; PINHO RAMOS, 2020). Since the governing shear transfer action of mechanical punching shear models may vary between the aggregate interlock (MUTTONI, 2008) and the compression chord capacity (MARÍ et al., 2018), the location of the enhanced material layer may influence the punching capacity differently accordingly for the reinforcement ratio of the slabs.

Figure 6-13 – Effect of the location of the UHPFRC at the tension or compression side of the specimens a) CU-B-H-1.8 and b) CU-B-H-0.6. Note: Thickness of the enhanced material equal to 0.5*h*.

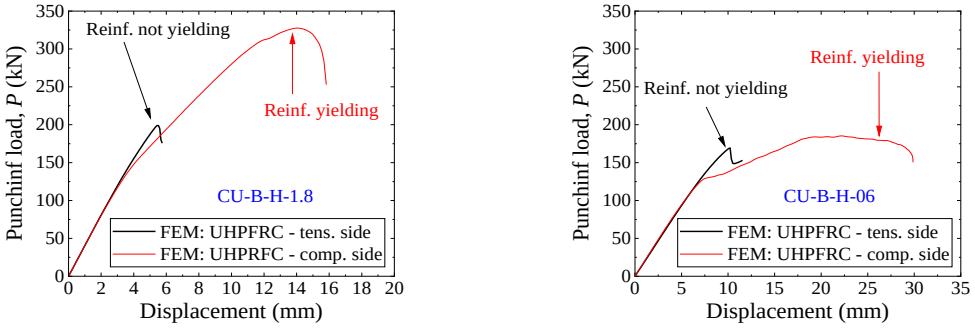

a) b)

Source: Author.

Figure 6-13a shows that placing the UHPFRC on the compression side for slabs with higher ratios of flexural reinforcement (CU-B-H-1.8) improves the punching capacity by around 64% compared to placing the UHPFRC at the tension side, and it increases the deformation capacity of the slab (ductility) markedly. For the slabs with a lower amount of flexural reinforcement (CU-B-H-0.6), the punching capacity did not change significantly comparing the two investigated options (Figure 6-13b). However, adding the UHPFRC on the compression side increased the deformation capacity of the slab-column connection. Since the flexure capacity is enhanced more efficiently with the UHPFRC placed at the tension side (see Table 6-9), this result was justified because placing the UHPFRC at the compression side hampers the development of the critical shear crack at failure more efficiently than placing the UHPFRC at the tension side of the slabs. Proof of this is that the critical shear crack did not cross the UHPFRC in the tests CU-B-H-1.8 and CU-B-H0.6 from Zohrevand et al. (2014).

6.7.2 Punching capacity enhancement with the rational use of UHPFRC

A parametric study was carried out to investigate the effect of different configurations of the UHPFRC layer placed in the shear-critical region for punching. In total, 48 numerical models were performed, varying the reinforcement ratio ρ (0.6%; 1.2% and 1.8%), the depth of the UHPFRC layer (0.25h, 0.33h, 0.50h, 1h), and the size of the UHPFRC region in plan view (square areas with edges at a distance 0.5h (configuration a), 1h (configuration b),1.5h (configuration c) and 2h (configuration d) from the column edges (Figure 6-14). The slabs had the geometry and support conditions of the hybrid slabs tested by Zohrevand et al. (2014). For these analyses, the material properties of the NSC were those of the slabs C1.8 and C0.6 tested by Zohrevand (2014): f_{cm} = 45 MPa and d_{ag} = 9.5 mm. The compressive strength and tensile strength of the UHPFRC were fixed as 140 MPa and 8 MPa, respectively, as previously studied. The material models used for both concretes are described in Table 6-7.

Figure 6-14 – Configurations studied for the rational use of UHPFRC.

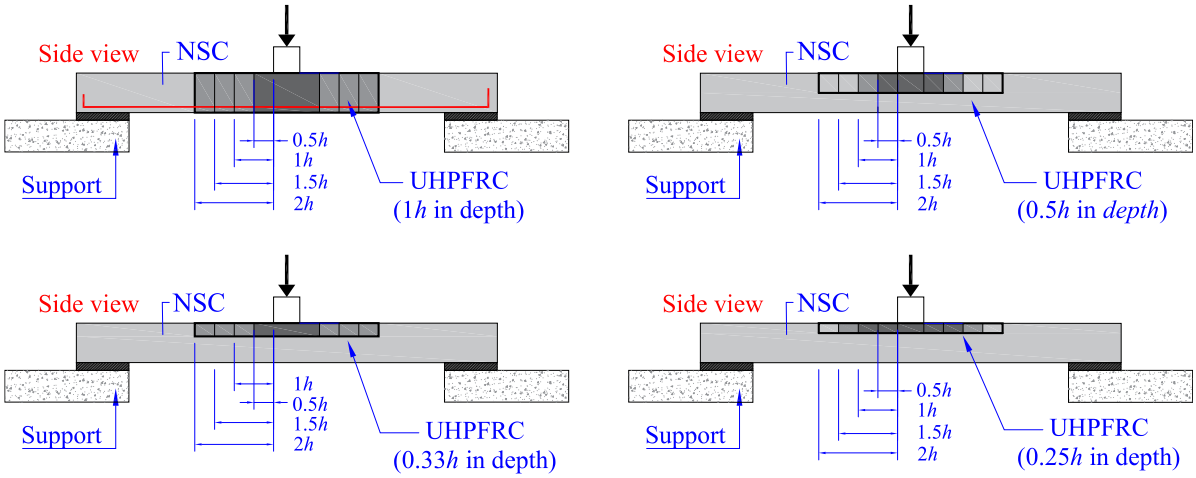

Source: Author.

Figure 6-15 shows that the use of enhanced material such as the UHPFRC increases the punching capacity regardless of the reinforcement ratios. The results of punching capacities enhancements herein reported are based on the comparison with the FEM predictions for specimens without UHPFRC (NSC flat slabs). The punching capacity enhancements varied between 26% and 156%, according to the reinforcement ratios and configurations of UHPFRC investigated. For the smaller thickness of the UHPFRC layer (0.25h) and the minimum area covered around the column load (0.5h from the load edge), the punching capacity enhancements varied between 26% and 29% according to the reinforcement ratios. Using the UHPFRC layer over the entire slab thickness and in a square area of 2h from the loading edges allowed reaching punching capacity enhancements of over 130% regardless of the reinforcement ratios.

However, different behaviors occurred according to the thickness of the UHPFRC layer. For the small thicknesses of the UHPFRC layer (0.25*h* and 0.33*h*), the increase of the UHPFRC layer in the horizontal plane did not significantly increase the punching capacity enhancements. On the other hand, when the UHPFRC layer was used over the entire slab thickness, the punching capacity enhancements increased almost linearly with the horizontal area of the UHPFRC layer, regardless of the reinforcement ratios. The increase of the punching capacity enhancements varied according to the reinforcement ratios for the slabs with the UHPFRC layer used at a half-thickness (0.5*h*). For the slabs with the smallest reinforcement ratio (ρ = 0.6%), the punching capacity enhancement increased from 42% to 62%, increasing the UHPFRC layer area from configuration 0.5*h* to configuration 2*h*. For the slabs with higher reinforcement ratios (ρ = 1.8%), the punching capacity enhancement varied between 54% and 94% according to the UHPFRC layer area.

Figure 6-15 - Punching capacity enhancements with the rational use of UHPFRC according to the UHPFRC layer thickness over the depth (0.25*h*, 0.33*h*, 0.50*h* and 1*h*), use of UHPFRC in plan (Figure 6-14) and for different values of the longitudinal reinforcement ratio: a) ρ = 0.6%; b) ρ = 1.2%; c) ρ = 1.8%. Legend: FY and PY indicate punching failures with full (FY) and partial (PY) yielding of flexural reinforcement.

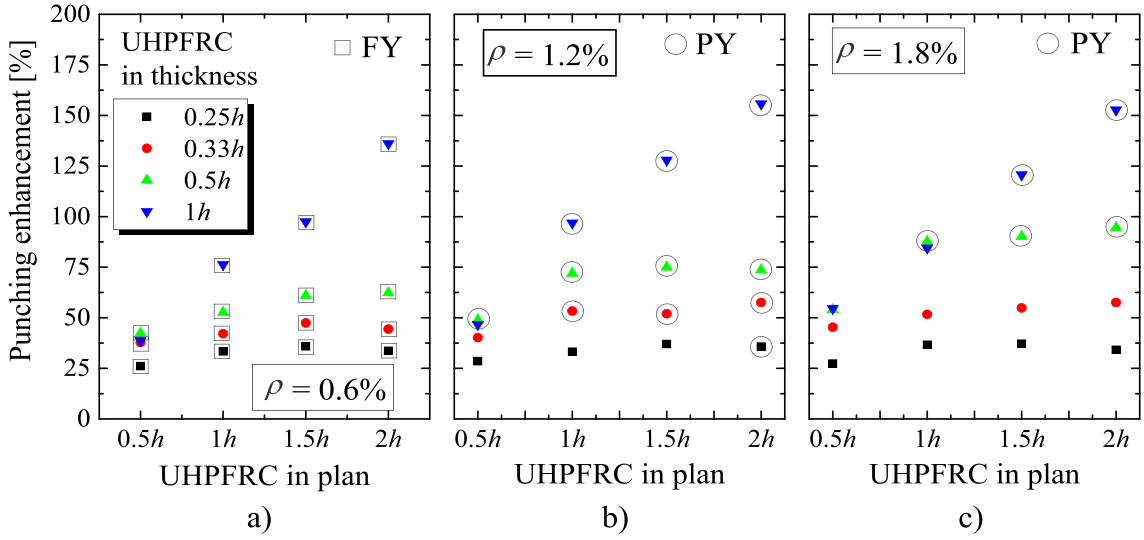

Source: Author.

As observed in the control tests from Zohrevand et al. (2014), different punching failure mechanisms were identified in the parametric analyses according to the reinforcement ratios. All slabs with the smallest reinforcement ratio (ρ = 0.6%) developed flexure-induced punching failures with full yielding of flexural reinforcement (FY). The failure mode from slabs with ρ equal to 1.2% and 1.8% varied between brittle punching failures (without any reinforcement yielding) and punching failure with partial yielding of the flexural reinforcement (PY). Figure

6-15 indicates which tests developed reinforcement yielding at failure. Notably, most configurations studied developed partial or full yielding of the flexural reinforcement, which assures higher deformation capacity for such joints. Even though some specimens showed no signal of flexural yielding at failure, the deformation capacity increased compared to the control slabs. Therefore, the failure mode in the slab-column connections with the rational use of UHPFRC tends to be less brittle than in NSC slab-column connections.

6.7.3 Comparison between NLFEA and analytical predictions for NSC-UHPFRC slabs

In daily engineering, analytical models are more practical for assessing problems such as the punching capacity in preliminary designs. In this section, the predicted punching capacities with the NLFEA in the parametric analyses (Section 7.2) were compared to those provided by the proposed analytical approach using the failure criteria from Moreillon (2013) and the proposed adjustments for the rational use of UHPFRC (Section 4.2).

Figure 6-16 shows the comparison between numerical and analytical predictions of punching capacity according to the configuration of UHPFRC used in the slabs. The mean ratio between numerical and analytical punching capacities for the entire dataset, including 48 results, was 1.09 with a COV equal to 10.3%. These results indicate a close approximation between the NLFEA and the mechanical punching shear model based on the CSCT. Therefore, the CSCT can be extended to the use of NSC-UHPFRC flat slabs in design practice.

Figure 6-16 - Comparison between numerical results and predicted punching shear capacities by the proposed approach for NSC-UHPFRC flat slabs: a) ρ = 0.6%; (b) ρ = 1.2% and c) ρ = 1.8%.

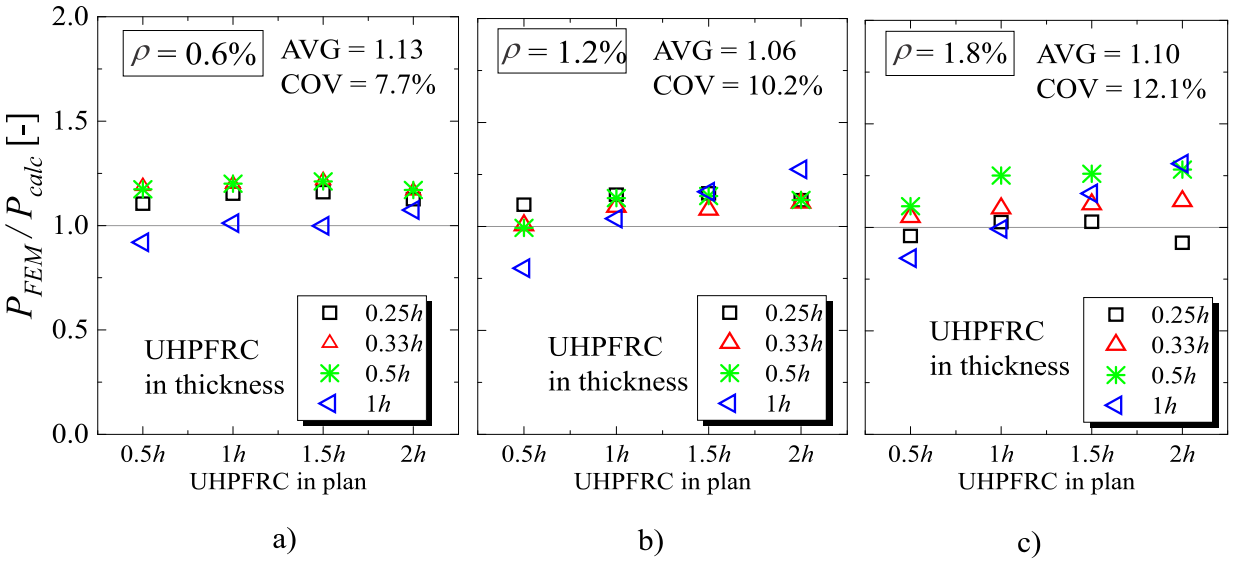

Source: Author.

6.8 Discussion of Chapter 6

Only a limited number of studies have investigated the punching capacity of flat slabs with total depth (MOREILLON, 2013; SHOUKRY; TARABIA; YASSIN, 2020) or the rational use of UHPFRC (ZOHREVAND et al., 2014) at the shear-critical regions, which has hampered the spreading of this design practice. Notably, most studies make use of the UHPFRC only on the tension side of the slab (BASTIEN-MASSE; BRÜHWILER, 2016a, 2016b; BRÜHWILER, 2019; FISET; BASTIEN; MITCHELL, 2016; MENNA; GENIKOMSOU, 2021; WU et al., 2019). At the same time, while modeling approaches are well established to investigate the behavior of flat slabs with NSC (GENIKOMSOU; POLAK, 2015, 2016, 2017a; MILLIGAN; POLAK; ZURELL, 2020, 2021), similar guidelines for UHPFRC involving the CDP are scarce (MENNA; GENIKOMSOU, 2021; WU et al., 2019). Furthermore, most of them were not validated to predict the behavior of UHPFRC-flat slabs since they used this material only as extra strengthening layer. Therefore, this chapter provides a useful tool to suggest how the CDP model can be calibrated to model UHPFRC and then, after proper calibration, to extend the knowledge about the punching behavior of UHPFRC flat slabs and hybrid slabs (NSC-UHPFRC) through parametric studies.

The calibrated FEM predicted precisely the punching shear capacity and the governing failure mode of NSC, UHPFRC, and NSC-UHPFRC flat slabs. Compared to other studies that also modeled UHPFRC with the CDP model (BAHIJ et al., 2018; FANG et al., 2019; JANG et al., 2018; MAHMUD; YANG; HASSAN, 2013; MARTÍN-SANZ et al., 2020; OTHMAN; MARZOUK, 2018; WU et al., 2019), most of the input parameters used herein were derived from inverse analyses of experimental investigations (KRAHL; CARRAZEDO; EL DEBS, 2018; KRAHL; GIDRÃO; CARRAZEDO, 2019), which increases the consistency of the selected parameters and the validity of the results. For instance, some authors proposed to use a dilation angle ranging from 10º to 15º due to the enhanced dense microstructure of the UHPFRC (CHEN; GRAYBEAL, 2011; OTHMAN; MARZOUK, 2018). However, the inverse analyses of triaxial tests indicated that a value of 54º should be considered for modeling UHPFRC (KRAHL; CARRAZEDO; EL DEBS, 2018). This occurs because the higher post-peak tensile strength from the UHPFRC increases the transversal deformation capacity of the material under high confining stresses.

Section 6 shows that the level of accuracy of the NLFEA proposed was similar to that provided with the CSCT for NSC flat slabs and UHPFRC flat slabs with the recommendations of Moreillon (2013). In contrast, the predictions with the modified CSCT (MAYA et al., 2012)

for SFRC provided more conservative predictions for UHPFRC flat slabs compared to the FEM results. This indicates that the behavior of UHPFRC flat slabs was not fully captured by the investigated approach, probably due to the higher toughness of UHPFRC compared to SFRC.

The parametric analyses (Section 6.7) indicate that placing the UHPFRC on the compression side of flat slabs is more efficient to improve the punching capacity of the slabs than placing the UHPFRC on the tension side of the slabs, mainly for those with higher reinforcement ratios (Figure 6-13a). Conversely, for slabs with lower reinforcement ratios (for instance, ρ = 0.6%), placing the UHPFRC on the tension or compression side did not enhance the punching capacity significantly (Figure 6-13b). However, the deformation capacity of the slabs with UHPFRC on the compression side for such cases was enhanced more efficiently. In summary, these results are in close agreement with those reported by Inácio et al. (2020), which showed by analytical calculations with the CSCT that the beneficial effect provided by the enhanced material such as UHPC increases for higher reinforcement ratios. This behavior occurs because the punching strength is benefited in different ways increasing the reinforcement ratios: (i) the flexural stiffness of the slab increases, which decreases the slab rotations and corresponding crack openings; (ii) the interlocking strength is improved due to the lower crack openings (INÁCIO; LAPI; PINHO RAMOS, 2020; MUTTONI, 2008) and (iii) due to the enhanced fiber bridging stresses along the failure surface (MOREILLON, 2013). Consistently, the CSCT model allows considering all these effects.

The proposed approach to predict the punching capacity of NSC-UHPFRC slabs (Section 4.2), based on the works of Moreillon (2013), Inácio et al. (2020) and Gouveia et al. (2019a) using different types of materials, provided accurate predictions of punching strength for the slabs tested by Zohrevand et al. (2014) (Section 6.2) and close predictions to advanced NLFEA developed in the parametric studies (Section 6.3). Therefore, the proposed approach may be used in the preliminary design for the punching capacity of flat slabs with the rational use of UHPFRC.

As suggestions for future works, the authors highlight that further experimental investigations should be performed to validate these results for other slab thicknesses and varying the material properties of NSC and UHPFRC.

6.9 Conclusions of Chapter 6

This study investigated the level of accuracy of NLFEA performed with 3D continuum elements to predict the punching capacity and failure mode of three types of specimens: (i) flat slabs fully made of NSC, (ii) flat slabs fully made of UHPFRC and (iii) flat slabs with the use

of UHPFRC only at a certain thickness of the slab and in the column vicinity. In the end, an analytical approach based on the CSCT was proposed to predict the punching capacity of hybrid slabs (NSC-UHPFRC slabs) with the rational use of UHPFRC, which was validated against experimental and numerical results.

From the parametric analyses, the following conclusions can be drawn:

- Placing the UHPFRC at the compression side of slabs is more efficient to improve the punching capacity, mainly for slabs with higher reinforcement ratios. Furthermore, the slabs showed higher deformation capacity with the use of UHPFRC in the shear-critical regions, which is an additional benefit for the performance of flat slabs in seismic regions.
- The parametric analyses also indicated that the punching shear enhancement with the rational use of UHPFRC at the compression side of the slabs depends significantly on the geometry of the UHPFRC layer. For slabs with reinforcement ratios of 1.8%, the punching capacity enhancement varied between 27% and 153%, changing the size of the UHPFRC layer (thickness and area around the loaded area). Although the higher punching capacity enhancements were reached using the UHPFRC over the entire thickness (> 100% in some analyses), significant enhancements in the punching capacity were also reached with layers of small thickness (0.25h and 0.33h) placed at the compression side of the slabs.

From the proposed analytical approach to predict the punching capacity, the following conclusions can be drawn:

- The proposed approach based on the CSCT (MAYA et al., 2012; MUTTONI, 2008) and inspired by the works of Moreillon (2013), Inácio et al. (2020) and Gouveia et al. (2019a) leads to good predictions of the punching capacity of NSC-UHPFRC slabs with the rational use of UHPFRC around the loaded area and at the compression side. This statement is supported by comparisons between the analytical predictions and the experimental results of Zohrevand et al. (2014), as well as by comparisons between the analytical calculations with advanced NLFEA developed in the parametric studies (Section 6.2 and Section 6.3).
- The bond factor k_b used to predict the punching capacity with the CSCT can be assumed equal to 1 due to the higher packing of the UHPFRC matrix, regardless of the fiber shape, when using the equations from Maya et al. (2012) developed for SFRC. However, more accurate predictions were reached with the CSCT following the proposed approach based on the works of Moreillon (2013) to predict the punching strength of UHPFRC flat slabs with the CSCT: (i) estimating the ultimate crack opening w_u from a relation with the fiber length ($w_u = l_f/4$); (ii)

considering the higher post-cracking tensile strength in the punching capacity; and (iii) calculating the contribution of the fibers $P_{R,f,CSCT}$ by Eq. (6.36).

In summary, the main significance of this research is that an economical and sustainable solution may be achieved by increasing the punching capacity of flat slabs without requiring stirrups with the rational use of UHPFRC. Since limited experiments are available about this kind of connection using this promising material (ZOHREVAND et al., 2014), numerical studies may be a useful tool to extend the knowledge in this field. The importance of identifying analytical methods that are able to predict the behavior of such joints is also highlighted, as such analytical methods are the main tools used in engineering practice. Therefore, the accurate predictions with the CSCT model with the proposed modifications should help to spread a design practice with the rational use of UHPFRC.

7 NLFEA OF ONE-WAY SLABS IN TRANSITION BETWEEN SHEAR AND PUNCHING: RECOMMENDATIONS FOR MODELING

This chapter deals with the non-linear finite element analyses of one-way slabs under concentrated loads. In this context, a numerical model was validated to represent different shear failure mechanisms observed in an experimental program from the literature. The challenges in predicting all possible shear failure mechanisms involved for such slabs are highlighted. Ultimately, the impact of different modeling choices in the predictions of ultimate capacity is investigated.

7.1 Context

One-way slabs under large concentrated loads are commonly found on bridge deck slabs, industrial floor slabs and even residential buildings during their building or use (BUI et al., 2017b; FERNÁNDEZ; MARÍ; OLLER, 2021; HENZE; ROMBACH; HARTER, 2020; LANTSOGHT; VAN DER VEEN; WALRAVEN, 2013). Assuming the use of such structures on bridge deck slabs, the reader may realize that the load position varies significantly during its use. In practice, different failure mechanisms may be critical for a given slab depending on the load position and other parameters such as the slab width (SOUSA et al., 2021a, 2021c). For instance, when the slab width is not so large compared to the load size in the width direction, the slab may fail as a wide beam in one-way shear (LANTSOGHT et al., 2014; REIßEN; CLASSEN; HEGGER, 2018). At the same time, when the load is placed close to the support and the slab width is considerably larger than the load size, not the entire slab strip may contribute effectively to the sectional shear capacity (LANTSOGHT et al., 2014). In such cases, a slab strip called effective shear width is assumed to contribute effectively to the sectional shear capacity (LANTSOGHT; VAN DER VEEN; WALRAVEN, 2013). On the other hand, when the distance from the load to the support increases, the shear flow around the load becomes predominantly radial; hence, the punching failure may become more critical than a wide beam in one-way shear. In such cases, the sectional shear capacity may eventually not be reached if the test fails by punching.

A large number of studies contributed to predicting the sectional shear capacity of reinforced concrete (RC) beams (RIBEIRO et al., 2020; SANTOS et al., 2019) and the punching capacity of flat slabs or slab-column connections (SOUSA et al., 2021b; GENIKOMSOU;

POLAK, 2015) using three-dimensional (3D) non-linear finite element analyses (NLFEA). However, a limited number of them addressed the challenge of using the same modeling strategy to assess the ultimate capacity of RC members that may develop different shear failure mechanisms (one-way shear and punching shear), such as one-way slabs under concentrated loads (HENZE, 2019; REIßEN, 2016). Moreover, the failure mechanism of such structures is not frequently discussed in detail. Consequently, the influence of some parameters on the ultimate capacity cannot be well understood when the failure mechanism may have changed in the test varying parameters such as the slab width and load position. Therefore, further studies are needed to discuss the problem from a most comprehensive perspective.

At the same time**,** another aspect also draws attention in recent publications addressing numerical studies: the methodology followed in several papers has some minor points subjected to discussions. For instance, during the validation step of the numerical models, it is frequent in the literature to use only one test result with a specific failure mechanism for validating the modeling strategy. However, other failure mechanisms could appear when performing parametric analyses with significant changes from material and geometry parameters. In this way, such different failure mechanisms should also be investigated during the validation step to assure that the modeling strategy would also represent them accurately. At this point, it is important to note that the primary purpose of this study is not to describe a modeling approach capable of representing several failure mechanisms for such slabs. As possible, this chapter tries to bring some light to problems that may occur when using numerical models validated against only one test result to investigate other parameters in parametric analyses.

Besides that, some modeling options are frequently not discussed in numerical studies. For instance, the influence of considering or not the concrete damage evolution (degradation of the elastic modulus) with the increasing loading was scarcely investigated (GENIKOMSOU; POLAK, 2015). Until now, most studies that propose not using the damage evolution law for simulating static tests assume that this material characteristic would influence only cyclic tests. However, some papers have already shown that this parameter may have a not insignificant influence on the numerical results (GENIKOMSOU; POLAK, 2015). Herein, it is assumed that the variation of the elastic stiffness from concrete could influence the confining conditions on three-dimensional problems. Additionally, some mechanical models of one-way shear strength already include the elastic modulus from concrete as a critical parameter in the predictions of ultimate capacity (TRAN, 2020). Since no specific study was found on this matter, the results of NLFEA with and without the damage evolution parameters should be investigated.

In this study, it is proposed to investigate the accuracy of a developed modeling strategy to represent different shear failure mechanisms that can take place for one-way slabs under concentrated loads: one-way shear as wide beams and punching shear. Besides that, a sensibility study is performed to show the influence of some modeling choices from the constitutive model adopted in the numerical results. Herein, the following parameters are investigated: (i) the influence of considering or not the concrete damage evolution (variation of the elastic modulus in the concrete non-linear phase); (ii) the influence of the stress-strain behavior adopted in compression and tension; and (iii) the viscosity parameter. In advance, one of the research significances of this chapter is to show how some assumptions and methodologies can lead to questionable results.

Ai this point, it is important to remember that in the Concrete Damaged Plasticity (CDP) model, the effective elastic modulus used in the simulations varies as a function of the damage parameter *d* through the following expression:

$$E = E_0 \cdot (1 - d) \tag{7.1}$$

E is the effective elastic modulus in the simulations and E_0 is the initial or undamaged elastic modulus. *d* is the damage variable that varies between 0 (undamaged) and 1 (fully damaged). Added to that, the damage parameter also changes the proportion between the inelastic strains and the plastic strains through the following expression:

$$\varepsilon_c^{\,pl} = \varepsilon_c - \varepsilon_{0c}^{\,el} = \varepsilon_c^{\,in} - \frac{d_c}{1 - d_c} \cdot \frac{\sigma_c}{E_0} \tag{7.2}$$

ε_c^{pl} is the compressive plastic strain; ε_c is the total compressive strain; ε_{0c}^{el} is the undamaged compressive elastic strain; ε_c^{in} is the damage inelastic strain. From expression (7.2) it can be noted that when the damage parameter is neglected (assumed null or $d = 0$), the plastic strains become equal to the damage inelastic strain. Therefore, even in simulations of static problems (not cyclic tests), neglecting the damage parameters influence may play influence the simulation results due to its influence on the evolution of plastic strains, which deserves more investigations.

First, the selected tests from Reiβen, Classen and Hegger (2018) used as reference are detailed in Section 7.2. In the following, the modeling strategy proposed is presented, detailing the constitutive models, material models, and finite element types used. In the validations step, the numerical results are compared to the experimental results in terms of failure mechanism and ultimate load. The sensibility study section presents the results of changing specific material

parameters of the numerical models. Next, the Discussions section provides a comprehensive look at the main results presented compared to the previous studies, highlighting the main contributions from this work. From this, a set of recommendations are stated in the Conclusions sections.

7.2 Control specimens from literature

This section details the motivation behind the choice of the control tests, the geometry and material properties of the studied slabs.

7.2.1 Choice of control specimens

This study uses one-way slabs under concentrated loads tested by Reiβen et al. (2018) as reference tests. This study selected a set of tests on which different failure mechanisms occurred, varying specifically parameters in the analyses, such as the load position and slab width, illustrating possible problems on using only one test to validate a defined modeling strategy. At this point, the reader may realize that the parameters varied could be selected to be investigated by parametric analyses on a hypothetical study but herein were investigated experimentally. In total, 13 tests were selected to be investigated in detail based on the key parameters in the reported paper by Reiβen, Classen and Hegger (2018). Herein, these parameters are mainly (i) the shear span a defined between axes of support and loading plate and (ii) the slab width b_{slab}. By varying these two parameters in the reported study, different failure mechanisms were observed (shear, punching or a mixed-mode between them).

7.2.2 Geometry of control experiments

Figure 7-1 shows the generic geometry of the one-way slabs (control specimens) tested by Reiβen, Classen and Hegger (2018). In this study, only the simply supported slabs were evaluated. In the selected tests, two main parameters were varied along with the tests: (i) the shear span a and (ii) the slab width b_{slab}. The span length l_{span} was also changed in some tests, particularly those on which it was possible to perform two tests on the same slab. However, no relation between the span length and the governing failure mechanism was identified (REIßEN; CLASSEN; HEGGER, 2018).

Figure 7-1 - Schematic view of the geometry of the one-way slabs tested by Reiβen, Classen and Hegger (2018) evaluated in this study: a) layout of the first test on the specimens and ; b) layout of the second test on the specimens.

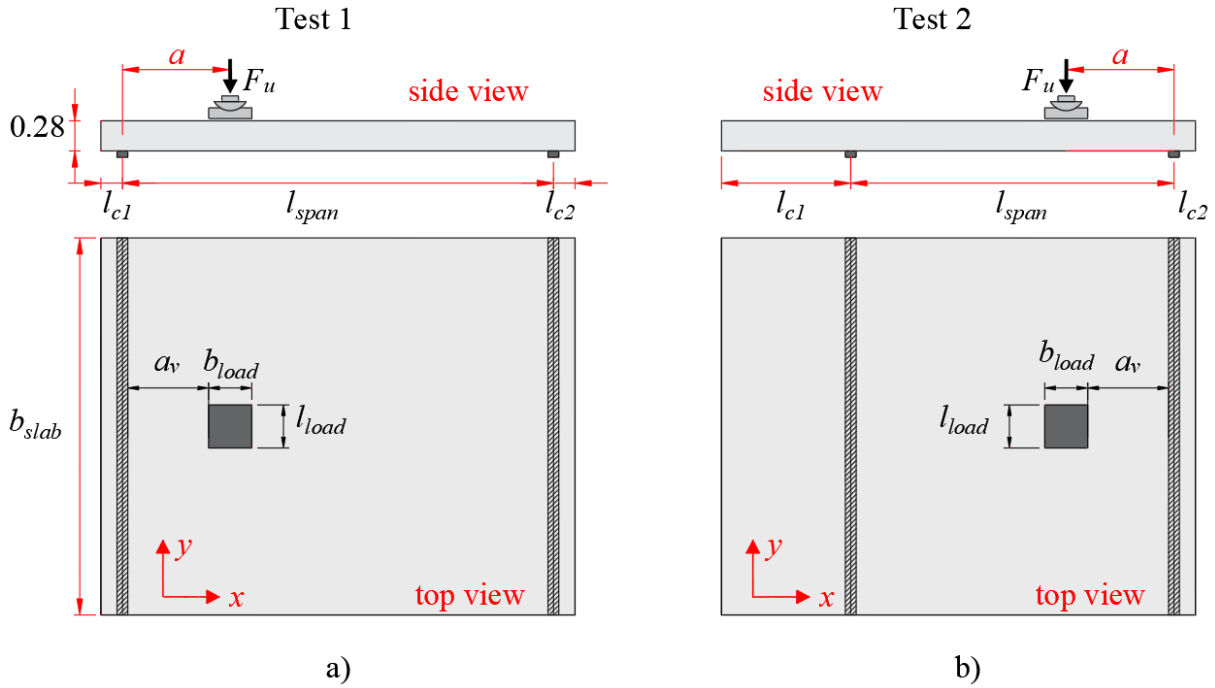

Source: Reiβen, Classen and Hegger (2018).

Table 7-1 describes the geometry of the slabs, the layout of the tests (see Figure 7-1), the reinforcement ratios in the longitudinal and transverse directions and the failure loads for the 13 investigated tests.

In the notation of the tests, for instance S25B-1: S means "slab"; the first two numbers following means the slab width in meter (5: b_{lsab} = 0.5 m; 15: b_{slab} = 1.5 m; 25: b_{slab} = 2.5 m; and 35: b_{slab} = 3.5 m). The last letter refer to the shear slenderness (A: a/d_l = 2.9; B: a/d_l = 4.2; C: a/d_l = 5.4). The last number means the number of the test (1 = first test; 2 = second test). The concrete cover was 20 mm for all slabs. High-strength steel bars ($f_{yk} \approx$ 900MPa) were used for the longitudinal reinforcement in the tensiled side of the slabs to ensure shear or punching failures instead of flexural failures without increasing the reinforcement ratios. Normal strength steel bars (f_{yk} = 500 MPa) were applied in the transverse direction. The longitudinal and transverse reinforcement ratios (ρ_l and ρ_t) on the slabs tensiled side were fixed on 0.98% and 0.45% respectively (Ø15/7.5 and Ø12/10). This resulted in an effective depth of the longitudinal bending reinforcement of d_l = 0.241 m and an effective depth of the transverse reinforcement of d_t = 0.254 m. The reinforcement layer on the compressed side consisted of normal strength steel bars ($f_{yk} \approx$ 500 MPa) with the following distribution: Ø10/15 in the longitudinal direction (0.22%) and Ø12/10 in the transverse direction (0.45%). Figure 7-2 shows the reinforcement

layout, including the stirrups (Ø12) placed at the support end at the midspan. Reiβen, Classen and Hegger (2018) used these stirrups to prevent shear failures out of the region studied, to improve the reinforcement anchorage at the supports and also to make easier the installing of the top reinforcement.

Table 7-1 – Geometry, test layout and failure load of the control slabs.

Test	l_{c1} (m)	l_{span} (m)	l_{c2} (m)	l_{total} (m)	b_{slab} (m)	h (m)	ρ_l (%)	ρ_t (%)	a/d (-)	a_v/d_l (-)	F_u (kN)	V_{Fu} (kN)
S5A	0.20	3.0	1.90	5.9	0.5	0.28	0.98	0.45	2.9	1.92	189	145
S5B-1	0.20	4.0	0.2	4.4	0.5	0.28	0.98	0.45	4.2	3.17	183	137
S5B-2	1.2	3.0	0.2	4.4	0.5	0.28	0.98	0.45	4.2	3.17	215	144
S15B-1	0.2	4.0	0.2	4.4	1.5	0.28	0.98	0.45	4.2	3.17	543	407
S15B-2	1.2	3.0	0.2	4.4	1.5	0.28	0.98	0.45	4.2	3.17	638	425
S25B-1	0.2	4.0	0.2	4.4	2.5	0.28	0.98	0.45	4.2	3.17	664	498
S25B-2	1.2	3.0	0.2	4.4	2.5	0.28	0.98	0.45	4.2	3.17	780	520
S35A-1	0.2	3.0	1.2	4.4	3.5	0.28	0.98	0.45	2.9	1.92	1143	876
S35A-2	0.2	3.0	1.2	4.4	3.5	0.28	0.98	0.45	2.9	1.92	892	684
S35B-1	0.2	4.0	0.2	4.4	3.5	0.28	0.98	0.45	4.2	3.17	985	739
S35B-2	1.2	3.0	0.2	4.4	3.5	0.28	0.98	0.45	4.2	3.17	1024	683
S35C-1	0.2	4.0	0.2	4.4	3.5	0.28	0.98	0.45	5.4	4.42	1066	787
S35C-2	0.2	4.0	0.2	4.4	3.5	0.28	0.98	0.45	5.4	4.42	924	623

Source: Reiβen, Classen and Hegger (2018).

Figure 7-2 - Reinforcement layout of simply supported slabs with l_{total} = 4.4 m tested by Reißen, Classen and Hegger (2018). Dimensions in cm.

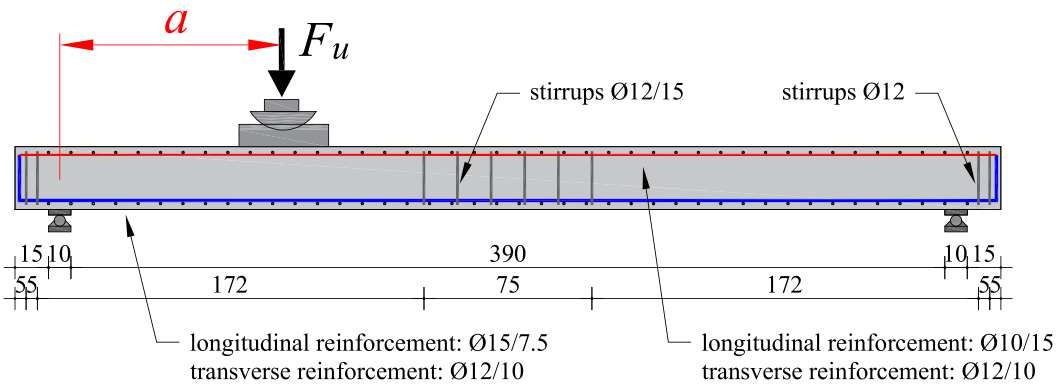

Source: Adapted from Reiβen, Classen and Hegger (2018).

7.2.3 Material properties of control slabs

Table 7-2 describes the material properties of the concrete used in the tests according to Reiβen (2016) and Reiβen et al. (2018). The main properties used to simulate the concrete behavior are the average tensile strength (f_{ctm}) measured on drill cores drawn from the slabs ($D \approx 54.5$ mm, $H \approx 110$ mm), the compressive strength measured on cylinder specimens $f_{c,cyl}$ (D = 150 mm, H = 300 mm), and the mean modulus of elasticity (secant modulus) of concrete E_{cm} (measured at 40% of f_{cm}). Coarse aggregate with a maximum size of 16 mm was used.

Table 7-2 - Concrete properties described in references.

Test	$f_{c,cube}$ (MPa)	$f_{c,cyl}$ *(MPa)*	f_{ctm} (MPa)	$f_{ct,sp}$ *(MPa)*	E_{cm} (MPa)
S5A	44.3	36.9	2.7	3.2	24200
S5B-1	43.7	39.2	3.0	3.5	26200
S5B-2	46.1	40.5	2.8	2.8	28100
S15B-1	43.4	37.7	2.8	3.1	27300
S15B-2	45.0	38.2	3.0	3.6	27600
S25B-1	32.0	27.9	2.5	2.3	22400
S25B-2	33.4	29.5	2.6	2.5	21000
S35A-1	47.5	41.3	2.7	3.2	29900
S35A-2	31.0	29.0	2.7	2.4	23300
S35B-1	45.3	35.9	2.8	3.1	28200
S35B-2	47.8	38.2	3.0	3.1	*28200
S35C-1	47.4	39.6	2.4	3.1	27200
S35C-2	31.0	29.5	2.5	2.5	22700

***assumed value. Source: Reiβen (2016).**

The measured yield strength varied between 822 MPa and 920 MPa for the 15 mm diameter bars; 540 MPa to 573 MPa for the 12 mm diameter bars; and it was assumed as 550 MPa for the 10 mm diameter bars. The ultimate tensile strength f_{ut} varied between 1077 MPa to 1110 MPa for the 15 mm diameter bars; 595 MPa to 639 MPa for the 12 mm diameter bars. The average steel elastic modulus E_s was 199 GPa for the 15 mm diameter bars and 200 GPa for the other bars.

7.3 Finite element simulations

This section presents the details of the modeling of the control slabs, with emphasis on (i) material models (ii) mesh discretization and (iii) boundary conditions.

7.3.1 Overview

The finite element software ABAQUS/CAE (DASSAULT SYSTEMS SIMULIA CORP., 2014) was used to model the reference tests. By considering specimens' symmetry, half of the slab's geometry was modeled to reduce the processing time of the numerical models (Figure 7-3a). Figure 7-3b shows a 3D view of the built numerical models in the simulations with highlighted to the boundary conditions and symmetry planes. A rigid body interaction was implemented between the center node of the loading plate (master node) and the top surface of the loading plate (slave surface) (Figure 7-3c). In this interaction, the rotation of the slab surface was free in relation to the master node. In this way, an axial hinge has been simulated above the loading plate. A similar interaction was also implemented in the supports to allow a free

rotation around the Z-axis while the vertical and horizontal displacements were fixed. Figure 7-3d shows all reinforcements modeled.

Figure 7-3 - Boundary conditions applied in the numerical models: a) detail of the symmetry axis b) three-dimensional view of the built numerical model; c) detail of the applied load using rigid body displacement with free rotation of the slave surface.

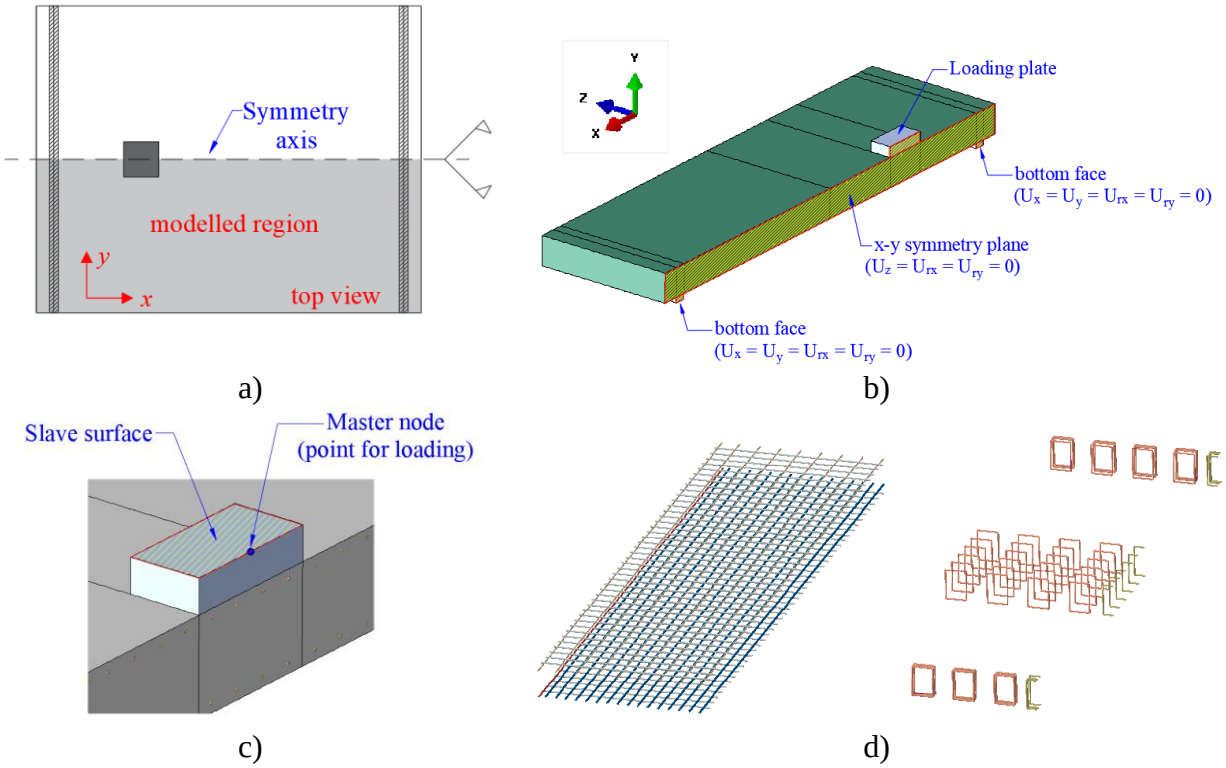

Source: Author.

7.3.2 Interfaces

The interface between the support plates and loading plate surface with the slab was modeled assuming (i) hard contact (allowing separation of the surfaces) and (ii) frictionless. A perfect bond between reinforcement and concrete was also assumed based in previous publications (SOUSA et al., 2021b) since no anchorage failure was reported.

7.3.3 Mesh and Procedure of solution

Concrete parts, supporting plates and loading plates meshed with 8-node hexahedral solid elements with reduced integration (C3D8R). Reduced integration was considered to avoid the undesirable shear locking of the brick elements (DASSAULT SYSTEMS SIMULIA CORP., 2014; NANA et al., 2017). The rebars were modeled with 2-node truss elements (T3D2). Two mesh discretizations were used for the concrete parts to optimize the time of processing. In the region closer to the loading plate (Figure 7-4), where failure was expected to

occur, the element size for concrete and reinforcement parts was chosen as 28 mm, which allows having 10 elements over the thickness of the model. In the second part of the slab, the element size used was approximately 56 mm. The interaction between the two parts of the slab was performed by a tied contact, which allows having different mesh discretizations between the two regions (Figure 7-4).

Figure 7-4 – Sketch of the mesh discretization applied in the numerical models.

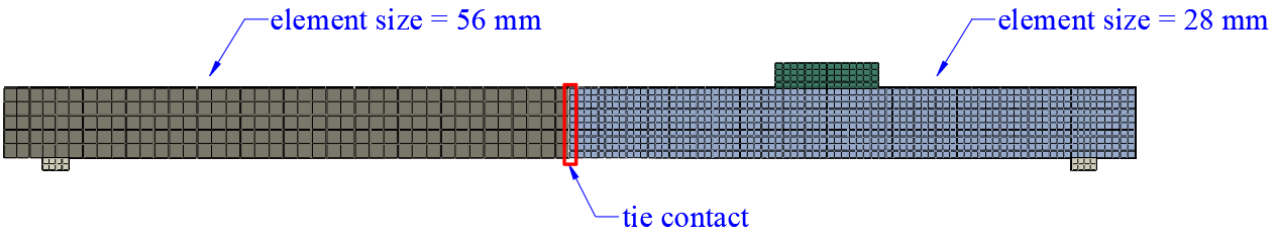

Source: Author.

7.3.4 Material modeling of the reference FEM

The Concrete Damaged Plasticity (CDP) model available on ABAQUS was used to simulate the concrete non-linear behavior. The CDP model is grounded on three main parts: (i) damage evolution, yield criterion, and plastic flow rule (DASSAULT SYSTEMS SIMULIA CORP., 2014). The damage evolution laws describe how the elastic stiffness E_c is degraded with increasing strains. The yield criterion is described according to Lubliner (1989) and further modified by Lee and Fenves (1998). The plastic flow in the CDP used the non-associated potential plastic flow hypothesis. In this way, the CDP uses a potential function G that assumes a Drucker-Prager type hyperbolic form (XENOS; GRASSL, 2016). Further details on the expressions that describe the CDP model can be consulted elsewhere (GENIKOMSOU; POLAK, 2015).

In summary, the required input data for CDP in ABAQUS to represent the concrete compressive behavior are the relations between (i) the compressive stress σ_c with the inelastic compressive strains ε_c^{in}; and (ii) the evolution of the compressive damage variable d_c according to the compressive damage inelastic strains ε_c^{in}. The tensile behavior data is inputted with the respective relations between (i) the tensile stress σ_t with tensile cracking strain ε_t^{in} and (iii) the evolution of the tension damage variable d_t with the tensile cracking strain ε_t^{in} (CHENG et al., 2020). The auxiliary input parameters to define the yield criterion and the plastic flow rule are

(i) dilation angle ψ; shape factor K_c; eccentricity parameter e; viscosity parameter μ and the ratio between the biaxial compressive strength σ_{b0} and the uniaxial compressive strength σ_{c0}.

The stress-strain behavior under compression was modeled herein according to the expressions from the current *fib* Model Code 2010 and EN 1992-1-1:2005 (CEN, 2005):

$$\frac{\sigma_c(\varepsilon_c)}{f_{cm}} = \frac{k\cdot\eta - \eta^2}{1+(k-2)\cdot\eta} \qquad (7.3)$$

Where:

$$\eta = \varepsilon_c / \varepsilon_{c1} \qquad (7.4)$$

$$k = 1.05\cdot E_{cm}\cdot\varepsilon_{c1} / f_{cm} \qquad (7.5)$$

In these expressions, ε_{c1} is the strain at peak stress and it was calculated according to EN 1991-1:2005 (CEN, 2005):

$$\varepsilon_{c1} = \frac{0.7\cdot f_{cm}^{0.31}}{1000} \qquad (7.6)$$

The stress-strain behavior under tensile stresses was modelled according to the model of Hordijk (1992), which considers the bandwidth l_{eq} to reduce the mesh sensitivity of the results through the same approach described by Genikomsou and Polak (2015). In this study, the value of l_{eq} was assumed to be equal to the average finite element size (28 mm and 56 mm, respectively in the different regions of the slab). In this model, first, a crack opening relationship with the tensile stress is given by:

$$\frac{\sigma_t(w)}{f_{ct}} = \left[1+\left(c_1\cdot\frac{w}{w_c}\right)^3\right]\cdot e^{-c_2\cdot\frac{w}{w_c}} - \frac{w}{w_c}\cdot\left(1+c^3\right)\cdot e^{-c_2} \qquad (7.7)$$

With: $c_1 = 3$; $c_2 = 6.93$; w_c is the critical crack opening or fracture crack opening given by:

$$w_c = 5.14\cdot\frac{G_f}{f_{ct}} \qquad (7.8)$$

The tensile strain in the descending segment of the tensile stress-strain curve can be described in terms of the crack opening from the following kinematic relation (GENIKOMSOU; POLAK, 2015):

$$\varepsilon_t = \frac{f_{ct}}{E_{ci}} + \frac{w}{l_{eq}} = \varepsilon_{t,cr} + \frac{w}{l_{eq}} \tag{7.9}$$

Table 7-3 shows the damage models used for the concrete. The model of Alfarah, López-Almansa and Oller (2017) was chosen since it accounts for the bandwidth length l_{eq} in tension. Therefore, this model can reduce mesh sensitivities due tension cracking.

Table 7-3 – Damage evolution laws used for normal strength concrete.

Reference	Tension damage
Alfarah, López-Almansa and Oller (2017)	$d_t = 1 - \frac{1}{2+a_t}\left[2(1+a_t)\exp\left(-b_t\varepsilon_t^{in}\right) - a_t\exp\left(-2b_t\varepsilon_t^{in}\right)\right]$ (7.10) $a_t = 1; b_t = \frac{3}{2}\frac{f_{ct}\cdot l_{eq}}{G_f}$ (7.11)
	Compression damage
Birtel and Mark (2006)	$d_c = 1 - \frac{\sigma_c / E_{ci}}{\varepsilon_c^{in}\cdot(1-b_c) + \sigma_c / E_{ci}}$ (7.12) $b_c = 0.7$ (7.13)

Source: Author.

7.3.5 Plasticity parameters of the reference FEM

The parameters used for NC were chosen based on the literature review (GENIKOMSOU; POLAK, 2015, 2016, 2017a; MILLIGAN; POLAK; ZURELL, 2020, 2021; NANA et al., 2017). The dilation angle adopted for the concrete was 30º. Notably, this value is close to that expected by Poliotti and Bairan (2019) for the maximum dilation angle of normal strength concretes (Ψ = 32º) based on inverse analyses of experimental investigations. The fracture energy G_f was calculated according to the *fib* Model Code 2010 (FÉDÉRATION INTERNATIONALE DU BÉTON (FIB), 2012) since the values with the Model Code 1990 (COMITÉ EURO-INTERNATIONAL DU BÉTON, 1993) underestimated the punching capacity of the tests that failed by punching. The default value of the ratio σ_{b0}/σ_{c0} in ABAQUS is 1.16 for NC. This value is based on the experimental tests of Kupfer et al. (1973; 1969).

The viscosity parameter value chosen was 0.00001 in such a way to decrease the sensibility of the results to the viscoplastic regularization in ABAQUS/Standard (implicit integration). However, in the literature, the values applied vary significantly between 0.00001 and 0.005, for instance. In practice, a viscosity parameter is a numerical tool used in the Concrete Damaged Plasticity model to improve convergence and eventually increase the speed

of the simulation through the damping of the crack propagation through the numerical models. In practice, using higher values of the viscosity parameter makes cracks not concentrate in small regions and the damaged region increases considerably (MICHAŁ; ANDRZEJ, 2015). However, for values of viscosity higher such as 0.001, for instance, the material may behave as a perfect elastoplastic behavior (which means that the residual tensile strength, for instance, keeps being the maximum tensile strength during the full simulation after cracking). In other words, the viscosity parameter has a similar effect to the mass scaling for problems of explicit integration (ABAQUS/Explicit). In the last case, the mass scaling allows an artificially increase mass of some elements of the model to speed up the simulation. However, this can also lead to inaccurate results in the same way that using high values of viscosity parameter. Since the effect of this parameter is not well discussed in most publications, we evaluated the influence of different values of the viscosity parameter in the numerical results in the next sections.

7.3.6 Summary of the material parameters of the reference FEM

In order to ease the identification of the material parameters used in the reference finite element models, Table 6-7 summarized the main information about the materials models used for behavior and damage evolution for concrete.

Table 7-4 - CDP model parameters used for the reference numerical analyses.

Parameter	**Reference**
Yield criterion	
Compressive behavior ($\sigma_c \; x \; \varepsilon_c^{in}$)	EN 1992-1-1:2005 (CEN, 2005)
Tensile behavior ($\sigma_t \; x \; \varepsilon_t^{in}$)	Hordijk (1992)
Damage evolution	
Compression damage ($d_c \; x \; \varepsilon_c^{in}$)	Birtel and Mark (2006)
Tensile damage ($d_t \; x \; \varepsilon_t^{in}$)	Alfarah, López-Almansa and Oller (2017)
Plasticity parameters	
Dilation angle, Ψ *(º)*	30
σ_{b0}/σ_{c0}	1.16 (KUPFER; GERSTLE, 1973; KUPFER; HILSDORF; RUSCH, 1969)
Parameter K_c	0.66 (DASSAULT SYSTEMS SIMULIA CORP., 2014)
Eccentricity, e	0.1
Viscosity parameter μ	0.00001
Fracture energy, G_f	*fib* Model Code 2010
f_{ct}	measured (Table 7-2)

Source: Author.

7.4 Validation of the modelling approach

This section presents the validation results of the proposed approach to describe the non-linear behavior of a different set of tests. In practice, this section tries to highlight how the proposed approach allowed to simulate the different shear failure modes identified for the slabs.

7.4.1 Level of accuracy of the NLFEA according to the slab width

Figure 7-5 compares the FEM results and test results in terms of applied load at failure and governing failure mechanism. The tested load × displacement graph of most tests was not reported in the references (REIßEN; CLASSEN; HEGGER, 2018). Consequently, only a horizontal dashed line was added to represent the test's maximum achieved load.

Figure 7-5 - Level of approximation of FE models for the tests a) S5A; b) S5B-1; c) S5B-2; d) S15B-1; e) S15B-2; f) S25B-1; g) S25B-2; h) S35B-1; and i) S35B-2.

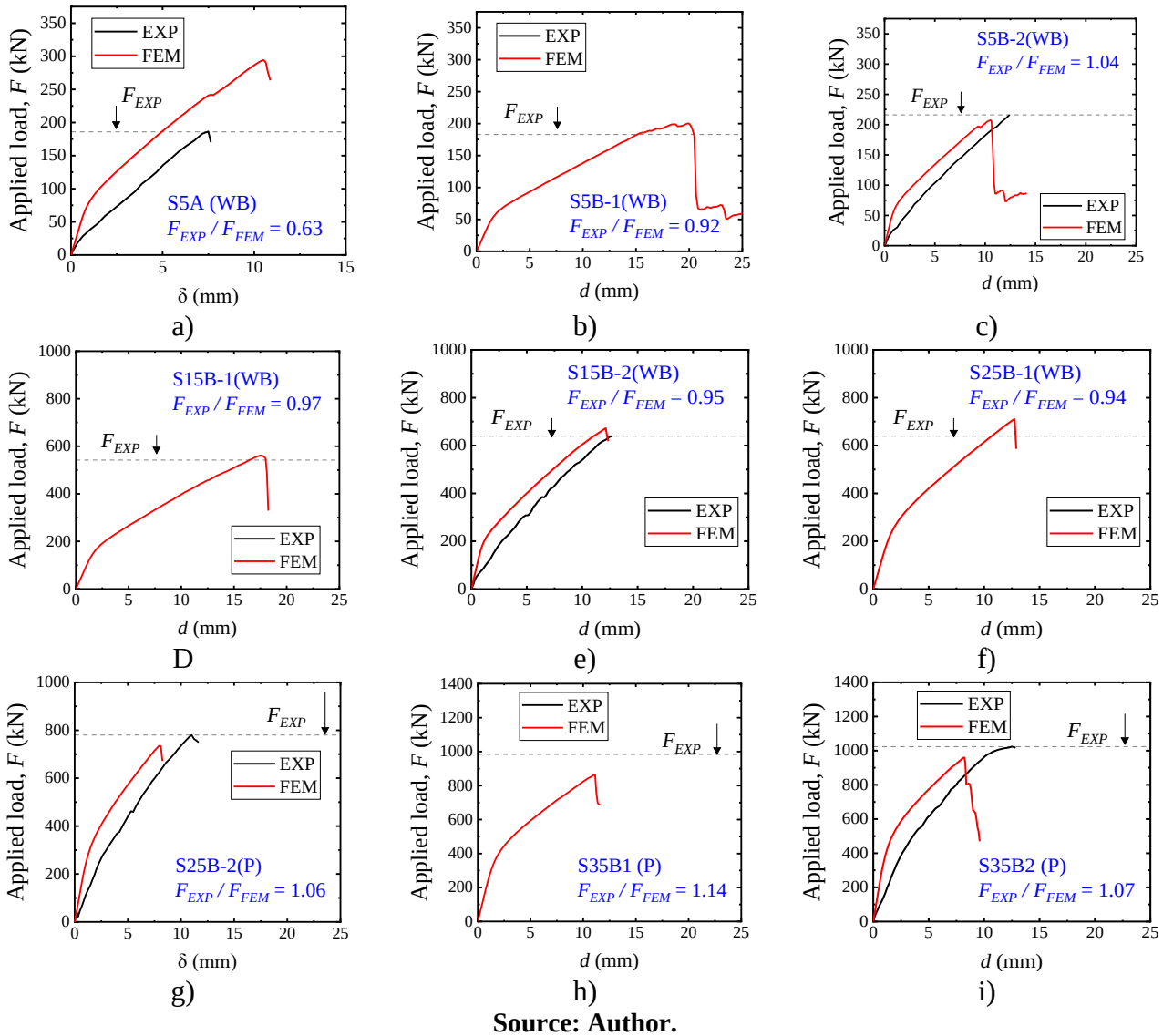

Source: Author.

Excluding the results of S5A, which will be described in more detail in the following, the results of the numerical models approximate fairly well from the test results regarding the applied loads at failure. Moreover, all numerical results clearly indicate a sharp decrease of the load capacity after failure, which is a well-known characteristic of brittle failure mechanisms from shear and punching failures. The FEM model from S5A overestimated the failure load in approximately 38%. The other numerical models deviate less than 20% from the test results regarding the ultimate load F_u. In none of the numerical models was identified reinforcement yielding at failure, which agrees with the test results evaluated.

Since the presented modeling approach does not include a specific calibration for each test, for instance, regarding the concrete tensile strength, fracture energy or dilation angle, the level of accuracy is considered satisfactory in a global way. In other words, by consistency, this study follows the same modeling strategy for all tests using the same expressions and values of material parameters for all tests.

However, it is important to note that the test S5A may indicate some limitations from the proposed modeling approach. Since these tests correspond to the lower shear slenderness (a/d_l = 2.9 or a_v/d_l = 1.92), this test may have benefited from arching action in the numerical model in a more straightforward way compared to the test result. In practice, comparing the test results of S5A and S5B-1, the ultimate load F_u from these tests is approximately the same, regardless of the lower shear slenderness a_v/d_l for the test S5A (1.92 compared to 3.17). This means that the numerical model may have some limitations to represent the one-way shear failure mechanism of non-slender beams. Similar problems were found by Henze modeling cantilever slabs when the load was placed too close to the support (a_v/d_l = 1 and a_v/d_l = 2). At the same time, this result could also indicate that the test result S5A does not behave as it would be expected. Proof of that is that other tests were performed by Reiβen, Classen and Hegger (2018) with lower shear slenderness, and they achieved a significantly higher failure load (tests S5-D, S5D-L8, S5E-L8).

In Figure 7-5, a small tendency of overestimation from the failure load was observed for the tests that failed as wide beams (one-way shear governing: b_{slab} = 0.50 m and 1.50 m). Nevertheless, the NLFE models predictions were slightly more conservative for the tests that failed by punching or a mixed failure mode between shear and punching (tests with b_{slab} = 2.5 m and b_{slab} = 3.5 m).

Figure 7-6 also shows that the cracking pattern from the test results was well reproduced by the numerical models, regardless of the governing failure mechanism. In Figure 7-6 and

Figure 7-7, the tensile damage variable (DAMAGET) is plotted to represent the cracking pattern. In Figure 7-6, the numerical models reproduced well the flexure cracks followed by the formation of an inclined crack that promotes the failure mechanism. However, some small differences shall also be highlighted (which are commonly neglected in most publications). While the cracking pattern of the test results of slender beams indicates an inclined crack with a convex/parabolic shape around the flexural cracks, the numerical models show inclined cracks with a more straightforward shape. In test S5A, this may explain the large difference in the failure loads observed. In practice, a parabolic cracking pattern disturbs more the load transfer in the struts between the load and the support. Therefore, it is reasonable that the failure load in the numerical model from S5A has achieved a large failure load.

Figure 7-6 - Comparison between crack patterns after the failure of experimental tests and FE models for a) S5A; b) S5B-1; c) S5B-2. Note: DAMAGET is the damage variable in tension.

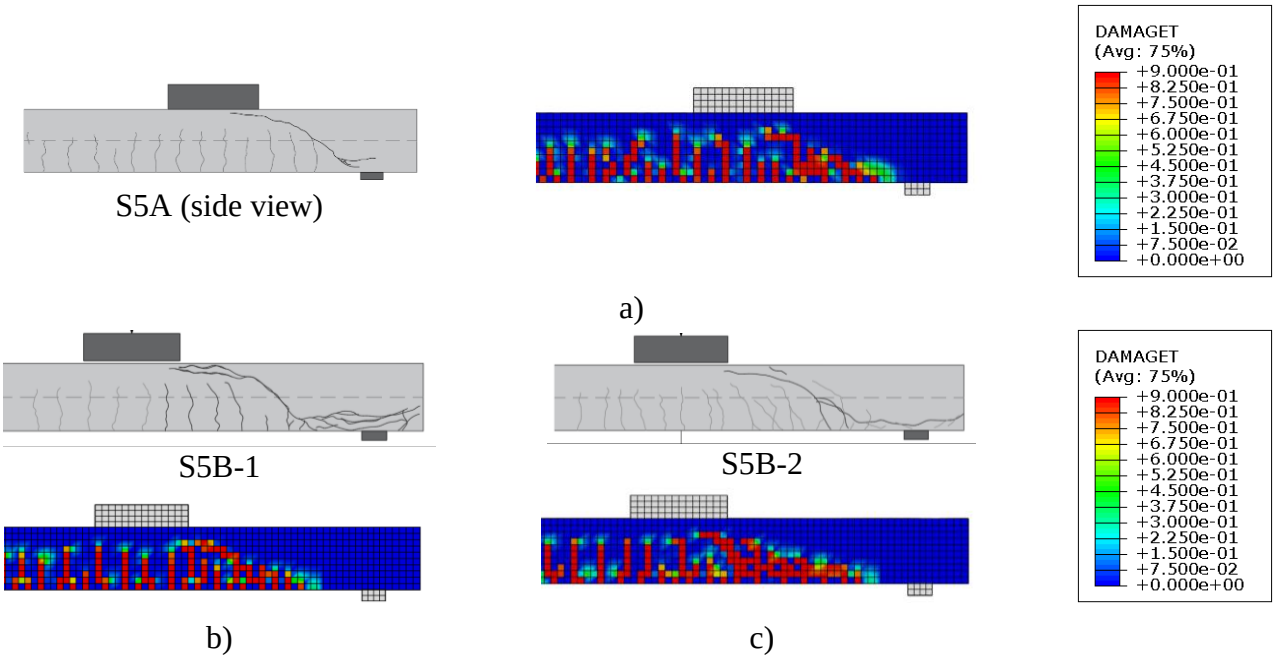

Source: Author.

Figure 7-7 shows that, as occurred in the experimental program, the numerical models started to fail by punching shear when the slab width increased to 2.5 m. At this point, noticeable differences between the cracking pattern of the tests S15B-1 and S25B-1 appear: (I) the inclined crack visible on the sides views from the test S15B-1 does not appear in the test S25B-1 at failure; (ii) the inclined crack in the test S25B-1 develops only in the vicinity of the load, visible though cut views (typical from punching failures); (iii) the shape of the cracks from S15B-1 and S25B-1 are significantly different: while the test S15B-1 develop an inclined crack the

connect different flexure cracks, the inclined crack in the test S25B-1arise within a strut region around the load.

Figure 7-7 - Comparison between the FE models and the test results in terms of the cracking pattern for: a) S35A-1; b) S35A-2; c) S35B-1; d) S35B-2; e) S35C-1; f) S35C-2. DAMAGET is the scalar damage variable in tension. Note: DAMAGET is the damage variable in tension.

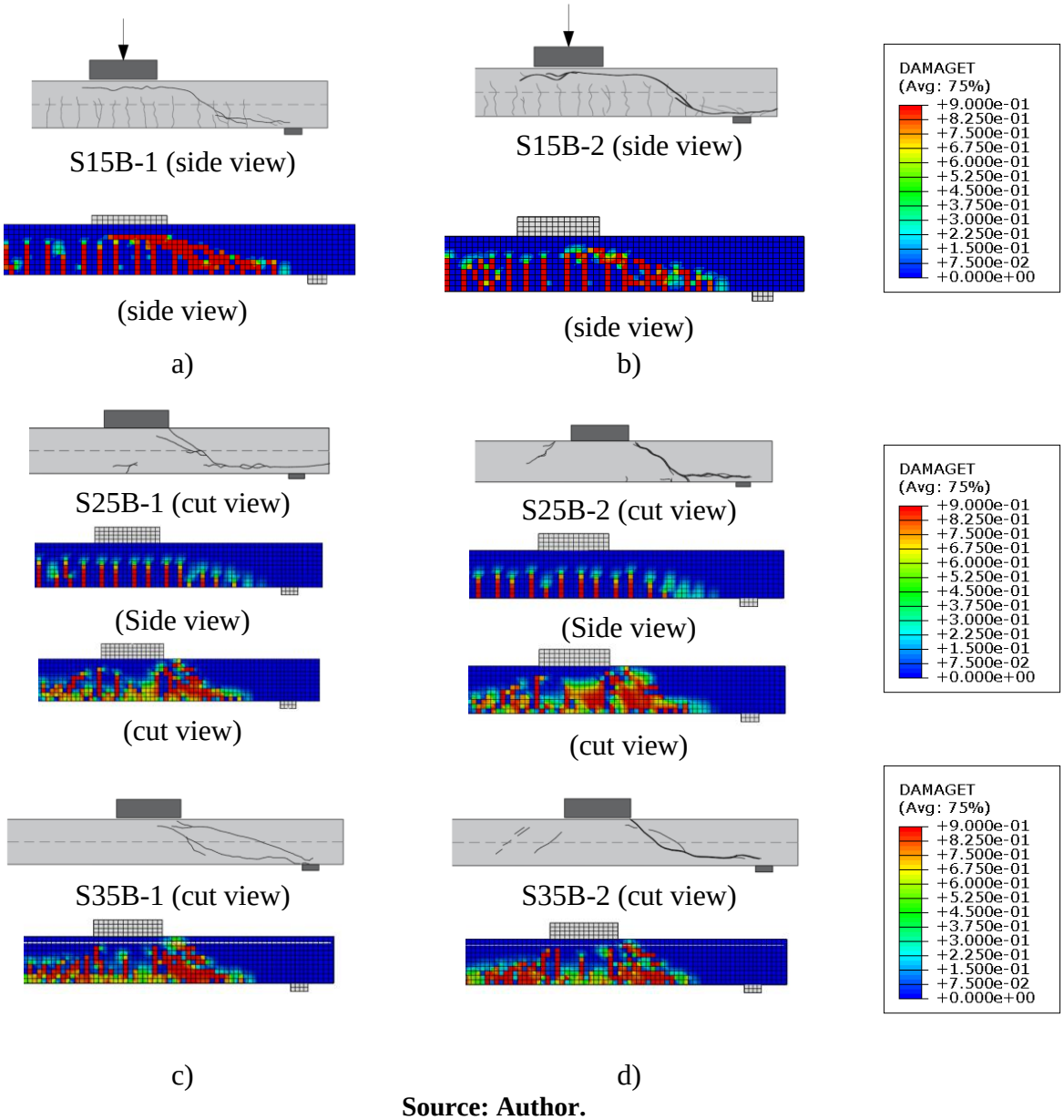

Source: Author.

7.4.2 Level of accuracy of the NLFEA according to the shear span for the wider slabs (b_{slab} = 3.5 m)

Figure 7-8 shows the load × displacement graphs of the numerical models and the ultimate load capacity of the tests (horizontal dashed lines - F_{EXP}). The tested load × displacement graph of most tests was not reported in the references (REIßEN; CLASSEN;

HEGGER, 2018). Figure 7-8 shows that the numerical model predicted well the ultimate capacity from most test results when varying the shear span, excepting for the test S35C-1 (a/d_l = 5.4). Besides that, it is notable that the results tend to become more conservative when the shear slenderness increased. In practice, increasing the shear span means decreasing the load eccentricity in relation to the span length between the supports.

Figure 7-8 - Level of approximation of FE models for the tests in terms of the failure load a) S35A-1; b) S35A-2; c) S35B-1; d) S35B-2; e) S35C-1; f) S35C-2.

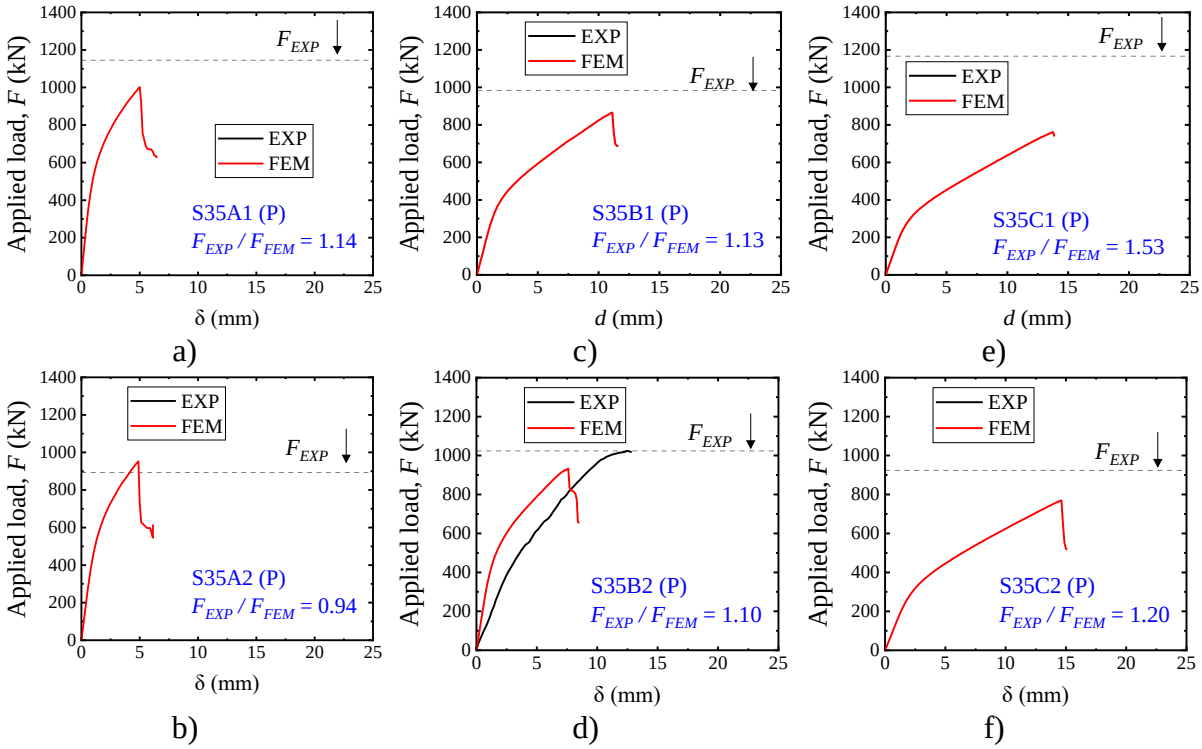

Source: Author.

Figure 7-9 shows that the punching shear failure that took place in the tests was well represented by the numerical models. Due to the higher shear demand in one of the sides of the load, an asymmetrical punching cone appeared in some tests. This characteristic was also well represented in the numerical models based on the higher concentration of tensile damage (DAMAGET) between the load and the closer support.

Figure 7-9 - Comparison between the FE models and the test results in terms of the cracking pattern for: a) S35A-1; b) S35A-2; c) S35B-1; d) S35B-2; e) S35C-1; f) S35C-2. Note: DAMAGET is the damage variable in tension.

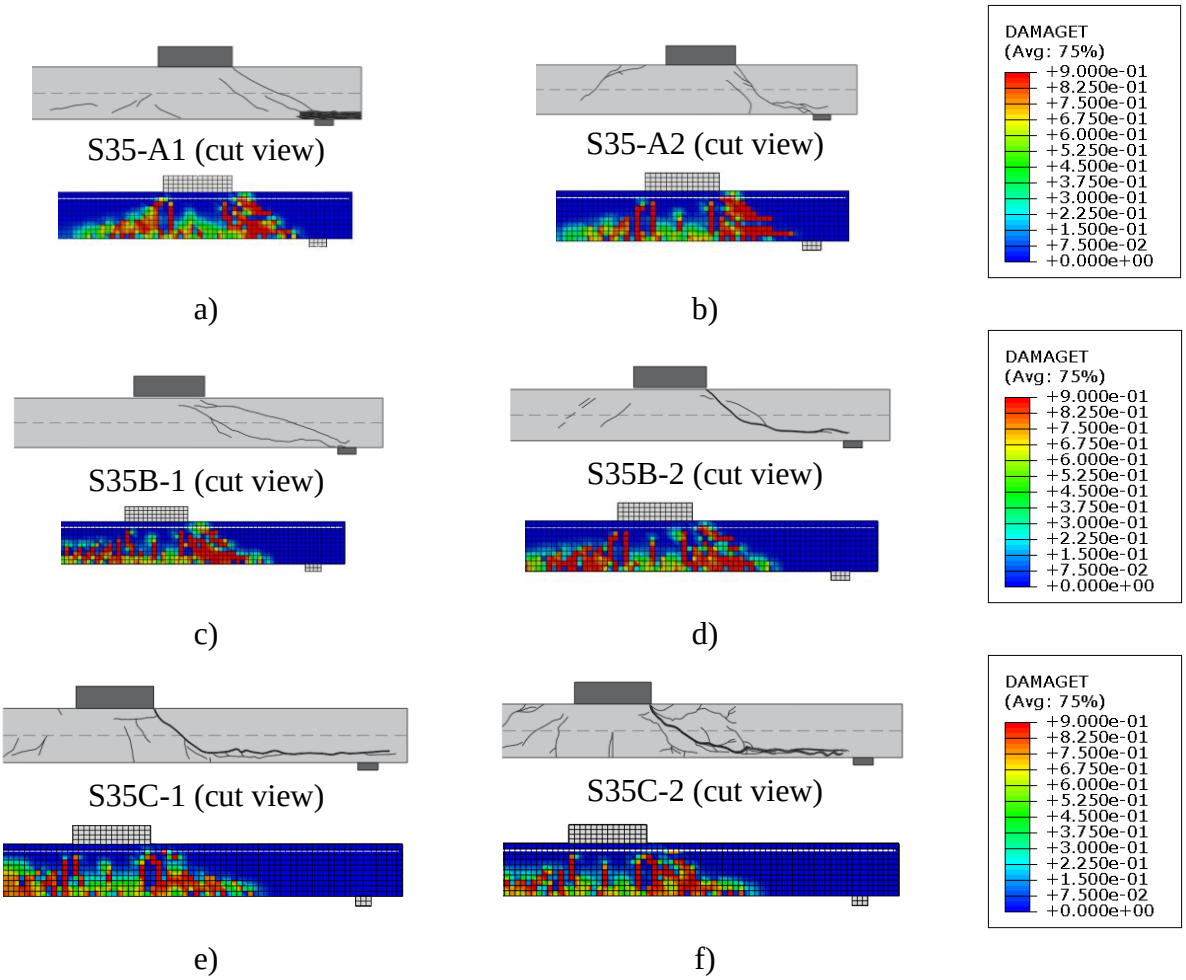

Source: Author.

7.4.3 Summary of the level of accuracy with the proposed approach

Table 7-5 describes a summary of the relation between the tested and predicted concentrated loads using the proposed approach for NLFEA. Different subsets were organized removing and not removing outliers identified in the predictions. Besides, subsets were organized to highlight the results according with the governing failure mechanism (wide beams shear = WB and punching shear = P).

Table 7-5 shows that the average ratio between tested and predicted applied loads at failure (F_{EXP}/F_{FEM}) was 1.07 with a coefficient of variation of only 17%. Since no specifical calibration of the fracture energy or dilation angle was performed for each single test (the values used followed the same values and expressions for all tests), this level of precision was satisfactory. Removing the outliers S5A and S35C-1, the coefficient of variation decreases to 11%, which highlights the excellent precision of the proposed approach.

Table 7-5 - Summary of the predictions of ultimate capacity with the proposed approach for different subsets.

Test	Failure mechanism	a_v/d_l [-]	a/d_l [-]	b_{slab}/l_{load} [-]	F_{EXP} / F_{FEM} [-]
S5A	WB = shear	1.91	2.91	1.25	0.63
S5B-1	WB = shear	3.13	4.17	1.25	0.92
S5B-2	WB = shear	3.13	4.17	1.25	0.92
S15B-1	WB = shear	3.13	4.17	3.75	1.18
S15B-2	WB = shear	3.13	4.17	3.75	1.24
S25B-1	P = Punching	3.13	4.17	6.25	0.97
S25B-2	P = Punching	3.13	4.17	6.25	1.06
S35A-1	P = Punching	1.91	2.91	8.75	1.14
S35A-2	P = Punching	1.91	2.91	8.75	0.94
S35B-1	P = Punching	3.13	4.17	8.75	1.10
S35B-2	P = Punching	3.13	4.17	8.75	1.10
S35C-1	P = Punching	4.375	5.42	8.75	1.55
S35C-2	P = Punching	4.375	5.42	8.75	1.20
All tests			AVG		1.07
All tests			COV		17%
All - S5A, S35C1			AVG		1.07
All - S5A, S35C1			COV		11%
WB	S5B-1; S5B-2; S15B1; S15B-2		AVG		1.06
WB	S5B-1; S5B-2; S15B1; S15B-2		COV		16%
P	S25(B1,B2); S35(A1; A2; B1; B2; C2)		AVG		1.07
P	S25(B1,B2); S35(A1; A2; B1; B2; C2)		COV		9%

Source: Author.

Organizing two subsets according with the governing failure mechanism, it can be seen that the level of precisions was very similar for both failure mechanisms (WB and P). The average ratio between tested and predicted loads F_{EXP}/F_{FEM} was 1.06, with a coefficient of variation of 16%, for the tests that failed as wide beams (WB). In turn, the tests that presented a punching failure (P), presented a average ratio F_{EXP}/F_{FEM} of 1.07 with a coefficient of variation of 9%. Therefore, a lower scatter was identified for the tests that failed by punching.

7.5 Sensibility study

This section presents the results from the sensibility study to show how some modelling options influence in the numerical results of NLFEA.

7.5.1 Effect of the concrete damage evolution

In the literature, there is no consensus about including or not including the concrete damage evolution in numerical simulations with static loading. Theoretically, including the damage evolution law decreases the elastic modulus according to the increase of the plastic

strain. Most researchers, however, consider that the lower elastic modulus along the simulation would play a significant role only on cyclic tests. In such tests, is expected that simulating the lower elastic modulus allows representing the crack closing more accurately and tracking the load × displacement relationships more closely.

Table 7-6 compares tested and predicted resistances with the FEM by considering and not considering the damage evaluation laws in the simulations. In general, it was observed that the predictions of ultimate capacity become less conservative without including the damage parameters. In other words, it was observed that the ultimate capacity predicted with the FEM decreased for all tests by including the damage parameters.

Table 7-6 - Comparison between tested and predicted resistances considering or not considering the damage parameters in the simulations.

Comparison					*With damage parameterd*	*Without damage parameters*	
Test	Failure mechanism	a_v/d_l [-]	a/d_l [-]	b_{slab}/l_{load} [-]	F_{EXP} / F_{FEM} [-]	F_{EXP} / F_{FEM} [-]	Δ (%)
S5A	WB = shear	1.91	2.91	1.25	0.63	0.60	-5%
S5B-1	WB = shear	3.13	4.17	1.25	0.92	0.85	-7%
S5B-2	WB = shear	3.13	4.17	1.25	0.92	0.90	-3%
S15B-1	WB = shear	3.13	4.17	3.75	1.18	1.15	-3%
S15B-2	WB = shear	3.13	4.17	3.75	1.24	1.17	-5%
S25B-1	P = Punching	3.13	4.17	6.25	0.97	0.87	-10%
S25B-2	P = Punching	3.13	4.17	6.25	1.06	0.95	-11%
S35A-1	P = Punching	1.91	2.91	8.75	1.14	1.09	-4%
S35A-2	P = Punching	1.91	2.91	8.75	0.94	0.89	-5%
S35B-1	P = Punching	3.13	4.17	8.75	1.10	1.05	-4%
S35B-2	P = Punching	3.13	4.17	8.75	1.10	1.06	-4%
S35C-1	P = Punching	4.375	5.42	8.75	1.55	1.39	-10%
S35C-2	P = Punching	4.375	5.42	8.75	1.20	1.16	-4%
All tests			AVG		1.07	1.01	-6%
All tests			COV		20%	19%	
All - S5A, S35C1			AVG		1.07	1.01	-5%
All - S5A, S35C1			COV		11%	12%	
WB	S5B-1; S5B-2; S15B1; S15B-2		AVG		1.06	1.02	-4%
WB	S5B-1; S5B-2; S15B1; S15B-2		COV		16%	16%	
P	S25(B1,B2); S35(A1; A2; B1; B2; C2)		AVG		1.07	1.01	-6%
P	S25(B1,B2); S35(A1; A2; B1; B2; C2)		COV		9%	11%	

Source: Author.

In Table 7-6, the ratio F_{EXP}/F_{FEM} varied between 3% and 11% by including the damage parameters. In practice, the same level of variation was observed regardless of the governing

failure mechanism being wide beam shear (WB) or punching (P). Since both approaches (including and not including the damage parameters) led to similar levels of accuracy, it can be stated that the simulations could be performed without the damage parameters for simplicity.

Figure 7-10 - Influence of including or not the damage parameters in the load – displacement curves of the numerical simulations.

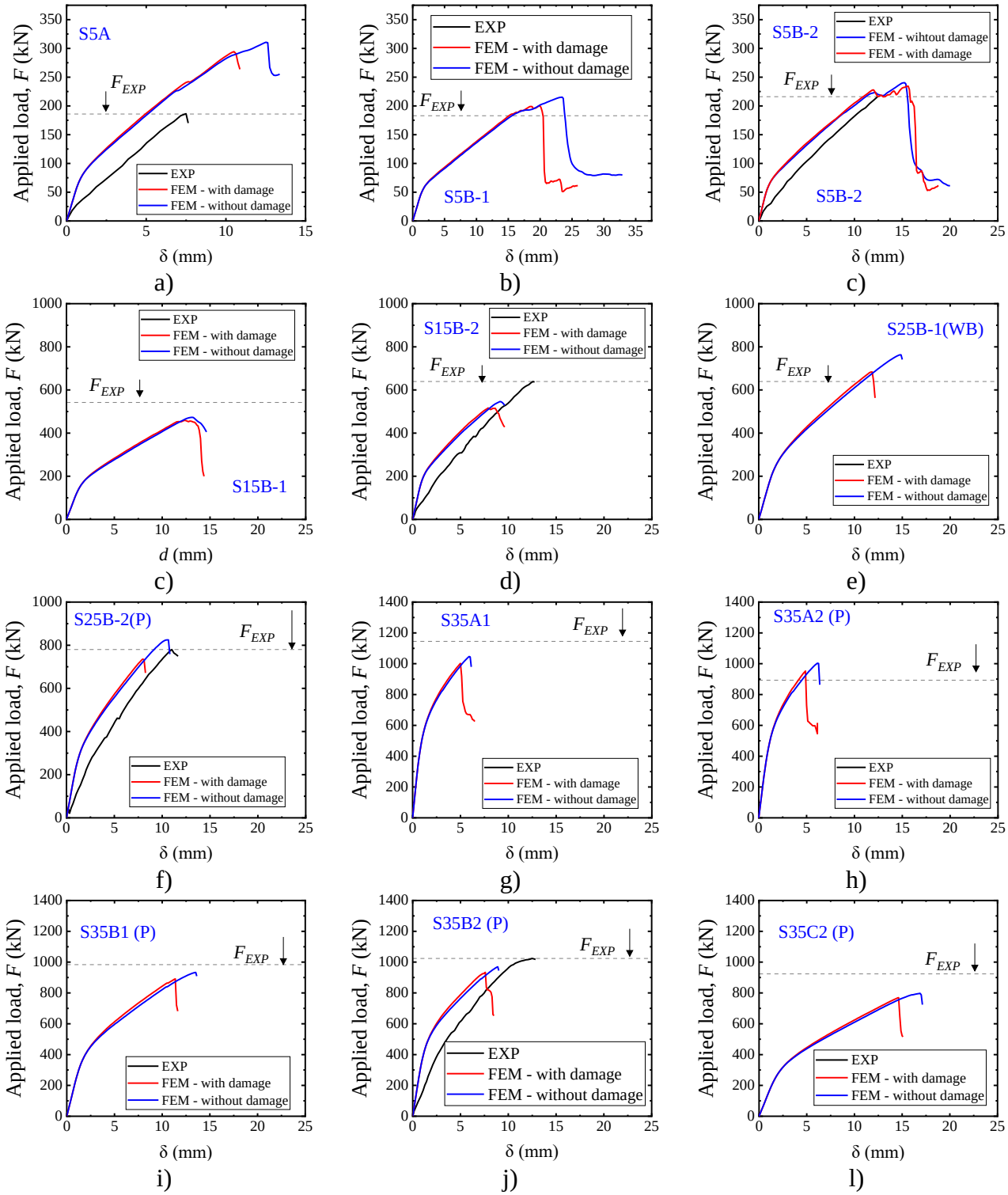

Source: Author.

Figure 7-10 shows the load-displacement graph of the simulations with and without the damage parameters. In general, including the damage parameters influence only marginally the ultimate load and deformation capacity. In other words, it was observed that the displacement at failure also varied by considering the damage parameters in the numerical simulations.

Besides, Figure 7-10 shows that in most cases, the brittle failure mechanism of the slabs was well represented with and without the damage parameters. Herein, this brittle mechanism is mainly related to the sharp decrease of the applied load at failure in numerical simulations.

These small differences in the ultimate loads and displacements at failure can be owned as a small influence of the elastic modulus of the concrete at failure (and consequently of the irreversible plastic strains). Despite the test be not cyclical, shear redistribution at failure allow load relief on some regions of the slab, and consequently some crack closing would be expected in these regions. This kind of shear redistribution is presented, for instance, in Natário, Fernandez Ruiz and Muttoni (2014), for cantilever slabs under concentrated loads. In these tests, it was observed that after reaching the ultimate shear capacity in the front side of the load, at the symmetry axis, the load was redistributed to the lateral zones.

Moreover, the elastic modulus of the concrete around the load influence the confining stresses in this region. Therefore, including the damage parameters allows consider more realistically some aspects of the problem. Nevertheless, the failure loads with and without including the damage parameters can be considered similar.

7.5.2 Effect of the stress-strain behavior in compression

Several models were proposed in the literature to describe the non-linear behavior of normal strength concrete in compression (CARREIRA; CHU, 1985; FEENSTRA, 1993; GUO, 2014; HOGNESTAD, 1953; KRÄTZIG; PÖLLING, 2004), which differ mainly in the post-peak behavior in compression and tension (Figure 7-11a). This occurs because some models include parameters related to the element size l_{eq} and crushing energy G_{ch} to softer the degradation of stresses under compression (FEENSTRA, 1993; KRÄTZIG; PÖLLING, 2004). In Figure 7-11a, the model of Krätzig and Pölling (2004) considers the crushing energy G_{ch}, which was calculated through the following expression (OLLER, 1988), which is dependent of the fracture energy:

$$G_{ch} = \left(\frac{f_{cm}}{f_{ct}} \right)^2 \cdot G_f \qquad (7.14)$$

Figure 7-11 - Comparison of different stress-strain models to describe the behavior under a) compression and b) tension for normal strength concretes.

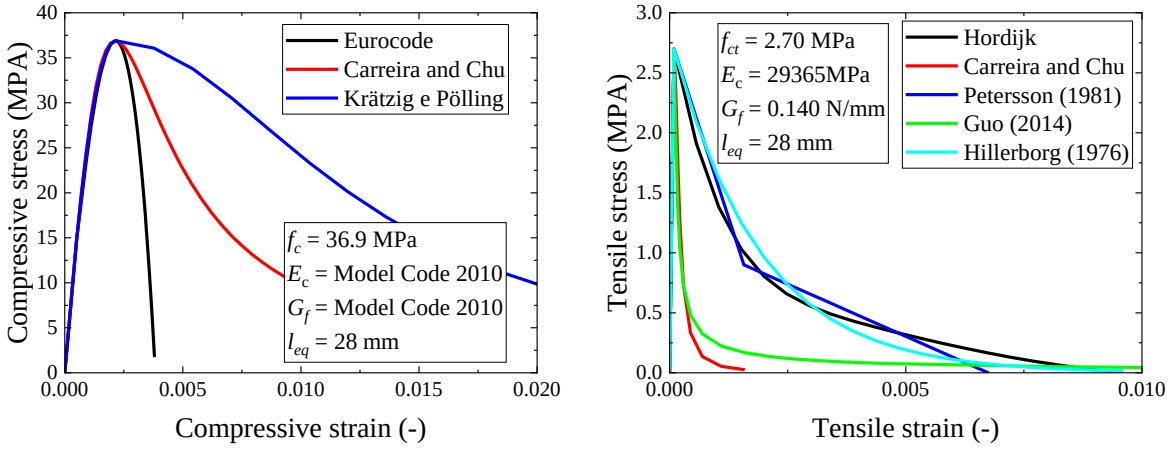

a) **b)**

Source: Author.

In tension, most models used to describe the non-linear behavior of the concrete provide similar results regarding the relation tensile stress-crack opening displacement (CORNELISSEN, H. A. W.; HORDIJK, D. A.; AND REINHARDT, 1986; FÉDÉRATION INTERNATIONALE DU BÉTON (FIB), 2012; HORDIJK, 1992; PETERSSON, 1981). In Figure 7-11b, the models from Hordijk (1992), Petersson (1981), and Hillerborg et al. (1976) account for the fracture energy G_f to describe the softening behavior of concrete in terms of tensile stress × crack opening ($\sigma_t \times w$). In Figure 7-11, the crack openings w are translated to tensile strains ε_t by the expression $\varepsilon_t = f_{ct}/E_c + w/l_{eq}$. It can be seen that the expressions from Peterson (1981), Hillerborg et al. (1976) and Hordijk (1992) provides quite similar results. Conversely, the curves built with the expressions from Carreira and Chu (1986) and Guo (2014) does not consider the finite element size in the expression and provides quite different post-peak tensile strengths.

Figure 7-7 shows the comparison between tested and predicted resistances with the FEM according to the different stress-strain behaviors in compression assumed to the concrete. In these analyses, the finite element models assume all properties of the reference finite element approach, except that the damage parameters were not considered in these evaluations.

Table 7-7 - Comparison between tested and predicted resistances F_{EXP}/F_{FEM} according to the stress-strain behavior assumed in compression.

					Stress-strain behavior in compression		
					EN 1992-1-1:2005 ***(Reference)***	Carreira and Chu	Krätzig and Pölling
Test	Failure mechanism	a_v/d_l [-]	a/d_l [-]	b_{slab}/l_{load} [-]	F_{EXP} / F_{FEM} [-]	F_{EXP} / F_{FEM} [-]	F_{EXP} / F_{FEM} [-]
S5A	shear	1.91	2.91	1.25	**0.60**	**0.59**	**0.55**
S5B-1	shear	3.13	4.17	1.25	**0.85**	**0.76**	**0.74**
S5B-2	shear	3.13	4.17	1.25	**0.90**	**0.75**	**0.89**
S15B-1	shear	3.13	4.17	3.75	**1.15**	**0.76**	**0.92**
S15B-2	shear	3.13	4.17	3.75	**1.17**	**1.02**	**0.97**
S25B-1	Punching	3.13	4.17	6.25	**0.87**	**0.82**	**0.85**
S25B-2	Punching	3.13	4.17	6.25	**0.95**	**0.90**	**0.87**
S35A-1	Punching	1.91	2.91	8.75	**1.09**	**1.10**	**1.07**
S35A-2	Punching	1.91	2.91	8.75	**0.89**	**0.89**	**0.89**
S35B-1	Punching	3.13	4.17	8.75	**1.05**	**1.16**	**1.04**
S35B-2	Punching	3.13	4.17	8.75	**1.06**	**1.00**	**1.01**
S35C-1	Punching	4.375	5.42	8.75	**1.39**	**1.31**	**1.24**
S35C-2	Punching	4.375	5.42	8.75	**1.16**	**1.08**	**1.02**
All tests				AVG	1.01	0.93	0.93
All tests				COV	19%	19%	14%
All tests (-) S5A, S35C1				AVG	1.01	0.93	0.93
All tests (-) S5A, S35C1				COV	12%	16%	10%
WB	S5B-1; S5B-2; S15B1; S15B-2			AVG	1.02	0.82	0.88
WB	S5B-1; S5B-2; S15B1; S15B-2			COV	16%	16%	11%
P	S25B1-2 ; S35A-1; A2; B1; B2; C2			AVG	1.01	0.99	0.96
P	S25B1-2 ; S35A-1; A2; B1; B2; C2			COV	11%	13%	9%

Source: Author.

Table 7-7 shows that the accuracy of the different approaches are quite similar for slabs failing by punching. However, the predictions deviates in >12% compared to the reference approach considering only the tests that failed as wide beams in shear. In practice, considering the large post-peak compressive strength according to the models from Carreira and Chu (1985) and Krätzig and Pölling (2004) overestimated the tested resistances in one-way shear. However, it can be seen re-calibrating other parameters such as the fracture energy and dilation angle, these approaches may lead to almost the same results. Therefore, any of these models could be used since other secondary parameters be well calibrated.

Figure 7-12 shows the influence of the different stress-strain behavior in compression assumed for the concrete. Figure 7-12 shows that in general, the studied models changed only slightly the ultimate loads and the displacements at failure. The stress-strain models with a large residual compressive strength (Eurocode < Carreira and Chu < Krätzig and Pölling) led in most cases to a higher ultimate load and displacement at failure. In most simulations, the governing failure mechanism was not changed by changing the stress-strain behavior in compression.

However, the tests S15B1- and S15B-2 showed that, in some cases, the use of the models from Carreira and Chu and Krätzig and Pölling might lead to less brittle failure mechanisms at failure (almost ductile, indeed). Therefore, it is necessary evaluate very carefully the use of models that assume a large residual tensile strength in compression.

Figure 7-12 - Influence of the stress-strain behavior in compression assumed for the concrete.

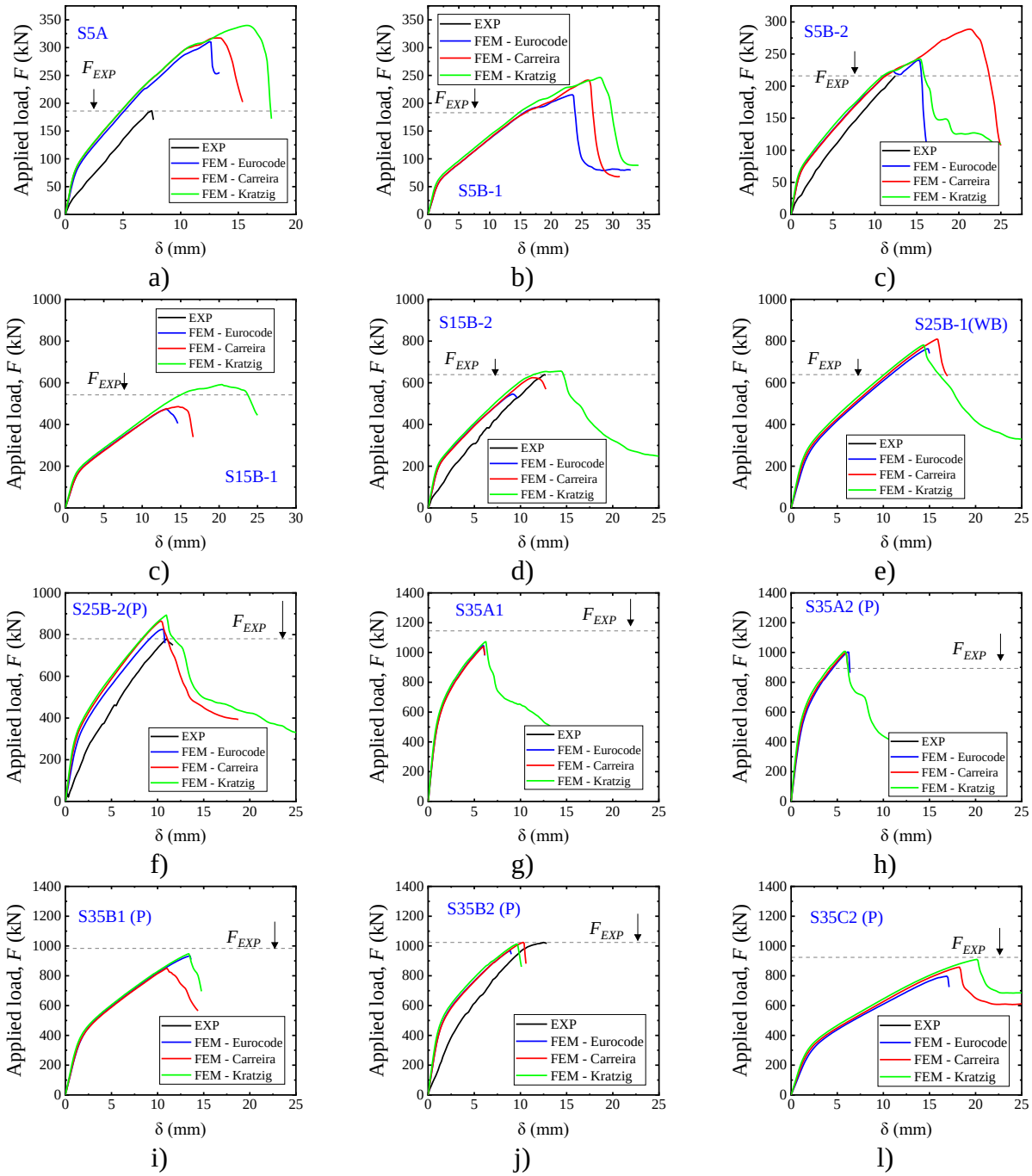

Source: Author.

7.5.3 Comparative analyses of different approaches from literature

In the literature, the numerical studies may differ in several modeling options. In the case of the Concrete Damaged Plasticity model, these modeling options may include the use of different dilation angles and fracture energy as well as the use of significantly different viscosity parameter values. This section intended to show how some different modeling options may lead to similar levels of accuracy and, in some cases, to overly erroneous predictions.

Figure 7-8 describes four modeling approaches that combine different modeling options involving: (i) stress-strain behaviors in compression and tension, (ii) dilation angles values, (iii) fracture energy values, and (iv) viscosity parameters. Approach 1 is the proposed one (reference) in this study. Approach 2 is a modeling approach commonly found in studies related to punching capacity (GENIKOMSOU; POLAK, 2015). Approach 3 is one commonly used in studies related to composite structures. In approach 3, the stress-strain behavior in tension (CARREIRA; CHU, 1986) does not include the finite element size and, in general, the result is a significantly lower residual tensile strength after the peak stress compared to the models from Hordijk (1992) and Petersson (1981) (see Figure 7-11). Based only on the stress-strain behavior in tension, someone could expect in this way a considerably lower ultimate capacity of the slabs considering Approach 3.

Table 7-8 - Modelling options proposed and from different approaches commonly found in the literature.

Parameter	Approach (1) - Reference	Approach (2)	Approach (3)	Approach (4)
$\sigma_c \times \varepsilon_c$	Eurocode (CEN, 2005)	(HOGNESTAD; HANSON; MCHENRY, 1955)	(CARREIRA; CHU, 1985)	(CARREIRA; CHU, 1985)
$\sigma_t \times \varepsilon_t$	(HORDIJK, 1992)	(PETERSSON, 1981)	(CARREIRA; CHU, 1986)	(CARREIRA; CHU, 1986)
$d_c \times \varepsilon_c$	-	-	-	-
$d_t \times \varepsilon_t$	-	-	-	-
Fracture energy	Model Code 2010	Model Code 1990	-	-
Dilation angle	30	40	40	40
viscosity	0.00001	0.00001	0.001	0.00001
Finite element	C3D8R	C3D8R	C3D8R	C3D8R

Source: Author.

Approach 4 is a modified approach from Approach 3, changing only the viscosity parameter. The damage parameters were not included in this section since it was observed that, in general, this parameter does not significantly change the global behavior from the numerical models in static problems.

Table 7-9 compares experimental and predicted resistances with the FEM using the different approaches (modeling options detailed in Table 7-8). Table 7-9 shows that even using significantly different values of fracture energy and dilation angle, approaches 1 and 2 led to similar levels of accuracy. In practice, this occurs because the higher fracture energy used in approach 1 is balanced with the lower dilation angle used. Comparing the predictions from approaches 1 and 2, the higher differences occurred for the tests that failed in wide beam shear (WB), reaching differences between 10 and 20% in the predicted failure load. Conversely, the punching capacity predictions were very similar for both approaches.

Table 7-9 – Comparison between tested and predicted resistances using the FEM based on different approaches (modelling options from Table 7-8).

					Approach 1	**Approach 2**	**Approach 3**	**Approach 4**
Test	F.M.	a_v/d_l [-]	a/d_l [-]	b_{slab}/l_{load} [-]	F_{EXP} / F_{FEM} [-]	F_{EXP} / F_{FEM} [-]	F_{EXP} / F_{FEM} [-]	F_{EXP} / F_{FEM} [-]
S5A	shear	1.91	2.91	1.25	0.60	0.55	0.36	0.63
S5B-1	shear	3.13	4.17	1.25	0.85	0.73	0.52	1.32
S5B-2	shear	3.13	4.17	1.25	0.90	0.71	0.54	1.22
S15B-1	shear	3.13	4.17	3.75	1.15	0.95	0.51	1.18
S15B-2	shear	3.13	4.17	3.75	1.17	1.01	0.51	1.30
S25B-1	Punching	3.13	4.17	6.25	0.87	0.87	0.40	1.02
S25B-2	Punching	3.13	4.17	6.25	0.95	0.92	0.43	1.08
S35A-1	Punching	1.91	2.91	8.75	1.09	1.07	0.49	1.51
S35A-2	Punching	1.91	2.91	8.75	0.89	0.89	0.37	1.43
S35B-1	Punching	3.13	4.17	8.75	1.05	1.02	0.53	1.51
S35B-2	Punching	3.13	4.17	8.75	1.06	0.95	0.51	1.43
S35C-1	Punching	4.375	5.42	8.75	1.39	1.20	0.74	2.21
S35C-2	Punching	4.375	5.42	8.75	1.16	1.07	0.56	1.30
All tests				AVG	1.01	0.92	0.50	1.32
All tests				COV	19%	19%	20%	27%
All tests (-) S5A, S35C1				AVG	1.01	0.93	0.49	1.30
All tests (-) S5A, S35C1				COV	12%	13%	12%	13%
WB	S5B-1; S5B-2; S15B1; S15B-2			AVG	1.02	0.85	0.52	1.25
WB	S5B-1; S5B-2; S15B1; S15B-2			COV	16%	18%	2%	5%
P	S25B1-2 ; S35A-1; A2; B1; B2; C2			AVG	1.01	0.97	0.47	1.32
P	S25B1-2 ; S35A-1; A2; B1; B2; C2			COV	11%	9%	15%	15%

Source: Author.

On the other hand, approach 3 led to errors in the predicted failure load higher than 50%. All FEM predicted an overly unsafe failure load using approach 3, even though this approach

is based on the use of a stress-strain behavior in tension with a considerably lower residual tensile strength after cracking. In practice, this occurred because the viscosity parameter used (0.001) changed the effective stress-strain behavior in tension completely. In practice, a value higher than 0.0001 may change the material behavior to a perfect-plastic material (MICHAŁ; ANDRZEJ, 2015). Consequently, the material never fails in the concrete and the slabs only fail after the reinforcement starts to yield.

In approach 4, the viscosity parameter from approach 3 was reduced to the value of 0.00001, which was demonstrated in other studies as being a value sufficiently low to not change the material behavior in an undesirable way and allow numerical convergence in the processing of the FEM (SOUSA et al., 2021b). Table 7-9 shows that the predicted failure load decreased markedly from approach 3 to approach 4, and most of the prediction failure loads arose on the safe side. In practice, the results from approach 4 become more conservative than the other approaches due to the lower residual tensile strength after cracking. This occurs because the model from Carreira and Chu (1986) to describe the stress-strain behavior in tension is not based on a stress-crack opening relationship and, hence, does not allow to include the finite element size in the expressions. In general, approach 4 still led to large errors in the predicted failure load (> 25%) for most tests and shall also be avoided.

Figure 7-13 shows the influence of different sets of modeling options on load × displacement graphs ($F \times \delta$) of the numerical models (see Table 7-8 for notations). From Figure 7-13, the main observation is that beyond overestimating the failure load with approach 3, the failure mechanism of the slabs is also not represented by the numerical models. In practice, all numerical models presented a ductile failure mode using approach 3. Therefore, viscosity values should be carefully evaluated since they can introduce a large bias in the numerical results. In other words, using high values of viscosity parameters, it cannot be possible to identify different failure mechanisms of the slabs.

Figure 7-13 - Influence of different set of modelling options (see Table 7-8) on load × displacement graphs of the numerical models (*F* × *δ*).

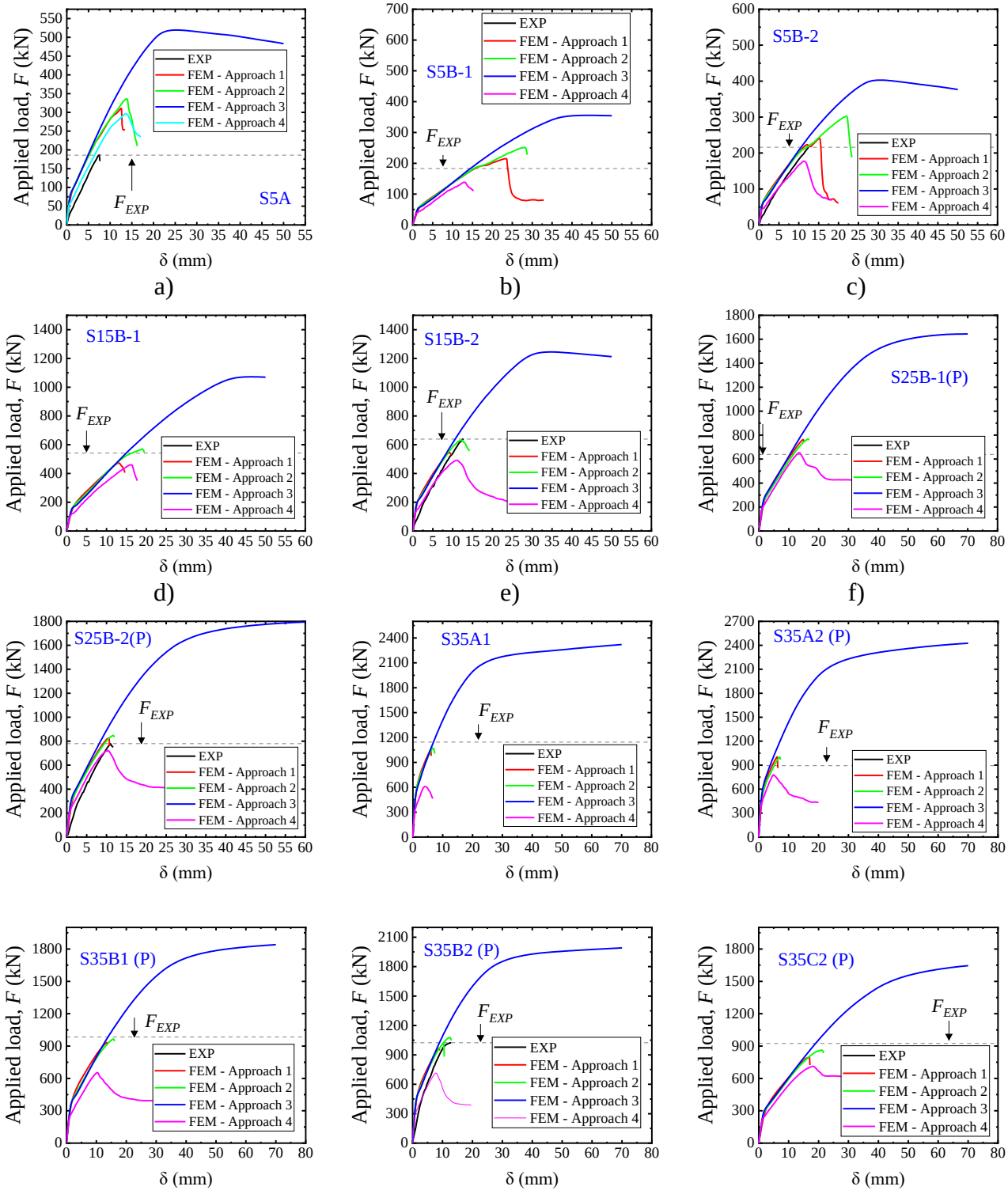

Source: Author.

7.6 Discussion of Chapter 7

Most publications with recommendations for modeling test results focus on the idea that the NLFEA can represent very well test results evaluated. However, some problems arise frequently in many studies: (i) the proposed approach is validated against one specific test results; (ii) the limitations of the numerical model are not discussed or investigated; (iii) the material parameters are calibrated without worry to the physical meaning of such. In this study, it was investigated the accuracy of an arbitrary modeling approach to bring some light to the discussion.

When the numerical model is validated against one specific test result, a severe problem may arise: (i) the proposed numerical model may have been validated against outlier test results and, hence may not represent well most similar problems. For instance, if material parameters from the numerical model are calibrated to represent the test results S5A (as tested), the numerical model would not represent most test results well. In practice, the error of some numerical models increased to more than 50% when the modeling approach was changed to represent better the test S5A. Therefore, calibrating the numerical models for only one test result before applying the modeling strategy for a parametric study can be dangerous.

Another main pitfall observed in several numerical studies is that the validations step from the study usually focuses on representing only one failure mechanism possible and does not cover all possible failure mechanisms that may arise in the parametric studies. For instance, in the testing program performed by Reiβen, Classen and Hegger (2018), it was identified that both one-way shear failures (as wide beams) and punching shear failures could occur by changing the slab width. Therefore, this study could not include (by consistency) a variable such as a slab width in the parametric analyses if the numerical model is not validated to represent both failure mechanisms. Although this methodology could appear as a rule of thumb for more experienced researchers, this practice is commonly not followed in many recent publications.

For instance, it was identified in the numerical studies presented herein that the numerical model might not represent failures like non-slender beams. Therefore, the variables investigated in a future parametric study could not include non-slender beams failure mechanisms. However, it was shown herein that the numerical model simulates well both one-way shear failures and punching failures. Therefore, the numerical models can be used to investigate situations in which both failure mechanisms can be critical.

In the context of NLFEA, it is also essential to understand the results of the outliers (numerical predictions that deviate overly from the test results). For instance, the difficulty of representing the failure load for the test S5A is not coincidental. The failure load from non-slender beams (or wide slabs) is very sensitive to the cracking pattern that develops during the loading and the strut efficiency to transfer shear forces (SOUSA; LANTSOGHT; EL DEBS, 2020; MIHAYLOV; BENTZ; COLLINS, 2013). Consequently, a large scatter in the failure loads appears for such members, even testing equal members. Therefore, it is more difficult for the numerical model to predict the right failure load from a more sensitive failure mechanism. In the case of test S35C-1, a similar interpretation occurs since the punching phenomenon also occurs in a region governed by strut and tie mechanisms (load vicinity) (MUTTONI; FERNANDEZ RUIZ, 2010a). Since this test represents an asymmetrical punching in terms of load position and reinforcement ratios and no specific calibration was applied for each test, it would be natural that some predictions deviate more from the test results.

In many numerical studies, damage evolution parameters are not considered in the CDP model. The main argument for this is that the degradation of elastic stiffness would play a significant role only on cyclic tests, on which the unloading would produce crack closing. However, an essential aspect of three-dimensional problems is neglected in this way: the degradation of the elastic modulus influences the triaxial state of concrete under confining problems. Since the yielding surface of the CDP model is pressure-sensitive, and the punching problems mobilize high confining stresses around the column, it can be expected that not including damage parameters could influence the numerical results. However, until now, no comprehensive investigation on this aspect has been conducted. This study showed that the failure load for shear and punching failure modes decreases around 5% to 10%, including the damage parameters. On the other hand, someone could also not include the damage parameters and change other parameters to reach similar results in terms of failure load. In practice, this would make the numerical models simpler.

One of the most common problems in numerical studies involving the Concrete Damaged Plasticity model is the value of the viscosity parameter used. In practice, many researchers are tempted to use high values such as 0.001 and 0.0001 due to the lower time of processing from the numerical models. In practice, increasing the viscosity parameter from 0.00001 to 0.001 may speed the processing more than 10 times (substantially decreasing the time required in the simulation). However, this has a cost that is not discussed in most papers. In practice, depending on the value of μ, the concrete may behave as a perfect plastic material

in tension and compressions. Michał and Andrzej (2015) show that after a certain value of the viscosity parameter, the post-peak behavior of concrete under tensions and compressions changes overly, losing the descending branch in the stress-strain relationships expected for such materials. While this characteristic may have a minor influence on problems governed by flexure mechanisms, using high values of viscosity parameters may induce flexure failures for all simulations. Therefore, using high viscosity values when more than one failure mechanism (eg. concrete crushing, shear or punching) can be critical in the study and should be avoided.

7.7 Conclusions of Chapter 7

This study discusses the level of accuracy of the proposed approach to predict the ultimate capacity of slabs strips and slabs under concentrated loads aided by NLFEA. The limitations and advantages of the proposed approach are highlighted. Besides, a sensibility study was performed to show the effect of modeling options such as the stress-strain behavior assumed in compression and the effect of including or not the damage parameters in simulation of static tests. The following conclusions can be drawn:

- The NLFEA proposed accurately predicts the ultimate capacity of slab strips and slabs under concentrated loads when the load is placed at distances $a_v > 2d_l$. When the concentrated loads are placed closer to the support ($a_v < 2d_l$), sometimes the ultimate capacity is not predicted accurately because such tests are mostly influenced by the efficiency of the struts between the load and the support. Since there is a large scatter of experimental results for such loading conditions, it can be expected that the numerical models also have more difficulty in representing such failure mechanisms. Considering the 13 tests evaluated (including the outlier results), the average ratio between tested and predicted resistances P_{EXP}/P_{FEM} with the NLFEA was 1.01 with a coefficient of variation of 19%., which is a satisfactory level of precision for a complex problem. Removing the two outlier results (S5A and S35C-1), the ratio P_{EXP}/P_{FEM} has an average value of 1.01 with a coefficient of variation of 12%.
- Including the damage parameters in the NLFEA allows for representing more accurately the change in the confining stresses around the load at failure. However, it was found that the effect of including the damage parameters in static tests was limited for the evaluated tests. The variations in the predicted ultimate loads were in the order of 3% to 11% including and not including the damage parameters. The failure mechanism of the tests did not change when not including the damage parameters. In practice, the tests'

predicted ultimate load and deformation capacity decrease by including the damage parameters. For simplicity, engineers may opt to use or not the damage parameters in static tests since other secondary parameters (fracture energy, dilation angle) be well calibrated within certain limits.

- The stress-strain behavior assumed in compression may influence the ultimate capacity of wide beams and slab strips by around 10%. The influence of this parameter on the slabs that failed by punching was lower (around 5%). In general, the assumed stress-strain behavior in compression did not change the failure mechanism of the slabs. However, some tests presented a less brittle failure mechanism at the maximum load when using models with considerably higher residual compressive strength (for instance, Krätzig and Pölling (2004), which is an undesirable characteristic.
- The use of large values of viscosity parameter (for instance 0.001) shall be avoided on NLFEA since these values change the effective material properties. In practice, the concrete becomes a perfectly plastic material; hence, the slabs' failure loads and mechanisms cannot be well represented. Even when flexure failure modes are well represented with large values of viscosity parameter, the reader shall be aware that using such values introduces a large bias in the numerical results. In practice, the members will almost always fail by flexure regardless of other material properties and geometric characteristics. Therefore, the numerical models with large values of viscosity parameter can be not used when different failure mechanisms are expected by changing specific material and geometric properties of the problem. Besides, large values of viscosity μ block any failure mechanism associated with concrete crushing in the simulations.
- Other approaches, even using considerably different values of fracture energy and dilation angle (stress-strain behavior under confining pressure), may lead to similar levels of accuracy for shear and punching. As possible, these parameters should be chosen based on characterization tests from the laboratory. Nevertheless, since these parameters are most difficult to measure in the laboratory and many uncertainties arise on the values that should be used, some recommendations may be useful. In practice, when a large value of dilation angle is used (for instance, 40 degrees), it is recommended to use a lower value of fracture energy (for instance, the one predicted with *fib* Model Code 1990). Conversely, when a higher value of fracture energy is used (for instance,

the one predicted with *fib* Model Code 2010), a lower dilation angle shall be employed ($\leq$ 30 degrees).

8 FAILURE MECHANISM OF ONE-WAY SLABS UNDER CONCENTRATED LOADS AFTER LOCAL REINFORCEMENT YIELDING

In this chapter, the experimental program conducted on the framework from this thesis is described. The motivation of the experimental program is discussed. Herein, the ultimate capacity of one-way slabs under concentrated loads subjected to local reinforcement yielding at failure is investigated in detail. In the end, a comparison between tested and predicted resistances with the current European and Brazilian code expressions is performed.

8.1 Introduction of chapter 8

One-way slabs under large concentrated loads are commonly found in parking floors, bridge deck slabs, industrial floor slabs, and even residential building slabs during their construction or use (BUI et al., 2017b; FERNÁNDEZ; MARÍ; OLLER, 2021; HENZE; ROMBACH; HARTER, 2020; LANTSOGHT; VAN DER VEEN; WALRAVEN, 2013). Assuming the use of such structures on parking floors or bridge decks, the reader may realize that the load position varies significantly during its use. In practice, different failure mechanisms may be critical for a given slab depending on the load position and other parameters such as the slab width (SOUSA et al., 2021a, 2021c). For instance, when the slab width b_{slab} is not large compared to the load size in the width direction l_{load}, the slab may fail as a wide beam in one-way shear (LANTSOGHT et al., 2014; REIßEN; CLASSEN; HEGGER, 2018) (Figure 8-1a). At the same time, when the load is placed close to the support or the slab width is considerably larger than the load size, the shear flow around the load becomes predominantly radial and, hence, the punching failure may become more critical than as a wide beam in one-way shear (Figure 8-1b). The same behavior occurs when the distance from the load to the support increases (SOUSA et al., 2021a). In this context, the sectional shear capacity may eventually not be reached if the test fails by punching. Since the entire slab strip does not always contribute effectively to the sectional shear capacity (LANTSOGHT et al., 2014), a slab strip called effective shear width (b_{eff} - Figure 8-1b) is commonly defined to evaluate the one-way shear capacity (LANTSOGHT; VAN DER VEEN; WALRAVEN, 2013) for such slabs. The effective shear width is commonly defined as the width on which the maximum shear force integrated along a this width equals the total shear force along the slab width (Figure 8-1b).

Most experimental studies on one-way slabs under concentrated loads focused on the one-way shear and punching capacity on tests without any reinforcement yielding (BUI et al., 2017a; HALVONIK; VIDAKOVIĆ; VIDA, 2020; HENZE; ROMBACH; HARTER, 2020; LANTSOGHT; VAN DER VEEN; WALRAVEN, 2013; NATÁRIO; FERNÁNDEZ RUIZ; MUTTONI, 2014). Investigations related to combined failure mechanisms between flexure and punching were conducted on slab-column connections or flat slabs under concentric loads (GAYED; PEIRIS; GHALI, 2017; WIDIANTO; BAYRAK; JIRSA, 2009). However, investigations related to one-way slabs under concentrated loads presenting local reinforcement yielding or at the transition between shear and flexural failure mechanisms were not often discussed (BELLETTI et al., 2014). Consequently, it is not clear in the literature if analytical expressions based on yield line analysis, for instance, could predict well the slab flexural capacity for a such loading condition. In practice, most design philosophies make the shear and punching capacities from such slabs higher than the flexural capacity to avoid brittle failure modes at ultimate limit state. In this context, it is likely that at failure due to an unexpected overload (for instance), the slabs start failing by flexure before shear or punching. Therefore, it is important to evaluate shear and punching capacity predictions for members with yielding of the flexural reinforcement.

In the case of concentric punching tests, some authors already pointed out that after limited reinforcement yielding a brittle punching failure mode could occur, named flexure-induced punching (GAYED; PEIRIS; GHALI, 2017; WIDIANTO; BAYRAK; JIRSA, 2009). For such cases, the ultimate load would be lower than the predicted punching capacity and also lower than the flexural capacity P_{flex} predicted by yield line analyses. For instance, Hawkins and Ospina (HAWKINS; OSPINA, 2017) pointed out that in some tests rated as critical in flexure the reinforcement started to yield at the load of 50% of P_{flex}, and flexure-induced punching occurred at 80% of P_{flex}. While this mechanism is well-understood in concentric punching tests from slab-column connections (GAYED; PEIRIS; GHALI, 2017; HAWKINS; OSPINA, 2017; WIDIANTO; BAYRAK; JIRSA, 2009), limited information is available on the case of one-way slabs under concentrated loads (FERREIRA et al., 2016).

Figure 8-1 – a) a) Sketch of a slab failing as a wide beam with a critical shear crack visible at the slab side due to the reduced ratio b_{slab}/l_{load} and b) slab failing by punching or a one-way shear mechanism along a limited slab strip due to the larger ratio b_{slab}/l_{load}.

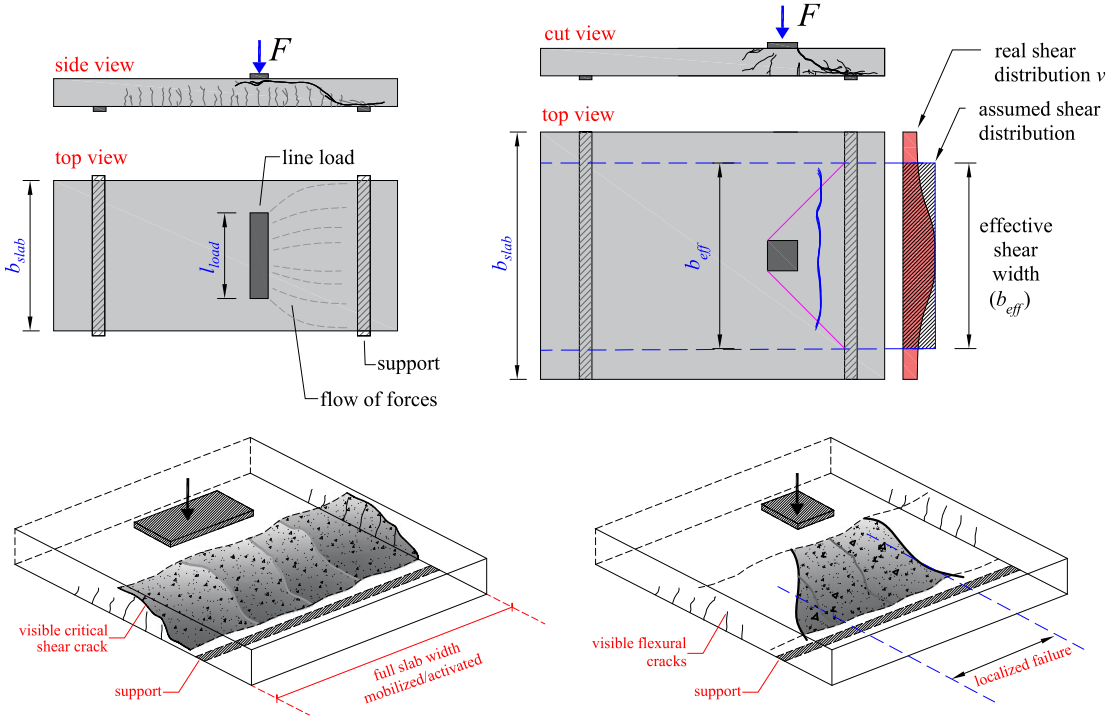

Source: Author.

This study investigates the ultimate capacity and failure mechanism of one-way slabs under concentrated loads subjected to local reinforcement yielding at failure. Compared to previous publications, this study tries to provide a most comprehensive look into the problem by evaluating three possible failure mechanisms: one-way shear as wide beams, the punching shear around the load and the flexural capacity by different yield line patterns.

First, the experimental design is described in detail in Section 8.2 addressing the test layout, material properties and instrumentation detailing. Consecutively (Section 8.3), the experimental results are discussed in terms of the ultimate loads reached, the failure mechanisms identified and load redistribution tracked by the instrumentation. In Section 8.4, the main results are discussed and compared to those observed in the literature. In the end, the main conclusions are described.

8.2 Experimental investigation

This section presents details from the (i) test setup, (ii) specimens and (iii) instrumentation of the tests.

8.2.1 Test setup

This study focuses on one-way slabs with a small thickness (150 mm) compared to previous investigations (HALVONIK; VIDAKOVIĆ; VIDA, 2020; HENZE; ROMBACH; HARTER, 2020; LANTSOGHT; VAN DER VEEN; WALRAVEN, 2013; NATÁRIO; FERNÁNDEZ RUIZ; MUTTONI, 2014; REIßEN; CLASSEN; HEGGER, 2018) and relatively high longitudinal reinforcement ratios (ρ_l = 0.99% ρ_l = 1.32%). This choice is motivated mainly to represent short-span bridges from rural roads typically found in Brazil. Besides, these thicknesses can also be representative of certain floor slabs found in industrial plants, nuclear buildings (LIMAM et al., 2017) or building slabs loaded by heavy equipment during their building or use (BUI et al., 2017b). In Brazil, a large number of rural bridges and culverts in reinforced concrete are built to facilitate the grain flow on farms and rural roads (BORGHI et al., 2021). These bridges and culverts have span lengths that can be very limited (2 m - 6 m) and the slab thickness varies between 150 mm and 250 mm. Nowadays, a large number of bridges are being replaced by reinforced concrete slabs (sometimes prefabricated) and reinforced concrete box culverts, as illustrated in Figure 8-2.

Figure 8-2 – Example of rural bridges commonly found in Brazil: a) prefabricated two-way slabs for a composite bridge b) culvert bridge c) prefabricated deck slab.

a) b) c)

Source: a) (PREFEITURA DE ARARAS, 2015); b) (PREFEITURA DE EXTREMA, 2020); c) (CONCRENORTE - PRÉ MOLDADOS E CONSTRUTORA, [s.d.]).

Figure 8-3 shows a sketch of the test setup as used in the experimental program for each slab. In total, 6 slabs were tested at the São Carlos School of Engineering (EESC) from the University of São Paulo, and each slab was tested twice. The specimens measured 3.40 m × 1.60 m with a thickness of 150 mm (h_{slab}). The line supports (sup 1 and sup 2 in Figure 8-3a) consist of a 100 mm wide steel hinge, a rubber layer of 10 mm thick and two instrumented

aluminum beams. A rubber layer was used between the slab bottom face and the steel hinged supports. The hinged supports are supported on instrumented aluminum beams to estimate the distribution of reaction forces, inspired by the work of Natário et al. (NATÁRIO; FERNÁNDEZ RUIZ; MUTTONI, 2014). Figure 8-4 shows a detail of the supports used in detail.

Figure 8-3 - Sketch of test setup as used in the experimental program for each slab: a) test 1 and b) test 2.

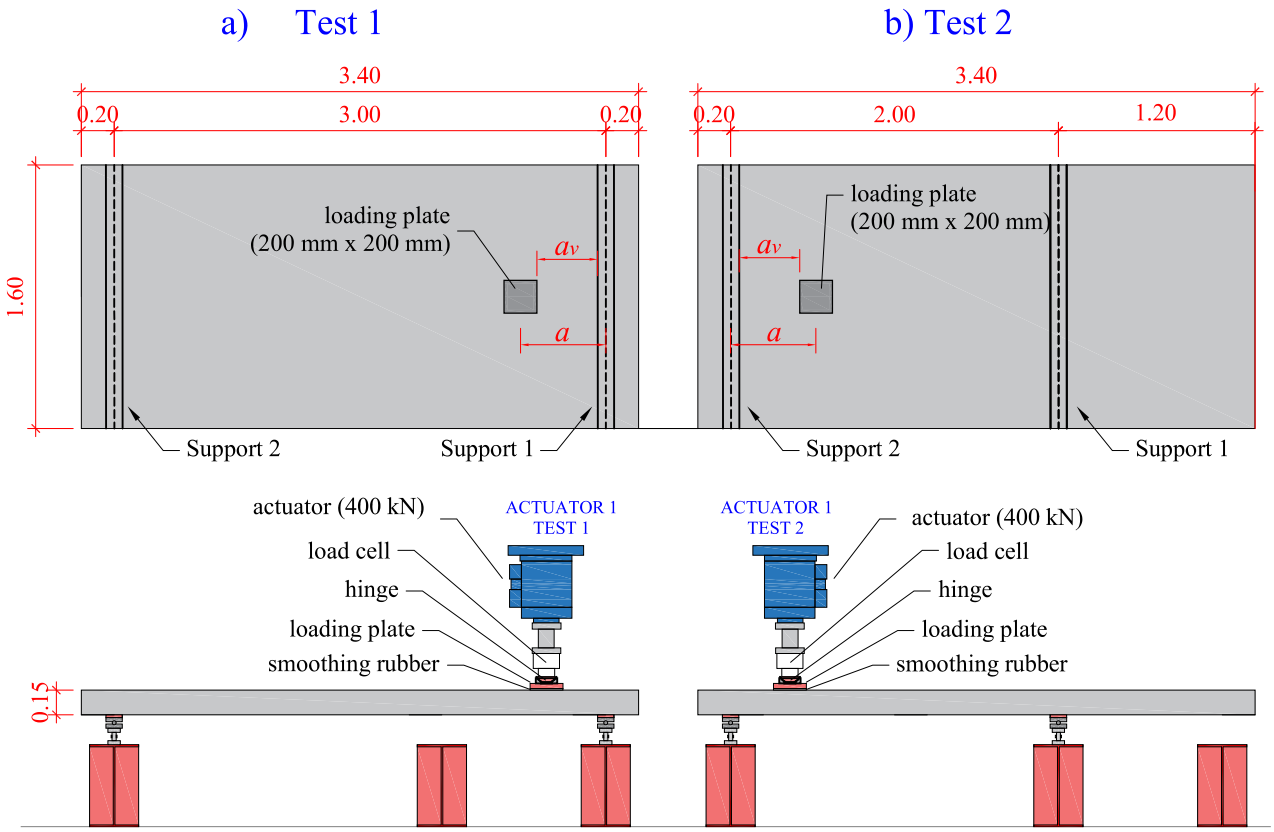

Source: Author.

In the first test of each slab, the span length between the supports was 3 m (Figure 8-3a). After conducting the first test close to support 1, a second test was conducted close to support 2 (Figure 8-3b). To remove the influence of failure caused by the first test for the second test, the span length was reduced in the second test to 2 m.

The measured rubber layer stiffness is approximately 110 MPa (Figure 8-4b) based on a direct compression test on samples of 100 mm × 100 mm × 10 mm as suggested in the literature (PROCHAZKOVA; LANTSOGHT, 2011).

The concentrated load was applied displacement-controlled through a 400 kN servo-controlled actuator. The loading was applied onto a 200 mm × 200 mm square plate and 30 mm

thick, representing a reduced scale (1:2) of the 400 mm × 400 mm tire contact area used in Load Model 1 of NEN-EN 1991-2:2003 for bridge design (CEN, 2003).

The load positions tested were a_v/d_l = 1, a_v/d_l = 2 and a_v/d_l = 3. Herein, a_v is the clear shear span (measured between the inner edges of the loading plate and support) and d_l is the effective depth of the longitudinal reinforcement (span direction). These values were chosen to study the failure mechanism of the slabs (shear, punching or flexure) when direct load transfer by strut mechanisms could play a significant role in the tests.

Figure 8-4 - a) Assembly of the support (rubber layer, hinged support and aluminum beam; b) calculation of the average elastic stiffness of the support.

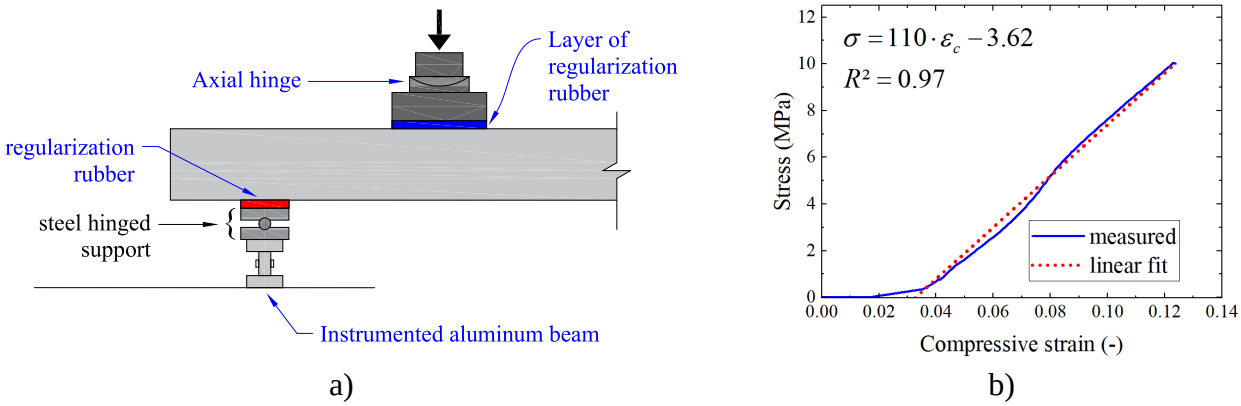

Source: Author.

8.2.2 Specimens

The experimental program consisted of six slabs of 3.4 m × 1.60 m × 0.15 m. The slab properties are given in Table 8-1. The letter “N” or “S” indicates the first or the second test (N = first test and S = second test). Two mixes of concrete were used for the slabs. The material properties presented are mean values. The concrete compressive strength ($f_{c,cyl}$) was measured at cylinder specimens of 100 mm × 200 mm (6 samples for each mix). The concrete tensile strength ($f_{ct,sp}$) was determined with splitting tests on cylinder specimens with 100 mm × 200 mm (6 samples for each mix). The fracture energy G_f was measured according to RILEM TCS (RILEM TECHNICAL COMMITTEES, 1985) on notched prismatic specimens (3 specimens for mix 1 and 2 specimens for mix 2). The only change concerning the RILEM guidelines is that the depth of the notch was reduced to 25 mm. Therefore, the value of 25 mm was used in the determination of G_f. Figure 8-5 shows the measured stress-strain behavior in compression for both concrete mixes used (6 cylindrical specimens for each mix). Both mixes develop a large post-peak regime.

Table 8-1 – Main properties of slabs L1 to L6. Note: the number between parenthesis represent the coefficient of variation; the presented material properties are mean values.

Ref-Teste	$f_{c,cyl}$ (MPa)	$f_{ct,sp}$ (MPa)	G_f (N/mm)	ρ_l (%)	ρ_t (%)	a_v/d_l [-]	a/d_l [-]	l_{span} (m)
L1-N	22.0 (12.0%)	2.36 (11.0%)	0.181	0.99	0.44	1.00	2.21	3
L1-S	22.0 (12.0%)	2.36 (11.0%)	0.181	0.99	0.44	1.00	2.21	2
L2-N	22.0 (12.0%)	2.36 (11.0%)	0.181	0.99	0.44	2.00	3.21	3
L2-S	22.0 (12.0%)	2.36 (11.0%)	0.181	0.99	0.44	2.00	3.21	2
L3-N	22.0 (12.0%)	2.36 (11.0%)	0.181	0.99	0.44	3.00	4.21	3
L3-S	22.0 (12.0%)	2.36 (11.0%)	0.181	0.99	0.44	3.00	4.21	2
L4-N	28.3 (12.0%)	2.63 (12.6%)	0.208	1.32	0.44	1.00	2.21	3
L4-S	28.3 (10.6%)	2.63 (12.6%)	0.208	1.32	0.44	1.00	2.21	2
L5-N	28.3 (10.6%)	2.63 (12.6%)	0.208	1.32	0.44	2.00	3.21	3
L5-S	28.3 (10.6%)	2.63 (12.6%)	0.208	1.32	0.44	2.00	3.21	2
L6-N	28.3 (10.6%)	2.63 (12.6%)	0.208	1.32	0.44	3.00	4.21	3
L6-S	28.3 (10.6%)	2.63 (12.6%)	0.208	1.32	0.44	3.00	4.21	2

Source: Author.

Figure 8-5 - Compression stress-strain behavior of the tested concrete mixes: a) 22 MPa mix and b) 28 MPa mix.

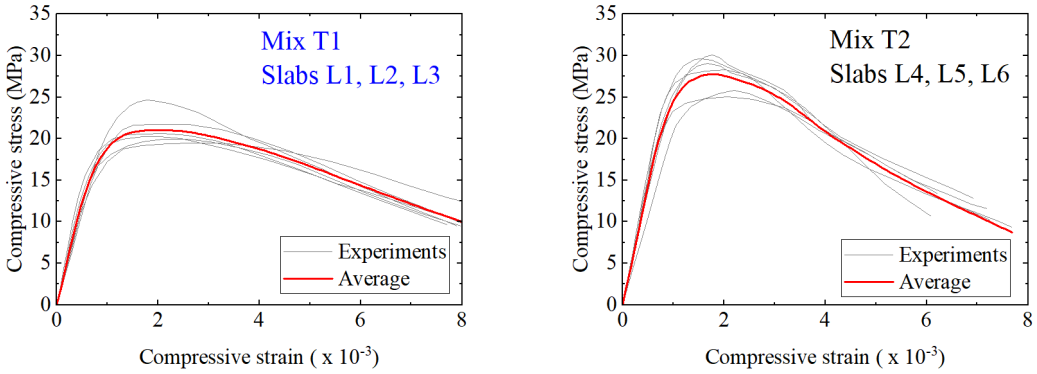

Source: Author.

Figure 8-6 shows the test results used to measure the fracture energy for both mixes. A different number of test results for each mix were used to determine the fracture energy due to brittle failures that occurred for some specimens and that influenced the ability to obtain the complete curve (Figure 8-6). The maximum aggregate size was 19.0 mm for both mixes. Basaltic coarse aggregates were used.

Figure 8-6 - Force-displacement relationship at the mid-span used to measure the fracture energy based on the RILEM TCS: a) test results for 22 MPa mix and b) test results for 28 MPa mix.

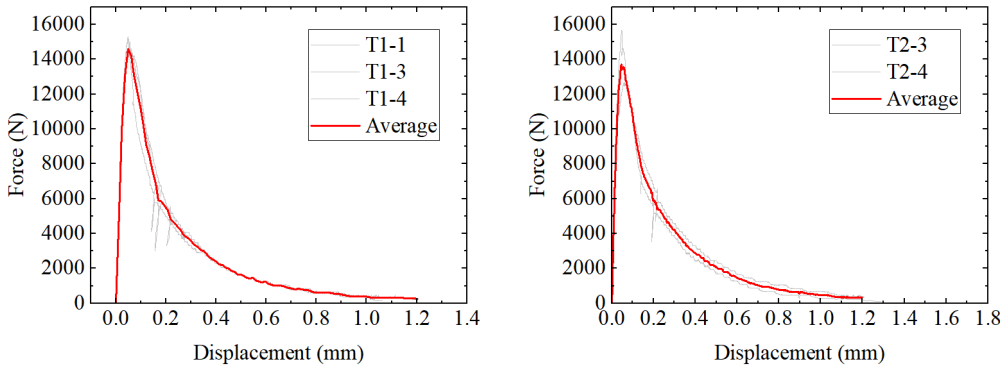

a) b)

Source: Author.

The longitudinal reinforcement ratios were chosen to reach shear or punching failure mechanisms at failure but allow some reinforcement yielding. The bottom longitudinal reinforcement of the slabs consisted of 12.5 mm bars spaced at each 100 mm (ρ_l = 0.99%) or 12.5 mm bars spaced every 75 mm (ρ_l = 1.32%). The bottom reinforcement in the transverse direction of the slabs consisted of 8 mm bars spaced at each 100 mm, resulting in ρ_t = 0.44%. The top reinforcement in the longitudinal and transverse directions (compressed reinforcement) consisted of 8 mm diameter bars spaced at each 200 mm ($\rho_{l,comp}$ = 0.20% and $\rho_{t,comp}$ = 0.21%). The reinforcement layout of the two series of slabs is shown in Figure 8-7. The reinforcement ratio was calculated based on the spacing of the flexural rebars.

Figure 8-7 – Geometry and reinforcement layout of the slabs a) L1, L2 and L3; b) L4, L5 and L6. Dimensions in mm.

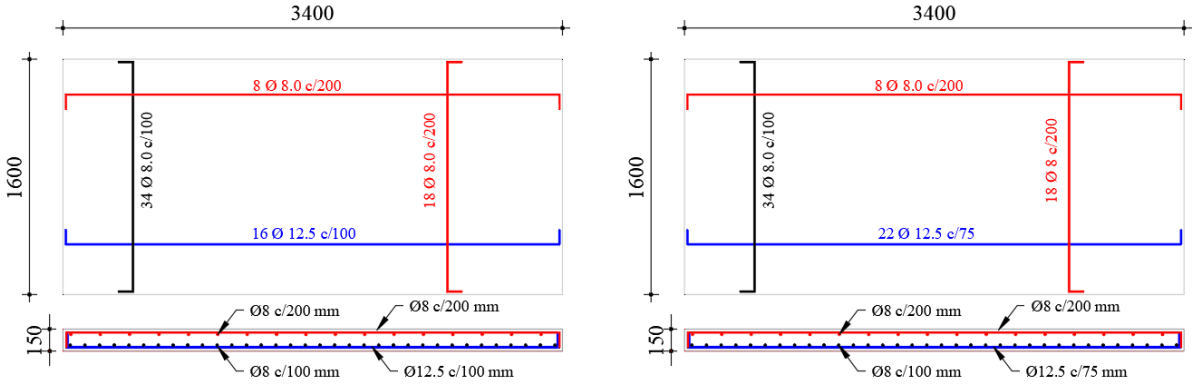

a) Slabs L1, L2, L3 b) Slabs L4, L5, L6

Source: Author.

The properties of the deformed bars were measured by performing direct tensile tests on rebar samples. The properties reported by the manufacturer of the 12.5 mm diameter bars

are: a yield strength, f_{ym} = 579 MPa and an ultimate strength, f_{um} = 803 MPa. The deformed bars with a diameter of 8 mm have the following properties: f_{ym} = 552 MPa and f_{um} = 764 MPa. Figure 8-8 show the results from the tensile tests conducted at our laboratory. A considerably lower yield strength was found for both rebars: (i) f_{ym} = 514 MPa for 12.5 mm rebars and (ii) f_{ym} = 513 MPa for 8.0 mm rebars. A concrete cover of 20 mm was applied, resulting in an effective depth to the longitudinal reinforcement of d_l = 123.75 mm.

Figure 8-8 - Stress-strain graphs of the rebars measured at our laboratory: a) 12.5 mm rebars; b) 8.0 mm rebars.

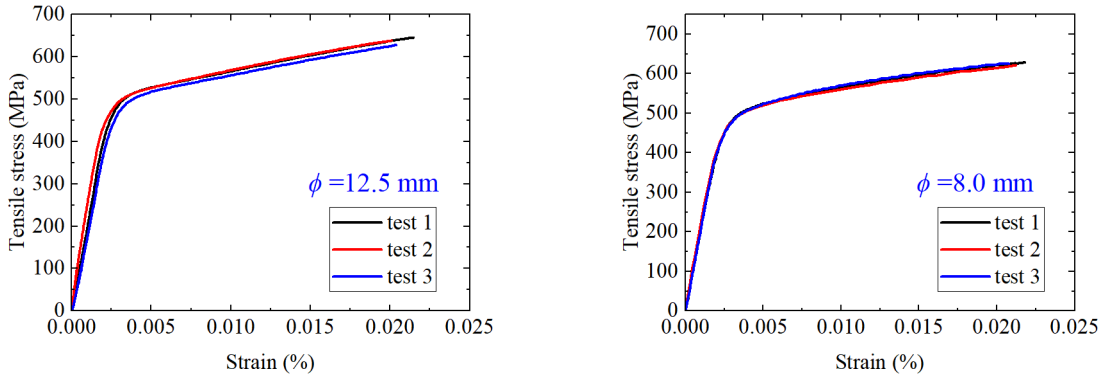

Source: Author.

8.2.3 Instrumentation

During the tests, the following parameters were measured: applied load, vertical displacements of the slab, concrete strain around the load, strains at the tensile reinforcement, and strain distribution along the support beam (aluminum beam). The actuator system directly measured the applied load. The vertical displacements of the slab were measured by linear variable differential transformers (LVDT's). LVDT's with range equal 50 mm and precision of 0.01 mm were applied for the slab vertical deflections. The main vertical displacements monitored were at the center of the slab and at one distance $d_l/2$ from the loading plate face. The arrangement of the LVDTs is shown in Figure 8-9a.

For each test, three extensometers were placed in the load vicinity (compression side of the slab) to measure the concrete compressive strain at failure (Figure 8-9b). Strains at the longitudinal and transverse reinforcement were also monitored by couples of strain gauges glued to the rebar in each direction (Figure 8-10). The position of the strain gauges was always within the square of the loading plate, as sketched in Figure 8-10. For other tests, the position of the extensometers was moved to fit with the different load positions.

Figure 8-9 - Sketch of the instrumentation: a) side view of the LVDT's position; b) top view of the strain gauges along the concrete surface.

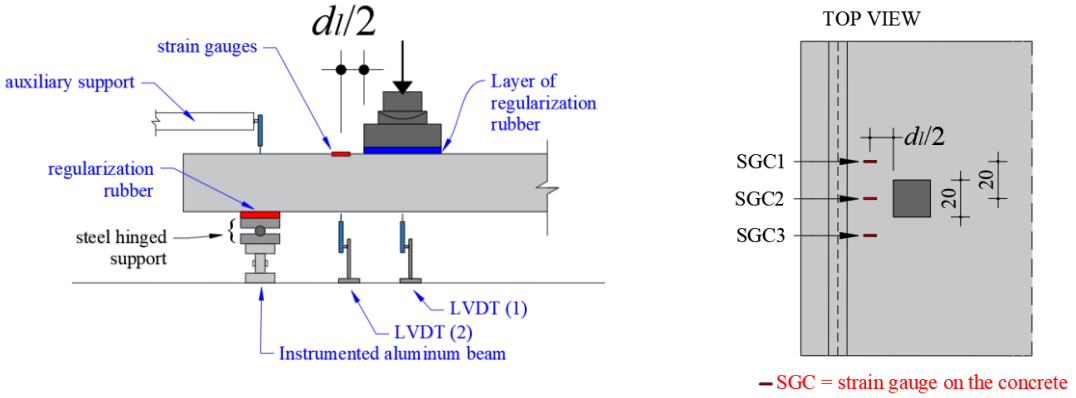

a) b)

Source: Author.

Figure 8-10 - Strain gauges position in the reinforcement for the test L1-N.

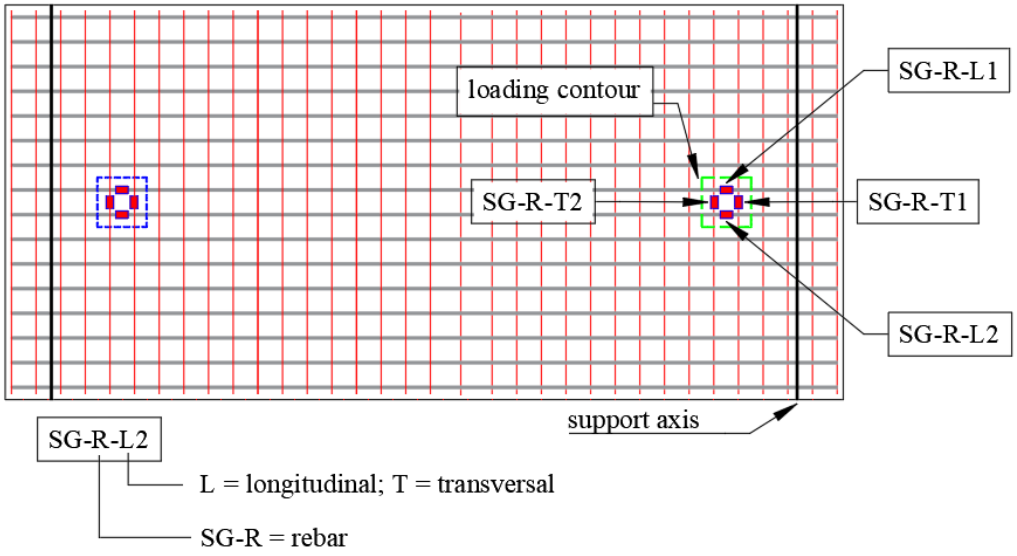

Source: Author.

Inspired by the work of Natário (2015), the web of two aluminum beams was instrumented to capture the distribution of reaction forces at the support. The strain gauges were placed between the fixing screws. The dimensions of the beams, position and spacing of strain gauges are described in Figure 8-11. Two extensometers were placed on each side of the web to remove the influence of eventual bending on the profile.

Figure 8-11 - Geometry of the instrumented beams and layout of the instrumentation with strain gauges. Dimensions in mm.

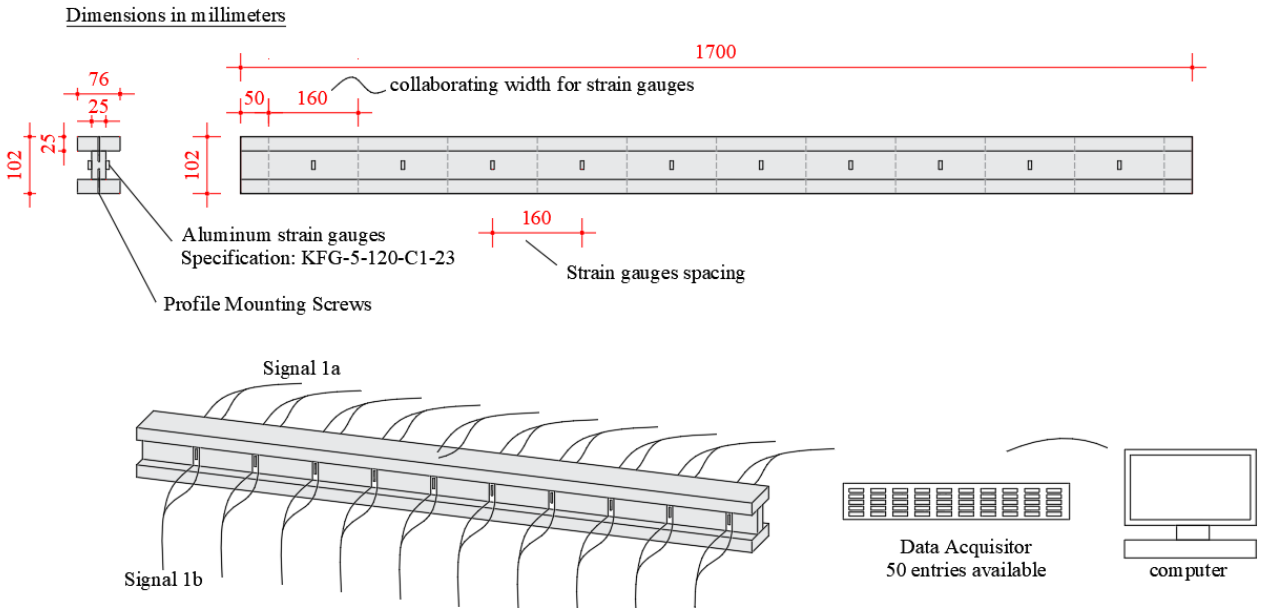

Source: Author.

Figure 8-12 shows some of the main phases of the specimen preparation. Three formworks were prepared to mold each series of the slabs (Figure 8-12a). The reinforcements bars were provided bent and cut by the manufacturers. The reinforcement meshes were assembled in the laboratory by the author (Figure 8-12b). After preparing the reinforcement mesh, including the instrumented rebars, the mesh was inserted into the formwork (Figure 8-12c). Lastly, the slabs were cast with concrete provided by local suppliers (Figure 8-12d). Figure 8-12e shows the details of the support assembly and instrumentation of the aluminum beam. Figure 8-12f shows the layout of the three steel beams and the two support assemblies that support the slab in each test. Only two support assemblies (roller support + aluminum beam) were used for each test. The steel beams were kept in the same position during the tests, and only one of the support assemblies was moved for the second test of each slab.

Figure 8-12 – Details of the slabs preparation: a) assembly of the formworks; b) assembly of the reinforcement mesh; c) assembly of the reinforcement in the formworks; and d) casting of the first three slabs.

a)

b)

c)

d)

e)

f)

Source: Author.

Figure 8-13a,b shows the layout of the tests with the position of the reaction frame, the actuator, loading plate and the rolling bridge that was used to move the reaction frame for each test (from test one to test two of each slab). Figure 8-13c shows an example of the cracking pattern on the compressed side of the slab, which indicates an initial punching failure

mechanism. Figure 8-13d shows an example of wide beams shear failure that arises after increasing the applied displacement due to shear redistribution.

Figure 8-13 – a) and b) Layout of the tests; c) example of the punching failure around the load visible on the compressed side of the slab; and d) example of wide beam shear failure visible on the slab sides.

a)

b)

c)

d)

Source: Author.

8.3 Experimental results

This section presents the main results of (i) ultimate loads and load x displacement graphs, (ii) reinforcement strains, (iii) cracking patterns, (iv) distribution of reaction forces at the support and (v) failure mechanism of the slabs.

8.3.1 Ultimate load and load-displacement curves

Until now, few studies investigated the failure mechanism of one-way slabs under concentrated loads with local reinforcement yielding (FERREIRA et al., 2016). In this study, all tests presented some degree of reinforcement-yielding at failure or failure at the onset of reinforcement yielding. Table 8-2 describes the peak loads (P_{test}) applied in the tests and the tested shear capacity (V_{test}), assuming the static scheme of a beam. The self-weight was considered in V_{test} by assuming γ_{self} = 25 kN/m^3 and the shear force V_{test} was calculated at the mid-shear span between the center of load and the support. Table 8-2 also describes the main material properties, failure mechanism and load layout for each test. The detailed description about the classification of the failure mechanism in Section 8.35.

Table 8-2 - Tested loads and failure mode for slabs L1 to L6.

Test	l_{span} (m)	$f_{c,meas}$ (MPa)	$f_{ct,meas}$ (MPa)	ρ_l (%)	ρ_t (%)	a_v/d_l (-)	a/d (-)	F.M.	P_{test} (kN)	V_{test} (kN)
L1-S	2	22.0	2.36	0.99	0.44	1	2.21	WB+P	332.1	291.6
L2-S	2	22.0	2.36	0.99	0.44	2	3.21	WB+P	270.4	221.3
L3-S	2	22.0	2.36	0.99	0.44	3	4.21	WB+P	253.9	192.0
L4-S	2	28.3	2.63	1.32	0.44	1	2.21	P	374.1	327.9
L5-S	2	28.3	2.63	1.32	0.44	2	3.21	WB+P	296.3	242.0
L6-S	2	28.3	2.63	1.32	0.44	3	4.21	P	314.8	237.0
L1-N	3	22.0	2.36	0.99	0.44	1	2.21	WB+P	273.5	256.4
L2-N	3	22.0	2.36	0.99	0.44	2	3.21	WF+P	282.1	252.3
L3-N	3	22.0	2.36	0.99	0.44	3	4.21	WB+P	275.4	234.7
L4-N	3	28.3	2.63	1.32	0.44	1	2.21	WB+P	351.5	327.3
L5-N	3	28.3	2.63	1.32	0.44	2	3.21	WB+P	321.6	286.5
L6-N	3	28.3	2.63	1.32	0.44	3	4.21	WB+P	267.0	227.8

F.M.: failure mode (WB = wide beam shear failure (one-way shear); P = punching; F = flexure). Source: Author.

Figure 8-14 shows the load-displacement (F–d) diagrams provided by the actuator for each specimen tested: a) tests L1-N to L3-N; b) tests L1-S to L3-S; c) tests L4-N to L5-N and d) tests L4-S to L6-S. All specimens presented a higher displacement at the peak load as the shear slenderness a_v/d_l increased (for instance, comparing the test results from L1-N to L3-N or from L4-N to L6-N). The only exception occurred for the pair of tests L4-S and L5-S, which developed almost the same deflection at the peak load. Conversely, even having reached similar

deflections at failure, the test L4-S developed a relatively stiffer behavior in the load-displacement graph compared to L5-S.

Comparing the deflections at the peak load for tests having the same reinforcement ratio and shear slenderness but with a lower span length, it can be seen that the displacements at the peak load decreased as the span length decreased, which is also consistent with flexural theory.

Figure 8-14 - Load–displacement (*F*–*d*) diagrams for: a) tests L1-N to L3-N; b) L1-S to L3-S; c) L4-N to L5-N and d) L4-S to L6-S.

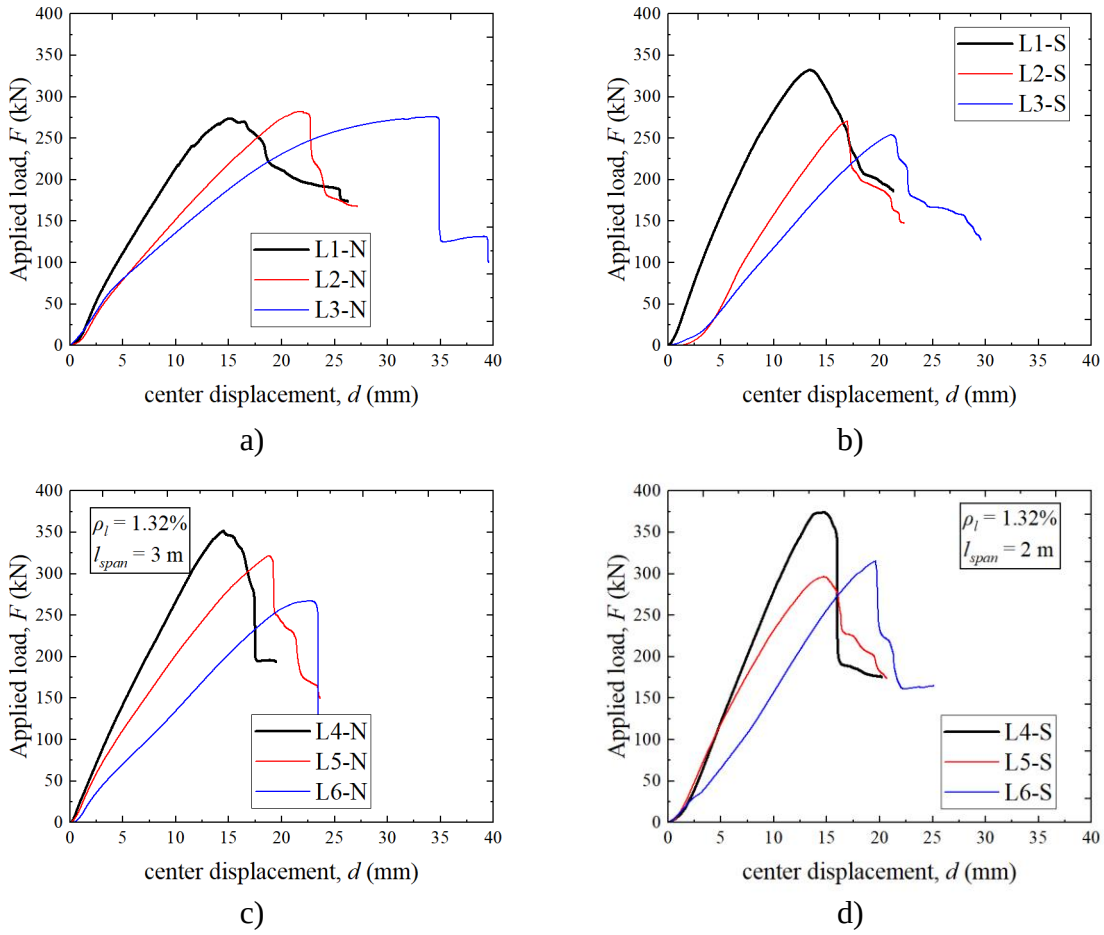

Source: Author.

Evaluating the shape of the curves around the peak load (Figure 8-14), typical brittle shear failures (L5-N and L6-N, for instance), and shear failures with a limited amount of post-peak ductility (test L1-N, for instance), were observed.

At the peak load, most tests developed a partial punching cone at the front face of the loading plate. After this, increasing the applied displacement in the loading plate resulted in a large redistribution of the shear forces and some slabs showed a wide beam failure mode (WB).

This mechanism is characterized by an inclined crack similar to those of beams failing in shear, visible at the sides of the slab.

Figure 8-15 shows how the peak loads and sectional shear forces vary as the shear slenderness increases for the four sets of tests. As can be seen in Figure 8-15a, the ultimate loads (P_{test}) did not change significantly (<5%) by increasing the shear slenderness from a_v/d_l = 2 to a_v/d_l = 3 for most tests. The only exception was the set of tests summarized in Figure 8-14c (L4-N to L6-N), which presented a decrease of the load P_{test} of 17% (comparing L5-N and L6-N). Conversely, the ultimate load increased considerably as the shear slenderness a_v/d_l decreased from 2 to 1 for most groups of tests. This increment was 18% between L1-S and L2-S, for instance. The only exception occurred for the set of tests L1-N and L2-N, which presented almost the same peak loads at failure. In this study, these deviations from tendencies identified can be attributed to the complex interaction between the shear failure mechanisms and the local yielding of the flexural reinforcements, which may trigger different failure mechanisms for some tests. The failure mechanism will be discussed in more detail in next sections.

Figure 8-15 - Influence of shear slenderness a_v/d_l or distance from the concentrated load to support: (a) on tested peak loads P_{test} and b) on calculated shear forces V_{test}.

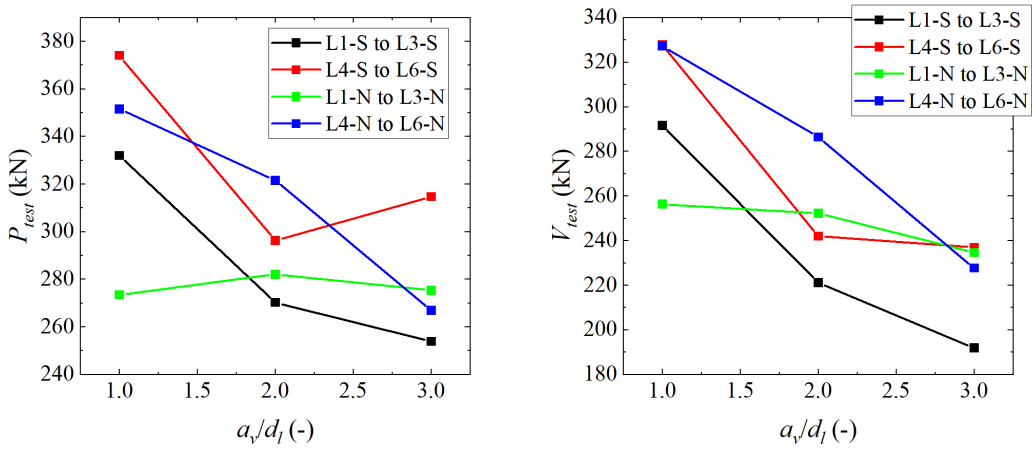

Source: Author.

As performed in previous publications (LANTSOGHT; VAN DER VEEN; WALRAVEN, 2013), the predicted one-way shear resistance enhancement was calculated based on the β factor from EN-1992-1-1:2005 (CEN, 2005), which relates the enhancement of the shear capacity to the ratio a_v/d_l. In practice, the code suggests decreasing the shear demand V_{test} instead of increasing the predicted shear resistance V_R for loads close to the support. However, herein it is assumed that both approaches are equivalent. By decreasing the ratio a_v/d_l from 2 to 1, an increase in the tested sectional shear V_{test} of 2 (or 100%) was expected. In

practice, the sectional shear capacity increased between 2% (L2-N to L1-N) and 35% (L5-S to L4-S). The higher enhancements in the shear capacity were achieved in the tests with a higher longitudinal reinforcement ratio. The lower increase in the shear resistance was previously explained (LANTSOGHT; VAN DER VEEN; WALRAVEN, 2013) by the lower compressive struts efficiency of slabs compared to beams. This occurs because in slabs, a fan of compressive struts develops between the load and the line support for slabs, resulting in different relations a_v/d_l for each strut. This study added the observation that if local reinforcement yields substantially at failure, as identified in the tests L1, L2 and L3, the increase of the sectional shear capacity by compressive struts can be significantly lower.

8.3.2 Reinforcement strains

The shear force redistribution in one-way slabs decreases the brittleness at failure(CANTONE; FERNÁNDEZ RUIZ; MUTTONI, 2021; NATÁRIO; FERNÁNDEZ RUIZ; MUTTONI, 2014; ROMBACH; LATTE, 2009). This phenomenon has been more investigated based on the redistribution of shear forces at the support (CANTONE; FERNÁNDEZ RUIZ; MUTTONI, 2021; LANTSOGHT et al., 2015b; LANTSOGHT; DE BOER; VAN DER VEEN, 2017a; NATÁRIO; FERNÁNDEZ RUIZ; MUTTONI, 2014; REIßEN; CLASSEN; HEGGER, 2018). In this study, the evolution of the strain on the instrumented rebars also confirms this phenomenon. Figure 8-16 and Figure 8-17 show the distribution of the strains at the longitudinal (L1 and L2) and transverse (T1 and T2) reinforcement with the applied load (F).

For instance, Figure 8-16a shows that after reaching the peak load, the longitudinal reinforcement strains stop increasing, even increasing the applied displacement into the actuator. On the other hand, the transverse reinforcement strain keeps increasing by increasing the applied displacement in the actuator. Monitoring the reinforcement strain confirms that after a local failure mechanism by punching, the transverse reinforcement allows redistribution of internal stresses around the load. On the other hand, after the first shear crack on the front side of the load, the longitudinal reinforcement seems to reach a plateau of strains.

Figure 8-16 - Evolution of reinforcement strains around the loaded area during the tests: a) test L1-N; b) test L1-S; c) test L2-N; d) test L2-S; e) test L3-N; f) test L3-S.

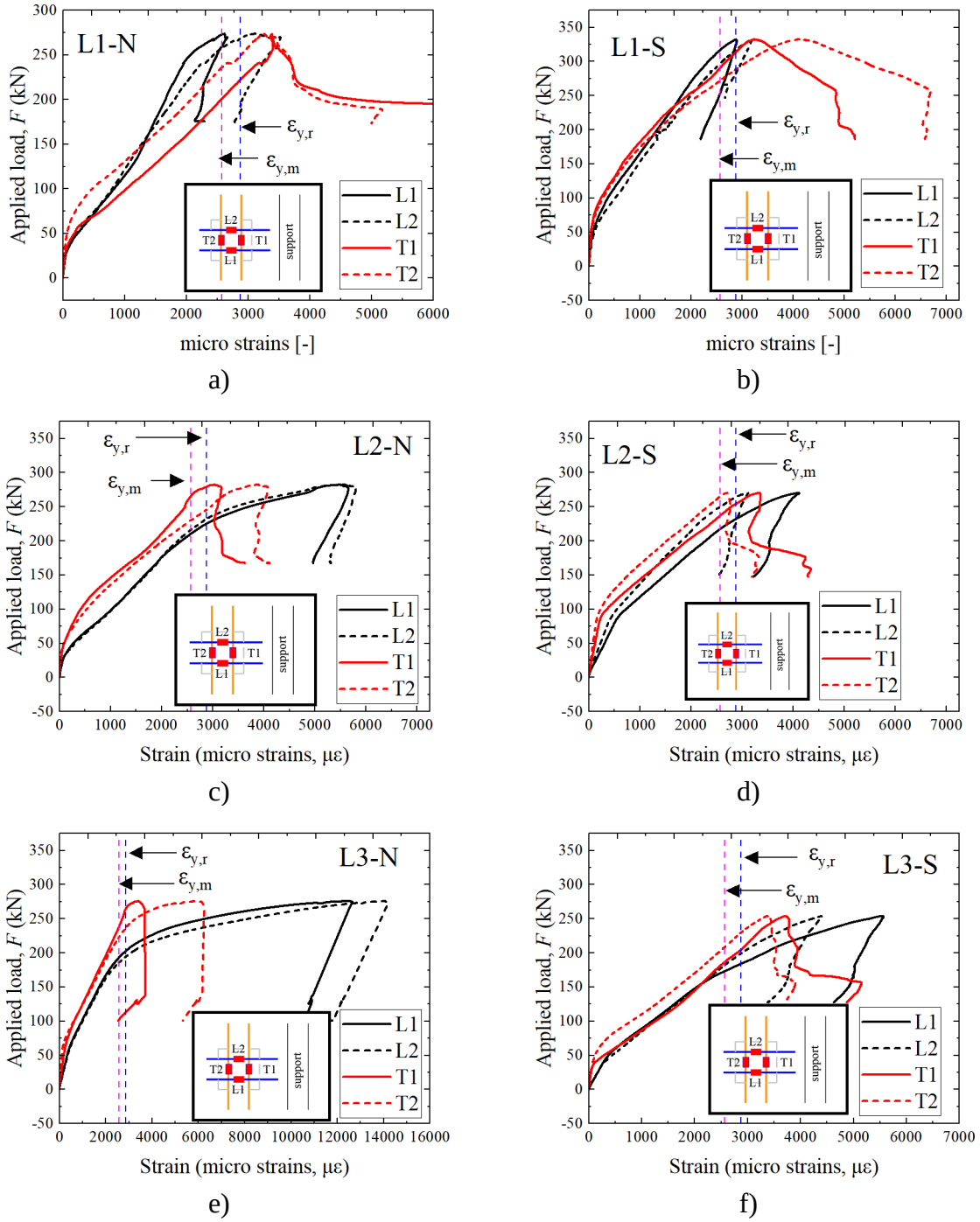

Source: Author.

Figure 8-17 - Evolution of reinforcement strains around the loaded area during the tests: a) test L4-N; b) test L4-S; c) test L5-N; d) test L5-S; e) test L6-N; f) test L6-S.

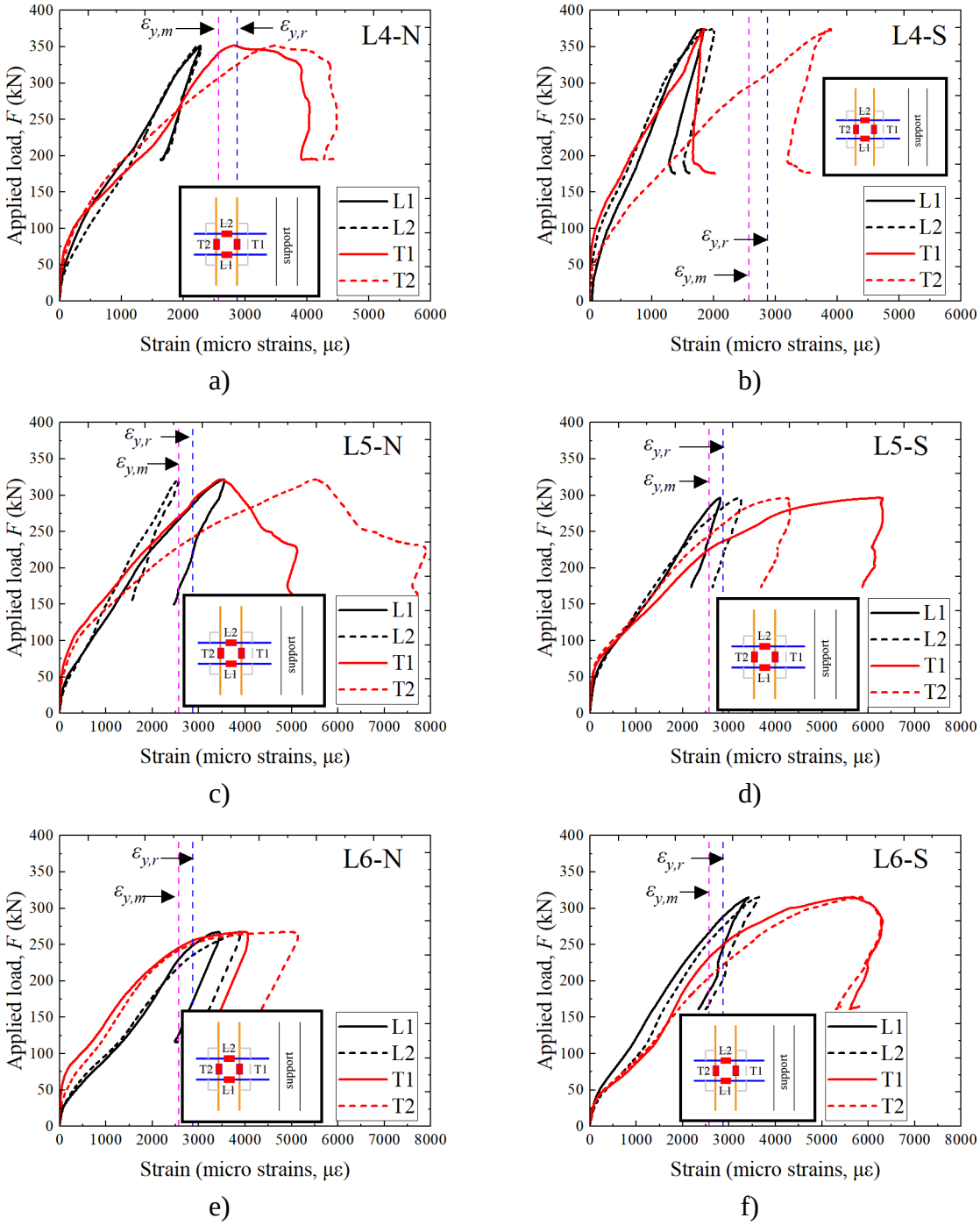

Source: Author.

The comparison between Figure 8-16a, Figure 8-16b and Figure 8-16c (increasing the shear span from L1-N to L3-N) demonstrates that the relation between the measured strains at the longitudinal reinforcement with the strains at the transverse reinforcement increases substantially.

These strains can distinguish another phenomenon. Most tests closely matched the reinforcement strains measured on the two longitudinal rebars, and this is the expected behavior due to the tests' intended geometric symmetry. In practice, some minor deviations of the loading frame or from the reinforcement position could occur during the frame assembly (< 5 mm) or during the concrete casting, resulting in small eccentricities. This aspect explains deviations in the measured strains at the longitudinal rebars from small load levels (for instance, L2-2). However, it is noteworthy that even in the tests on which a close match of measured strains was possible at the beginning of the tests ($F < 0.5\ F_{max}$) (L2-N, L3-N, L3-S), the deviations in the reinforcement strains at some point increase due to the asymmetrical cracking pattern of concrete structures.

8.3.3 Cracking pattern

The cracking pattern is one of the best parameters to indicate the failure mechanisms that took place in the slabs. Figure 8-18 and Figure 8-19 show the cracking pattern of the slabs around the loaded area for each test. Cracks in the top view, bottom view and side views were tracked mainly after unloading the slabs. Different from shear and punching cracks, some flexural cracks closed after unloading and are not visible for some slabs (for instance, side views of L6 in Figure 8-19).

The top view of the slabs shows that all tests presented an asymmetrical punching failure starting between the front sides load and support. The bottom view of the slabs L1, L2 and L3 shows a large presence of tangential and circumferential cracks around the load, as expected for punching failures (Figure 8-18). Slabs L4, L5 and L6 presented a lower number of visible cracks due to the higher reinforcement ratio, which decreased the crack openings at failure (Figure 8-19).

In most tests, concrete detachment close to the support was visible, which helps to explain why most publications considered the most critical section at the support for one-way shear analyses for simply supported slabs. Nowadays, with the aid of finite element models, the idea that the section near the load is governing is more common, which explains the punching failures visible in the top views.

Figure 8-18 - Cracking pattern of the slabs L1, L2 and L3 in terms of top view, bottom view and side views.

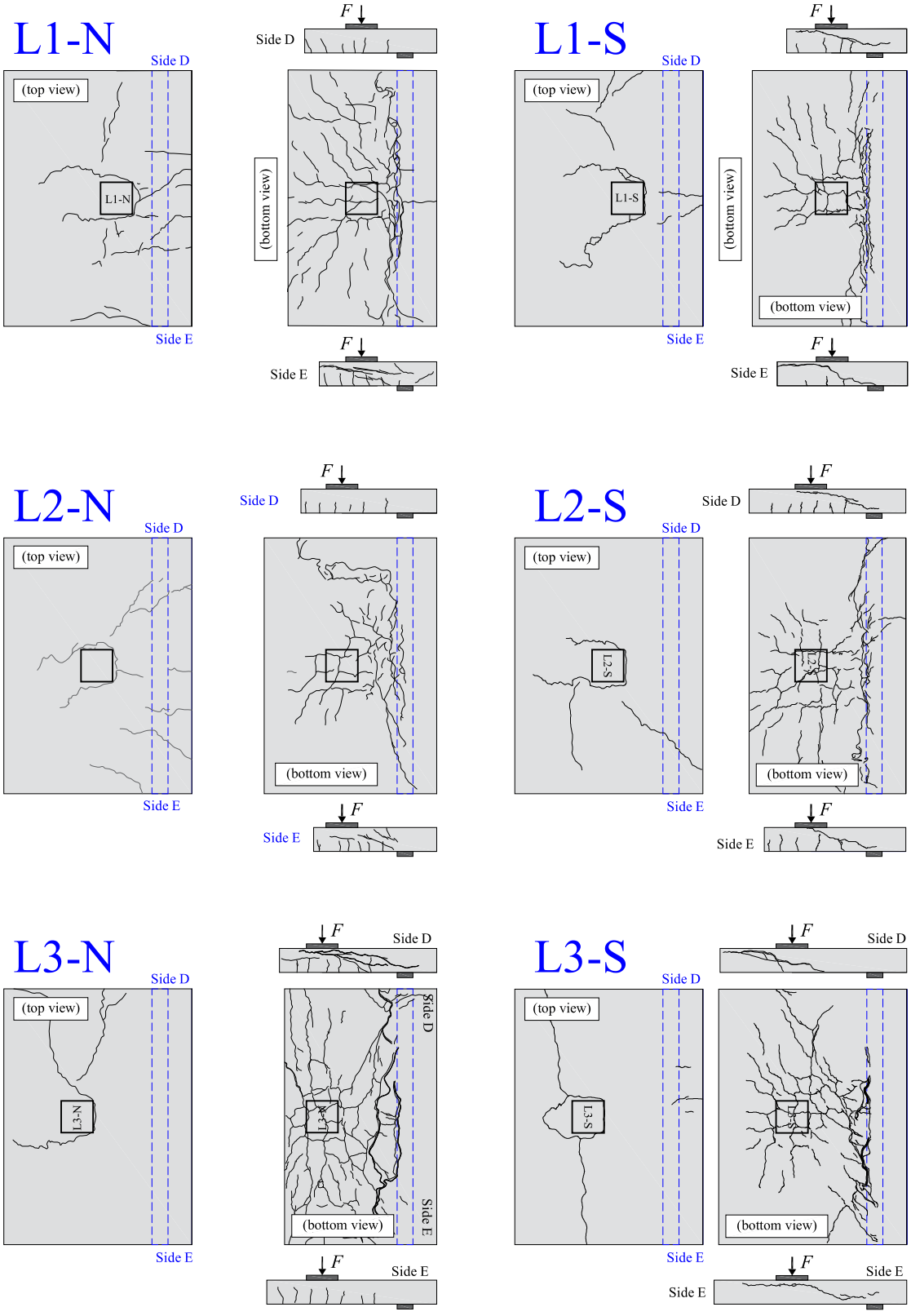

Source: Author.

Figure 8-19 - Cracking pattern of the slabs L4, L5 and L6 in terms of top view, bottom view and side views.

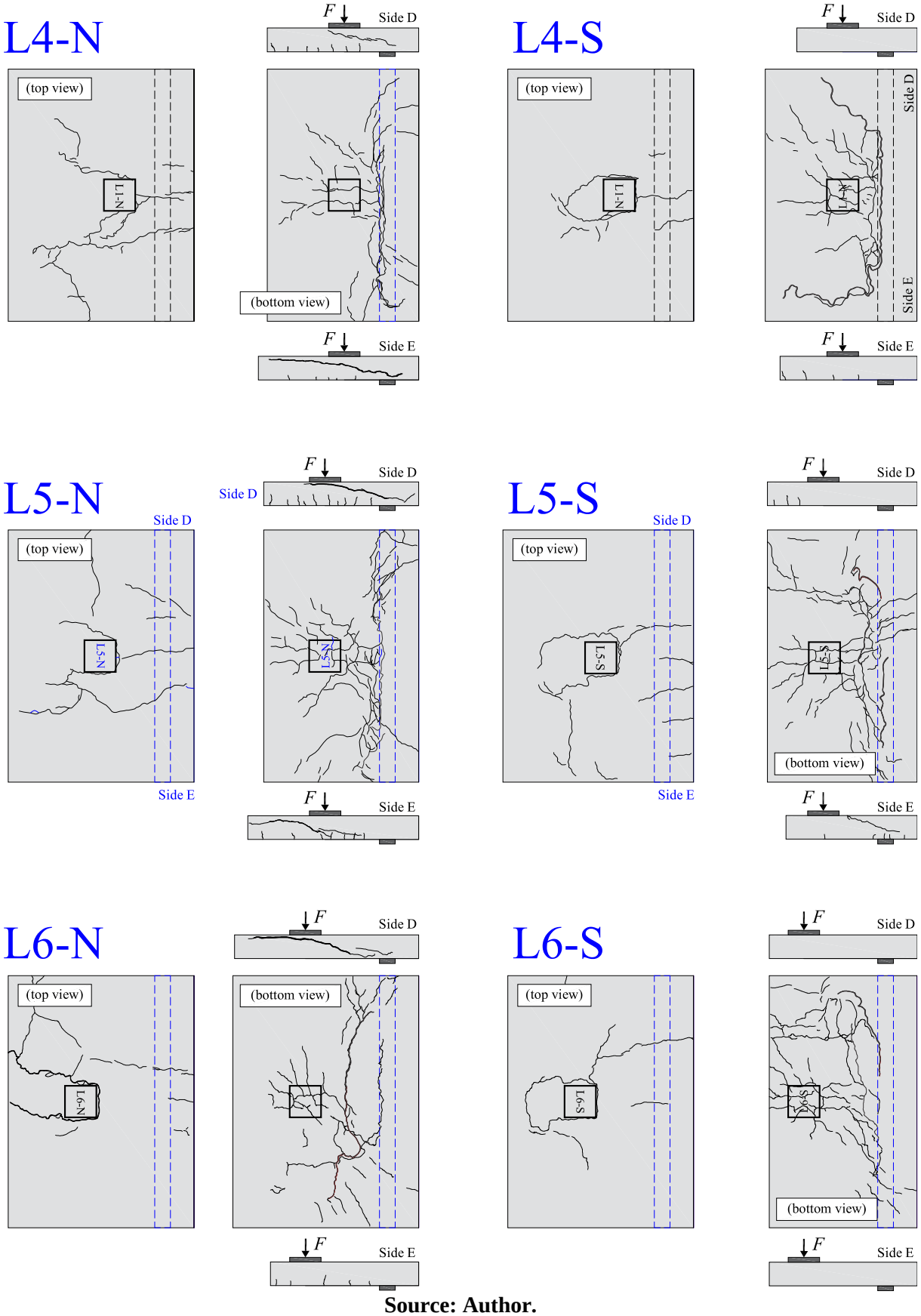

Source: Author.

The side views of the tests show that, after a first punching failure, many tests experienced a large redistribution of forces due to the relatively large transverse reinforcement ratio for one-way slabs (half of the longitudinal reinforcement ratio in tests L1, L2 and L3 and a third for slabs L4, L5 and L6). The tests L1-S, L2-S and L3-N and L4-S show cracks typical of beam-shear failures (named wide beam shear failure = WB) on at least one of the sides. The tests L1-N (side E) and L2-N (side E) developed a form of beam shear failure on one of the sides, but the inclination of the cracks indicates failure in the strut zone (steeper cracks not following the flexural cracks). Since these tests were performed with the load close to the support, such failures could be expected due to the large shear transfer by strut mechanisms in such tests.

In the tests L1-S, L2-S, L3-N and L3-S, the shear cracks clearly develop from the flexural cracks in the critical shear zone, and indicate thus flexure-shear failures. In the tests L1-S (side E) and L3-S (side E), the shape of the critical shear crack closely matches the shear failure of wide beams from the literature by the presence of two horizontal branches, one at the reinforcement level and another at the compression chord, joined by an inclined crack that developes between two flexure cracks.

In the tests L4-N, L5-N and L6-N, a wide beam shear failure was visible on at least one of the sides of the slabs after a punching failure. The shape of the shear crack indicates a failure as slender beams on such regions (cracking arising above flexure cracks). In the tests L4-S, L5-S and L6-S, punching failures occurred at the beginning and a wide beam shear failure was visible in only one of the tests (L5-S, side E). Therefore, the failure was more concentrated around the loaded area as the span length between the supports decreased.

8.3.4 Distribution of reaction forces in the support

The distribution of reaction forces in the support close to the loaded area was measured for all tests. In total, 10 sections of the aluminum beams were instrumented on two sides (= 20 strain gauges for each support). Each section has an influence length of 160 mm (or 0.160 m). The reaction force on each section $F_{reaction}$ is given by the product of the compressive stress measured on the section ($\sigma_{c,measured} = E_{aluminium} \cdot \varepsilon_{c,measured}$) by the influence area over the support (160 mm × 25 mm). The shear force per meter is calculated by the ratio between the calculated force and the length of 0.160 m ($v_{measured} = F_{reaction}$ / 0.160 m).

Figure 8-20 shows the distribution of the reaction forces in the support for the tests L1-S and L4-S, which differ mainly in the longitudinal reinforcement ratios. Figure 8-19 shows that the overall shape of the curves is quite similar for both tests, with a more pronounced concentration of reaction forces in the symmetry axis of the slab and a smaller concentration of reaction forces at the outer edges. This behavior is similar to that reported by Natário et al. (NATÁRIO; FERNÁNDEZ RUIZ; MUTTONI, 2014) for cantilever slabs and that reported by Reißen, Classen and Hegger (2018) for tests performed close to continuous support. This distribution of reaction forces is also consistent with studies conducted with linear elastic finite element analyses (SOUSA et al., 2021a; NATÁRIO; FERNÁNDEZ RUIZ; MUTTONI, 2014).

Figure 8-20 - Distribution of reaction forces in the support as a function of the percentage of the maximum applied load (F_{test}): a) test L1-S and b) test L4-S.

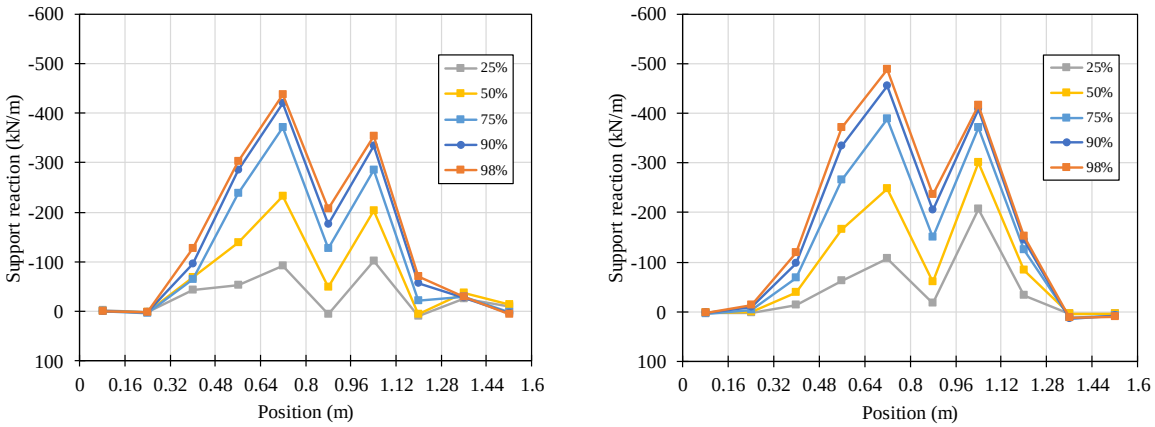

a) L1-S b) L4-S

Source: Author.

The sharp valleys of strains measured in the vicinity of the symmetry axes were also reported in the studies from Natário (NATÁRIO; FERNÁNDEZ RUIZ; MUTTONI, 2014) but were not expected based on finite element analyses. Reißen, Classen and Hegger (2018) attribute these measurements to minor irregularities in the support constructions. However, this valley remains inexplicable since a thin layer of rubber was placed at the support to prevent such irregularities.

By integrating the calculated reaction forces in each section and comparing the support reaction measured with that predicted by static equilibrium, an error of around 10% was achieved for both tests at the maximum applied load. Comparatively, this error is slightly higher than that reported by Natário et al. (NATÁRIO; FERNÁNDEZ RUIZ; MUTTONI, 2014) and Reiβen et al. (5% and 4%, respectively). Therefore, improvements in the instrumentation should be performed in future investigations to achieve better performance with such an approach.

8.3.5 Failure mechanism

Table 8-3 shows a summary of the major characteristics considered in the classification of the failure mechanism. The failure mechanism was determined based on three aspects: (i) the shape of the force-displacement curve measured by the actuator; (ii) the tensile strains from the instrumented rebars around the load; and (iii) the cracking pattern. In most tests, the strain gauges indicated some reinforcement yielding at the peak load F_{exp}, which means that a local flexural failure mechanism started to occur first.

Table 8-3 - Mains aspects considered in the determination of the governing failure mechanism of the slabs.

Test	Sharp decrease of the applied load on failure?	Yielding of all rebars at F_{max} ?	Punching cone at the top view?	Shear crack visible at the slab sides?	Shear crack visible at the bottom side?	Failure mode
L1-N	not clear	No = Shear	Yes	Yes: one side	Yes: linear	WB+P
L2-N	Yes = Shear	Yes	Yes	Yes: one side	Yes: linear + conical	WB+P
L3-N	Yes = Shear	Yes	Yes	Yes: one side	Yes: linear	WB+P
L1-S	Yes = Shear	Yes	Yes	Yes: two sides	Yes: linear	WB+P
L2-S	Yes = Shear	Yes	Yes	Yes: two sides	Yes: linear	WB+P
L3-S	Yes = Shear	Yes	Yes	Yes: two sides	Yes: linear	WB+P
L4-N	not clear	No = shear	Yes	Yes: two sides	Yes: linear	WB+P
L5-N	Yes = shear	No = shear	Yes	Yes: two sides	Yes: linear	WB+P
L6-N	Yes = shear	Yes	Yes	Yes: one side	Yes: linear + conical	WB+P
L4-S	Yes/No	No = shear	Yes	No	Yes: conical	P
L5-S	Yes/No	No = shear	Yes	Yes: one side	Yes: linear + conical	WB+P
L6-S	Yes = shear	Yes	Yes	No	Yes: conical	P

Source: Author.

However, to be classified as a clear flexural mechanism that is expected with the yield line analyses, a plateau would be necessary for the load-displacement curves (such as commonly found on tests of beams that fail by flexure). Because of this, no test was classified as failing by flexure, although some of them presented large reinforcement yielding at failure (tests L3 and L6) or a smooth decrease in the applied load prior to failure (tests L1-N, L4-N, L4-S and L5-S). Consequently, it is assumed herein that the failure of all tests was governed by shear and punching.

The main aspect considered to determine if a punching failure mechanism arose in the tests (letter “P” in the failure mode) was the appearance of a conical crack surrounding the load on the compression side. These cracks occurred for all tests. The conical crack on the tension side was not evident in the tests due to the large reinforcement ratios employed in the longitudinal and transverse directions, which allowed large shear redistribution around the first failed region.

To classify if a wide beam shear failure mechanism also occurred in the tests, at least one of the sides of the slab should present a beam shear crack at the slab sides. This mechanism occurred for most tests. Therefore, it can be stated that most tests (10/12) failed by a combination of wide beam shear and punching shear (WB+P), while two tests failed only by punching.

8.4 Comparison between experimental and predicted strengths

This section presents the equations and approaches used to predict the shear and punching capacities, as well as the theoretical governing failure mechanism of the tests. In the end, this section compares tested and predicted resistances with different design codes and expressions.

8.4.1 Design code expressions

In most design codes the sectional shear capacity V_R (or one-way shear capacity) of slabs is determined by multiplying the nominal shear capacity (shear force capacity per unit area, $v_{R,shear}$) by a given length, usually called effective shear width b_{eff}, and by the effective depth to the longitudinal reinforcement d_l.

Table 8-4 shows the expressions of some of the main design codes to determine the sectional shear capacity of the tested slabs.

The effective shear width herein was determined based on the French guidelines, which assumes the load spreading from the back faces of the loading plate towards the support with 45 degree angles (Figure 8-21a). According to this approach, the effective shear width increases as the shear slenderness a_v/d_l increases. This choice was motivated based on previous investigations that showed the best accuracy of this approach (LANTSOGHT et al., 2015d; SOUSA; EL DEBS, 2019).

The NEN EN1992-1-1:2005 (CEN, 2005) accounts for the influence of direct load transfer depending on the clear shear span to effective depth ratio a_v/d_l. According to this code, the contribution of a load applied within a distance $0.5d_l < a_v < 2d_l$ from the edge of a support to the shear force caused by the concentrated load (V_{Fu}) may be multiplied by the reduction factor β_{CEN}:

$$\beta_{CEN} = \frac{a_v}{2d_l} \begin{cases} \geq 0.25 \\ \leq 1.00 \end{cases} \quad (8.1)$$

Consequently, the determination of the reduced shear demand ($V_{Ed,red}$) that shall be compared to the one-way shear resistance assume the following expression:

$$V_{Ed,red} = V_{Fu} \cdot \beta_{CEN} + (v_g + v_{fq}) \cdot b_{eff} \quad (8.2)$$

On which v_g is the shear force per unit meter caused by the self-weight and v_{fq} is the shear force caused by line loads or other axles of loads on the control section (not applied in this study).

Table 8-4 - Expressions used to determine the one-way shear capacity according to the Brazilian (ABNT NBR 6118, 2014) and European design codes (CEN, 2005).

Code	Reference	Expression
ABNT NBR 6118:2014	(ABNT NBR 6118, 2014)	$V_{Rd,NBR} = v_{Rd,NBR} \cdot b_w \cdot d_l$ $v_{Rd,NBR} = \left[\tau_{Rd} k_{NBR} (1.2 + 40\rho_1) + 0.15\sigma_{cp} \right]$ (8.3) with τ_{Rd} and σ_{cp} in [MPa], b_w in [m] and d in [mm] $k_{NBR} = \begin{cases} 1 \text{ , if at least } 0.50A_s \text{ does not reach the support} \\ \lvert 1.6 - d_l \rvert, \text{ with } d_l \text{ in [m]} \end{cases}$ (8.4) $\tau_{Rd} = 0.25 f_{ctd}$ (8.5) $f_{ctd} = f_{ctk,\inf} / \gamma_c$ (8.6) $f_{ctk,\inf} = 0.7 f_{ctm}$ (8.7) $f_{ctm} = \begin{cases} 0.3 f_{ck}^{2/3} \text{ for } f_{ck} \leq 50 \text{ MPa} \\ 2.12 \ln(1 + 0.11 f_{ck}) \text{ for } 50 \text{ MPa} < f_{ck} \leq 90 \text{MPa} \end{cases}$ (8.8)
NEN EN 1992-1-1:2005	(CEN, 2005)	$V_{Rd,CEN} = v_{Rd,CEN} \cdot b_w d_l$ $V_{Rd,CEN} = \max \begin{cases} \left[C_{Rd,c} k_{CEN} (100\rho_l f_{ck})^{1/3} + k_1 \sigma_{cp} \right] b_w d_l = V_{Rd,c1} \\ \left(v_{\min} + k_1 \sigma_{cp} \right) b_w d_l = V_{Rd,c2} \end{cases}$ with d_l in [mm] and f_{ck} in [MPa] (8.9) $v_{\min} = 0.035 k_{CEN}^{3/2} f_{ck}^{1/2}$ (8.10) $C_{Rd,c} = 0.18$ for NEN EN 1992-1-1:2005 $k_{CEN} = 1 + \sqrt{\frac{200}{d_l}} \leq 2$, with d_l in [mm] and f_{ck} in [MPa] (8.11)

Source: Author.

Figure 8-21 – a) Determination of the effective shear width for one-way shear resistance analyses according to the French practice (FD P 18-717, 2013); b) determination of the shear resisting control perimeter according to the Brazilian and European design codes. Note: dimensions in mm.

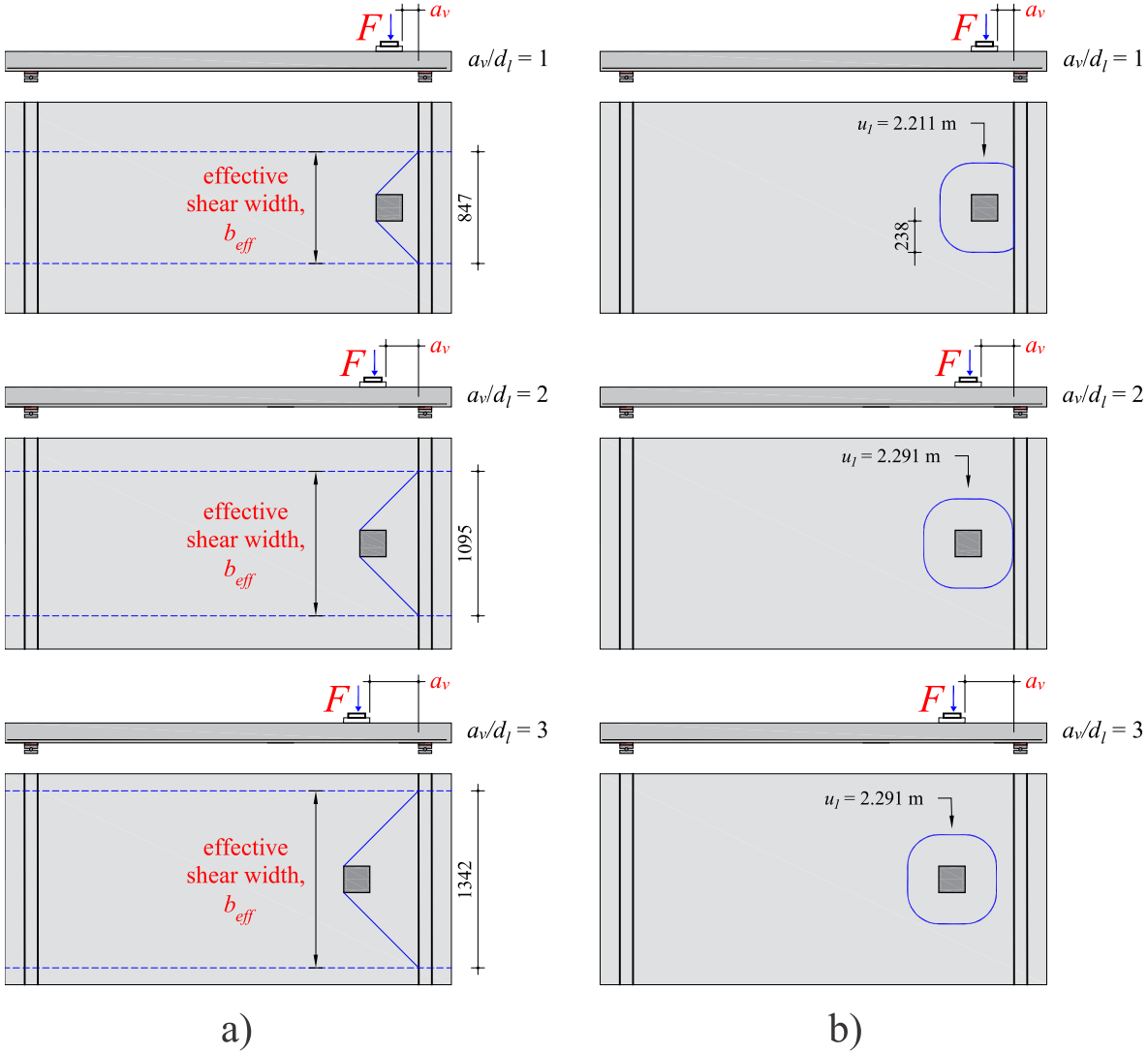

Source: Author.

According to some authors (BAIRÁN et al., 2020; NATÁRIO, 2015), direct load transfer could be considered an enhancement to the sectional shear capacity equivalent to the decrease of the shear demand. Therefore, it was included β_{CEN} in the determination of the nominal shear capacity by multiplying the calculated nominal shear capacity v_R for $1/\beta_{CEN}$ and V_{Ed} becomes:

$$V_{Ed,red} = V_{Fu} + v_g \cdot b_{eff} \tag{8.12}$$

The punching capacity P_R is commonly determined as the product of the unitary punching capacity (shear force capacity per unit length, $v_{R,punch}$) by the calculated resisting

control perimeter u_1. The Brazilian and European code expressions for calculating the punching capacity of slabs without shear reinforcement are based on the same expressions (Table 8-5).

Table 8-5 - Expressions for calculating the unitary punching capacity according the Brazilian (ABNT NBR 6118, 2014) and European codes (CEN, 2005).

Code	Reference	Expression
ABNT NBR 6118:2014 and NEN EN 1992-1-1:2005	(ABNT NBR 6118, 2014) and (CEN, 2005)	$P_R = v_{Rd,CEN} \cdot \left(u_1 \cdot d_{avg}\right)$; $v_{Rd,CEN} = \max \begin{cases} \left[0.18 k_{CEN} (100 \rho_{avg} f_{ck})^{1/3}\right] \\ \left(v_{\min} + k_1 \sigma_{cp}\right) \end{cases}$ (8.13) with d_{avg} in [mm] and f_{ck} in [MPa] $\rho_{avg} = \left(\rho_l \cdot \rho_t\right)^{1/2}$ (8.14) $v_{\min} = 0.035 k_{CEN}^{3/2} f_{ck}^{1/2}$ (8.15) $k_{CEN} = 1 + \sqrt{\frac{200}{d_{avg}}} \leq 2$, with d_{avg} in [mm] and f_{ck} in [MPa] (8.16)

Source: Author.

8.4.2 Determination of the most critical failure mechanism

In this study, it was compared the tested and predicted resistances to determine which would be the most critical failure mechanism theoretically. In order to compare which would be the most critical failure mechanism in a clear way, it was compared the predicted ultimate loads F that would cause a one-way shear failure ($F_{predicted,shear}$) with those causing a punching failure ($F_{predicted,punching}$). It was assumed the punching capacity P_R is approximately equal to the applied load $F_{predicted,punching}$ at failure when using the punching expressions (the influence of the self-weight on the control perimeter was neglected due to the small thickness of the slab). To determine the concentrated load $F_{predicted,shear}$ associated with the predicted sectional shear capacity $V_{R,predicted}$, the influence of the self-weight was considered in the following way. Firstly, the net value of the shear capacity that should resist only the concentrated load was calculated, since part of the shear capacity is used to resist the self-weight v_g.

$$V_{R,net} = V_R \cdot \left(1 / \beta_{CEN}\right) - v_g \cdot b_{eff} \quad (8.17)$$

Next, the relation between the applied load and the respective shear force (F ↔ V_{Fu}) caused by the concentrated load was used (fixed value which depends only of the statics of the

problem to determine the applied load ($F_{predicted,shear}$) corresponding to the sectional shear capacity $V_{R,net}$.

$$F_{predicted,shear} = V_{R,net} \cdot \frac{F_{test}}{V_{Fu,test}} \tag{8.18}$$

Comparing the relations V_{test}/V_R with $F_{test}/F_{predictedshear}$, the differences were commonly lower than 2% due to the limited influence of the self-weight on the calculations. Therefore, one can also compare directly the relations V_{test}/V_R with P_{test}/P_R to determine the most critical failure mechanism. Comparing the ratios $F_{test}/F_{predicted,shear}$ and $F_{test}/F_{predicted,punching}$, one can observe that the higher value determines the most conservative prediction and the theoretical most critical failure mechanism.

8.4.3 Extended Strip Model calculations

The Extended Strip Model (ESM) is a plasticity-based model that describes a lower-bound solution to the load capacity of slabs under concentrated loads (LANTSOGHT et al., 2017; LANTSOGHT; VAN DER VEEN; DE BOER, 2017). This model was inspired in the bond model developed for concentric punching shear (ALEXANDER; SIMMONDS, 1992), which combines the two-way shear transfer mechanism within the quadrants with arching action from one-way shear in the strips (Figure 8-12).

Figure 8-22 – Layout of the original bond model with strips and quadrants.

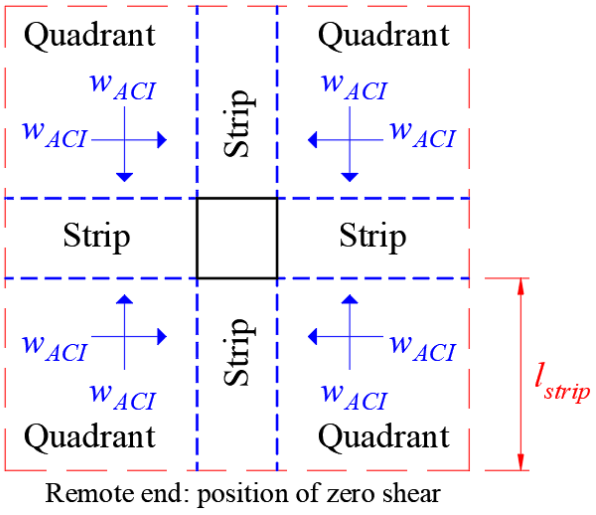

Source: Adapted from Lantsoght, van der Veen and de Boer (2017).

According to this model, the maximum concentrated load P_{ESM} is predicted by the following expressions (Figure 8-23):

$$P_{ESM} = P_x + P_{\sup} + P_y + P_{edge} \tag{8.19}$$

$$P_x = \sqrt{2 \cdot (1 + \beta_{torsion}) \cdot M_{sag,x} \cdot w_{ACI,x}} \tag{8.20}$$

$$P_{\sup} = \frac{2 \cdot d_l}{a_v} \cdot \sqrt{2 \cdot (1 + \beta_{torsion}) \cdot M_{s,x} \cdot w_{ACI,x}} \tag{8.21}$$

$$P_y = \sqrt{2 \cdot \left(\frac{L}{L - a_M} \right) \cdot M_{s,y} \cdot \left(w_{ACI,y} - v_{DL} \right)} \tag{8.22}$$

$$P_{edge} = \begin{cases} \sqrt{2 \cdot \beta_{torsion} \cdot \left(\frac{L}{L - a_M} \right) \cdot M_{s,y} \cdot \left(w_{ACI,y} - v_{DL} \right)} & \text{for } l_w < l_{edge} \\ \sqrt{\beta_{torsion} \cdot \left(\frac{L}{L - a_M} \right) \cdot \left(w_{ACI,y} - v_{DL} \right) \cdot l_{edge}} & \text{for } l_w \geq l_{edge} \end{cases} \tag{8.23}$$

P_{sup}, P_x, P_y and P_{edge} are the capacities of the four strips around the load for simply supported or continuous slabs. P_{sup} is the capacity of the strip between the closer support and the load in the longitudinal direction; P_x is the capacity of the strip between the load and the far support in the longitudinal direction. P_y and P_{edge} are the capacities of the strips in the transverse direction. When the concentrated load is placed at the center of the slab width, P_{edge} is calculated as P_y and no torsion is considered in the transverse direction.

Figure 8-23 - Layout of the strips and quadrants for the Extended Strip Model in simply supported slabs.

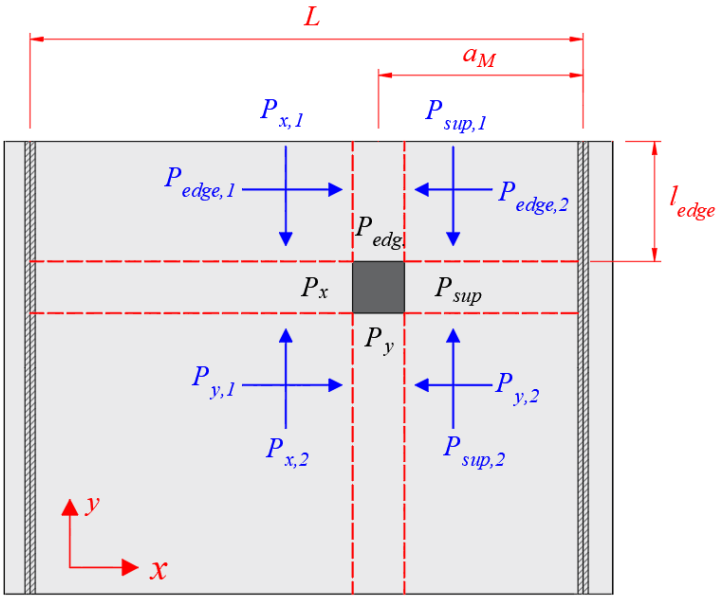

Source: Adapted from Lantsoght, van der Veen and de Boer (2017).

$\beta_{torsion}$ is the parameter that considers the relative effect of torsion on the capacity of the strips:

$$\beta_{torsion} = 0.8 \cdot \frac{a}{d_x} \cdot \frac{b_r}{b_{slab}}, \text{ for } 0 \le \frac{a}{d_x} \le 2.5 \text{ and } 0 \le \frac{b_r}{b_{slab}} \le \frac{1}{2} \tag{8.24}$$

l_{edge} is the distance between the free edge and the edge of the concentrated loads in the slab width direction. b_r is the distance between the slab free edge and the load axis. The loaded length of the strip l_w is a reference parameter for loads close to the free edge of one-way slabs and is calculated as:

$$l_w = \sqrt{\frac{2 \cdot M_{s,y}}{\beta_{torsion} \cdot \left(w_{ACI,y} - v_{DL} \right) \cdot \frac{L}{L - a_M}}} \tag{8.25}$$

L is the span length between two supports for simply supported slabs and the largest distance between the farthest support from the load and the point of contraflexure for loads close to continuous support. a_M is equal to the shear span a for simply supported slabs and the distance between the load center to the point of contraflexure for continuous slabs. v_{DL} is the unitary shear demand due to the dead load over the strips in the y-direction.

According to Lantsoght, van der Veen and de Boer (2017), the moment capacities in the longitudinal and transverse directions of the slab are calculated as:

$$M_{s,x} = M_{sag,x} + \lambda_{moment} \cdot M_{hog,x} \tag{8.26}$$

$$M_{s,y} = M_{sag,y} + \lambda_{moment} \cdot M_{hog,y} \tag{8.27}$$

With:

$$\lambda_{moment} = \frac{M_{\sup}}{M_{span}} \tag{8.28}$$

M_{sup} and M_{span} are the bending moments at the support and load axes of the slabs assuming a beam behavior or the slab loaded over the entire width. Besides, M_{sup} and M_{span} consider all loads applied in the slab. When the concentrated load is placed close to a simple support (hinged support), λ_{moment} = 0 and the moment capacities from $M_{s,x}$ and $M_{s,y}$ become $M_{sag,x}$ and $M_{sag,y}$. Herein, $M_{sag,x}$ and $M_{sag,y}$ are the moment capacities per unit length to sagging moment (tensile in the bottom side of the slab) in the longitudinal and transverse directions.

$M_{hog,x}$ and $M_{hog,y}$ are the moment capacities to hogging moment (tensile in the top side of the slab) in the longitudinal and transverse directions. The following expressions were applied to compute $M_{sag,x}$, $M_{sag,y}$, $M_{hog,x}$ and $M_{hog,y}$:

$$M_{sag,x} = \rho_{x,bottom} \cdot f_{y,x,bottom} \cdot l_{load} \cdot d_{x,bottom}{}^2 \cdot \left(1 - \frac{f_{y,x} \cdot \rho_{x,bottom}}{1.7 \cdot f_c}\right) \quad (8.29)$$

$$M_{sag,y} = \rho_{y,bottom} \cdot f_{y,y,bottom} \cdot b_{load} \cdot d_{y,bottom}{}^2 \cdot \left(1 - \frac{f_{y,y,bottom} \cdot \rho_{y,bottom}}{1.7 \cdot f_c}\right) \quad (8.30)$$

$$M_{hog,x} = \rho_{x,top} \cdot f_{y,x,top} \cdot l_{load} \cdot d_{l,top}{}^2 \cdot \left(1 - \frac{f_{y,x,top} \cdot \rho_{x,top}}{1.7 \cdot f_c}\right) \quad (8.31)$$

$$M_{hog,y} = \rho_{y,top} \cdot f_{y,y,top} \cdot b_{load} \cdot d_{y,top}{}^2 \cdot \left(1 - \frac{f_{y,y,top} \cdot \rho_{y,top}}{1.7 \cdot f_c}\right) \quad (8.32)$$

$w_{ACI,x}$ and $w_{ACI,y}$ are the unitary capacities (shear force per unit length) calculated according to the ACI 318-14 and corrected by a size effect factor as:

$$w_{ACI,x} = 0.1666 \cdot d_{y,bottom} \cdot \sqrt{f_{ck}} \cdot \left(\frac{100}{d_{y,bottom}}\right)^{1//3} \quad (8.33)$$

$$w_{ACI,y} = 0.166 \cdot d_{x,bottom} \cdot \sqrt{f_{ck}} \cdot \left(\frac{100}{d_{x,bottom}}\right)^{1/3} \quad (8.34)$$

8.4.4 Results of the comparison between test results and theoretical predictions

Table 6 shows the comparison between tested and predicted resistances using the shear and punching shear calculations. Added to the calculations using the Brazilian (ABNT NBR 6118, 2014) and European code provisions (CEN, 2005), it was also included a set of predictions using the lower-bound plasticity-based model named Extended Strip Method (ESM) (LANTSOGHT et al., 2017; LANTSOGHT; VAN DER VEEN; DE BOER, 2017).

In columns #5 and #6, Table 8-6 shows that the comparison between tested and predicted shear capacities (V_{test}/V_{pred}) can provide a good measurement of the tested and predicted concentrated loads that caused the one-way shear failure ($F_{test}/F_{pred,shear}$). This occurs mainly when the effect of the self-weight is negligible compared to the concentrated loads that cause failure.

Comparing columns #6 and #7, it can be seen that both one-way shear and punching shear predictions provided accurate results with the Brazilian code, with a coefficient of variation (COV) lower than 20%. Notably, the predictions of the punching capacity fitted slightly better with the experimental results (average F_{test} / $F_{pred,shear}$ = 1.37 compared to $F_{test}/F_{pred,punching}$ = 1.19). Therefore, these results agree well with the experimental observations that the failure mechanism started with a local punching between the front faces of load and support. Since the punching provisions from Brazilian (ABNT NBR 6118, 2014) and European codes (CEN, 2004) are equal, similar predictions were achieved with both codes ($F_{test}/F_{pred,punching}$ with an average of 1.19 and COV of 11.7%).

Table 8-6 - Comparison between tested and predicted resistances according to different design codes and the ESM (LANTSOGHT et al., 2017; LANTSOGHT; VAN DER VEEN; DE BOER, 2017).

#1	#2	#3	#4	#5	#6	#7	#8	#9	#10
Test	l_{span} (m)	a_v/d_l (-)	a/d_l (-)	$\frac{V_{test}}{V_{pred}}$	$\frac{F_{test}}{F_{pred,shear}}$	$\frac{F_{test}}{F_{pred,punching}}$	$\frac{F_{test}}{F_{pred,shear}}$	$\frac{F_{test}}{F_{pred,punching}}$	$\frac{F_{test}}{F_{pred}}$
Details				*ABNT* β_{CEN}	*ABNT* β_{CEN}	*ABNT* β_{CEN}	*CEN* β_{CEN}	*CEN* β_{CEN}	*ESM*
L1-N	3	1	2.21	1.24	1.22	1.19	1.18	1.19	1.00
L2-N	3	2	3.21	1.90	1.86	1.18	1.80	1.18	1.33
L3-N	3	3	4.21	1.45	1.41	1.15	1.36	1.15	1.29
L1-S	2	1	2.21	1.43	1.41	1.44	1.36	1.44	1.21
L2-S	2	2	3.21	1.68	1.65	1.13	1.59	1.13	1.26
L3-S	2	3	4.21	1.20	1.16	1.06	1.12	1.06	1.17
L4-N	3	1	2.21	1.24	1.22	1.34	1.26	1.34	1.09
L5-N	3	2	3.21	1.68	1.65	1.18	1.71	1.18	1.29
L6-N	3	3	4.21	1.10	1.07	0.98	1.10	0.98	1.06
L4-S	2	1	2.21	1.25	1.24	1.42	1.28	1.42	1.15
L5-S	2	2	3.21	1.44	1.41	1.09	1.46	1.09	1.18
L6-S	2	3	4.21	1.15	1.13	1.15	1.16	1.15	1.23
			AVG	1.40	1.37	1.19	1.37	1.19	1.19
			COV (%)	17.8%	17.8%	11.7%	16.9%	11.7%	8.5%

Source: Author.

Notably, despite being based on different expressions, the predictions of capacity based on the one-way shear expressions from ABNT NBR 6118:2014 (ABNT NBR 6118, 2014) and NEN-EN 1992-1-1:2005 (CEN, 2004) resulted in almost equal values (comparing columns #6 and #8). However, these results are not surprising since both one-way shear expressions from these design codes were calibrated using similar test results (small and heavily reinforced slender reinforced concrete beams, typically tested in a four-point-bending test). Besides, it is

noteworthy that the most conservative predictions ($F_{test}/F_{pred,shear}$ >1.50) occurred for the tests with shear slenderness a_v/d_l = 2, for which no arching action was considered in the expressions. This result indicates that arching action should be considered in a larger range of shear slenderness. Natário et al.(NATÁRIO; FERNÁNDEZ RUIZ; MUTTONI, 2014), for instance, suggested considering arching action for $0 < a_v < 2.75d_l$ instead of $0 < a_v < 2d_l$.

In column #10, it can be seen that the Extended Strip Model (LANTSOGHT et al., 2017; LANTSOGHT; VAN DER VEEN; DE BOER, 2017) provided the best predictions, with an average ratio $F_{test}/F_{pred,punching}$ of 1.19 and a coefficient of variation equal to 8.5%.

8.5 Discussions of Chapter 8

Most previous publications in the field of one-way slabs under concentrated loads focused on conditions in which the shear and punching capacity are considerably larger than the slab's flexural capacity (BUI et al., 2017a; HALVONIK; VIDAKOVIĆ; VIDA, 2020; HENZE; ROMBACH; HARTER, 2020; LANTSOGHT; VAN DER VEEN; WALRAVEN, 2013; NATÁRIO; FERNÁNDEZ RUIZ; MUTTONI, 2014; REIßEN; CLASSEN; HEGGER, 2018).These studies contributed to a better understanding of the problem when no local yielding of the flexural reinforcement occurs at failure. However, traditionally slabs are designed in such a way that the flexural capacity is lower than the shear and punching capacities to assure ductility at failure. Consequently, most slabs may present some reinforcement yielding before reaching failure by one-way shear or punching shear. In this study, slabs were tested in such a way as to identify if the local reinforcement yielding at failure could modify the behavior of the slabs failing by shear. In practice, the results indicated that after local reinforcement yielding of the slabs, the load may keep increasing until reaching another failure mechanism as the punching or the one-way shear and fail in a brittle manner (mainly seeing the force × displacement graph from test L3-N).

In other tests, such as the test L1-N (a_v/d_l =1), it was expected a most brittle failure mechanism due to the smaller distance from the load to the support and the predominant of direct shear transfer from the load towards the support by struts(LANTSOGHT; VAN DER VEEN; WALRAVEN, 2013). However, a smooth drop in the measured load was observed in such test (see Figure 8-14a). Therefore, this test may have not failed at the strut, but eventually had the ultimate capacity limited by the reinforcement yielding. Since the ultimate load of the tests L2-N and L1-N was almost the same, this could explain why the shear capacity did not increase considerably by decreasing the ratio a_v/d_l from 2 to 1 between the tests L2-N and L1-

N. Therefore, the enhancement in the shear capacity for loads close to the support due to direct load transfer may be disturbed by local reinforcement yielding.

In this study, an important evaluation commonly not performed was also added: the comparison between the ultimate concentrated loads predicted by one-way shear mechanisms and two-way shear mechanisms (punching)(HALVONIK; VIDAKOVIĆ; VIDA, 2020; HENZE; ROMBACH; HARTER, 2020; NATÁRIO; FERNÁNDEZ RUIZ; MUTTONI, 2014). In this study, it was observed that both Brazilian (ABNT NBR 6118, 2014) and European code expressions (CEN, 2004) provided conservative determinations of the ultimate capacity, when using both the one-way shear or punching shear expressions. When arching action was considered in a most appropriate way for the one-way shear predictions (considering a large length of influence of arching action until $2.5d_l$), both one-way shear and punching shear predictions provided close estimations of ultimate capacity. Since both one-way shear failure mechanisms were observed at failure (punching followed by one-way shear at most slabs), both one-way shear and punching shear capacities predicted should perform well for such slabs. Conversely, if the slabs failed only by one-way shear, it would be reasonably that the punching shear approach does not lead to accurate values of resistance.

8.6 Conclusions of chapter 8

In this study, the failure mechanism is studied of one-way slabs under concentrated loads with some local reinforcement yielding at failure. The load × displacement graphs, cracking pattern, reinforcement strains and support reactions were monitored along the tests. Besides, analytical predictions with the current Brazilian (ABNT NBR 6118, 2014) and European code expressions (CEN, 2004) were performed and compared to those provided with the Extended Strip Method (LANTSOGHT et al., 2017; LANTSOGHT; VAN DER VEEN; DE BOER, 2017). The following conclusions can be drawn:

- One-way slabs under concentrated loads may fail in a complex way when reinforcement yields at failure. In practice, the resistance enhancement expected for loads close to the support may not be achieved. Besides, brittle failure mechanisms can also occur after large reinforcement yielding.
- Shear redistribution can occur around the load after punching and activate a secondary failure mechanism of one-way shear visible at the slab sides, called wide beam shear failure. In this study, this level of redistribution was attributed to the high reinforcement ratio in the transverse direction compared to the longitudinal direction (ρ_t / ρ_l = 0.34 and 0.50,

approximately) and also due to the reduced ratio between the slabs width and load size (b_{slab}/l_{load} = 8).

- The Extended Strip Model stands out as solution to predict the ultimate capacity of reinforced concrete slabs under concentrated loads, especially when the slabs are subjected to some local reinforcement yielding at failure.
- Combining the predictions of ultimate capacity (concentrated loads) that would cause a one-way shear failure or a punching failure in tested slabs, a conservative determination is achieved with the Brazilian (ABNT NBR 6118, 2014) and European design codes (CEN, 2004).

9 CONCLUSIONS OF THE THESIS

This chapter highlights the main contributions from this research to the state of knowledge. In the end, the main aspects that need further investigations in future studies are also described.

9.1 Introduction of chapter 9: an overview of main contributions

This chapter brings together a summary of the main contributions from this work to the state of knowledge in the field of reinforced concrete slabs under concentrated loads without shear reinforcement.

In this thesis, a comprehensive review of the behavior and failure mechanism of one-way slabs under concentrated loads was firstly performed in Chapter 2. This review aided in highlighting the different shear failure mechanisms that can take place: one-way shear as wide beams, punching shear, or a mixed mode between them. The main shear transfer mechanisms and cracking patterns of different tests from the literature were discussed and evaluated. The main parameters influencing the ultimate load and failure mechanism of such slabs were identified.

After that, the study presented a close look to the evaluation of the one-way shear capacity of reinforced concrete slabs loaded over the entire width (predominant one-way shear behavior). At this point, the purpose was trying to improve the understanding of a smaller problem (the one-way shear capacity of members loaded over the entire width) before trying to develop an approach to predict the shear capacity of slabs under concentrated loads (a most complex problem that requires the definition of an effective or contributing slabs strip to the sectional shear capacity). In this framework, a database of wide beams and slabs loaded over the entire width was firstly organized, which aided in identifying the key parameters influencing the unitary shear capacity. Added to that, this database was also used to evaluate several one-way shear expressions from codes of practice and mechanical-based models. These expressions were evaluated according to fewer study parameters, such as the support conditions and slab width-member depth ratio.

In the following, the idea was to bring a proposal to predict the sectional shear capacity of one-way slabs under concentrated loads based on the use of a mechanical-based model to calculate the unitary shear capacity. Until now, most publications had focused on the evaluation

using only semi-empirical expressions or combining mechanical-based models with linear elastic finite element analyses. An effective shear width expression was also proposed to improve the predictions of sectional shear capacity for tests that could be critical in punching. In this way, conservative estimations of resistance could be achieved.

In the framework of this thesis, other approaches based on the use of more sophisticated tools were also explored to predict the shear and punching capacity of the slabs. Herein, the proposed approach from Natário (2015), which uses linear elastic finite element analyses combined with the Critical Shear Crack Theory expressions, was investigated. Small improvements on the approach from Natário were suggested based on the use of parameters that consider the change in the governing failure mechanism of the slabs according to the slab width-to-load size ratio. Besides that, it was also shows how the same expressions could be used without the need of linear elastic finite element analyses.

In Chapter 6, non-linear finite element analyses were explored to predict the ultimate capacity of flat slabs designed with the rational use of Ultra-high-performance fiber-reinforced concrete. Added to that, it was shown how the Critical Shear Crack Theory expressions could be used to predict the punching capacity of such kinds of slabs or connections.

In Chapter 7, the NLFEA was applied to predict the ultimate capacity of one-way slabs under concentrated loads tested from the literature. The level of accuracy and precision from different approaches and according to different modeling options was discussed. In this chapter, the author highlights how some modeling options may differ and still lead to similar levels of precisions and also show how some modeling options may result in worrying predictions and introduce large bias in the results.

In the end, Chapter 8 shows the results of the proposed experimental program under a different look. The ultimate capacity and failure mechanism of the slabs were evaluated under the conditions that the shear and flexure capacities of the slabs were close. Therefore, reinforcement yielding at failure took place before failure. In practice, since the slabs are most likely designed to fail by flexure prior to shear or punching, such an experimental program could improve the understanding of the problem under the most realistic circumstances.

In summary, the main contributions from this thesis can be summarized as:

- Different approaches to evaluate the shear and punching capacity of one-way slabs under concentrated loads were investigated: (i) using only analytical expressions; (ii)

using analytical expressions combined with linear elastic finite element analyses; (iii) using three-dimensional non-linear finite element analyses; (iv) and using experimentation testing.

- Different mechanical-based models, mainly the Critical Shear Displacement Theory (CSDT) and the Critical Shear Crack Theory (CSCT), were explored to predict the shear and punching capacity of one-way slabs under concentrated loads.
- Different recommendations were developed to enhance the predictions of shear and punching capacity of one-way slabs under concentrated loads and two-way slabs with rational use of UHPFRC.
- The ultimate capacity of one-way slabs under concentrated loads was investigated experimentally under a not frequent circumstance in the literature: when the shear and flexure capacity of the slabs are closer to each other.

9.2 Summary of conclusions and research findings

This section reviews and details the main conclusions chapter by chapter of this thesis.

9.2.1 Transition between one-way shear and two-way shear

In Chapter 2, it was highlighted that different shear failure mechanisms could take place for one-way slabs under concentrated loads: one-way shear as wide beams, two-way shear by punching, or a mixed mode between them. The main parameters influencing the ultimate capacity and failure mechanism of one-way slabs under concentrated loads are the shear slenderness a_v/d_l (a_v being the clear shear span or the face-to-face distance between the load and the support and d_l the effective depth of the longitudinal reinforcement), and the slab width-to-load size ratio b_{slab}/l_{load}. Therefore, these parameters can be used in the current approaches of evaluations to improve the predictions of shear capacity when the slabs are critical in punching; or improve the predictions of punching capacity when the slabs are critical in one-way shear.

9.2.2 One-way shear strength of wide reinforced concrete members without shear reinforcement

The most influencing parameters in the unitary shear capacity of wide beams and slabs are (i) the shear slenderness, (ii) the reinforcement ratio, and (iii) the size effect. However, the shear slenderness seems to have a marked influence only in the region that benefited from arching action (strut mechanisms). Consequently, many expressions that do not include any parameter related to the shear slenderness become more conservative in such loading

conditions. The reinforcement spacing and the slab width did not play a marked influence on the global capacity. Besides that, the support condition did not significantly influence the ultimate loads compared to parameters such as the shear slenderness. In practice, the support conditions are well considered in most mechanical-based models according to the shear slenderness $M/V \cdot d_l$.

Despite being based on different theories or calibrations, most mechanical based-models and semi-empirical models from codes of practice lead to similar levels of accuracy in predicting the one-way shear capacity of wide beams and slabs. Since these expressions are commonly devised using similar databases, this finding is not surprising. However, an important finding was that the one-way shear capacity of non-slender slabs ($\lambda < 3$) could be reasonably well predicted with the same expressions devised to slender conditions ($\lambda > 3$). This is accomplished by considering arching action through a semi-empirical factor related to the shear slenderness (a_v/d_l).

The comparison between tested and predicted resistances according to several expressions showed that the ones based on the Critical Shear Displacement Theory (CSDT) and Critical Shear Crack Theory (CSCT) stand out. In other words, the expressions based on the CSDT and CSCT led to the best levels of accuracy regardless of the evaluated conditions.

9.2.3 Assessment of one-way slabs under concentrated loads using only analytical expressions and the CSDT

The one-way shear capacity of one-way slabs under concentrated loads can be predicted with the CSDT expressions. When the slabs are critical in one-way shear, the French effective shear width model can be used to define the slab strip that contributes effectively to the sectional shear capacity. In practice, this occurs mainly when the shear slenderness $M/V \cdot d_l < 3$. Despite being devised to deal only with slender loading conditions, which means $M/V \cdot d_l > 3$, the use of a correction factor β that considers arching action allows extending the use of such expressions to $M/V \cdot d_l < 3$ in a conservative way.

When the governing failure mechanism of the slabs is unknown, the effective shear width predicted with the French approach shall be corrected according to the shear slenderness a_v/d_l. In practice, this means decreasing the effective shear width calculated to large distances of the load to the support. In this way, conservative and precise estimations of shear capacity can be observed even if the tests failed by punching.

9.2.4 Approach using linear elastic finite element analyses combined to analytical expressions

The proposed approach by Natário (2015) accurately predicts the one-way shear capacity of one-way slabs under concentrated loads. In practice, it was observed that the one-way shear approach presented excellent levels of accuracy regardless of the governing failure mechanism being one-way shear or punching shear. However, the predictions of punching capacity combining the CSCT expressions with LEFEA were accurate only when the slabs failed by punching. In this study, it was shown that the predictions of punching capacity could be enhanced by considering the lower contribution of the sides of the critical perimeter parallels to the free edges depending on the ratio slab width-to-load size ratio b_{slab}/l_{load}. In this way, both approaches can lead to similar levels of accuracy.

Besides that, this study shows how the predictions of shear and punching capacity based on the CSCT can also be based only on analytical calculations (without the use of LEFEA). To this, simplifications in the approach from Natário were proposed, and factors related to the shear slenderness a_v/d_l and b_{slab}/l_{load} were derived. In practice, the simplified approach leads to the same accuracy level as the refined approach from Natário.

9.2.5 Assessing the punching capacity of flat slabs designed with rational use of UHPFRC in the load vicinity by NLFEA

The use of the proposed NLFEA analyses allowed tracking accurately the behavior and punching capacity of slabs designed with rational use of UHPFRC. Between the main finding in the parametric analyses, it was confirmed that the use of the UHPFRC in the compressed side of the slabs allows for improving the punching capacity and deformation capacity of the slabs compared to its use on the tensiled side. Added to that, it was observed that the punching capacity increases only until certain limits when the area of the UHPFRC is increased in the plan. Conversely, the punching capacity always increases by increasing the proportion of the UHPFRC in the slab thickness.

In this study, using CSCT expressions with simple adjustments accurately predicts the punching capacity of the slabs designed with rational use of UHPFRC. In practice, the main adjustments required compared to the version devised by Maya et al. (2012) are (i) that UHPFRC present a higher residual tensile strength after cracking compared to SFRC that needs be considered in the flexure capacity calculations, (ii) and that punching capacity enhancement is proportional to the UHPFRC layer thickness on the slab thickness. Besides, the flexure

capacity of the slabs or connections needs to consider the spatial distribution of UHPFRC over the slab plan.

9.2.6 Assessing the ultimate capacity of one-way slabs under concentrated loads aided by NLFEA

In this study, the proposed modeling approach allowed accurately predicting the governing failure mechanism and ultimate capacity of slabs with different failure mechanisms. In practice, both one-way shear and punching shear failure modes were accurately represented. Along the sensibility study, the influence of some modeling options was tracked:

- The inclusion of damage parameters in simulations of static tests allows representing more accurately the confining stresses around the load at failure due to the variable elastic modulus with increasing cracking. However, the failure mechanism of the slabs did not change, including or not the damage parameters. Besides, the influence of including the damage parameters was relatively small. In practice, the ultimate loads varied between 5% and 10%, including the damage parameters in static tests. Consequently, someone could perform the analyses without the damage parameters and recalibrate other parameters (such as the fracture energy and dilation capacity) to achieve similar results to the analyses that include the damage parameters.
- The influence of the stress-train behavior assumed in compression in the numerical simulations may also affect the ultimate capacity of the FEM. In practice, using models with a large residual post-peak compressive strength may increase the ultimate capacity of the FEM around 15%.
- The use of a large viscosity parameter in the Concrete Damaged Plasticity shall be avoided since this overestimates the ultimate capacity of FEM when they present some failure mechanism related to the concrete (for instance, shear or concrete crushing). In practice, using values around 0.001 introduce a significant bias in the numerical results since all models fail in a ductile manner. In this study, it was concluded that using a value of 0.00001 can allow convergence in the simulations without changing the behavior of the numerical models.

9.2.7 Experimental program: slabs under concentrated loads with local reinforcement yielding

In this study, it was found that one-way slabs under concentrated loads can present a first failure mechanism initiated by punching. After this, depending on the reinforcement ratio

used in the transverse direction of the slabs, large shear redistribution can occur around the load and activate a second failure mechanism as wide beam shear.

The reinforcement yielding around the load may limit the contribution of arching action to the direct shear transfer. As a consequence, the ultimate capacity of the slabs may not increase by decreasing the shear slenderness a_v/d_l.

The combination of the french effective shear width with the expressions preconized by the ABNT NBR 6118:2014 for predicting the unitary shear capacity allows reaching good levels of accuracy for slabs loaded by concentrated loads at distances $a_v \leq 3d_l$. Besides, the punching capacity predictions from the same code also led to good levels of accuracy for the tested slabs. In general, the Extended Strip Model allowed presented the best levels of accuracy in predicting the ultimate capacity of the tested slabs.

9.3 Recommendations for future studies

In this study, most slabs evaluated were tested under a single concentrated load. In practice, bridge deck slabs are loaded by a combination of the concentrated loads. Therefore, further studies shall be developed to increase the number of tests or numerical studies simulating the combination of loads on the slabs.

In this framework, it is also interesting to note that slab bridge decks can also be supported on four sides (typically, two longitudinal girders and two transverse beams). Therefore, it is important in the future to extend this kind of study from one-way slabs to other boundary conditions that may arise in practice.

REFERENCES[1]

AASHTO. **AASHTO LRFD Bridge Design Specifications**. 8th Edition ed. Washington D.C.: American Association of State Highway and Transportation Officials (AASHTO), 2017.

ABNT NBR 6023. **NBR 6023: Information and documentation — References — Developing** (in portuguese). Rio de Janeiro: Associação Brasileira de Normas Técnicas (ABNT), 2018.

ABNT NBR 6118. **NBR 6118: Design and execution of reinforced concrete buildings** (in portuguese). Rio de Janeiro: Associação Brasileira de Normas Técnicas (ABNT), 1980.

ABNT NBR 6118. **NBR 6118: Design of concrete structures — Procedure** (in portuguese). Rio de Janeiro: Associação Brasileira de Normas Técnicas (ABNT), 2014.

ACI COMMITTEE 318. **Building code requirements for structural concrete (ACI 318-11) and commentary**, American Concrete Institute, Farmington Hills, MI, 2011.

ACI COMMITTEE 318. **Building Code Requirements for Structural Concrete (ACI 318-14) and Commentary**, American Concrete Institute, Farmington Hills, MI, 2014.

ACI COMMITTEE 318. **Building Code Requirements for Structural Concrete (ACI 318-19), American Concrete Institute**, Farmington Hills, MI, 2019.

ACI COMMITTEE 446. **Fracture Mechanics of Concrete: Concepts, Models and Determination of Material Properties**. ACI 446.1 R-91 (Reapproved 1999), American Concrete Institute, Detroit, p. 1–146, 1991.

ACI-ASCE COMMITTEE 326. Shear and Diagonal Tension. **ACI Journal Proceedings**, v. 59, n. 1, p. 1–30, 1962a.

ACI-ASCE COMMITTEE 326. Shear and Diagonal Tension. **ACI Journal Proceedings**, v. 59, n. 2, p. 277–334, 1962b.

ACI-ASCE COMMITTEE 326. Shear and Diagonal Tension. **ACI Journal Proceedings**, v. 59, n. 3, p. 353–396, 1962c.

ADAM, V.; CLASSEN, M.; HILLEBRAND, M.; HEGGER, J. Shear in continuous slab segments without shear reinforcement under distributed loads. In: **Proceedings of the fib Symposium 2019 - Concrete - Innovations in Materials, Design and Structures,** Krakow, Poland, 2019.

ADAM, V.; HERBRAND, M.; CLASSEN, M. Experimentelle Untersuchungen zum Einfluss der Bauteilbreite und der Schubschlankheit auf die Querkrafttragfähigkeit von Stahlbetonplatten ohne Querkraftbewehrung. **Bauingenieur**, v. 93, n. January, 2018.

ADAM, V.; REIßEN, K.; HEGGER, J. Influence of support conditions on shear in RC members without shear reinforcement. In: (D. A. Hordijk, M. Luković, Eds.) **High Tech**

[1] According to the Associação Brasileira de Normas Técnicas (ABNT NBR 6023).

Concrete: Where Technology and Engineering Meet - Proceedings of the 2017 *fib* Symposium, Maastricht, The Netherlands, 2018.

ALEXANDER, S. D. B.; SIMMONDS, S. H. Bond Model for Concentric Punching Shear. **ACI Structural Journal**, v. 89, n. 3, p. 325–334, 1992.

ALFARAH, B.; LÓPEZ-ALMANSA, F.; OLLER, S. New methodology for calculating damage variables evolution in Plastic Damage Model for RC structures. **Engineering Structures**, v. 132, p. 70–86, 2017.

AL-QURAISHI, H. A. A. **Punching Shear Behavior of UHPC Flat Slabs**. 2014. Faculty of Civil and Environmental Engineering of the University of Kassel, PhD Thesis, 2014.

ASCE–ACI COMMITTEE 445. Recent Approaches to Shear Design of Structural Concrete. **Journal of Structural Engineering**, v. 124, n. 12, p. 1375–1417, 1998.

ASTER, H.; KOCH, R. Shear capacity of deep concrete slabs. **Beton- und Stahlbetonbau**, v. 69, n. 11, p. 266–270, 1974.

AZMEE, N. M.; SHAFIQ, N. Ultra-high performance concrete: From fundamental to applications. **Case Studies in Construction Materials**, v. 9, p. e00197, 2018.

BABANAJAD, S. K.; FARNAM, Y.; SHEKARCHI, M. Failure criteria and triaxial behaviour of HPFRC containing high reactivity metakaolin and silica fume. **Construction and Building Materials**, v. 29, p. 215–229, 2012.

BAHIJ, S.; ADEKUNLE, S. K.; AL-OSTA, M.; AHMAD, S.; AL-DULAIJAN, S. U.; RAHMAN, M. K. Numerical investigation of the shear behavior of reinforced ultra-high-performance concrete beams. **Structural Concrete**, v. 19, n. 1, p. 305–317, 2018.

BAIRÁN, J. M.; MENDUIÑA, R.; MARÍ, A.; CLADERA, A. Shear Strength of Non-Slender Reinforced Concrete Beams. **ACI Structural Journal**, n. 117, p. 277–290, 2020.

BALOMENOS, G. P.; GENIKOMSOU, A. S.; POLAK, M. A. Investigation of the effect of openings of interior reinforced concrete flat slabs. **Structural Concrete**, n. September 2017, p. 1–10, 2018.

BASTIEN-MASSE, M.; BRÜHWILER, E. Composite model for predicting the punching resistance of R-UHPFRC-RC composite slabs. **Engineering Structures**, v. 117, p. 603–616, 2016b.

BASTIEN-MASSE, M.; BRÜHWILER, E. Experimental investigation on punching resistance of R-UHPFRC–RC composite slabs. **Materials and Structures/Materiaux et Constructions**, v. 49, n. 5, p. 1573–1590, 2016a.

BAUER, T.; MÜLLER, M. **Straßenbrücken in Massivbauweise nach DIN- Fachbericht - Beispiele prüffähiger Standsicherheitsnachweise**. 2. Auflage ed. Berlin: Bauwerk, 2003.

BAUER, T.; MÜLLER, M.; BLASE, T. **Strassenbrücken in Massivbauweise nach DIN-Fachbericht : Beispiele prüffähiger Standsicherheitsnachweise** ; Stahlbeton- und Spannbetonüberbau nach DIN-Fachbericht 101 und 102 ; mit CD-ROM. [s.l.] : Bauwerk, 2005.

BAUMANN, T.; RUSCH, H. **Versuche zum studien der verdübe- lungswirkung der biegezugbewehrung eines stahlbetonbalkens** [Experimental study on dowel action in reinforced concrete beam]. [s.l.] : Deutscher Ausschuss für Stahlbeton (DAfStb), Ernst, Berlin (in German), 1970.

BAZANT, Z. P.; KIM, J.-K. Size Effect in Shear Failure of Longitudinally Reinforced Beams. **ACI Journal Proceedings**, v. 81, n. 5, p. 456–468, 1984.

BBK (STATENS BETONG KOMMITTE). **Regulations for concrete structures – Part 1: Design**. BBK, Stockholm, Sweden, 1979.

BELLETTI, B.; DAMONI, C.; HENDRIKS, M. A. N.; DE BOER, A. Analytical and numerical evaluation of the design shear resistance of reinforced concrete slabs. **Structural Concrete**, v. 15, n. 3, p. 317–330, 2014.

BELLETTI, B.; SCOLARI, M.; MUTTONI, A.; CANTONE, R. Shear strength evaluation of RC bridge deck slabs according to CSCT with multi – layered shell elements and PARC_CL Crack Model. In: **IABSE Conference Geneva 2015,** Geneva, Switzerland, 2015.

BENTZ, E. C.; VECCHIO, F. J.; COLLINS, M. P. Simplified modified compression field theory for calculating shear strength of reinforced concrete elements. **ACI Structural Journal**, v. 103, n. 4, p. 614–624, 2006.

BIRTEL, V.; MARK, P. Parameterised Finite Element Modelling of RC Beam Shear Failure. In: **ABABQUS USER'S CONFERENCE,** 2006.

BORGHI, T. M.; OLIVEIRA, L. A. M.; EL DEBS, A. L. H. de C.; BECK, A. T. Desempenho de Pontes Rurais com o avanço agrícola dos Rodotrens canavieiros - Análise baseada em Confiabilidade Estrutural. In: **XII CONGRESSO BRASILEIRO DE PONTES E ESTRUTURAS**, 2021.

BRÜHWILER, E. UHPFRC technology to enhance the performance of existing concrete bridges. **Structure and Infrastructure Engineering**, p. 1–12, 2019.

BUI, T. T.; ABOURI, S.; LIMAM, A.; NANA, W. S. A.; TEDOLDI, B.; ROURE, T. Experimental investigation of shear strength of full-scale concrete slabs subjected to concentrated loads in nuclear buildings. **Engineering Structures**, v. 131, p. 405–420, 2017a.

BUI, T. T.; LIMAM, A.; NANA, W.-S.-A.; FERRIER, E.; BOST, M.; BUI, Q.-B. Evaluation of one-way shear behaviour of reinforced concrete slabs: experimental and numerical analysis. **European Journal of Environmental and Civil Engineering**, n. September, p. 1–27, 2017b.

CALDENTEY, A. P.; PADILLA, P.; MUTTONI, A.; FERNÁNDEZ RUIZ, M. Effect of load distribution and variable depth on shear resistance of slender beams without stirrups. **ACI Structural Journal**, v. 109, n. 5, p. 595–603, 2012.

CALVI, P. M.; BENTZ, E. C.; COLLINS, M. P. Model for assessment of cracked reinforced concrete membrane elements subjected to shear and axial loads. **ACI Structural Journal**, v. 115, n. 2, p. 501–509, 2018.

CAMPANA, S.; FERNÁNDEZ RUIZ, M.; ANASTASI, A.; MUTTONI, A. Analysis of shear-transfer actions on one-way RC members based on measured cracking pattern and failure kinematics. **Magazine of Concrete Research**, v. 65, n. 6, p. 386–404, 2013.

CANTONE, R.; FERNÁNDEZ RUIZ, M.; MUTTONI, A. Shear force redistributions and resistance of slabs and wide beams. **Structural Concrete**, 2021.

CARREIRA, D. J.; CHU, K. H. Stress-strain relationship for plain concrete in compression. **ACI Journal**, v. 82(6), n. 6, p. 797–804, 1985.

CARREIRA, D. J.; CHU, K. H. Stress-strain relationship for reinforced concrete in tension. **Journal of the American Concrete Institute**, v. 83, n. 1, p. 21–28, 1986.

CAVAGNIS, F.; FERNÁNDEZ RUIZ, M.; MUTTONI, A. A mechanical model for failures in shear of members without transverse reinforcement based on development of a critical shear crack. **Engineering Structures**, v. 157, p. 300–315, 2018a.

CAVAGNIS, F.; FERNÁNDEZ RUIZ, M.; MUTTONI, A. An analysis of the shear-transfer actions in reinforced concrete members without transverse reinforcement based on refined experimental measurements. **Structural Concrete**, v. 19, n. 1, p. 49–64, 2018b.

CAVAGNIS, F.; FERNÁNDEZ RUIZ, M.; MUTTONI, A. Shear failures in reinforced concrete members without transverse reinforcement: An analysis of the critical shear crack development on the basis of test results. **Engineering Structures**, v. 103, p. 157–173, 2015.

CEN. EN 1992-1-1: Eurocode 2: Design of concrete structures -Part 1-1: General rules and rules for buildings, **EN 1992-1-1:2004**, Comité Européen de Normalisation, Brussels, Belgium, 2004.

CEN. EN 1992-1-1: Eurocode 2: Design of concrete structures -Part 1-1: General rules and rules for buildings, **EN 1992-1-1:2005**, Comité Européen de Normalisation, Brussels, Belgium, 2005.

CEN. Eurocode 1: Actions on structures - Part 2: Traffic loads on bridges, **NEN- EN 1991–2:2003**. Brussels, Belgium: Comité Européen de Normalisation, 2003.

CHANA, P. S. Investigation of the mechanism of shear failure of reinforced concrete beams. **Magazine of Concrete Research**, v. 39, n. 141, p. 196–204, 1987.

CHEN, L.; GRAYBEAL, B. A. Modeling Structural Performance of Ultrahigh Performance Concrete I-Girders. **Journal of Bridge Engineering**, v. 17, n. 5, p. 754–764, 2011.

CHENG, H.; PAZ, C. M.; PINHEIRO, B. C.; ESTEFEN, S. F. Experimentally based parameters applied to concrete damage plasticity model for strain hardening cementitious composite in sandwich pipes. **Materials and Structures/Materiaux et Constructions**, v. 53, n. 4, p. 1–17, 2020.

CHENG, M.-Y.; PARRA-MONTESINOS, G. J. Evaluation of Steel Fiber Reinforcement for Punching Shear Resistance in Slab-Column Connections - Part I: Monotonically Increased Load. **ACI Structural Journal**, v. 107, n. S11, 2010.

CLADERA, A.; MARÍ, A. R. Shear design procedure for reinforced normal and high-strength concrete beams using artificial neural networks. Part I: beams without stirrups. **Engineering Structures**, v. 26, p. 917–926, 2004.

CLADERA, A.; MARÍ, A.; BAIRÁN, J. M.; RIBAS, C.; OLLER, E.; DUARTE, N. The compression chord capacity model for the shear design and assessment of reinforced and prestressed concrete beams. **Structural Concrete**, v. 17, n. 6, p. 1017–1032, 2016.

CLADERA, A.; PÉREZ-ORDÓÑEZ, J. L.; MARTÍNEZ-ABELLA, F. Shear strength of RC beams. Precision, accuracy, safety and simplicity using genetic programming. **Computers and Concrete**, v. 14, n. 4, p. 479–501, 2014.

COLLINS, M. P.; BENTZ, E. C.; SHERWOOD, E. G. Where is shear reinforcement required? Review of research results and design procedures. **ACI Structural Journal**, v. 105, n. 5, p. 590–600, 2008.

Comité Euro-International du Béton, **CEB-FIP MODEL CODE 1990**. Design Code, 1993.

CONCRENORTE - PRÉ MOLDADOS E CONSTRUTORA. Como são fabricadas as pontes rurais de concreto? [s.d.]. Disponível em: <https://concrenorte.com.br/como-sao-fabricadas-as-pontes-rurais-de-concreto/>. Accessed in August 03, 2022.

CONFORTI, A.; MINELLI, F.; PLIZZARI, G. A. Influence of width-to-effective depth ratio on shear strength of reinforced concrete elements without web reinforcement. **ACI Structural Journal**, v. 114, n. 4, p. 995–1006, 2017.

CONFORTI, A.; MINELLI, F.; PLIZZARI, G. A. Wide-shallow beams with and without steel fibres: A peculiar behaviour in shear and flexure. **Composites Part B: Engineering**, v. 51, p. 282–290, 2013.

CONFORTI, A.; MINELLI, F.; TININI, A.; PLIZZARI, G. A. Influence of polypropylene fibre reinforcement and width-to-effective depth ratio in wide-shallow beams. **Engineering Structures**, v. 88, p. 12–21, 2015.

CORNELISSEN, H. A. W.; HORDIJK, D. A.; AND REINHARDT, H. W. Experimental Determination of Crack Softening Characteristics of Normal Weight and Lightweight Concrete. **Heron**, v. 31, n. 2, p. 45–56, 1986.

CRISWELL, M. E.; HAWKINS, N. W. Shear Strength of Slabs: Basic Principle and Their Relation to Current Methods of Analysis. **Special Publication 42: Shear in Reinforced Concrete - Volume 1 and 2**, p. 641–676, 1974.

CULLINGTON, D. W.; DALY, A. F.; HILL, M. E. Assessment of reinforced concrete bridges: Collapse tests on Thurloxton underpass. **Bridge Management**, v. Vol. 3, p. 667–674, 1996.

DAFSTB. **Deutscher Ausschuss für Stahlbeton Heft 240: Hilfsmittel zur Berechnung der Schnittgrößen und Formänderungen von Stahlbetonbauwerken**. (German Committee for Structural Concrete Book 240: Tools for calculation of internal forces and changes in shape of rein. Berlin / Germany: Beuth Verlag, 1991.

DAMASCENO, L. S. R. **Experimental analysis of one-way reinforced concrete flat slabs in punching shear with rectangular columns** (in Portuguese: Análise experimental de lajes lisas unidirecionais de concreto armado com pilares retangulares ao puncionamento). PhD Thesis, Departamento de Engenharia Civil, Universidade Federal do Pará, 2007.

DASSAULT SYSTEMS SIMULIA CORP. **Abaqus Analysis user's manual 6.14**. Providence, Rhode Island (USA): Dassault Systems Simulia Corp., 2014.

DENARIÉ, E.; HABEL, K.; BRÜHWILER, E. Structural behavior of hybrid elements with Advanced Cementitious Materials (HPFRCC). **4th international Workshop on High Performance Fiber Reinforced Cement Composites**, n. January 2003, p. 12, 2003.

DIN 1045. **Beton und Stahlbeton - Bemessung und Ausführung**. Berlin: Deutsches Institut für Normung (DIN), 1988.

DIN 1045-1. **Bemessung und Konstruktion von Stahlbeton- und Spannbetonbauteilen**. Berlin: Deutsches Institut für Normung (DIN), 2001.

DOORGEEST, J. **Transition Between One-way Shear and Punching Shear**. 2012. Master of Science Thesis, Delft University of Technology, 2012.

DULACSKA, H. Dowel Action of Reinforcement Crossing Cracks in Concrete. **ACI Journal Proceedings**, v. 69, n. 12, p. 754–757, 1972.

FANG, C.; ALI, M. S. M.; SHEIKH, A. H.; SINGH, M. Numerical and Finite-Element Analysis of Short Ultrahigh-Performance Fiber-Reinforced Concrete Columns. **Journal of Structural Engineering**, v. 145, n. 10, p. 1–17, 2019.

FD P 18-717. Eurocode 2 - Calcul des structures en béton - Guide d'application des normes NF EN 1992, 2013.

FÉDÉRATION INTERNATIONALE DU BÉTON (*fib*). ***fib* Model Code for Concrete Structures 2010**. Lausanne, Switzerland: Ernst & Sohn - fédération internationale du béton, Bulletin 65, 2012. v. Vol. 1-2

FEENSTRA, P. H. **Computational aspects of biaxial stress in plain and reinforced concrete**. 1993. PhD Thesis, Delft University of Technology: Civil Engineering and Geosciences, 1993.

FEHLING, E.; SCHMIDT, M.; WALRAVEN, J. C.; LEUTBECHER, T.; FRÖHLICH, S. **Ultra-high performance concrete UHPC : fundamentals, design, examples**. [s.l.] : Ernst & Sohn, 2014.

FELIPE, T. R. C.; LEONEL, E. D.; HAACH, V. G.; BECK, A. T. A comprehensive ductile damage model for 3D truss structures. **International Journal of Non-Linear Mechanics**, v. 112, p. 13–24, 2019.

FERNÁNDEZ RUIZ, M.; MUTTONI, A.; SAGASETA, J. Shear strength of concrete members without transverse reinforcement: A mechanical approach to consistently account for size and strain effects. **Engineering Structures**, v. 99, p. 360–372, 2015.

FERNÁNDEZ RUIZ, M.; VAZ RODRIGUES, R.; MUTTONI, A. **Dimensionnement et vérification des dalles de roulement des ponts routiers**. [s.l.] : Rapport: Projet de recherche AGB 2002/028 sur demande du Groupe de travail Recherche en matière de ponts (AGB), 2009.

FERNÁNDEZ RUIZ, M.; ZANUY, C.; NATÁRIO, F.; GALLEGO, J. M.; ALBAJAR, L.; MUTTONI, A. Influence of Fatigue Loading in Shear Failures of Reinforced Concrete Members without Transverse Reinforcement. **Journal of Advanced Concrete Technology**, v. 13, n. 5, p. 263–274, 2015.

FERNÁNDEZ, P. G.; MARÍ, A.; OLLER, E. Theoretical prediction of the shear strength of reinforced concrete slabs under concentrated loads close to linear supports. **Structure and Infrastructure Engineering**, p. 1–14, 2021.

FERREIRA, M. P. **Experimental analysis of one-way reinforced concrete flat slabs in axis or non-axis-symmetric punching shear** (in Portuguese: Análise experimental de lajes lisas unidirecionais de concreto armado ao puncionamento simétrico ou assimétrico). 2006. Tese (Doutorado), Universidade Federal do Pará, 2006.

FERREIRA, M. P.; SACRAMENTO, P. V. P.; LIMA NETO, A. F.; TEIXEIRA, M. R.; DE OLIVEIRA, D. R. C. Punching strength of RC slabs with asymmetric point loads. **Acta Scientiarum - Technology**, v. 38, n. 1, p. 71–80, 2016.

FISET, M.; BASTIEN, J.; MITCHELL, D. Methods for Shear Strengthening of Thick Concrete Slabs. **Journal of Performance of Constructed Facilities**, v. 31, n. 3, p. 04016103, 2016.

FURUUCHI, H.; TAKAHASHI, Y.; UEDA, T.; KAKUTA, Y. Effective width for shear failure of RC deep slabs. **Transactions of the Japan concrete institute**, v. 20, p. pp.209-216, 1998.

GASTEBLED, O. J.; MAY, I. M. Fracture Mechanics Model Applied to Shear Failure of Reinforced Concrete Beams Without Stirrups. **ACI Structural Journal**, v. 98, n. 2, p. 184–190, 2001.

GAYED, R. B.; PEIRIS, C.; GHALI, A. Flexure-induced punching of concrete flat plates. **ACI Special Publication**, v. 315, p. 73–99, 2017.

GENIKOMSOU, A. S.; POLAK, M. A. 3D finite element investigation of the compressive membrane action effect in reinforced concrete flat slabs. **Engineering Structures**, v. 136, p. 233–244, 2017b.

GENIKOMSOU, A. S.; POLAK, M. A. Effect of openings on punching shear strength of reinforced concrete slabs-finite element investigation. **ACI Structural Journal**, v. 114, n. 5, p. 1249–1262, 2017a.

GENIKOMSOU, A. S.; POLAK, M. A. Finite element analysis of punching shear of concrete slabs using damaged plasticity model in ABAQUS. **Engineering Structures**, v. 98, p. 38–48, 2015.

GENIKOMSOU, A. S.; POLAK, M. A. Finite-Element Analysis of Reinforced Concrete Slabs with Punching Shear Reinforcement. **Journal of Structural Engineering**, v. 142, n. 12, p. 1–15, 2016.

GHANNOUM, W. M. **Size Effect on Shear Strength of Reinforced Concrete Beams**, Thesis (Master of Engineering), McGill University, Department of Civil Engineering and Applied Mechanics, Montreal, Canadá, 1998.

GOLDBECK, A. T. The Influence of Total Width of the Effective Width of Reinforced-Concrete Slabs Subjected to Central Concentrated Loading. **ACI Journal Proceedings**, v. 13, n. 2, p. 78–88, 1917.

GOLDBECK, A. T.; SMITH, E. B. Tests of Large Reinforced Concrete Slabs. **ACI Journal Proceedings**, v. 12, n. 2, p. 324–333, 1916.

GOUVEIA, N. D.; FARIA, D. M. V.; RAMOS, A. P. Assessment of SFRC flat slab punching behaviour – part I: monotonic vertical loading. **Magazine of Concrete Research**, v. 71, n. 11, p. 587–598, 2019a.

GOUVEIA, N. D.; FARIA, D. M. V.; RAMOS, A. P. Assessment of SFRC flat slab punching behaviour – part II: reversed horizontal cyclic loading. **Magazine of Concrete Research**, v. 71, n. 1, p. 26–42, 2019b.

GRASSER, E.; THIELEN, G. **Hilfsmittel zur Berechnung der Schnittgrößen und Formänderungen von Stahlbetontragwerken : nach DIN 1045**, Ausg. Juli 1988. 3o revised ed. Berlin: Beuth Verlag GmbH, 1991.

GRAYBEAL, B. A. Compressive behavior of ultra-high-performance fiber-reinforced concrete. **ACI Materials Journal**, v. 104, n. 2, p. 146–152, 2007.

GRAYBEAL, B.; BRÜHWILER, E.; KIM, B.-S.; TOUTLEMONDE, F.; VOO, Y. L.; ZAGHI, A. International Perspective on UHPC in Bridge Engineering. **Journal of Bridge Engineering**, v. 25, n. 11, p. 04020094, 2020.

GUANDALINI, S.; BURDET, O. L.; MUTTONI, A. Punching tests of slabs with low reinforcement ratios. **ACI Structural Journal**, v. 106, n. 6, p. 87–95, 2009.

GUO, Z. **Principles of Reinforced Concrete Design**, Elsevier: Butterworth-Heinemann, Waltham, MA, 2014.

GURUTZEAGA, M.; OLLER, E.; RIBAS, C.; CLADERA, A.; MARÍ, A. Influence of the longitudinal reinforcement on the shear strength of one-way concrete slabs. **Materials and Structures/Materiaux et Constructions**, v. 48, n. 8, p. 2597–2612, 2015.

HALVONIK, J.; VIDAKOVIĆ, A.; VIDA, R. Shear Capacity of Clamped Deck Slabs Subjected to a Concentrated Load. **Journal of Bridge Engineering**, v. 25, n. 7, p. 04020037, 2020.

HARRIS, D. K. Characterization of Punching Shear Capacity of Thin Uhpc Plates. 2004. Virginia Tech, 2004.

HAWKINS, N. M.; MITCHELL, D. Progressive Collapse of Flat Plate Structures. **ACI Journal Proceedings**, v. 76, n. 7, p. 775–808, 1979.

HAWKINS, N. M.; OSPINA, C. E. Effect of slab flexural reinforcement and depth on punching strength. **ACI-fib International Symposium: Punching shear of structural concrete slabs (Special Publication)**. [s.l: s.n.]. 2017.

HEGER, F. J.; MCGRATH, T. J. **Design method for reinforced concrete pipe and box sections**. Massachusetts; San Francisco, California: Simpson Gumpertz & Heger Inc., 1980.

HENZE, L. **Querkrafttragverhalten von Stahlbeton-Fahrbahnplatten**. 2019. PhD Thesis, Institute for Concrete Structures, Technische Universität Hamburg (TUHH), 2019.

HENZE, L.; HARTER, M.; ROMBACH, G. A. Querkrafttragfähigkeit von Stahlbetonplatten ohne Querkraftbewehrung unter konzentrierten Einzellasten (Shear capacity of reinforced concrete slabs without transverse reinforcement under concentrated loads Part 2: Proposal for a new design model). **Beton- und Stahlbetonbau**, 2019.

HENZE, L.; ROMBACH, G. A. **Versuche zur Querkrafttragfähigkeit von Stahlbetonplatten unter auflagernahen Einzellasten; Versuchsbericht** (Experimental investigations on shear capacity of concrete slabs with concentrated loads close to the support). Technical Report, Hamburg, 2017.

HENZE, L.; ROMBACH, G. A.; HARTER, M. New approach for shear design of reinforced concrete slabs under concentrated loads based on tests and statistical analysis. **Engineering Structures**, v. 219, n. May, p. 110795, 2020.

HILLERBORG, A.; MODÉER, M.; PETERSSON, P.-E. Analysis of crack formation and crack growth in concrete by means of fracture mechanics and finite elements. **Cement and Concrete Research**, v. 6, n. 6, p. 773–781, 1976.

HOANG, A. Le; FEHLING, E. Numerical analysis of circular steel tube confined UHPC stub columns. **Computers and Concrete**, v. 19, n. 3, p. 263–273, 2017.

HOGNESTAD, E. Yield-Line Theory for the Ultimate Flexural Strength of Reinforced Concrete Slabs. **ACI Journal Proceedings**, v. 49, n. 3, p. 637–656, 1953.

HOGNESTAD, E.; HANSON, N. W.; MCHENRY, D. Concrete Stress Distribution in Ultimate Strength Design. **ACI Journal Proceedings**, v. 52, n. 12, p. 455–480, 1955.

HORDIJK, D. A. Tensile and tensile fatigue behaviour of concrete — experiments, modelling and analyses. **Heron**, v. 37, n. 1, p. 3–79, 1992.

INÁCIO, M. M. G.; LAPI, M.; PINHO RAMOS, A. Punching of reinforced concrete flat slabs – Rational use of high strength concrete. **Engineering Structures**, v. 206, 2020.

INÁCIO, M.; ISUFI, B.; LAPI, M.; PINHO RAMOS, A. Rational Use of High-Strength Concrete in Flat Slab-Column Connections under Seismic Loading. **ACI Structural Journal**, v. 117, n. 6, 2020.

ISLAM, M. S.; PAM, H. J.; KWAN, A. K. H. Shear capacity of high-strength concrete beams with their point of inflection within the shear span. **Proceedings of the Institution of Civil Engineers: Structures and Buildings**., v. 128, p. 91–99, 1998.

JÄGER, T. **Querkraftwiderstand und Verformungsvermögen von Stahlbetonplatten** (Shear and Deformation Capacity of Reinforced Concrete Slabs). 2007. PhD thesis, ETH Zurich, Zurich, Switzerland, 2007.

JÄGER, T. Shear strength and deformation capacity of reinforced concrete slabs. In: **Proceedings of the 4th International PhD Symposium in Civil Engineering**. 2002, Munich, Germany.

JÄGER, T.; MARTI, P. **Versuche zum Querkraftwiderstand und zum Verformungsvermogen von Stahlbetonplatten** (Experiments on the Shear and Deformation Capacity of Reinforced Concrete Slabs). 2005. Monograph, ETH Zurich, Zurich, Switzerland, 2005.

JANG, H.-O.; LEE, H.-S.; CHO, K.; KIM, J. Numerical and Experimental Analysis of the Shear Behavior of Ultrahigh-Performance Concrete Construction Joints. **Advances in Materials Science and Engineering**, v. 2018, p. 1–17, 2018.

JOH, C.; HWANG, H.; KIM, B. Punching shear and flexural strengths of ultra high performance concrete slabs. In: **HIGH PERFORMANCE STRUCTURES AND MATERIALS IV.** Southampton, UK, 2008.

JOHANSEN, K. W. **Yield-Line Formulae for Slabs**. [s.l.] : CRC Press, 1972.

JØRGENSEN, H. B.; HOANG, L. C.; FABRIN, L. S.; MAAGAARD, J. Influence of high axial tension on the shear strength of non-shear RC beams. In: **Proceedings of the International IABSE Conference: Assessment, Upgrading, Refurbishment of Infrastructures**. 2013.

KADHIM, M. M. A.; JAWDHARI, A.; PEIRIS, A. Development of hybrid UHPC-NC beams: A numerical study. **Engineering Structures**, v. 233, p. 111893, 2021a.

KADHIM, M. M. A.; SALEH, A. R.; CUNNINGHAM, L. S.; SEMENDARY, A. A. Numerical investigation of non-shear-reinforced UHPC hybrid flat slabs subject to punching shear. **Engineering Structures**, v. 241, p. 112444, 2021b.

KANI, G. N. J. How Safe are Our Large Reinforced Concrete Beams? **ACI Journal Proceedings**, v. 64, n. 3, p. 128–141, 1967.

KANI, G. N. J. The Riddle of Shear Failure and its Solution. **ACI Journal Proceedings**, v. 61, n. 4, p. 441–468, 1964.

KANI, M. W.; HUGGINS, M. W.; WITTKOPP, R. R. **Kani on shear in reinforced concrete**. [s.l.] : University of Toronto, Dept. of Civil Engineering, 1979.

KIM, D.; KIM, W.; WHITE, R. N. Arch Action in Reinforced Concrete Beams—A Rational Prediction of Shear Strength. **ACI Structural Journal**, v. 96, n. 4, p. 586–593, 1999.

KONIG, G.; FISCHER, J. Model uncertainties concerning design equations for the shear capacity of concrete members without shear reinforcement. In: **CEB BULLETIN 224, MODEL UNCERTAINTIES AND CONCRETE BARRIER FOR ENVIRONMENTAL PROTECTION**. Lausanne, Switzerland, 1995.

KRAHL, P. A.; CARRAZEDO, R.; EL DEBS, M. K. Mechanical damage evolution in UHPFRC: Experimental and numerical investigation. **Engineering Structures**, v. 170, n. May 2017, p. 63–77, 2018.

KRAHL, P. A.; GIDRÃO, G. M. S.; CARRAZEDO, R. Compressive behavior of UHPFRC under quasi-static and seismic strain rates considering the effect of fiber content. **Construction and Building Materials**, v. 188, p. 633–644, 2018.

KRAHL, P. A.; GIDRÃO, G. M. S.; CARRAZEDO, R. Cyclic behavior of UHPFRC under compression. **Cement and Concrete Composites**, v. 104, p. 103363, 2019.

KRÄTZIG, W. B.; PÖLLING, R. An elasto-plastic damage model for reinforced concrete with minimum number of material parameters. **Computers & Structures**, v. 82, n. 15–16, p. 1201–1215, 2004.

KRIPS, M. **Rißbreitenbeschränkung im Stahlbeton und Spannbeton** (Crack width restriction in reinforced concrete and prestressed concrete). Berlin: Ernst & Sohn, 1985.

KUCHMA, D. A.; WEI, S.; SANDERS, D. H.; BELARBI, A.; NOVAK, L. C. Development of One-Way Shear Design Provisions of ACI 318-19 for Reinforced Concrete. **ACI Structural Journal**, v. 116, n. 4, p. 285–295, 2019.

KUPFER, H. B.; GERSTLE, K. H. Behavior of Concrete under Biaxial Stresses. **Journal of the Engineering Mechanics Division**, v. 99, n. 4, p. 853–866, 1973.

KUPFER, H. B.; HILSDORF, H. K.; RUSCH, H. Behavior of Concrete Under Biaxial Stresses. **ACI Journal Proceedings**, v. 66, n. 8, p. 656–666, 1969.

LANTSOGHT, E. O. L. Shear capacity of reinforced concrete slab bridges under a wheel load close to the support - Literature review. **Report nr. 25.5-12-11**. Delft, 2012.

LANTSOGHT, E. O. L. **Shear in Reinforced Concrete Slabs under Concentrated Loads Close to Supports**. 2013. PhD Thesis, Faculty of Civil Engineering and Geosciences, Delft University of Technology, 2013.

LANTSOGHT, E. O. L.; DE BOER, A.; VAN DER VEEN, C. Distribution of peak shear stress in finite element models of reinforced concrete slabs. **Engineering Structures**, v. 148, p. 571–583, 2017b.

LANTSOGHT, E. O. L.; DE BOER, A.; VAN DER VEEN, C. Levels of approximation for the shear assessment of reinforced concrete slab bridges. **Structural Concrete**, v. 18, n. 1, p. 143–152, 2017a.

LANTSOGHT, E. O. L.; DE BOER, A.; VAN DER VEEN, C.; WALRAVEN, J. C. Effective shear width of concrete slab bridges. **Proceedings of the Institution of Civil Engineers - Bridge Engineering**, v. 168, n. 4, p. 287–298, 2015a.

LANTSOGHT, E. O. L.; VAN DER VEEN, C.; DE BOER, A. Extended Strip Model for slabs subjected to load combinations. **Engineering Structures**, v. 145, p. 60–69, 2017.

LANTSOGHT, E. O. L.; VAN DER VEEN, C.; DE BOER, A.; ALEXANDER, S. D. B. Extended strip model for reinforced concrete slabs under concentrated loads. **ACI Structural Journal**, v. 114, n. 2, p. 565–574, 2017.

LANTSOGHT, E. O. L.; VAN DER VEEN, C.; DE BOER, A.; WALRAVEN, J. C. Using Eurocodes and Aashto for assessing shear in slab bridges. **Proceedings of the Institution of Civil Engineers - Bridge Engineering**, v. 169, n. 4, p. 285–297, 2016.

LANTSOGHT, E. O. L.; VAN DER VEEN, C.; DE BOER, A.; WALRAVEN, J. C. Transverse load redistribution and effective shear width in reinforced concrete slabs. **Heron**, v. 60, n. 3, p. 145–179, 2015b.

LANTSOGHT, E. O. L.; VAN DER VEEN, C.; DE BOER, A.; WALRAVEN, J. C. Influence of width on shear capacity of reinforced concrete members. **ACI Structural Journal**, v. 111, n. 6, p. 1441–1449, 2014.

LANTSOGHT, E. O. L.; VAN DER VEEN, C.; WALRAVEN, J. C. Shear in one-way slabs under concentrated load close to support. **ACI Structural Journal**, v. 110, n. 2, p. 275–284, 2013a.

LANTSOGHT, E. O. L.; VAN DER VEEN, C.; WALRAVEN, J. C.; DE BOER, A. Transition from one-way to two-way shear in slabs under concentrated loads. **Magazine of Concrete Research**, v. 67, n. 17, p. 909–922, 2015c.

LANTSOGHT, E. O. L.; VAN DER VEEN, C.; WALRAVEN, J. C.; DE BOER, A. Database of wide concrete members failing in shear. **Magazine of Concrete Research**, v. 67, n. 1, p. 33–52, 2015d.

LANTSOGHT, E. O. L.; VAN DER VEEN, C.; WALRAVEN, J. C.; DE BOER, A. Experimental investigation on shear capacity of reinforced concrete slabs with plain bars and slabs on elastomeric bearings. **Engineering Structures**, v. 103, p. 1–14, 2015e.

LANTSOGHT, E. O. L.; VAN DER VEEN, C.; WALRAVEN, J. C.; DE. BOER, A. Peak shear stress distribution in finite element models of concrete slabs. In: ZINGONI, A. (Ed.). **Research and Applications in Structural Engineering, Mechanics and Computation**. London, UK: CRC Press, Taylor & Francis Group, 2013. p. 475–480.

LANWER, J.; OETTEL, V.; EMPELMANN, M.; HÖPER, S.; KOWALSKY, U.; DINKLER, D. Bond behavior of micro steel fibers embedded in ultra-high performance concrete subjected to monotonic and cyclic loading. **Structural Concrete**, v. 20, n. 4, p. 1243–1253, 2019.

LEE, J. H.; HONG, S. G.; JOH, C.; KWAHK, I.; LEE, J. W. Biaxial tension–compression strength behaviour of UHPFRC in-plane elements. **Materials and Structures/Materiaux et Constructions**, v. 50, n. 1, p. 1–17, 2017.

LEE, J.; FENVES, G. L. Plastic-Damage Model for Cyclic Loading of Concrete Structures. **Journal of Engineering Mechanics**, v. 124, n. 8, p. 892–900, 1998.

LEONHARDT, F.; WALTHER, R. **Schubversuche an einfeldrigen Stahlbetonbalken mit und ohne Schubbewehrung** [Shear tests on single-span reinforced concrete beams with and without shear reinforcement]. Berlin: Beuth, 1962.

LIMAM, S.; NANA, W. S. A.; BUI, T. T.; LIMAM, A.; ABOURI, S. Experimental investigation and analytical calculations on shear strength of full-scale RC slabs with shear reinforcement for nuclear power plants. **Nuclear Engineering and Design**, v. 324, p. 143–157, 2017.

LUBELL, A. S. **Shear in Wide Reinforced Concrete Members**. 2006. PhD dissertation. University of Toronto, Canadá, 2006.

LUBELL, A. S.; SHERWOOD, T.; BENTZ, E.; COLLINS, M. P. Safe shear design of large, wide beams. **Concrete International**, v. 26, n. 1, p. 66–78, 2004.

LUBLINER, J.; OLIVER, J.; OLLER, S.; OÑATE, E. A plastic-damage model for concrete. **International Journal of Solids and Structures**, v. 25, n. 3, p. 299–326, 1989.

MAHMUD, G. H.; YANG, Z.; HASSAN, A. M. T. Experimental and numerical studies of size effects of Ultra High Performance Steel Fibre Reinforced Concrete (UHPFRC) beams. **Construction and Building Materials**, v. 48, p. 1027–1034, 2013.

MANSUR, M. A.; CHIN, M. S.; WEE, T. H. Stress-Strain Relationship of High-Strength Fiber Concrete in Compression. **Journal of Materials in Civil Engineering**, v. 11, n. 1, p. 21–29, 1999.

MARÍ, A.; BAIRÁN, J. M.; CLADERA, A.; OLLER, E. Shear Design and Assessment of Reinforced and Prestressed Concrete Beams Based on a Mechanical Model. **Journal of Structural Engineering**, v. 142, n. 10, p. 17p., 2016.

MARÍ, A.; BAIRÁN, J. M.; CLADERA, A.; OLLER, E.; RIBAS, C. Shear-flexural strength mechanical model for the design and assessment of reinforced concrete beams. **Structure and Infrastructure Engineering**, v. 11, n. 11, p. 1399–1419, 2015.

MARÍ, A.; CLADERA, A.; BAIRÁN, J. M.; OLLER, E.; RIBAS, C. Shear-flexural strength mechanical model for the design and assessment of reinforced concrete beams subjected to point or distributed loads. **Frontiers of Structural and Civil Engineering**, v. 8, n. 4, p. 337–353, 2014.

MARÍ, A.; CLADERA, A.; OLLER, E.; BAIRÁN, J. M. A punching shear mechanical model for reinforced concrete flat slabs with and without shear reinforcement. **Engineering Structures**, v. 166, n. October 2017, p. 413–426, 2018.

MARQUES, M. G.; LIBERATI, E. A. P.; PIMENTEL, M. J.; DE SOUZA, R. A.; TRAUTWEIN, L. M. Nonlinear finite element analysis (NLFEA) of reinforced concrete flat slabs with holes. **Structures**, v. 27, n. November 2019, p. 1–11, 2020.

MARTÍN-SANZ, H.; HERRAIZ, B.; BRÜHWILER, E.; CHATZI, E. Shear-bending failure modeling of concrete ribbed slabs strengthened with UHPFRC. **Engineering Structures**, v. 222, p. 110846, 2020.

MAYA, L. F.; FERNÁNDEZ RUIZ, M.; MUTTONI, A.; FOSTER, S. J. Punching shear strength of steel fibre reinforced concrete slabs. **Engineering Structures**, v. 40, p. 83–94, 2012.

MENÉTREY, P. Synthesis of punching failure in reinforced concrete. **Cement and Concrete Composites**, v. 24, n. 6, p. 497–507, 2002.

MENNA, D. W.; GENIKOMSOU, A. S. Punching Shear Response of Concrete Slabs Strengthened with Ultrahigh-Performance Fiber-Reinforced Concrete Using Finite-Element Methods. **Practice Periodical on Structural Design and Construction**, v. 26, n. 1, p. 04020057, 2021.

MICHAŁ, S.; ANDRZEJ, W. Calibration of the CDP model parameters in Abaqus. In: **THE 2015 WOURLD CONGRESS ON ADVANCES IN STRUCTURAL ENGINEERING AND MECHANICS (ASEM15)**, Incheon, Korea, 2015.

MIHAYLOV, B. I.; BENTZ, E. C.; COLLINS, M. P. Two-parameter kinematic theory for shear behavior of deep beams. **ACI Structural Journal**, v. 110, n. 3, p. 447–455, 2013.

MILLIGAN, G. J.; POLAK, M. A.; ZURELL, C. Finite element analysis of punching shear behaviour of concrete slabs supported on rectangular columns. **Engineering Structures**, v. 224, p. 111189, 2020.

MILLIGAN, G. J.; POLAK, M. A.; ZURELL, C. Impact of Column Rectangularity on Punching Shear Strength: Code Predictions versus Finite Element Analysis. **Journal of Structural Engineering**, v. 147, n. 2, p. 04020331, 2021.

MOMAYEZ, A.; EHSANI, M. R.; RAMEZANIANPOUR, A. A.; RAJAIE, H. Comparison of methods for evaluating bond strength between concrete substrate and repair materials. **Cement and Concrete Research**, v. 35, n. 4, p. 748–757, 2005.

MOREILLON, L. **Shear strength of structural elements in high performance fibre reinforced concrete (HPFRC)**. 2013. PhD Thesis (Docteur ès Sciences), Université Paris-Est, 2013.

MÖRSCH, E. **Der Eisenbetonbau** [Concrete-steel construction]. New York.: Engineering News Publishing, 1909.

MUTTONI, A. Punching Shear Strength of Reinforced Concrete Slabs without Transverse Reinforcement. **ACI Structural Journal**, v. 105, n. 4, p. 440–450, 2008.

MUTTONI, A.; CALDENTEY, A. P.; HEGGER, J.; VILL, M.; SHAVE, J. D.; MENEGOTTO, M. **PT-SC2-T1 D3BG - Background documents to prEN 1992-1-1:2018**, 2018.

MUTTONI, A.; FERNÁNDEZ RUIZ, M. MC2010: the critical shear crack theory as a mechanical model for punching shear design and its application to code provisions. In: **FIB BULLETIN 57: SHEAR AND PUNCHING SHEAR IN RC AND FRC ELEMENTS**, Lausanne (Switzerland), 2010b.

MUTTONI, A.; FERNÁNDEZ RUIZ, M. Shear in slabs and beams: should they be treated in the same way? In: **FIB BULLETIN 57: Shear and Punching Shear in RC and FRC Elements**. 2010a.

MUTTONI, A.; FERNÁNDEZ RUIZ, M. Shear Strength of Members without Transverse Reinforcement as Function of Critical Shear Crack Width. **ACI Structural Journal**, v. 105, n. 2, p. 163–172, 2008.

MUTTONI, A.; FERNÁNDEZ RUIZ, M. The levels-of-approximation approach in MC 2010: Application to punching shear provisions. **Structural Concrete**, v. 13, n. 1, p. 32–41, 2012.

MUTTONI, A.; FERNÁNDEZ RUIZ, M.; BENTZ, E.; FOSTER, S.; SIGRIST, V. Background to fib Model Code 2010 shear provisions - part II: punching shear. **Structural Concrete**, v. 14, n. 3, p. 204–214, 2013.

MUTTONI, A.; SCHWARTZ, J. Behavior of Beams and Punching in Slabs without Shear Reinforcement. **IABSE Colloquium**, v. 62, n. January 1991, p. 703–708, 1991.

NAAMAN, A. E.; LIKHITRUANGSILP, V.; PARRA-MONTESINOS, G. Punching shear response of high-performance fiber-reinforced cementitious composite slabs. **ACI Structural Journal**, v. 104, n. 2, p. 170–179, 2007.

NANA, W. S. A.; BUI, T. T.; LIMAM, A.; ABOURI, S. Experimental and Numerical Modelling of Shear Behaviour of Full-scale RC Slabs Under Concentrated Loads. **Structures**, v. 10, p. 96–116, 2017.

NATÁRIO, F. **Static and Fatigue Shear Strength of Reinforced Concrete Slabs Under Concentrated Loads Near Linear Support**. 2015. PhD Thesis (Docteur ès Sciences), École Polytechnique Fédérale de Lausanne, 2015.

NATÁRIO, F.; FERNÁNDEZ RUIZ, M.; MUTTONI, A. Experimental investigation on fatigue of concrete cantilever bridge deck slabs subjected to concentrated loads. **Engineering Structures**, v. 89, p. 191–203, 2015.

NATÁRIO, F.; FERNÁNDEZ RUIZ, M.; MUTTONI, A. Shear strength of RC slabs under concentrated loads near clamped linear supports. **Engineering Structures**, v. 76, n. September, p. 10–23, 2014.

NAVARRO, M.; IVORRA, S.; VARONA, F. B. Parametric computational analysis for punching shear in RC slabs. **Engineering Structures**, v. 165, p. 254–263, 2018.

NAVARRO, M.; IVORRA, S.; VARONA, F. B. Parametric finite element analysis of punching shear behaviour of RC slabs reinforced with bolts. **Computers and Structures**, v. 228, p. 106147, 2020.

NGUYEN, T. N.; NGUYEN, T. T.; PANSUK, W. Experimental study of the punching shear behavior of high performance steel fiber reinforced concrete slabs considering casting directions. **Engineering Structures**, v. 131, p. 564–573, 2017.

NORMCOMISSIE 351001. NEN 6720 Technische Grondslagen voor Bouwvoorschriften, Voorschriften Beton TGB 1990–Constructieve Eisen em Rekenmethoden (VBC 1995), 1995.

OLLER, S. A continuous damage model for frictional materials (*in spanish*). PhD Thesis, Technical University of Catalonia, 1988.

OLONISAKIN, A. A.; ALEXANDER, S. D. B. Mechanism of shear transfer in a reinforced concrete beam. **Canadian Journal of Civil Engineering**, v. 26, n. 6, p. 810–817, 1999.

OTHMAN, H.; MARZOUK, H. Applicability of damage plasticity constitutive model for ultra-high performance fibre-reinforced concrete under impact loads. **International Journal of Impact Engineering**, v. 114, p. 20–31, 2018.

ÖZTEKIN, E.; PUL, S.; HÜSEM, M. Experimental determination of Drucker-Prager yield criterion parameters for normal and high strength concretes under triaxial compression. **Construction and Building Materials**, v. 112, p. 725–732, 2016.

PETERSSON, P. Crack growth and development of fracture zones in plain concrete and similar materials. Division of building materials, p. 1–174, 1981.

POLIOTTI, M.; BAIRÁN, J. M. A new concrete plastic-damage model with an evolutive dilatancy parameter. **Engineering Structures**, v. 189, p. 541–549, 2019.

POURBABA, M.; JOGHATAIE, A.; MIRMIRAN, A. Shear behavior of ultra-high performance concrete. **Construction and Building Materials**, v. 183, p. 554–564, 2018.

PREFEITURA DE ARARAS. Mais duas pontes são instaladas na zona rural de Araras. 2015. Available in: <https://araras.sp.gov.br/noticias/15901>. Accessed in August 03, 2022.

PREFEITURA DE EXTREMA. 20a ponte de aduelas de concreto está sendo finalizada na Zona Rural. 2020. Available in: <https://www.extrema.mg.gov.br/noticias/20a-ponte-de-aduelas-de-concreto-esta-sendo-finalizada-na-zona-rural/>. Accessed in August 03, 2022.

PROCHAZKOVA, Z.; LANTSOGHT, E. O. L. **Material properties – Felt and Reinforcement For Shear test of Reinforced Concrete Slab**, Report nr. 25.5-11-11, Delft University of Technology, Faculty of Civil Engineering and Geosciences, Department of Design & Construction – Concrete Structures, 2011.

QI, J.; CHENG, Z.; ZHOU, K.; ZHU, Y.; WANG, J.; BAO, Y. Experimental and theoretical investigations of UHPC-NC composite slabs subjected to punching shear-flexural failure. **Journal of Building Engineering**, p. 102662, 2021.

RAJAGOPALAN, K. S.; FERGUSON, P. M. Exploratory Shear Tests Emphasizing Percentage of Longitudinal Steel. **ACI Journal Proceedings**, v. 65, n. 8, p. 634–638, 1968.

REGAN, P. E. **Shear Resistance of Concrete Slabs at Concentrated Loads Close to Supports**. Polytechnic of Central London, UK, 1982.

REGAN, P. E. **Shear Resistance of Members without Shear Reinforcement; Proposal for CEB Model Code MC90**, 1987.

REGAN, P. E.; REZAI-JORABI, H. Shear Resistance of One-Way Slabs Under Concentrated Loads. **ACI Structural Journal**, v. 85, n. 2, p. 150–157, 1988.

REINECK, K.-H. Model for Structural Concrete Members without Transverse Reinforcement. In: **IABSE colloquium structural concrete**, IABSE REPORT, IABSE, Zurich, 1991a.

REINECK, K.-H. Ultimate shear force of structural concrete members Without Transverse Reinforcement Derived From a Mechanical Model (SP-885). **ACI Structural Journal**, v. 88, n. 5, p. 592–602, 1991. b.

REINECK, K.-H.; BENTZ, E. C.; FITIK, B.; KUCHMA, D. A.; BAYRAK, O. ACI-DAfStb Database of Shear Tests on Slender Reinforced Concrete Beams without Stirrups. **ACI Structural Journal**, v. 110, n. 5, p. 867–876, 2013.

REIßEN, K. **Zum Querkrafttragverhalten von einachsig gespannten Stahlbe- tonplatten ohne Querkraftbewehrung unter Einzellasten**. 2016. Doctor of Engineering - PhD Thesis (Doctor of Engineering), Faculty of Civil Engineering, RWTH Aachen University, Aachen, Germany, 2016.

REIßEN, K.; CLASSEN, M.; HEGGER, J. Shear in reinforced concrete slabs-Experimental investigations in the effective shear width of one-way slabs under concentrated loads and with different degrees of rotational restraint. **Structural Concrete**, v. 19, n. 1, p. 36–48, 2018.

REIßEN, K.; HEGGER, J. Database of shear tests on RC slabs without shear reinforcement under concentrated loads – Assessment of design rules according to Eurocode 2. In: **16TH EUROPEAN BRIDGE CONFERENCE**, Edinburgh, Scotland, 2015.

REIßEN, K.; HEGGER, J. Experimental investigations on the effective width for shear. In: **Maintenance, monitoring, safety, risk and resilience of bridges and bridge networks - proceedings of the 8th international conference on bridge maintenance, safety and management**, IABMAS, 2016.

REIßEN, K.; HEGGER, J. Experimentelle Untersuchungen zum Querkrafttragverhalten von auskragenden Fahrbahnplatten unter Radlasten. **Beton- und Stahlbetonbau**, v. 108, n. 5, p. 315–324, 2013a.

REIßEN, K.; HEGGER, J. Experimentelle Untersuchungen zur mitwirkenden Breite für Querkraft von einfeldrigen Fahrbahnplatten. **Beton- und Stahlbetonbau**, v. 108, n. 2, p. 96–103, 2013b.

REIßEN, K.; HEGGER, J. Numerical investigations on the shear capacity of reinforced concrete slabs under concentrated loads. In: **Research and applications in structural engineering, mechanics and computation**, CRC Press, 2013c.

REIßEN, K.; HEGGER, J. Shear Capacity of Reinforced Concrete Slabs under Concentrated Loads. In: **8TH IABSE CONGRESS 2012**: INNOVATIVE INFRASTRUCTURES - TOWARD HUMAN URBANISM, Seoul, Südkorea, 2012.

RIBEIRO, P. O.; GIDRÃO, G. M. S.; VAREDA, L. V.; CARRAZEDO, R.; MALITE, M. Numerical and experimental study of concrete I-beam subjected to bending test with cyclic load. **Latin American Journal of Solids and Structures**, v. 17, n. 3, p. 266, 2020.

RILEM TECHNICAL COMMITTEES (RILEM TCS). Determination of the fracture energy of mortar and concrete by means of three-point bend tests on notched beams. **Materials and Structures**, v. 18, n. 106, p. 287–290, 1985.

ROMBACH, G. A.; HENZE, L. Querkrafttragfähigkeit von Stahlbetonplatten ohne Querkraftbewehrung unter konzentrierten Einzellasten. **Beton- und Stahlbetonbau**, v. 112, n. 9, p. 568–578, 2017.

ROMBACH, G. A.; LATTE, S. Shear resistance of bridge decks without shear reinforcement. In: **Proceedings of the International Fib Symposium**, Tailor Made Concrete Structures, 2008.

ROMBACH, G. A.; VELASCO, R. R. Schnittgrößen auskragender fahrbahnplatten infolge von radlasten nach DIN-fachbericht. **Beton- und Stahlbetonbau**, v. 100, n. 5, p. 376–384, 2005.

ROMBACH, G.; LATTE, S. Querkrafttragfähigkeit Von Fahrbahnplatten Ohne Querkraftbewehrung. **Beton- und Stahlbetonbau**, v. 104, n. 10, p. 642–656, 2009.

SAGASETA, J.; MUTTONI, A.; FERNÁNDEZ RUIZ, M.; TASSINARI, L. Non-axis-symmetrical punching shear around internal columns of RC slabs without transverse reinforcement. **Magazine of Concrete Research**, v. 63, n. 6, p. 441–457, 2011.

SAGASETA, J.; TASSINARI, L.; FERNÁNDEZ RUIZ, M.; MUTTONI, A. Punching of flat slabs supported on rectangular columns. **Engineering Structures**, v. 77, p. 17–33, 2014.

SAGASETA, J.; VOLLUM, R. L. Influence of aggregate fracture on shear transfer through cracks in reinforced concrete. **Magazine of Concrete Research**, v. 63, n. 2, p. 119–137, 2011.

SAGASETA, J.; VOLLUM, R. L. Shear design of short-span beams. **Magazine of Concrete Research**v. 62, n. 4, p. 267–282, 2010.

SAHMARAN, M.; YÜCEL, H. E.; YILDIRIM, G.; AL-EMAM, M.; LACHEMI, M. Investigation of the Bond between Concrete Substrate and ECC Overlays. **Journal of Materials in Civil Engineering**, v. 26, n. 1, p. 167–174, 2014.

SANTOS, D. P.; FERNANDES NETO, J. A. D.; REGINATO, L.; CARRAZEDO, R. Optimized design of RC deep beams based on performance metrics applied to strut and tie model and in-plane stress conditions. **Latin American Journal of Solids and Structures**, v. 16, n. 7, p. 212, 2019.

SERNA-ROS, P.; FERNANDEZ-PRADA, M. A.; MIGUEL-SOSA, P.; DEBB, O. A. R. Influence of stirrup distribution and support width on the shear strength of reinforced concrete wide beams. **Magazine of Concrete Research**v. 54, n. 3, p. 181–191, 2002.

SETIAWAN, A.; VOLLUM, R. L.; MACORINI, L.; IZZUDDIN, B. A. Punching of RC slabs without transverse reinforcement supported on elongated columns. **Structures**, v. 27, p. 2048–2068, 2020.

SHOUKRY, M. E.; TARABIA, A. M.; YASSIN, A. M. Punching shear strength of ultra-high-performance fibre concrete slab–column connections. **Proceedings of the Institution of Civil Engineers - Structures and Buildings**, v. 14, p. 1–13, 2020.

SHU, J.; PLOS, M.; ZANDI, K.; ASHRAF, A. Distribution of shear force: A multi-level assessment of a cantilever RC slab. **Engineering Structures**, v. 190, p. 345–359, 2019.

SIA. **Code 262 for concrete structures**. Zürich: Swiss Society of Engineers and Architects, 2013.

SIGRIST, V.; BENTZ, E.; FERNÁNDEZ RUIZ, M.; FOSTER, S.; MUTTONI, A. Background to the fib Model Code 2010 shear provisions - part I: beams and slabs. **Structural Concrete**, v. 14, n. 3, p. 195–203, 2013.

SOUSA, A. M. D.; EL DEBS, M. K. Shear strength analysis of slabs without transverse reinforcement under concentrated loads according to ABNT NBR 6118:2014. **IBRACON Structures and Materials Journal**, v. 12, n. 3, p. 658–693, 2019.

SOUSA, A. M. D.; LANTSOGHT, E. O. L.; EL DEBS, M. K. Database of wide beams and slabs under concentrated loads failing in different shear failure modes. **Zenodo**, 2020. Available in: https://zenodo.org/record/4059803#.Y3OQXOTMJPY.

SOUSA, A. M. D.; LANTSOGHT, E. O. L.; EL DEBS, M. K. Database of wide members without Stirrups Failing in Shear. **Zenodo**. 2019. Available in: https://zenodo.org/record/3530823#.Y3OX-OTMJPY

SOUSA, A. M. D.; LANTSOGHT, E. O. L.; EL DEBS, M. K. Databases of one-way slabs under concentrated loads: parameter analyses and validation of the proposed approach. **Zenodo**, 2022. Available in: https://zenodo.org/record/5911469.

SOUSA, A. M. D.; LANTSOGHT, E. O. L.; EL DEBS, M. K. One-way shear strength of wide reinforced concrete members without stirrups. **Structural Concrete**, n. January, p. 1–25, 2020.

SOUSA, A. M. D.; LANTSOGHT, E. O. L.; GENIKOMSOU, A. S.; KRAHL, P. A.; EL DEBS, M. K. Behavior and punching capacity of flat slabs with the rational use of UHPFRC: NLFEA and analytical predictions. **Engineering Structures**, v. 244, p. 112774, 2021b.

SOUSA, A. M. D.; LANTSOGHT, E. O. L.; SETIAWAN, A.; EL DEBS, M. Transition from one-way to two-way shear by coupling LEFEA and the CSCT models. In: **Proceedings of the fib symposium 2021, concrete structures: new trends for eco-efficiency and performance,** Lisbon, Portugal, 2021a.

SOUSA, A. M. D.; LANTSOGHT, E. O. L.; YANG, Y.; EL DEBS, M. K. Extended CSDT model for shear capacity assessments of bridge deck slabs. **Engineering Structures**, v. 234, p. 111897, 2021c.

SPASOJEVIC, A.; REDAELLI, D.; MUTTONI, A. Thin UHPFRC slabs without conventional reinforcement as light-weight structural elements. In: **fib symposium london 2009**, London, UK¸ 2009

SPECK, K. **Beton unter mehraxialer Beanspruchung Concrete under multiaxial loading conditions**. PhD Thesis. University of Dresden, 2008.

SUTER. R, MOREILLON, L. Punching shear strength of high performance fiber reinforced concrete slabs. In: **3rd fib international congress**, WASHINGTON (USA) 2010.

TAYLOR, H. P. Investigation of the dowel shear forces carried by the tensile steel in reinforced concrete beams. **Cement and Concrete Association**, 1969.

TAYLOR, H. P. J. The fundamental behavior of reinforced concrete beams in bending and shear. **ACI Special Publication**, v. 42, p. 43–78, 1974.

TENÓRIO, D. A.; GOMES, P. C. C.; DÉSIR, J. M.; UCHÔA, E. L. M. Analysis of accidental loads on garage floors. **IBRACON Structures and Materials Journal**, v. 7, n. 4, p. 560–571, 2014.

THEODORAKOPOULOS, D. D.; SWAMY, N. Contribution of steel fibers to the strength characteristics of lightweight concrete slab-column connections failing in punching shear. **ACI Structural Journal**, v. 90, n. 4, p. 342–355, 1993.

TRAN, N. L. A mechanical model for the shear capacity of slender reinforced concrete members without shear reinforcement. **Engineering Structures**, v. 219, p. 110803, 2020.

TUNG, N. D.; TUE, N. V. A new approach to shear design of slender reinforced concrete members without transverse reinforcement. **Engineering Structures**, v. 107, p. 180–194, 2016a.

TUNG, N. D.; TUE, N. V. Effect of support condition and load arrangement on the shear response of reinforced concrete beams without transverse reinforcement. **Engineering Structures**, v. 111, p. 370- 382, 2016b.

VAZ RODRIGUES, R.; FERNÁNDEZ RUIZ, M.; MUTTONI, A. Shear strength of R/C bridge cantilever slabs. **Engineering Structures**, v. 30, p. 3024–3033, 2008.

VAZ RODRIGUES, R.; MUTTONI, A.; BURDET, O. Large Scale Tests on Bridge Slabs Cantilevers Subjected to Traffic Loads. In: **Proceedings of the 2nd international congress fib,** Naples, Italy. 2006.

VECCHIO, F. J.; COLLINS, M. P. The Modified Compression-Field Theory for Reinforced Concrete Elements Subjected to Shear. **ACI Journal Proceedings**, v. 83, n. 2, p. 219–231, 1986.

VIDA, R.; HALVONIK, J. Experimentálne overovanie šmykovej odolnosti mostovkových dosiek (Experimental verification of shear resistance of bridge deck slabs). **Inžinierske stavby/Inženýrské stavby**, n. 4, p. 2–6, 2018.

VIDAKOVI, A.; HALVONIK, J. Shear resistance of clamped deck slabs assessed using design equations and FEM analysis. In: **13th international conference modern building materials, structures and techniques,** 2019.

VOLLUM, R. L.; FANG, L. Shear enhancement near supports in RC beams. **Magazine of Concrete Research**, v. 67, n. 9, p. 443–458, 2015.

VOO, J. Y. L.; FOSTER, S. J. Tensile-fracture of fibre-reinforced concrete: variable engagement mode. **6th International RILEM Symposium on Fibre Reinforced Concretes**, n. September, p. 875–884, 2004.

VOO, J. Y. L.; FOSTER, S. J. Variable Engagement Model for the Fibre Reinforced Concrete in Tension. In: **Proceedings Advanced Materials for Construction of Bridges, Buildings, and Other Structures III**, Davos, Switzerland, 2003.

WALRAVEN, J. C. **Aggregate Interlock: a Theoretical and Experimental Analysis**. 1980. PhD. Thesis, Delft University of Technology, 1980.

WALRAVEN, J. C. Fundamental Analysis of Aggregate Interlock. **Journal of the Structural Division**, ASCE, v. 107, n. 11, p. 2245–2270, 1981.

WALRAVEN, J. C.; LEHWALTER, N. Size Effects in Short Beams Loaded in Shear. **ACI Structural Journal**, v. 91, n. 5, p. 585–593, 1994.

WEI, J.; WU, C.; CHEN, Y.; LEUNG, C. K. Y. Shear strengthening of reinforced concrete beams with high strength strain-hardening cementitious composites (HS-SHCC). **Materials and Structures/Materiaux et Constructions**, v. 53, n. 4, p. 1–15, 2020.

WIDIANTO; BAYRAK, O.; JIRSA, J. O. Two-Way Shear Strength of Slab-Column Connections: Reexamination of ACI 318 Provisions. **ACI Structural Journal**, v. 106, n. 2, p. 160–170, 2009.

WU, X.; YU, S.; XUE, S.; KANG, T. H.-K.; HWANG, H.-J. Punching shear strength of UHPFRC-RC composite flat plates. **Engineering Structures**, v. 184, p. 278–286, 2019.

XENOS, D.; GRASSL, P. Modelling the failure of reinforced concrete with nonlocal and crack band approaches using the damage-plasticity model CDPM2. **Finite Elements in Analysis and Design**, v. 117–118, p. 11–20, 2016.

YANG, Y. **Shear Behaviour of Reinforced Concrete Members without Shear Reinforcement: A New Look at an Old Problem**. PhD. Thesis, Delft University of Technology, 2014.

YANG, Y.; DEN UIJL, J.; WALRAVEN, J. C. Critical shear displacement theory: on the way to extending the scope of shear design and assessment for members without shear reinforcement. **Structural Concrete**, v. 17, n. 5, p. 790–798, 2016.

YANG, Y.; DEN UIJL, J.; WALRAVEN, J. C. Residual Shear Capacity of 50 years Old RC Solid Slab Bridge Decks. In: **INTERNATIONAL IABSE CONFERENCE: ASSESSMENT, UPGRADING AND REFURBISHMENT OF INFRASTRUCTURES**, Rotterdam, 2013.

YANG, Y.; WALRAVEN, J. C.; DEN UIJL, J.. Shear Behavior of Reinforced Concrete Beams without Transverse Reinforcement Based on Critical Shear Displacement. **Journal of Structural Engineering**, v. 143, n. 1, p. 04016146, 2017.

YU, Q.; LE, J. L.; HUBLER, M. H.; WENDNER, R.; CUSATIS, G.; BAŽANT, Z. P. Comparison of main models for size effect on shear strength of reinforced and prestressed concrete beams. **Structural Concrete**, v. 17, n. 5, p. 778–789, 2016.

YU, Q.; LE, J. L.; HUBLER, M. H.; WENDNER, R.; CUSATIS, G.; BAŽANT, Z. P. **Comparison of main models for size effect on shear strength of reinforced and prestressed concrete beams**, Structural Engineering Report No. 15-03/936x, Prepared for ACI Committee 445, Shear and Torsion, 2015.

ZHENG, Y.; TAYLOR, S.; ROBINSON, D.; CLELAND, D. Investigation of ultimate strength of deck slabs in steel-concrete bridges. **ACI Structural Journal**, v. 107, n. 1, p. 82–91, 2010.

ZHU, H.-G.; LEUNG, C. K. Y.; CAO, Q. Preliminary Study on the Bond Properties of the PDCC Concrete Repair System. **Journal of Materials in Civil Engineering**, v. 23, n. 9, p. 1360–1364, 2011.

ZHU, Y.; ZHANG, Y.; HUSSEIN, H. H.; CHEN, G. Numerical modeling for damaged reinforced concrete slab strengthened by ultra-high performance concrete (UHPC) layer. **Engineering Structures**, v. 209, p. 110031, 2020.

ZHU, Z.; YUAN, T.; XIANG, Z.; HUANG, Y.; ZHOU, Y. E.; SHAO, X. Behavior and Fatigue Performance of Details in an Orthotropic Steel Bridge with UHPC-Deck Plate Composite System under In-Service Traffic Flows. **Journal of Bridge Engineering**, v. 23, n. 3, p. 04017142, 2018.

ZOHREVAND, P.; MIRMIRAN, A. Behavior of Ultrahigh-Performance Concrete Confined by Fiber-Reinforced Polymers. **Journal of Materials in Civil Engineering**, v. 23, n. 12, p. 1727–1734, 2011.

ZOHREVAND, P.; YANG, X.; JIAO, X.; MIRMIRAN, A. Punching Shear Enhancement of Flat Slabs with Partial Use of Ultrahigh-Performance Concrete. **Journal of Materials in Civil Engineering**, v. 27, n. 9, p. 04014255, 2014.

ZSUTTY, B. Beam Shear Strength Prediction by Analysis of Existing Data. **ACI Journal Proceedings**, v. 5, n. 65–71, p. 943–951, 1968.